School of Science
Department of Physics and Astronomy

Novel Enhancements of Cyclotron Based Production, Purification & Applications of the PET Radionuclide Copper-61: Complexation to Nanospheres for Biomedical Imaging

Ali Haidar Kasim Asad

This Thesis is presented for the Degree of

Doctor of Philosophy

of

Curtin University

April 2016

Declaration

To the best of my knowledge and belief this thesis contains no material previously published by any other person except where due acknowledgment has been made.

This thesis contains no material which has been accepted for the award of any other degree or diploma in any university.

The research presented and reported in this thesis was conducted in compliance with the National Health and Medical Research Council Australian code for the care and use of animals for scientific purposes 8th edition (2013). The proposed research study received animal ethics approval from the Curtin University Animal Ethics Committee, Approval Number # AEC_2015_26 (CP212015).

Signature: Ali Asad

Date: 5 April 2016

Abstract

Over the last three decades, cyclotron-produced radioisotopes have attracted considerable interest for biomedical applications. For example, the positron emission tomography (PET) isotopes ^{18}F, ^{11}C, ^{13}N and ^{15}O have established roles in diagnosis and management of human diseases, or in research into their mechanisms, particularly in oncology, cardiology and neurology. However, in recent years many advanced cyclotron sites have also added solid targetry systems to produce PET radiometals and radiohalides with half-lives ranging from several minutes (e.g. ^{60}Cu) to several days (e.g. ^{89}Zr & ^{124}I). The predominant reactions are (p,x), with equipment-limited primary proton energies of less than 19 MeV. These transmutations facilitate chemical extraction and purification of products with high no-carrier-added (NCA) specific activities because the product atomic number (Z) is usually different from that of the target. The relatively long physical half-lives of some of the products are in accord with the characteristic lifetimes of biodistributions of numerous therapeutic and diagnostic (theranostic) agents that utilise monoclonal antibodies, their bioengineered constructs or nanoparticles as target-seeking delivery platforms. A typical target would be a tumour-cell surface receptor. Though the radioisotope may be chosen for its half-life and radioactive emission, its independent chemical properties may pose challenges for bonding or complexing to a targeting ligand. Copper isotopes are an exemplar.

Recent advances in the complexation of copper isotopes using bifunctional macrocyclic chelators such as DOTA, NOTA and sarcophagine (sar) derivatives have facilitated biomedical applications of the PET-reporter isotopes ^{61}Cu and ^{64}Cu, as well as the promising radiotherapy isotope ^{67}Cu. With its 'intermediate' half-life of 3.33 h, ^{61}Cu seems particularly well-positioned to; (i) map the biodistributions of engineered-antibody immunoPET constructs such as diabodies and minibodies; (ii) label nanospheres (NS) delivering theranostic agents to tumours using the enhanced permeation-retention (EPR) effect and;

(iii) construct metal-chelator imaging compounds such as Cu-ATSM that target hypoxic tissue, for example in the cores of some solid tumours. However, in order to apply these tools to phase-I studies of human diseases, numerous preliminary validation studies (including dosimetry) are required to be performed on cell cultures and animal models.

This thesis describes novel contributions to the production and purification of ^{61}Cu, its complexation to bifunctional macrocyclic and sarcophagine chelators and its application as a PET imaging agent in a murine model for quantitatively mapping the *in vivo* biodistribution of functionalised silica nanospheres (Si NS). The thesis has been divided into three parts, according to the linked categories of investigations.

The first category focussed on optimization of the cyclotron-based production of ^{61}Cu by refining the solid targetry technique and measuring the excitation functions for products arising from the chosen production nuclear reaction. Specifically;

(i) using ^{nat}Cu(p,xn) monitor reactions, the stacked-foils technique was used to devise a novel simple and precise method for measuring the primary proton beam energy of an isochronous auto-extraction cyclotron. This was performed before and following a major upgrade of the ion sources and non-magnetic beam controls, converting a (nominal) 18/9 MeV (proton/deuteron) configuration to 18/18 MeV (proton/proton). This acquired knowledge assisted in optimizing solid-targetry yields and facilitated subsequent precise measurements of reaction cross sections, particularly that yielding ^{61}Cu. Measured proton beam energy was 18.03 MeV ± 0.02 (SD) and 18.11 MeV ± 0.05 (NS) before and following the upgrade, respectively.

(ii) This study also evaluated the excitation functions of ^{nat}Zn (p,x) reactions using a high purity natural-zinc target, proton energies up to 17.6 MeV and employing the stacked-foils technique; yielding the products ^{61}Cu, ^{66,67,68}Ga and

^{65}Zn. Thick-target integral yields were also deduced from the measured excitation functions, in particular for the ^{nat}Zn(p,α)^{61}Cu reaction. All results agreed well with the recent published literature and can contribute to the statistical weighting of published data for assembly of the 'best' composite excitation function from published results, for most of the reactions of the ^{nat}Zn(p,x) set.

The second category of investigations devised an improved method for the production and chemical separation of ^{61}Cu from ^{nat}Zn or enriched ^{64}Zn targets. Subsequently, the complexation of ^{61}Cu by three different chelators was compared, using the macrocyclic bifunctional chelators NOTA-NCS and DOTA-NCS plus the macrobicyclic sarcophagine diamsar. Specifically;

(i) an improved chemical separation method using one or three types of resins (for ^{64}Zn target and ^{nat}Zn target respectively) was developed to rapidly isolate ^{61}Cu as the chloride with high (> 99%) radionuclide purity from the co-produced gallium radionuclides and the target material into separate collections, allowing recycling of target ^{64}Zn, if relevant.

(ii) In replicated experiments the effective specific activity of ^{61}Cu was determined by titration with each of the three chelating agents. Results ranged from 4.7 ± 0.2 (SD) to 412.5 ± 15.3 MBq/μg (corrected to EOB), with diamsar yielding the highest value. For comparison, NCA specific activity determined following radioactive decay using ICP-MS ranged from 143.3 ± 14.3 to 506.2 ± 50.6 MBq/μg. There was reasonable agreement between the two estimates of specific activity for diamsar only. ICP-MS also revealed that the good results for diamsar were achieved despite relatively high background concentrations of Zn^{+2} and Pb^{2+}, demonstrating the high specificity of the sarcophagine for Cu^{2+}. These metals compete with Cu^{2+} when using DOTA or NOTA and explain the lack of agreement between titration and ICP-MS for these chelators. This study revealed the importance of choice of chelator when determining the specific activity using the titration method.

In the final category of investigations functionalised polystyrene nanospheres (PS NS) of different sizes and functionalised silica nanospheres (Si NS) were radiolabelled with ^{64}Cu (plus ^{57}Co as comparator) and ^{61}Cu, respectively, using the bifunctional chelators SarAr-NH_2 (PS NS only), NOTA-NCS, DOTA-NCS and 'MeSar-Ph-NCS' (the last, Si NS only). This last molecule is a novel Cu^{2+}-chelating sarcophagine, [Mg(CH_3)(*p*-NCS-Ph)Sar](CF_3SO_3)$_2$, developed recently by collaborators of our laboratory. (The metal protector magnesium ion is extruded from the molecule following conjugation to the nanosphere and prior to radiolabelling). Copper-61 labelled Si NS were then injected into normal immunodeficient mice and their *in vivo* biodistributions were measured by μPET/CT imaging. Biodistributions were also measured directly by post-imaging dissection and γ-counting of major organs and tissues. Specifically;

(i) carboxylate-functionalised PS NS of three sizes ranging from 365 to 840 nm were conjugated with SarAr-NH_2 and labelled with $^{57}Co^{2+}$ and $^{64}Cu^{2+}$ (the latter 680 nm only). Increasing the labelling temperature (23^{o}C to 37^{o}C) and reaction time (1.25 h to 24 h) improved the labelling efficiency for ^{57}Co but not for ^{64}Cu. The number of SarAr molecules conjugated to the NS depended on available functional groups present on the surfaces of the NS. This study provided valuable pilot data for subsequent radiolabelling of Si NS.

(ii) In separate and replicated experiments, amino-functionalised Si NS of nominal diameter 100 nm were conjugated with the novel bifunctional chelator MeSar-Ph-NCS and compared with NOTA-NCS and DOTA-NCS for stability of radiocopper labelling and chelator occupancy on the nanosphere surface. The *in vitro* stabilities of all ^{61}Cu-chelator-Si NS complexes were approximately equal; however the occupancy areal density of radiolabelled MeSar-Ph-NCS molecules on the Si NS surface was approximately double the areal densities of radiolabelled NOTA-NCS or DOTA-NCS.

(iii) In replicated experiments the *in vivo* biodistributions at one and four hours post-injection of the radiolabels ^{61}Cu (delivered as the aqueous chloride),

^{61}Cu-MeSar-Ph-NCS-Si NS, ^{61}Cu-NOTA-NCS-Si NS and ^{61}Cu-DOTA-NCS-Si NS were evaluated using µPET/CT. A normal immunodeficient-mouse model was chosen in anticipation of later parallel experiments employing xenograft tumours (beyond the scope of this thesis). Immediately following the four-hour imaging time-point, the biodistribution for each radiolabel was also determined directly by dissection and γ-counting.

For the control group injected with ^{61}Cu-chloride, the dissection-derived biodistribution (4 h) revealed mainly uptake in liver (including gallbladder) and kidneys as expected, with lower uptakes in lung, stomach, spleen and bladder. The quantitative µPET images at 1 and 4 h confirmed the liver uptake. Dissection-derived biodistributions for the three ^{61}Cu-chelator-Si NS radiolabels at 4 h were broadly similar, showing marked uptake in the spleen (43-70% of injected dose/g tissue [%ID/g]) with substantial but less uptake in the liver-plus-gall bladder (39-48%ID/g), and approximately the same levels as controls in the kidneys (6-10%ID/g). However the activity level of ^{61}Cu-MeSar-Ph-NCS-Si NS in the lungs and bladder exceeded (37.4 ± 5.7%ID/g and 14.9 ± 1.9%ID/g that for the ^{61}Cu-NOTA-NCS and ^{61}Cu-DOTA-NCS (macrocyclic) radiolabelled NS. These results were broadly confirmed by analysis of µPET images at both 1 and 4 h, though the apparent lungs uptake of ^{61}Cu-MeSar-Ph-NCS-Si NS was not as markedly different from the other chelators as for the dissection-derived data.

These are the first reported *in vivo* biodistribution studies for the novel bifunctional sarcophagine chelator MeSar-Ph-NCS conjugated to NS. The reason for the enhanced uptake of MeSar-Ph-NCS-conjugated NS in the lungs compared to two commonly used (macrocyclic) bifunctional copper chelators is unknown. It may have been caused by deconjugation of ^{61}Cu-MeSar-Ph-NCS from the NS *in vivo*, or it may be an intrinsic pharmacokinetic property of the entire radiolabelled complex. A possible explanation is a relatively high net positive charge on the ^{61}Cu-MeSar moiety, leading to binding of the sarcophagine-mediated complex to the net negatively charged lung interstitial tissues. A relatively high uptake of ^{61}Cu-MeSar-Si NS was not seen in the

kidneys compared with NOTA and DOTA, where net negatively charged basal cells of the glomerulus might have been expected to elicit the same qualitative effect as in the lungs. However, the Si NS size of about 100 nm may preclude any of the ^{61}Cu-labelled Si NS complexes from accumulating in the kidneys, which are refractory to NS sizes above about 5 nm.

In any event, these results strongly suggest that despite the relative advantages of MeSar-Ph-NCS as a bifunctional chelator (room-temperature conjugation chemistry, relatively rapid conjugation, relatively high occupancy areal-density on NS, high elemental specificity for copper-chelation), its accumulation and (when radiolabelled) related dose burden in the lungs require further study.

These linked studies of the PET radioisotope ^{61}Cu, from cyclotron-based production to its radiotracer application in a murine model, have contributed to its more efficient production and purification plus its comparative evaluation in radiolabelling of Si NS using different Cu^{2+} bifunctional chelators, including a novel sarcophagine chelator developed by a collaborating laboratory. This 'proof-of-principle' application of ^{61}Cu as a PET imaging agent for mapping the temporal biodistributions of Si NS in an immunodeficient murine model will contribute to future laboratory-based studies of the growth mechanisms and treatments of human tumours such as (metastatic ovarian cancer), plus other applications using Si NS with less than 100 nm size. Some of the outcomes may in time be translated to the patient bedside.

Acknowledgments

First and foremost, I give my sincere gratitude to my supervisor Adjunct Professor Roger Price for giving me the opportunity to do my PhD project work in the Department of Medical Technology and Physics, Sir Charles Gairdner Hospital. I also want to thank him for his support and patience during the course my thesis, and for sharing his knowledge with so much enthusiasm as well as encouraging me to work independently.

I am very much thankful to my co-supervisors, Adjunct Professor Suzanne Smith and Dr Laurence Morandeau for their expert guidance, valuable suggestions and for their patience in answering all my questions.

My warmest thanks to Dr Salim Siddiqui for his support during the completion of my PhD program at Curtin University of Technology.

I also want to thank the friendly and cheerful group of radiochemists and engineers from the RAPID (Radiopharmaceutical Production and Development) Laboratories whom I was blessed to share my daily work with, especially Charmaine Jeffery, David Cryer, Dr Joe Ioppolo and Sun Chan for their help and support.

I thank A/ Prof. Paul Donnelly from Melbourne University for kindly providing the MeSar-Ph-NCS chelator and for his advice. I would also like to thank the ChemCentre (Bentley, WA) and the Department of Physics (Curtin University) for ICP-MS and TEM images analyses.

It has been a privilege to collaborate with some wonderful researchers from around Australia. Sincere thanks to Dr Carleen Cullinane and her group for giving me the opportunity to visit Peter MacCallum Cancer Centre and work in her laboratory. I would also like to thank Adjunct Professor Suzanne Smith's

group at ANSTO, especially Dr Eskender Mume and Dr Linggen Kong for their help and support during my time over there. Big thanks to the staff of the CIF at the Harry Perkins Institute for Medical Research (particularly Kirsty Richardson and Penny Maton) for their assistance with the small-animal PET imaging and Prof. Juliana Hamzah for her help with the retro-orbital injections of the mice.

Finally, my special thanks go to all my family, especially my mum for her unconditional support and my wife for her patience and encouragement throughout my studies. Words cannot express my happiness and love for my newborn son Amin, who came to the world during the final editing of this thesis. Thank you.

Primary Publications

- Asad, A.H., Smith, S.V., Morandeau, L.M., Chan, S., Jeffery, C.M., & Price, R.I. (2014). Production of ^{61}Cu by the ^{nat}Zn(p,a) reaction: improved separation and specific activity determination by titration with three chelators. *Journal of Radioanalytical & Nuclear Chemistry, 307,*899-906.

- Asad, A.H., Chan, S., Cryer, D., Burrage, J.W., Siddiqui, S.A., & Price, R.I. (2015). A new, simple and precise method for measuring cyclotron proton beam energies using the activity vs. depth profile of zinc-65 in a thick target of stacked copper foils. *Applied Radiation and Isotopes, 105,* 20-25.

- Asad, A.H., Chan, S., Morandeau, L.,Cryer, D., Smith, S.V., & Price, R.I. (2014). Excitation functions of ^{nat}Zn(p,x) nuclear reactions with proton beam energy below 18 MeV . *Applied Radiation and Isotopes, 94,* 67-71.

Secondary Publications

- Burrage, J.W., Asad, A.H., Fox, R.A., Price, R.I., Campbell, A.M., & Siddiqui, S. (2009). A Simple Method to Measure Proton Beam Energy in a Standard Medical Cyclotron. *Australian Physical & Engineering Sciences in Medicine, 32,* 92-97. Kenneth Clarke Journal Prize for the best paper in volume 32.

- Mume, E., Asad, A., Di Bartolo, N.M., Kong, L., Smith, C., Sargeson, A.M., Price, R., & Smith, S.V. (2013). Synthesis of hexa aza cages, SarAr-NCS and AmBaSar and a study of their metal complexation, conjugation to nanomaterials and proteins for application in radioimaging and therapy. *Dalton Transactions, 42,* 14402-14410.

Refereed Conference Proceedings

- Asad, A.H., Smith, S.V., Chan, S., Jeffery, C.M., Morandeau, & L., Price, R.I. (2012). Cyclotron Production of ^{61}Cu using Natural Zn & Enriched ^{64}Zn Targets. *AIP Conference Proceedings, 1509,* 91-95; doi: 10.1063/1.4773947.

- Jeffery, C.M., Smith, S.V., Asad, A.H., Chan, S., & Price, R.I. (2012). Routine production of copper-64 using 11.7MeV protons. *AIP Conference Proceedings, 1509,* 84-90; doi: 10.1063/1.4773946.

- Scharli, R.K., Price, R.I., Chan, S., Cryer, D., Jeffery, C.M., Asad, A.H., Morandeau, L., Cullinane, C., Kasbollah, A., & Katsifis, A. (2012). Establishing reliable production of the PET isotope ^{89}Zr for research use: from target fabrication to preclinical imaging. *AIP Conference Proceedings, 1509,* 101-107: doi: 10.1063/1.4773949.

Conference Presentations and Posters

- Ali.H.Asad et al., Precise Measurement of the Primary Proton Beam Energy of an IBA 18/9 Cyclotron Using the Stacked Copper Foils Technique: Effect of Foils Thickness & Beam Straggling, Australian and New Zealand Society of Nuclear Medicine Conference Sydney, Australia, 23-27 April, 2009.

- Ali.H.Asad et al., Precise Measurement of the Primary Proton Beam Energy of an IBA 18/9 Cyclotron Using the Stacked Copper Foils Technique: Effect of Foils Thickness & Beam Straggling, 7th IBA Users' Meeting, Istanbul, Turkey, 2009.

- Ali.H.Asad et al., Production of no carrier added ^{64}Cu & ^{55}Co from a natural nickel solid target using an 18MeV cyclotron proton beam, Proceedings of the 13th International Workshop on Targetry and Target Chemistry. Riso, Denmark, 2010.

- Ali.H.Asad et al., Cyclotron Production of ^{61}Cu using an Natural Zn and Enriched ^{64}Zn Targets, Proceedings of the 14th International Workshop on Targetry and Target Chemistry. Cancun, Mexico, 26-29 August, 2012.

- Ali.H.Asad et al., Optimisation of conjugation & ^{64}Cu-radiolabelling efficiency of carboxylic acid-functionalised polystyrene nanoparticles using the bifunctional copper chelator SarAr, Australian and New Zealand Society of Nuclear Medicine conference, Perth, Australia, 11-15 April, 2013.

- Ali.H.Asad et al., Solid-targetry production & purification of the radiometal PET isotope ^{61}Cu & its chelation by the sarcophagine DiamSar, Australian and New Zealand Society of Nuclear Medicine conference, Perth, Australia, 11-15 April, 2013.

- Ali.H.Asad et al., Optimisation of conjugation & ^{64}Cu-radiolabelling efficiency of polystyrene nanoparticles functionalised with carboxylate groups using the bifunctional copper chelator SarAr, Proceedings of the 13th International Symposium on Radiopharmaceutical Sciences 2013. Jeju Island, Korea, 12-17 May, 2013.

- Ali.H.Asad et al., Excitation Functions of ^{nat}Zn(p,x) Nuclear Reactions with Proton Beam Energy Below 18MeV, Proceedings of the 14th International Workshop on Targetry and Target Chemistry. Prague, Czech Republic Mexico, 18-21 August, 2014.

- Ali.H.Asad et al., Quality assurance of ^{61}Cu using ICP mass spectroscopy and metal complexation, Proceedings of the 14th International Workshop on Targetry and Target Chemistry. Prague, Czech Republic Mexico, 18-21 August, 2014.

Table of Contents

List of Figures

CHAPTER ONE

CHAPTER TWO

CHAPTER THREE

CHAPTER FOUR

CHAPTER FIVE

CHAPTER SIX

List of Tables

CHAPTER ONE

CHAPTER TWO

CHAPTER THREE

CHAPTER FOUR

CHAPTER FIVE

CHAPTER SIX

List of Abbreviations

%ID/g	Percentage injected dosage per gram
AG 1-X8	Anion exchange column packed with AG 1-X8 resin
AG50W-X8	Cation exchange column packed with AG50W-X8
ANSTO	Australian Nuclear Science and Technology Organisation
ATSM	Diacetyl-bis (N^4- methylthiosemicarbazone)
BFCs	Bifunctional chelators
diamsar	3,6,10,13,16,19 hexaazabicyclo[6.6.6] eicosane- 1, 8-diamine pentahydrate
DOTA	1,4,7,10-tetra-azacylcododecane-N,N′,N″,N‴-tetraacetic acid
DTPA	Diethylenetriamine pentaacetic acid
EBT	Gafchromic films
EDC	*N*-(3-Dimethylaminopropyl)-ethyl-*N*′-carbodiimide hydrochloride
EDTA	Ethylenediamine tetraacetic acid

EOB	End of bombardment
EOS	End of synthesis
EPR	Enhanced permeability and retention
ESA	Effective specific activity
EXFOR	Experimental nuclear reaction
FBS	Fetal bovine serum
FDG	[^{18}F]2-fluoro-D-deoxyglucose
HCl	Hydrochloric acid
HPGe	High-purity germanium detector
IAEA	International atomic energy agency
ICP-MS	Inductively coupled mass spectrometry
ITLC	Instant thin layer chromatography
MES	2-(N-morpholino)-ethanesulfonic acid
MRI	Magnetic resonance imaging
NCA	No-carrier-added
NCA-SA	Non-carrier-added specific activity

NOTA	1,4,7,10-triazacyclononane-1,4,7-N,N′,N″,N‴-triacetic acid
NPs	Nanoparticles
OI	Optical imaging
OSEM	Ordered-subset expectation maximization
PBS	Phosphate buffer saline
PEG	Polyethylene glycol
PET	Positron emission tomography
P NPs	Polymeric nanoparticles
PS NS	Polystyrene nanospheres
DOTA-NCS	2-(4-isothiocyanatobenzyl)-1,4,7,10-tetraazacyclododecane-1,4,7,10-tetraacetic acid
NOTA-NCS	S-2-(4-isothiocyanatobenzyl)-1,4,7-triazacyclononane-1,4,7-tetraacetic acid
PTSM	Pyruvaldehyde-bis(N^4-methylthiosemicarbazone)
RBC	Red blood cells
RES	Reticuloendothelial system
RF	Electric field

ROI	Region of interest
RT	Room temperature
SarAr	1-*N*-(4-aminobenzyl)-3,6,10,13,16,19 hexaazabicyclo[6.6.6] eicosame-1,8-diamine
Si NS	Silica nanospheres
SPECT	Single photon emission computed tomography
SRIM	Stopping and range ions in matter
TEM	Transmission electron microscope
TEOS	Tetraethyl orthosilicate
TETA	1,4,8,11-tetraazacyclotetradecane-N,N′,N″,N‴-tetraacetic acid
TLA	Thin layer activation

List of Symbols

ε	Detection efficiency
A_{EOB}	Activity at end of bombardment
B	Magnetic field
CI	Confidence interval
CV	Coefficient of variation
D-	Deuteron
dE/dX	Stopping power
E	Beam energy in MeV
EC	Electron capture
E_p	Beam energy
E_{th}	Reaction threshold energy
F	Atom fraction
F	Lorentz force
F_f	Centrifugal force
H-	Hydrogen
I	Target current in μA
M	Molar mass
m	Particle mass
n	Neutron
n	Number of target nuclei per cm
N_A	Avogadro's number

N_c	Net peak area
P	Proton
Q	Charge
r	Orbit radius
SD	Standard deviation
T	Bombardment time
T	Kinetic energy
$T_{1/2}$	Half-life
T_c	Counting time
T_e	Elapsed time
T_{max}	Maximum kinetic energy
W_T	Thermal power
α	Alpha particle
β^-	Beta particle
β^+	Positron
γ	Gamma-ray
η	Branching fraction
λ	Decay constant
μm	Micrometer
ν	Velocity
ρ	Target material density
σ	Cross section
$\sigma(E)$	Excitation function

Φ	Incident proton flux (particles $s^{-1}.cm^{-2}$)
ω	Angular velocity
ν_e	Neutrino

CHAPTER ONE

INTRODUCTION AND LITERATURE REVIEW

1.1 Molecular Imaging

Molecular imaging allows the non-invasive visualization of molecular processes *in vivo*. The term "molecular imaging" implies the convergence of various disciplines from cell and molecular biology, chemistry, medicine, pharmacology, physics, bioinformatics, through to engineering (Ottobrini, Ciana, Biserni, Lucignani, & Maggi, 2006). Several modalities including positron emission tomography (PET), single photon emission computed tomography (SPECT), magnetic resonance imaging (MRI) and optical imaging (OI) have been developed for molecular imaging. A major advantage of PET and SPECT in molecular imaging is their high sensitivity and use of highly specific imaging agents (Saji et al., 2004; Massoud & Gambhir, 2003; Hong, Zhang, Sun, & Cai, 2009).

Molecular imaging has its roots in nuclear medicine and in many ways is a direct extension of that existing discipline. Nuclear medicine is a medical field that employs molecular imaging through the use of radioactive agents (e.g. radiopharmaceuticals), for the purpose of diagnosis and therapy of diseases. Radiopharmaceuticals range from tracers to measure blood flow and inflammation, to chemical species for measuring basic physiological function (e.g. energy metabolism) as well as the size and location of diseased tissues. These radiopharmaceuticals are used at low concentration levels and incorporate gamma (γ) ray- emitting radionuclides. The γ rays used in imaging are energetic enough to pass through the human tissues and can be externally detected. Thus, this process is markedly different from anatomical methods of imaging, such as x-ray imaging and magnetic resonance imaging (MRI). These latter methods are primarily used to characterise differences in density either by transmission (x-ray imaging) or by interactions of radiofrequency radiation with hydrogen nuclei

(MRI). Another difference is that in order to acquire a signal with sufficient spatial resolution by MRI about a millimole of material is required in each voxel (e.g. tissue mass, proton abundance) compared with only picomoles (radioactive nuclei) for radioisotopic imaging.

Molecular imaging is used as a tool for phenotype screening in drug development programs (Hoit, 2001). Transgenic or immune compromised animals are used in early drug discovery to "validate" target proteins and to evaluate the efficacy and toxicological effects of new test compounds for their potential use in humans (Livingston, 1999). The use of molecular imaging tools such as PET and SPECT in the drug discovery process offers an opportunity to study the pharmacokinetics of drugs and to identify dose-limiting toxicity *in vivo*. More importantly, trialing those drugs in animal models helps identify molecules most likely to succeed in humans. As an example, Figure 1.1 shows the types of receptors in breast cancers that have been selectively targeted using molecular imaging techniques. The contrast in the uptake of the molecular imaging agents allows one to identify where the breast cancers cells are in the body.

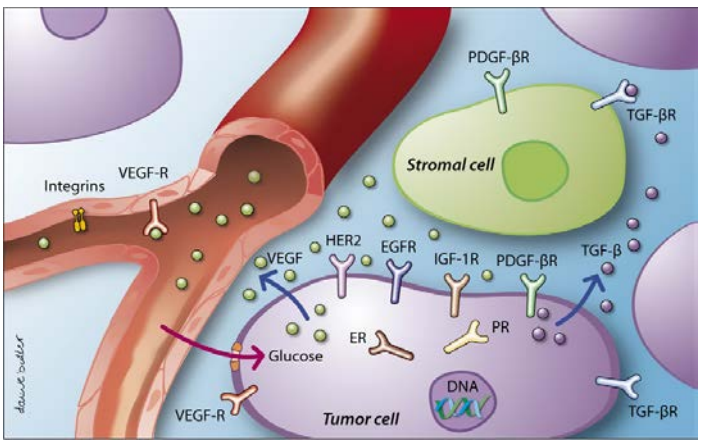

Figure 1.1 The potential targets for breast cancer molecular imaging (adapted from Oude Munnink et al., 2009).

1.2 Basic Principles of Positron Emission Tomography

Positron emission tomography (PET) is one of the most sensitive and specific techniques for imaging molecular pathways *in vivo.* It is based on the detection of small (nano-to picomolar) quantities of active molecules labelled with a positron emitter. Common PET radioisotopes currently used in the clinic include fluorine-18 (half-life=109.8 min), carbon-11 (half-life=20.33 min), nitrogen-13 (half-life=9.97 min) and oxygen-15 (half-life=2.03 min) (Ziegler, 2005), as well as other radioisotopes such as ^{60,61,64}Cu, ^{68}Ga, ^{89}Zr, ^{86}Y and ^{124}I (McCarthy et al., 1999; Avila-Rodriguez, Nye, & Nickles, 2007; Suzuki et al., 2011; Deri, Zeglis, Francesconi, & Lewis, 2013; Sadeghi, Kakavand, Mokhtari, & Giholamzadel, 2009B; Nye, Avila-Rodriguez, & Nickles, 2007) which are being investigated for various novel diagnostic and/or radiotherapeutic applications. These radionuclides are generally incorporated into biologically active compounds that play a specific role in living organisms (see Table 1.1) (Welch & Redvanly, 2005).

PET images are obtained from the administration of a radiopharmaceutical incorporating a positron (β^+) emitting radioisotope. The radioactive decay of positron emitting radioisotope occurs in the following manner

$$p \rightarrow n + \beta^+ + \nu_e \qquad (1)$$

The positron is a positively charged particle that is the antimatter counterpart to the electron. The emitted positron collides with matter as it travels a few millimetres into the tissue, losing its kinetic energy. Once most of the energy has been lost, the positron associates with an electron, forms a positronium intermediate which is unstable, and completely annihilates to give off two annihilation gamma photons (each energy = 511 keV) emitted at 180° from each other (Figure 1.2). When detected, within a short time window (~ nsec) (effectively in coincidence) their directions and the small difference in their arrival times at the detector are used in a statistical analysis of many such events

to resolve where the radioisotope is positioned in the body (Martinez, Ziegler, & Beyer, 2008).

A PET scanner consists of an array of detectors surrounding the subject, and linked by coincidence circuitry. A decay event is recorded when a pair of photons are received at connected detectors positioned 180^{o} from each other (Figure 1.3).

A large number of coincidence events are recorded across the detectors of the scanner. This information is used in complex computer algorithms to reconstruct the numerous events that have been registered into an image. This gives information on the spatial distribution of radioactivity as a function of time. Eventually, the recorded radioactivities can be calculated (in Bq/mL) as values representing the different voxel intensities of the reconstructed 3D images.

Several factors affect image resolution; these include photon attenuation, positron range and random coincidences from scattered and truly random photons. In some cases, it may not be possible to localize an area of increased activity on a PET scan alone due to poor anatomic resolution. In general, whole body PET has a spatial resolution of ~ 4 mm. Brain PET imaging can achieve a spatial resolution of ~2.5 mm. The strength of PET imaging lies in its ability to image a range of positron emitting radioisotopes attached to a wide range of carrier agents, as well as its exquisitely high sensitivity compared to other modalities. It is particularly powerful when used in understanding metabolic processes (Kapoor, McCook, & Torok, 2004).

In comparison to the higher spatial resolution (~1 mm) of CT images, PET resolution is lower but it gives important metabolic or biochemical functional information whereas CT (particularly when used in conjunction with PET) largely provides anatomical information. The modern combination of PET/CT scanners provide a powerful tool that capitalises on the complementary strengths

of the two imaging technologies for accurate localisation of functional abnormalities (Beyer et al., 2000).

The success of these combined modalities has also led to the development of a wide range of small animal (preclinical) PET/CT, SPECT/CT and PET/MRI cameras that are in routine use in drug discovery programs around the world (Nanni et al., 2007; Cherry & Gambhir, 2001). Spatial resolution (1.9-3.2 mm) and sensitivity (2.1-3.4%) are routinely achieved with small animal cameras (Tai et al., 2005), which allow the study of neoplastic masses at an early stage.

Table 1.1 PET isotopes employed in common clinical and preclinical applications.

Radionuclide Production Route (direct [D]/generator [G])	**Half-life**	**βmax (keV), max. range in H_2O (mm)**	**Radiolabelling Chemistry**	**Applications**
^{15}O (D)	1.03 min	1732 keV, 8.0 mm	Fast on-line None – Gas phase Chemistry	• [^{15}O]H_2O; **c**erebral blood flow • $^{15}O^{16}O$; oxygen metabolism • Blood volume • Local use only
^{13}N (D)	9.97 min	1198 keV, 5.1 mm	Covalently attached to target agent	• ^{13}N ammonia; heart blood flow • ^{13}N amino acids; protein synthesis • Local use only
^{11}C (D)	20.33 min	960keV, 3.9 mm	Covalently attached to target agent	• ^{11}C-acetate; heart metabolism • ^{11}C-MET; amino acid metabolism • ^{11}C-PIB; β-amyloid deposit in Alzheimer's disease • ^{11}C-Choline; prostate cancer imaging. Local use only

^{68}Ga (G)	68 min	1899keV, 8.9 mm	Chelated	• ^{68}Ga-DOTA-TATE ^{68}Ga-DOTA-NOC; neuroendocrine tumours • ^{68}Ga-PSMA; prostate cancer imaging • Local use only
^{18}F (D)	109.8 min	634keV, 2.3 mm	Covalently attached to target agent	• ^{18}F-FDG; glucose metabolism • ^{18}F-FLT; DNA synthesis, cell proliferation • ^{18}F-FET; amino acid transport • ^{18}F-FMISO; hypoxia • Non-local transport possible
^{64}Cu (D)	12.7 h	653 keV, 2.4 mm	Chelated	• Radiolabelling of small molecules (^{64}Cu-ATSM, ^{64}Cu-peptides) and larger molecules (^{64}Cu-antibodies, ^{64}Cu nanoparticles) • •Non-local transport possible
^{89}Zr (D)	78.4 h	897 keV, 3.6 mm	Chelated	• Radiolabelling of small molecules (e.g. ^{89}Zr- peptides) and larger molecules (^{89}Zr-transferrin, ^{89}Zr-antibodies) • Non-local transport possible
^{124}I (D)	4.17 d	1535 keV , 6.9 mm 2138 keV , 10.2 mm	Covalently attached to target agent	• ^{124}I-MIBG, ^{124}I-β CIT • ^{124}I-antibodies; thyroid cancer • Non-local transport possible

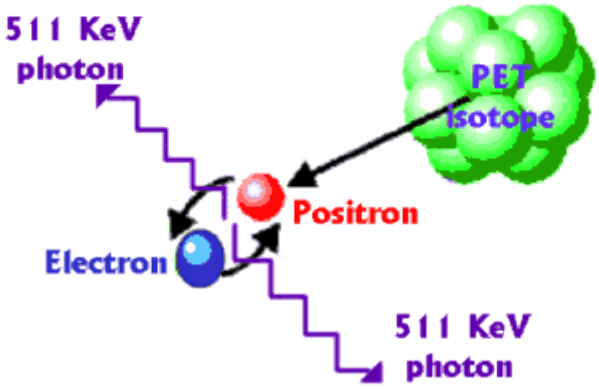

Figure 1.2 A positron is emitted from an unstable proton-rich nucleus. After travelling a short distance, it annihilates upon binding with an electron to form a positronium. The positronium has a short half-life (10^{-10} seconds) and decays almost instantly to give off two detectable 511 keV gamma photons approximately 180° apart (adapted from Royal Adelaide Hospital, 2015).

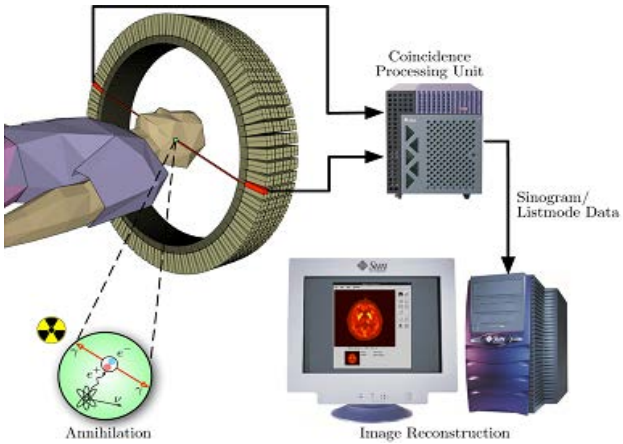

Figure 1.3 A clinical PET scanner. A circular array of detectors surrounds the patient and records the coincident photon pairs (adapted from University of Michigan Medical School, 2015).

1.3 Cyclotron

A cyclotron is a charged particle accelerator used to accelerate nuclear particles such as H^-, D^- ions to very high energies (5-90 MeV and 8-35 MeV, respectively) by an applied electrical field (Papash & Alenitsky, 2008). It also

has a magnetic field to guide these particles into a spiral flight path inside a vacuum chamber. The electric fields are generated by a pair of hollow semicircular metal electrodes called “dees” because of their D-shape (see Figure 1.4). The accelerating particles are produced in an ion source, constrained in a spiralling path by a magnetic static field, and are accelerated in their orbit by an alternating (RF) electric field. The alternating electric field is applied to 2 hollow “dees”. The radius of the particle orbit is determined by the magnetic field strength, the particle charge/mass ratio and the particle kinetic energy. The magnitude of the magnetic field does not change during the acceleration of the beam, except to compensate for relativistic effects on particle mass.

A charge Q moving with a velocity **v** in a static magnetic field is subject to the magnetic component of the Lorentz force

$$\mathbf{F} = Q\,(\mathbf{v} \times \mathbf{B}) \qquad (1)$$

In the simplest case of the particle moving perpendicularly to a constant magnetic field, the equation of motion describes a circular orbit constrained by an inward radially directed *centripetal force* F_f

$$F_f = m.\,v^2/\,r = Q.v.B \qquad (2)$$

where m is the particle mass and r the orbit radius. The centripetal force is balanced exactly by an outward radially directed *centrifugal* force.
Using equation (2) the angular velocity $\omega = v/r$ is;

$$\omega = Q.B/m \qquad (3)$$

and is independent of the orbital radius.
From the equation (3) the kinetic energy T is given by:

$$T_{max} = m.v^2/2 = Q^2.B^2.r^2/\,2m = m.\omega^2.r^2\,/2 \qquad (4)$$

The maximum kinetic energy, T_{max}, is reached when the radius of the beam orbit is at its maximum value, r_{max}, at the outer perimeter of the high-vacuum accelerating chamber, immediately prior to deflecting the beam onto the target. Since according to eqaution (3) the angular velocity of the beam does not depend on particle energy and therefore its orbital radius; the acceleration is *isochronous*. The alternating electric field placed across the dees has amplitude of tens of kilovolts and an angular frequency equal to the Larmor angular frequency ω of the circulating particle beam, enabling a resonant ramping of particle energy on every pass of the beam through a dee. Modern cyclotrons used in biomedical applications usually accelerate negative ions. In the case of the acceleration of H^- or D^-, once they reach T_{max}, the negative ions hit a stripping foil (usually 5 μm thick graphite), which removes their electrons revealing a proton (from H^-) or a deuteron (from D^-). These new particles are positively charged, they instantaneously reverse the sense of their orbit and are thus directed onto a target (Strijckmans, 2001). Modern medium-energy cyclotrons, including the IBA 18/9 (IBA, Louvain la Neuve, Belgium) are specially designed for the production of radioisotopes by (p,x) and (if deuterons are provided) (d,x) reactions in gaseous, liquid and (with some additional equipment) solid targets. These isotopes find widespread applications in nuclear medicine for both diagnostic and therapeutic purposes. The IBA 18/9 proton/deuteron isochronous cyclotron utilised in this study was upgraded into a 18/18 MeV proton/proton configuration during the course of this thesis, with the maximum beam current upgraded from 75 μA to 150 μA.

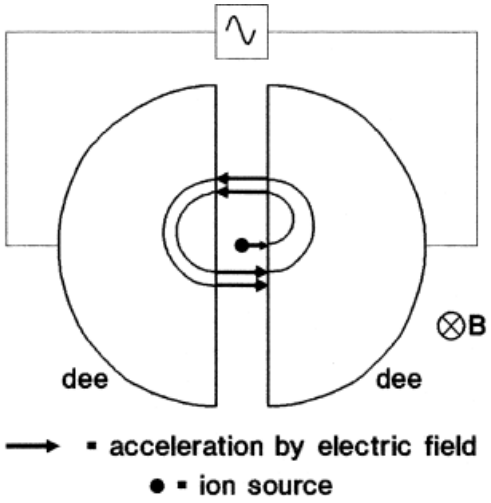

Figure 1.4 Schematic of the operation of a simplified cyclotron (adapted from Strijchmans, 2001).

Cyclotron-produced radioisotopes are often of:

- High Specific Activity - Chemically different from the target material; for example, ^{18}F is produced from an ^{18}O target and ^{61}Cu from a Zn or Ni target depending on the nuclear reaction.

.

- Neutron Poor - Have more protons than neutrons in their nucleus, decaying by electron capture (EC) or positron ($ß^{+}$) emission, and giving off gamma rays that are imageable by SPECT or PET.

1.3.1 Solid Targetry

Figure 1.5 shows a targetry system demonstrating these elements, for irradiation of solids in the form of foil discs (Scharli et al., 2012), partly based on a design by Ĉomor, Stevanoviü, Rajþeviü, & Košutiü (2004). This is optimised for a biomedical cyclotron of 18 MeV or less. A ten-mm graphite beam collimator up-beam of a Havar® vacuum foil 'window' (see Worked Example 4 for its elemental compostion) incorporates a removable beam-degrading insert of the same material, both cooled by chilled water. Cooled helium gas is passed over

the front of the target, between the vacuum foil and the front face of the target, to assist in heat removal. Pressurised chilled water (250 mL/s; 18^{o}C) is applied to the target backing plate. For a cyclotron with a proton beam energy of nominally 18 MeV this system is capable of beam currents exceeding 40 μA at energies up to 17.6 MeV (after losses in the vacuum and vacuum foil window), requiring removal of about (potential x current) = (17.6 MeV x 40 μA) = 700 W of heat energy. Only a tiny proportion of beam kinetic energy contributes to nuclear reactions.

The target consists of 25-mm diameter foil discs, which depending on requirements, may be packed in a stack of sufficent thickness to achieve the 'thick-target' condition. Typical solid-target materials are ^{nat}Cu, ^{89}Y, ^{45}Sc, ^{nat}Zn, ^{124}Te and ^{64}Ni to produce the radiometal isotopes ^{63,65}Zn, ^{89}Zr, ^{45}Ti, ^{61}Cu, ^{124}I and ^{64}Cu, respectively. Isotopically enriched targets such as ^{124}Te and ^{64}Ni are usually electroplated onto substrates that are inert to the chemical processes applied following irradiation, to remove the target material for subsequent separation and purification of product. For example, ^{64}Ni for the ^{64}Ni (p,n)^{64}Cu reaction can be electro-deposited onto a gold foil using a 10 mL aqueous electroplating solution of $^{64}NiSO_4$ (150 mg per target) and $(NH_4)_2SO_4$ (60-500 mg) (Jeffery, Smith, Asad, Chan, & Price, 2012). The thicknesses of such target preparations (typically < 100 μm) will not satisfy the 'thick-target' condition, unlike what is achievable with stacks of foils of naturally monoisotopic elements such as ^{89}Y and ^{45}Sc, or natural isotopic mixtures such as ^{nat}Cu and ^{nat}Zn.

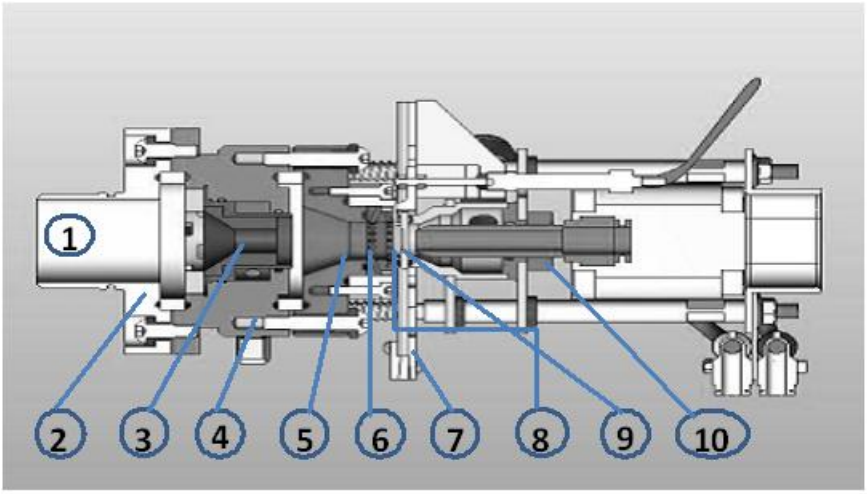

Figure 1.5 Schematic of external beam line and solid targetry apparatus for 18/18 MeV IBA cyclotron. (1) Proton beam entry; (2) connection flange; (3) graphite collimator; (4) collimator water cooling; (5) connecting body; (6) Havar® foil window; (7) target guiding plate; (8) window-target helium cooling cavity; (9) target disc(s) & backing plate; (10) cooling water jet for backing plate (adapted from Scharli et al., 2012).

The following criteria are essential in the design of a solid target station:

1. Target holder: should be heat resistant and have high thermal conductivity.

2. Cooling system: can be gas, liquid or both. Figure 1.5 shows a target cooled on its front face by helium gas flow and on the back by firm connection to a backing plate over which flows chilled water. The ability to remove heat is important for maintaining high current on the target and to prevent loss of product.

3. Automated release and target expulsion mechanism to deliver the irradiated target into a shielded container to reduce radiation exposure.

4. Robust vacuum window that prevents target material being sucked into cyclotron vacuum in the event of mechanical failure.

5. Ability to insert materials of varying thickness to degrade the beam energy on the target. Degraders are made of materials that minimally scatter the beam (e.g. graphite, stainless steel, aluminium or copper) and are a good thermal conductor.

6. Ability to degrade the beam to produce a particle of suitable energy to ensure optimal production of the desired isotope and minimal production of contaminating isotopes. For example, in the production of ^{64}Cu from enriched ^{64}Ni target (> 95%), the ^{64}Ni(p,n)^{64}Cu reaction can be optimised. An energy < 12 MeV captures a productive section of the excitation curve for this reaction but minimises the undesired nuclear reactions, such as ^{58}Ni(p,α)^{55}Co, ^{60}Ni(p,n)^{60}Cu, ^{64}Ni(p,α)^{61}Co, ^{61}Ni(p,n)^{61}Cu and ^{62}Ni(p,n)^{62}Cu.

1.3.2 Target Cooling

The thermal power delivered to a target, W_T is given by:

$$W_T = I.\ E \qquad (4)$$

where I is the target current expressed in μA and E the beam energy expressed in MeV. W_T is typically a few hundred W (watts). For a typical cyclotron system, this energy is delivered over a target area of approximately 1 cm^2. Therefore, it is essential that there is good contact between the target material and backing plate to ensure adequate cooling of the target assembly. The front of the target face is cooled with He gas and the foil target cover must be adequately sealed with an “O” ring to ensure no loss of He gas, to promote adequate cooling.

1.4 PET Isotopes: Targeted Radiopharmaceuticals

Only a small number of the radionuclides have the appropriate physical and chemical properties to become suitable candidates for the preparation of diagnostic or therapeutic radiotracers. In general, radiopharmaceuticals may be divided into two types; *substrate specific* and *non-substrate specific* agents. The more common substrate specific radiopharmaceuticals are designed to target a specific biological process, receptor or other type of protein expressed in distinct regions of the body, and usually in a specific cell types (metabolic substrates, drugs or analogs and antibodies). Non-substrate specific agents include radiolabelled liposomes, microspheres, perfusion agents and inert gases.

Many positron emitting nuclides of biomedical importance can be produced in a cyclotron by a specific target irradiated with protons of energy up to 18 MeV. The number of isotopes produced on a target depends on both the energy of the proton beam and the elemental composition of the target (target impurities). Selection of the prepared radionuclide in radiopharmaceutical design is very important and depends on several factors. The half-life of the radionuclide should allow sufficient uptake and distribution to yield quality images with good contrast. Also, the mode of decay and energies of the radionuclide emission should be suitable for the chosen imaging modality (Asabella, Cascini, Altini, & Paparella, 2014).

Fluorine-18 is probably the most widely used isotope for the synthesis of PET radiopharmaceuticals. It has a small positron range (2.3 mm) and a reasonable half-life (109.8 min) allowing the preparation of the widely used radiotracer [^{18}F]-2-fluoro-D-deoxyglucose (FDG) relatively quickly (< 30 min synthesis time) with acceptable radiochemical yields. FDG is used for the diagnosis of a large variety of cancers (e.g. lung, colorectal carcinomas, breast, and lymphomas) (Abouzied, Crawford, Nabi, 2005).

The relatively short physical half-life of ^{18}F inhibits its application in labelling antibodies. The 'slow' pharmacokinetics of antibodies require that they be radiolabelled with isotopes that have longer half-lives, such as ^{64}Cu, ^{89}Zr and ^{124}I, to match the biological half-life of the biodistribution of the antibody. The radiometals (^{64}Cu, ^{89}Zr) can be readily attached to targeting agent (e.g. antibodies, peptides and nanoparticles) using bifunctional chelators (BFCs). The BFC is either attached to the targeting agent and then radiolabelled with the desired radiometal, or the radiometal is complexed to the BFC and then attached to the targeting agent.

In all cases the BFC complexation/radiolabelling chemistry should be well-established and should have no significant effect on the targeting agents' ability to bind to the target receptors *in vivo*. As noted above, a range of radiometals with different half-lives are available, allowing the investigator to match the radiological half-life of the resultant radiolabelled agent to the biological half-life of the agent (Reichert, Lewis, & Anderson, 1999).

1.5 Production of Copper Radiosotopes

There are five copper radioisotopes (^{60}Cu, ^{61}Cu, ^{62}Cu, ^{64}Cu, and ^{67}Cu) that are used in nuclear medicine and molecular imaging; their physical properties are summarised in Table 1.2 (Wadas, Wong, Weisman, & Anderson, 2007). Though ^{64}Cu and ^{67}Cu can in theory be produced in nuclear reactors, they are mostly produced using accelerators via the (p,x) nuclear reactions. Copper isotopes ($^{60,61,62\&64}Cu$) are produced efficiently at energies < 18 MeV and can be produced on medium-energy cyclotrons commonly used in nuclear medicine PET centres, while ^{67}Cu requires higher energies. Production of ^{61}Cu and ^{64}Cu are of greatest interest to the current study as they have the physical characteristics most suited for radiolabelling nanomaterials, which could be the next generation of carrier agents in molecular imaging.

Table 1.2 Decay Characteristics of Copper Radionuclides (adapted from Wadas et al., 2007).

Isotope	**$T_{1/2}$**	**β^+ MeV(%)**	**β^- MeV (%)**	**EC (%)**	**γ MeV (%)**
^{60}Cu	23.4 min	2.00(69%) 3.00(18%) 3.92(6%)	-	7.4%	0.511(186%) 0.85(15%) 1.33(80%) 1.76(52%) 2.13(6%)
^{61}Cu	3.33 h	1.22(61.5%)	-	38.5%	0.284(12%) 0.656(10.6%) 0.511(120%)
^{62}Cu	9.76 min	2.91(97%)	-	2%	0.511(194%)
^{64}Cu	12.7 h	0.655(17.4%)	0.573(39.6%)	41%	0.511(34.8%) 1.35(0.6%)
^{67}Cu	62.0 h		0.395(45%) 0.484(35%) 0.577(50%)	-	0.184(40%)

1.5.1 Current Production Methods for ^{61}Cu

Copper-61 (^{61}Cu) is a positron emitter (β^+=61.5%, EC= 38.5%). It has a 3.33 h physical half-life and a $E_{\beta+}$ max of 2.237 MeV (Table of Nuclides; http://atom.kaeri.re.kr/). Its half-life is most suited to radiolabelling small molecules with short biological half-lives. It has been used for radiolabelling TETA-octreotide (where TETA is the chelating group 1,4,8,11-tetraazacyclotetradecane-N,N′,N″,N‴-tetraacetic acid), ATSM (diacetyl-bis(N^4-methylthiosemicarbazone) and PTSM (pyruvaldehyde-bis(N^4-methylthiosemicarbazone)) for imaging of tumours (McCarthy et al., 1997).

Nickel and zinc are generally used as target materials for the production of ^{61}Cu. Reactions reported in the literature include:

(1) **^{61}Ni(p,n)^{61}Cu** (Singh, Sharma, Mustafa, Bharwaj, & Prasad, 2006; Szelecsènyi, Blessing, & Qaim, 1993; Antropov et al., 1992; Tingwell, Hansper, Tims, Scott, & Sargood, 1988; Johnson, Trail, & Galonsky, 1964; Tanaka, Furukawa, & Chiba, 1972), ^{62}Ni(p,2n)^{61}Cu (Piel, Qaim, & Stoecklin,1992 ; Levkovskij, 1991).

(2) **^{64}Zn(p,α)^{61}Cu** (Barradon, Deburn, Kohn & Spear, 1975; Cohen, Newman, Charpie, & Handly,1954).

(3) **^{64}Zn(d,αn)^{61}Cu** (Daraban, Abbas, Simonelli, Rebeles, & Gibson, 2008; Williams & Irvine, 1963).

In deciding the optimum nuclear reaction route for production of ^{61}Cu, one must consider:

1) Target material purity and cost.

2) Nuclear yield.

3) Beam characteristics; that is particle type (i.e proton, deuteron or alpha particle) energy and current.

Target isotopic abundances are one of the main factors involved in target material selection. For example, we note that natural nickel contains the following five stable isotopes ^{58}Ni (68.77%), ^{60}Ni (26.223%), ^{61}Ni (1.140%), ^{62}Ni (3.634%) and ^{64}Ni (0.926%). Considering the relatively low natural abundance of ^{61}Ni, in the quest to produce ^{61}Cu irradiation of a natural nickel will give arise to cobalt and other copper radioisotopic contaminants with half-lives ranging from 23.2 min to 271 days, using energies up to 27.5 MeV (Al

Saleh, Al Mugren, & Azzam, 2009). Therefore, enriched target material is required to reduce these sources of contamination and also to increase ^{61}Cu production yield. Thus, production of the desired radioisotope in sufficiently high yield often requires the use of expensive, highly enriched target materials. In the case of ^{61}Cu, only a low fraction (< 0.004%) of the target is converted to the desired radioisotopes, so the (expensive) target material needs to be recycled after each irradiation to keep the cost of production to a minimum.

1.5.1.1 ^{61}Cu Production Using Nickel Targets

As discussed above, copper-61 can be produced from enriched ^{61,62}Ni targets (Figure 1.6 and 1.7) but not from natural Ni targets, because of the low natural abundance of ^{61}Ni (1.16%) and ^{62}Ni (3.634%). Figure 1.6 shows the cross section for protons on ^{61}Ni target over a proton energy range of 2.5-18.6 MeV (Szelecsènyi et al., 1993; Antropov et al., 1992; Tingwell et al., 1988; Johnson et al., 1964; Tanaka et al., 1972; Tanaka & Furukawa, 1959). There are less reported data for the ^{62}Ni(p,2n)^{61}Cu reactions, and while there is some variation, there is good agreement between Piel et al. (1992) and Levkovskij (1991) in the energy range of 13.8-18.3 MeV (see Figure 1.7). McCarthy et al. (1997) reported that the most cost-effective way of making ^{61}Cu (starting with Ni as a target) was from a ^{61}Ni target using protons from a biomedical cyclotron (14.7 MeV).

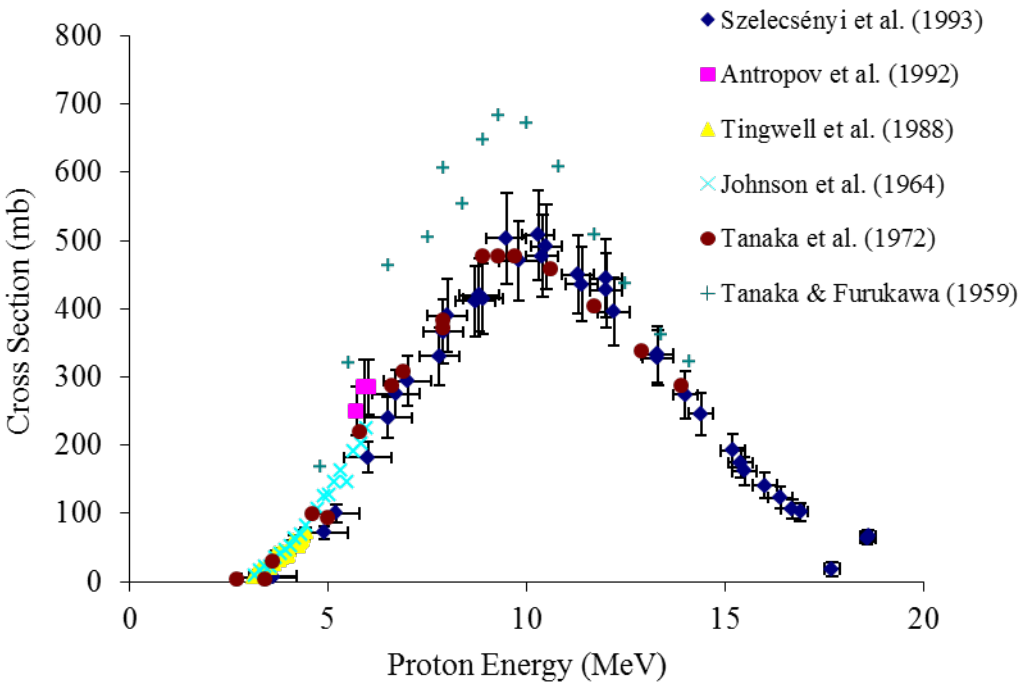

Figure 1.6 Experimentally determined excitation function of $^{61}Ni(p,n)^{61}Cu$ reaction (adapted from EXFOR).

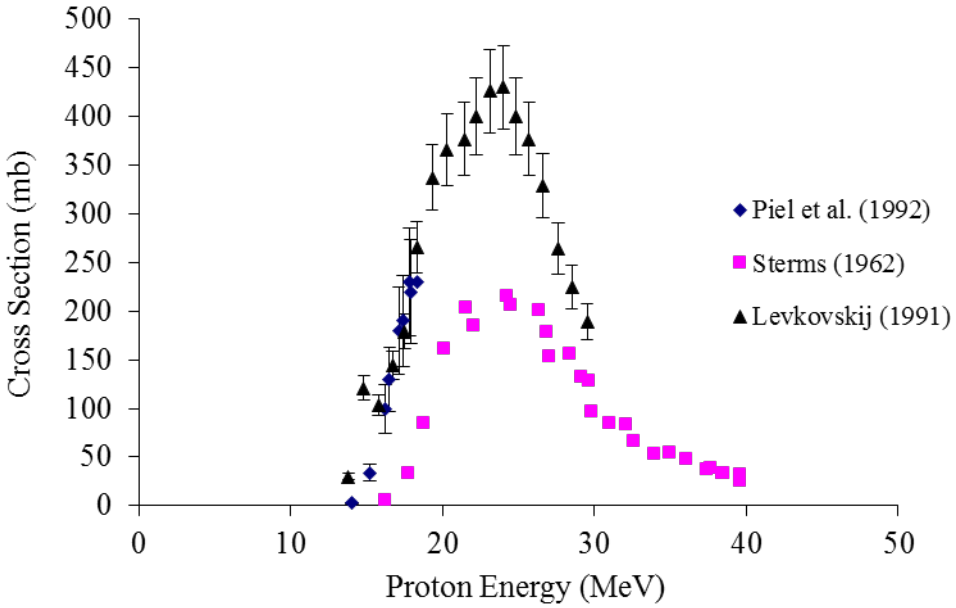

Figure 1.7 Experimentally determined excitation function of $^{62}Ni(p,2n)^{61}Cu$ reaction (adapted from EXFOR).

1.5.1.2 ^{61}Cu Production Using Zinc Targets

Alternatively, ^{61}Cu can be produced from irradiation of natural Zn (natural abundance of ^{64}Zn (48.8%)) or enriched ^{64}Zn targets. They have the following advantages over Ni targets:

(i) Zn target materials are much cheaper.

(ii) The predominant nuclear reaction is ^{nat}Zn(p,α)^{61}Cu and the main radiocontaminants arise from the reaction ^{nat}Zn(p,x)^{66,67,68}Ga. That is, only one contaminating element is produced. Furthermore, a natural Zn target does not need to undergo a recovery process for cost-related reasons.

(iii) Zn targets are commercially available in either foil or powder form.

Figure 1.8 shows the cross sections for ^{nat}Zn target over a proton energy range of 6.0-18.3 MeV (Uddin, Khandaker, Kim, Lee, & Kim, 2007; Szelecsènyi et al., 2005 ; Barrandon et al., 1975). As Figure 1.9 shows, there are less data available for the ^{64}Zn (p,α) reaction, with some variation up to 16 MeV (Levkovskij, 1991; Cohen et al., 1954). The ^{64}Zn(d,n+α)^{61}Cu reaction is another route used for the production of ^{61}Cu, with a similar range of particle energies, as shown in Figure 1.10. Deuteron energies range from 7.5 to 25.8 MeV. However, this range is unsuitable for production in low- and medium-energy cyclotrons commonly found in biomedical institutions, where the 'rule of thumb' is that the deuteron beam energy is 50% of the proton beam energy from the same machine.

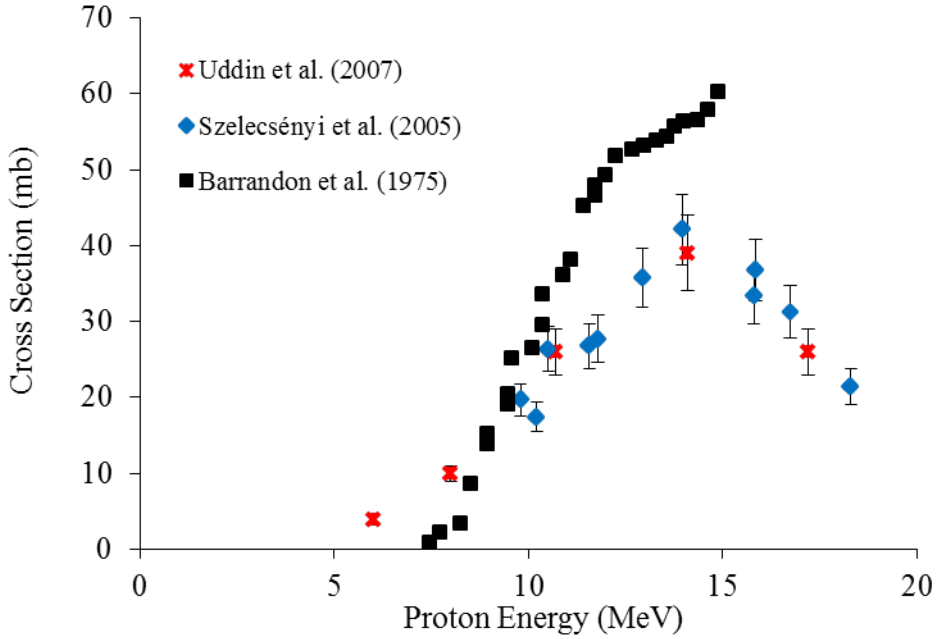

Figure 1.8 Experimentally determined excitation function of $^{nat}Zn(p,\alpha)^{61}Cu$ reaction **(**adapted from EXFOR).

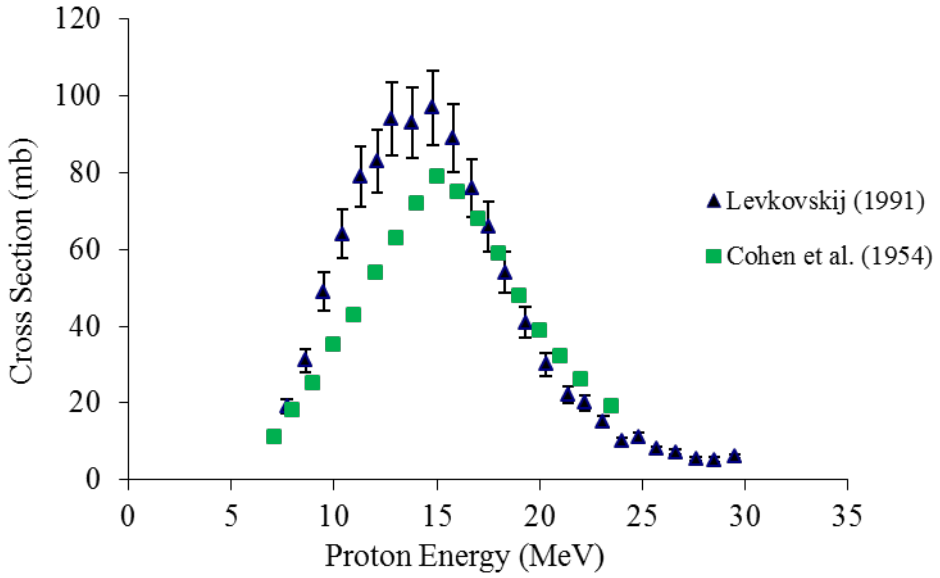

Figure 1.9 Experimentally determined excitation function of $^{64}Zn(p,\alpha)^{61}Cu$ reaction (adapted from EXFOR).

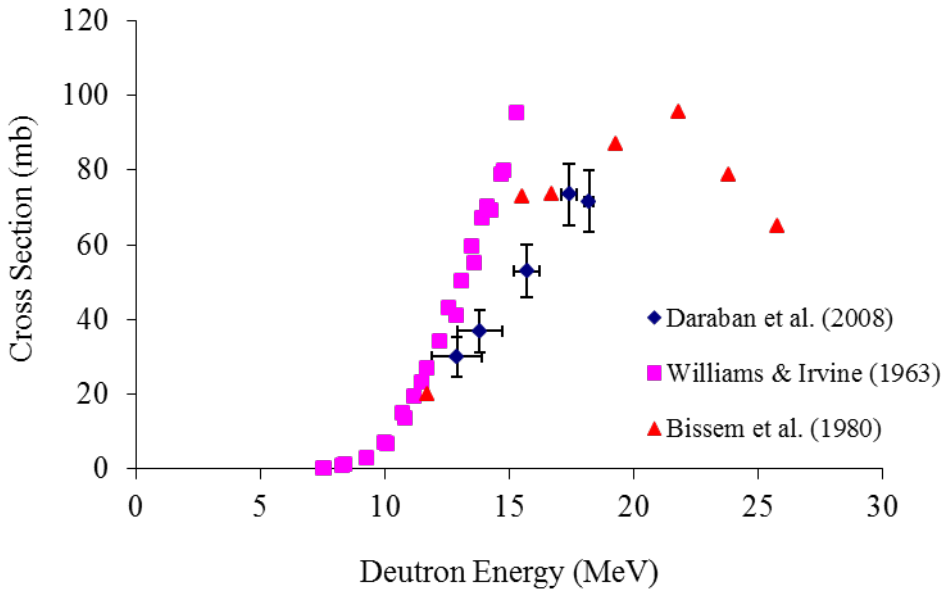

Figure 1.10 Experimentally determined excitation functions of $^{64}Zn(d,n+\alpha)^{61}Cu$ reaction (adapted from EXFOR).

1.5.2 Current Methods of Radiochemical Separation of ^{61}Cu

Table 1.3 below summarises the production methods for ^{61}Cu reported in the literature (McCarthy et al., 1997; Rowshanfarzad, Sabet, Jalilian & Kamalidehghan, 2006; Thieme et al., 2013). McCarthy et al. (1997) used ion exchange chromatography to separate the ^{61}Cu from the Ni target material and the Co isotopes by-products. Other methods have also been reported for separating Cu and Ga from the Zn target materials by cation and anion exchange chromatography (Rowshanfarzad et al., 2006; Dasgupta, Mausner, & Srivastava, 1991; Schwarzbach, Zimmermann, Blaeuenstein, Smith, & Schubiger, 1995; Asad et al., 2012). Briefly, the irradiated zinc target was dissolved in concentrated hydrochloric acid. The solution was evaporated to dryness, redissolved in concentrated hydrochloric acid and transferred to a cation exchange column (AG50W-X8) to separate the ^{61}Cu and Zn target material from the Ga isotopes. In the next step, ^{61}Cu was eluted through an anion exchange column (AG 1-X8) with 2 M HCl while the Zn remained on the column.

Table 1.3 Published cyclotron-derived production methods for ^{61}Cu.

Reaction	**Target Enrichment (%)**	**Energy (MeV)**	**Yield (MBq/μAh/mg)**	**References**
^{61}Ni(p,n)	99.44	14.7	7.65-14.1	McCarthy et al. (1997)
^{60}Ni(d,n)	99.59	14.7	1.35-2.93	McCarthy et al. (1997)
^{62}Ni(p,2n)	3.63	≥17.8	-	Piel et al. (1992)
^{nat}Zn(p,α)	99.99	12-22	0.67	Rowshanfarzad et al. (2006)
^{64}Zn(p,α)	99.30	16	0.25-0.47	Thieme et al. (2013)

1.5.3 Current Production Methods for ^{64}Cu

^{64}Cu is produced by (p,n) or (d,x) nuclear reactions by cyclotron or (n,γ) and (n,p) reactions using a reactor. The decay properties of ^{64}Cu (β^+ = 17.4%, β^- = 39.6% and EC = 41%) make it potentially useful in nuclear medicine for PET imaging and possibly for molecular radiotherapy (Wadas et al., 2007). Several production methods for ^{64}Cu have been published in the literature (Elomaa, Jurttila, Rajander, & Solin, 2014; Obata et al., 2003; Szelecsényi et al., 1993; Abbas et al., 2006; Tarkànyi et al., 2005; Hilgers, Stoll, Skakun, Coenen, & Qaim, 2003; Rebeles, Winkel, Hermanne, & Tàrkànyi, 2009; Zweit, Smith, Downey, & Sharma, 1991; Szelecsényi et al., 2005B; Matarrese et al., 2010). The most widely used method is the ^{64}Ni(p,n)^{64}Cu reaction leading to high yield and high specific activity of the product (McCarthy et al., 1997; Szelecsényi et al., 1993). Table 1.4 summarises potential nuclear reactions and their respective yields reported in the literature.

^{64}Ni target disks are produced by direct electroplating onto silver or gold target foils. The expensive enriched ^{64}Ni can be recovered after irradiation of the target during the purification process (Hou, Jacobsen, & Jørgenesen, 2002). The advantages of using the ^{64}Ni(p,n)^{64}Cu reaction are its very high cross section, [836.7 mb at 10.6 MeV (Rebeles et al., 2009)] and its very high product specific activity (> 370,000 GBq/mmol) which can easily be produced at low proton currents. It was also reported that ^{64}Cu may be produced using a zinc target.

Table 1.4 Published cyclotron-derived production methods for ^{64}Cu.

Reaction	**Target Enrichment (%)**	**Energy Range (MeV)**	**Yield (MBq/µAh/mg)**	**Reference**
^{64}Ni(p,n)	94.80	12 → 9	4.5-6.2	Obata et al. (2003)
^{64}Ni(d,2n)	96.48	19 → 15	19.04	Zweit et al. (1991)
^{64}Zn(d,2p)	99.40	19.5	0.40	Abbas et al. (2006)
^{66}Zn(d,α)	99.00	13 → 7	-*	Hilgers et al. (2003)
^{68}Zn(p,αn)	≥99.00	35 → 20	-*	Hilgers et al. (2003)

* The yield was reported as thick target yield (6.6 MBq/µAh, 65 MBq/µAh for ^{66}Zn(d,α) and ^{68}Zn(p,αn), respectively. The masses of each target are not reported.

All the reactions presented in Table 1.4 require high target isotopic enrichment to suppress contaminating co-produced radionuclides and to optimise yields. They can all be perfomed using a standard biomedcial cyclotron with solid targetry enhancement. The major production pathways for ^{64}Cu are considered in more

detail below. Figure 1.11 shows the excitation functions for the nuclear reactions summarised in Table 1.4.

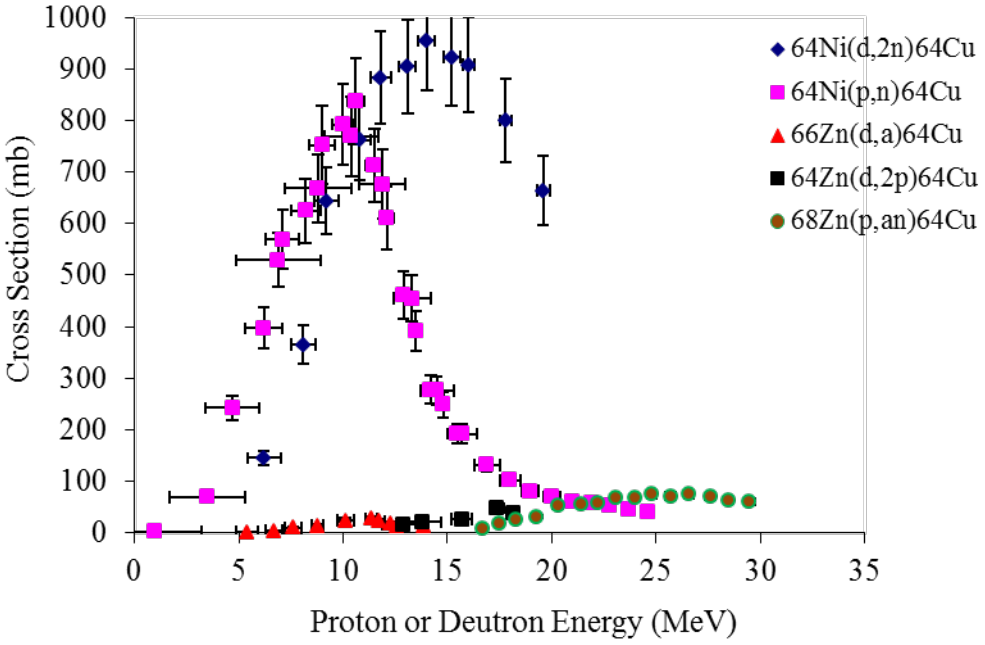

Figure 1.11 Experimentally determined excitation functions for different nuclear reactions to produce ^{64}Cu (adapted from EXFOR).

1.5.3.1 ^{64}Cu Production Using Nickel Targets

1.5.3.1.1 ^{nat}Ni(p,n)^{64}Cu Reaction

Copper-64 has also been produced from the irradiation of natural Ni, using the same chemical separation process as the one used for the enriched target (Antropov et al., 1992). However, very low yields of ^{64}Cu were obtained, due to the low abundance (0.926%) of ^{64}Ni in natural Ni (Table of Nuclides; http://atom.kaeri.re.kr/). Furthermore, other isotopes such as ^{57}Co, ^{58}Co and ^{61}Cu are also produced from the other naturally abundant Ni isotopes (^{58}Ni 68.077%, ^{60}Ni 26.223%, ^{61}Ni 1.140%, ^{62}Ni 3.634%, ^{64}Ni 0.926%). An enriched ^{64}Ni target is therefore the target of choice for the production of ^{64}Cu with high yield and high radionuclidic purity.

1.5.3.1.2 $^{64}Ni(p,n)^{64}Cu$ Reaction

Figure 1.12 compares published data on the cross sections of the $^{64}Ni(p,n)^{64}Cu$ reaction. This is the most efficient and the most widely used reaction for the production of ^{64}Cu because it has a wide energy range for production. ^{64}Cu is also easily separated from the Ni target (Wadas et al., 2007). Enriched ^{64}Ni (> 95%) is required as a target material, and is commercially available as a powder (metal or metal oxide) from Isoflex and Trace Sciences International. As reported previously by Avila-Rodriguez et al. (2007), the optimum proton energy for high-yielding production of ^{64}Cu from a ^{64}Ni thin target was 11-12 MeV.

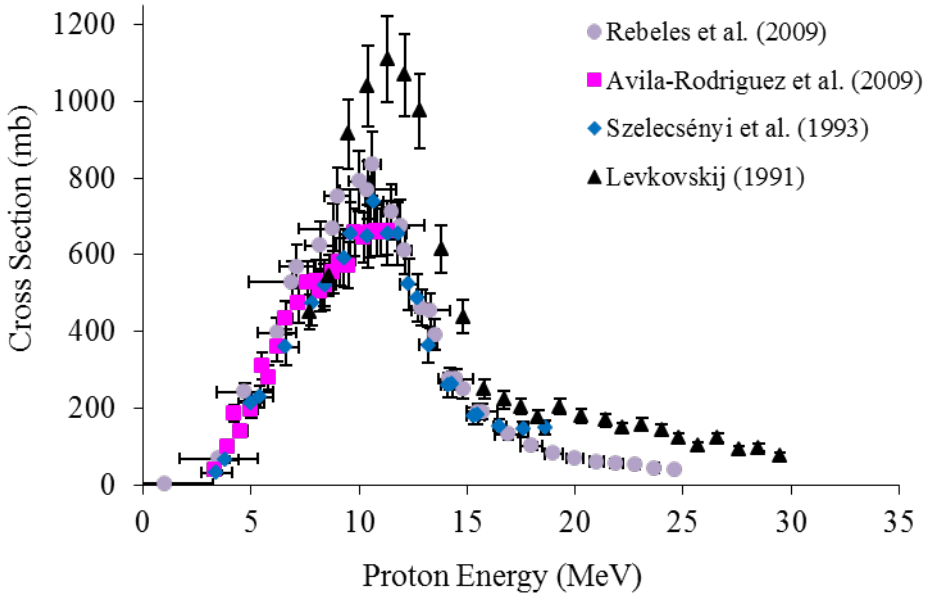

Figure 1.12 Experimentally determined excitation function of $^{64}Ni(p,n)^{64}Cu$ reaction (adapted from EXFOR).

1.5.3.1.3 ^{64}Ni(d,2n)^{64}Cu Reaction

The ^{64}Ni(d,2n)^{64}Cu reaction is another route used for the production of ^{64}Cu with relatively high yields. As shown in Figure 1.13, deuteron energies ranging from 5.0 to 9.5 MeV are most suitable and today this is achievable with low to medium energy cyclotrons [i.e. 18/9 MeV (protons/deuterons)]. Unfortunately ^{65}Ni ($T_{1/2}$= 2.5 h) is co-produced (via a d,p reaction) along with copper and cobalt radioisotopes, making this pathway less attractive (Daraban, Rebeles, & Hermanne, 2009).

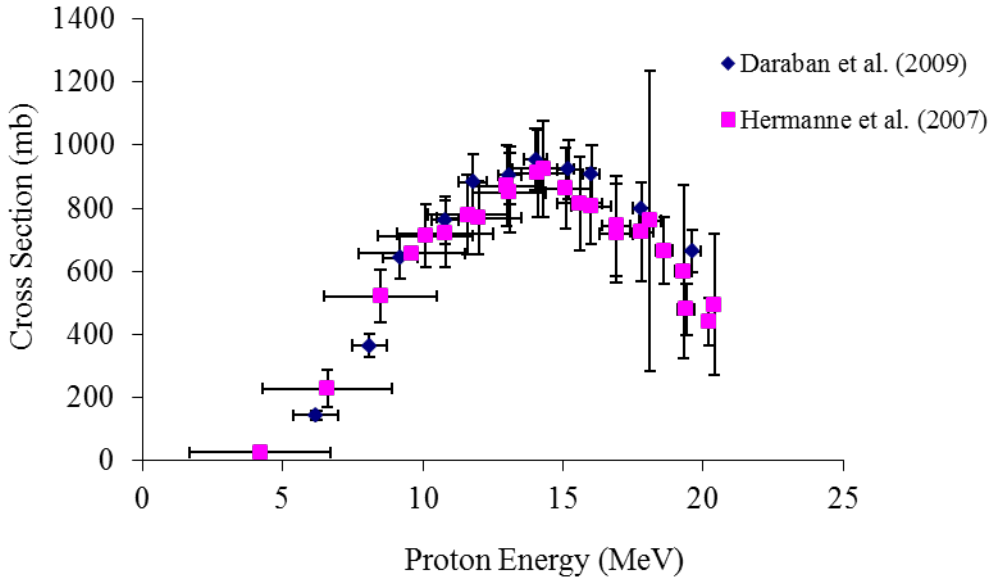

Figure 1.13 Experimentally determined excitation function of ^{64}Ni(d,2n)^{64}Cu reaction (adapted from EXFOR).

1.5.3.2 ^{64}Cu Production Using Zinc Targets

1.5.3.2.1 ^{nat}Zn(p,x)^{64}Cu Reaction

The proton irradiation of natural Zn target can be used to produce ^{64}Cu at higher proton energies (> 25 MeV, Figure 1.14). The natural Zn target possesses the advantage of being available in both powder and foil forms and of being much cheaper than the enriched targets. However, this reaction produces other radionuclides such as ^{61}Cu, ^{66,67}Ga, ^{57,58}Co and ^{65,69m}Zn, as well as requiring a medium-energy cyclotron.

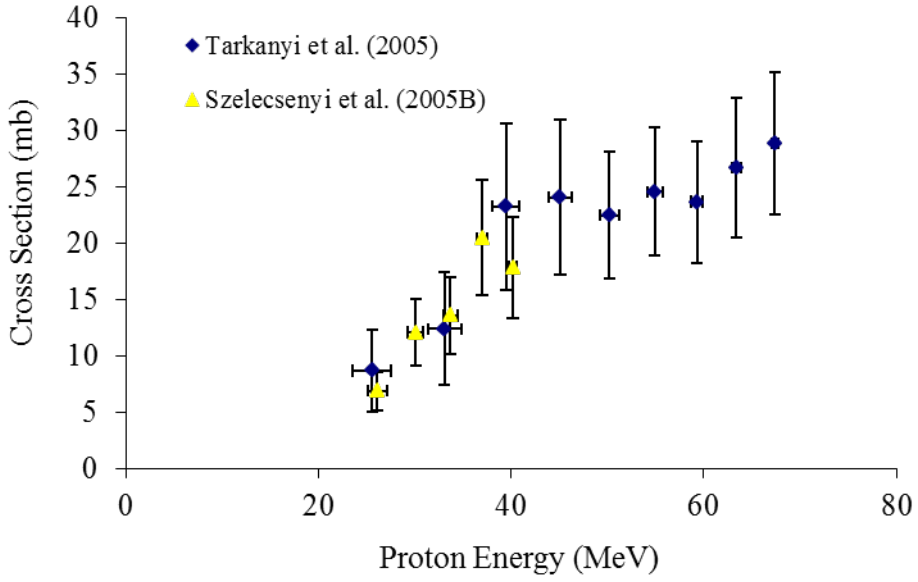

Figure 1.14 Experimentally determined excitation function of ^{nat}Zn(p,x)^{64}Cu reaction (adapted from EXFOR).

1.5.3.2.2 $^{68}Zn(p,n+\alpha)^{64}Cu$ Reaction

There are only two published data of this reaction. However, they are in marked disagreement (see Figure 1.15) . The most useful energies for this reaction lie between 10 and 35 MeV. The production of ^{64}Cu from this reaction is not recommended due to the low measured cross sections.

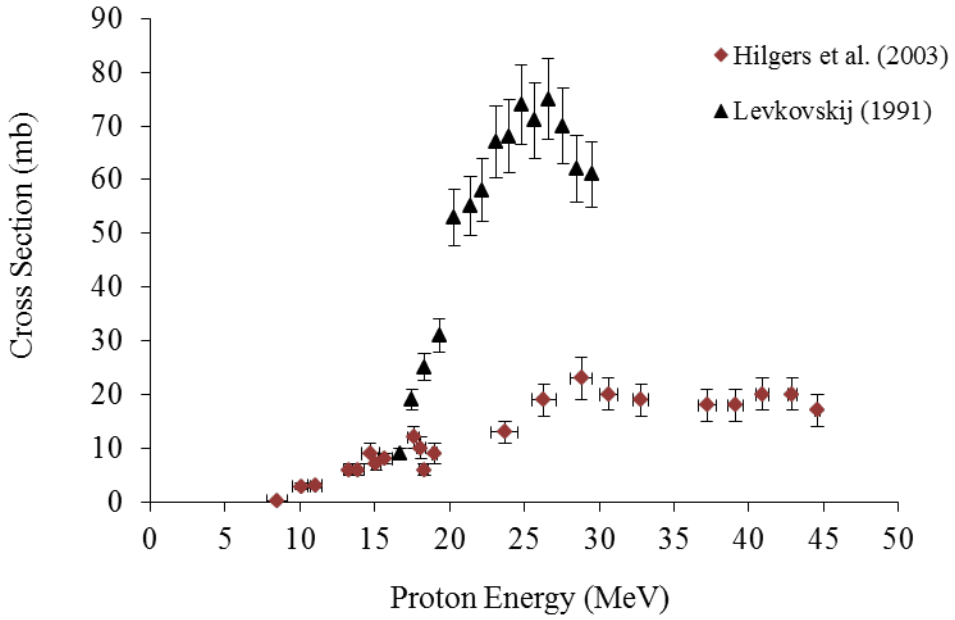

Figure 1.15 Experimentally determined excitation function of $^{68}Zn(p,n+\alpha)^{64}Cu$ reaction (adapted from EXFOR).

1.5.3.2.3 $^{64}Zn(d,2p)^{64}Cu$ Reaction

The excitation function of the $^{64}Zn(d,2p)^{64}Cu$ reaction is higher than the excitation functions of other isotopic Zn targets with a maximum cross section of 65.5 mb at 15.5 MeV (see Figure 1.16) (Williams & Irvine, 1963). However, this reaction produces lower yields of ^{64}Cu than that produced via the $^{64}Ni(d,2n)^{64}Cu$ and the $^{64}Ni(p,n)^{64}Cu$ reactions, and requires a relatively high energy deuteron (i.e. up to 16 MeV).

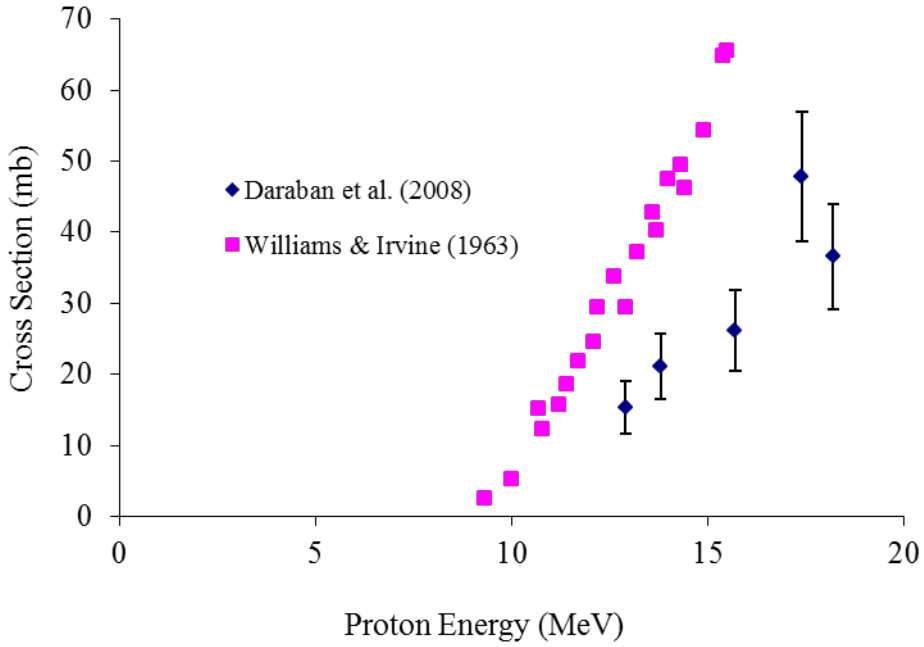

Figure 1.16 Experimentally determined excitation function of $^{64}Zn(d,2p)^{64}Cu$ reaction (adapted from EXFOR).

1.5.3.2.4 $^{66}Zn(d,\alpha)^{64}Cu$ Reaction

The $^{66}Zn(d,\alpha)^{64}Cu$ reaction has a maximum cross section of 28 mb at 11 MeV deuteron energy (see Figure 1.17). The best energy deuterons for this reaction are between 7-13 MeV. Although enriched ^{66}Zn is much cheaper than enriched ^{64}Ni. However, ^{64}Ni is still preferred in most sites due to its relatively high reaction cross section with a proton beam (Hilgers, Qaim, & Coenen, 2004).

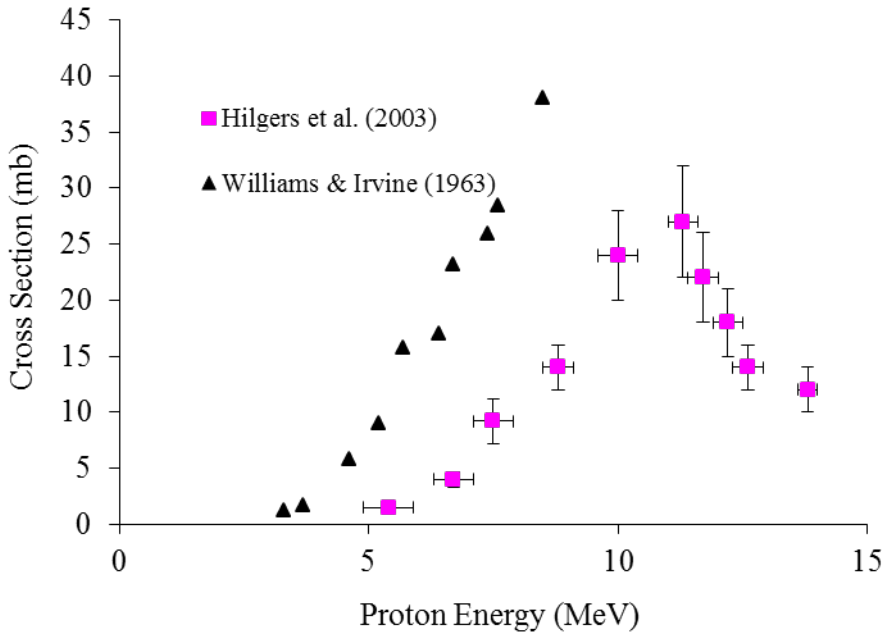

Figure 1.17 Experimentally determined excitation function of $^{64}Zn(d,\alpha)^{64}Cu$ reaction (adapted from EXFOR).

1.5.4 ^{64}Cu Target Preparation

Natural foils such as ^{89}Y and ^{45}Sc used for the production of ^{89}Zr and ^{45}Ti, respectively are commercially available. Foils of enriched ^{64}Zn for the production of ^{61}Cu are also commercially available (Asad et al., 2014; Holland, Sheh, & Lewis, 2009; Sadeghi, Enferadi, & Nadi, 2011). However, in the case of ^{64}Cu, enriched nickel foils are not readily available, and electroplating with enriched ^{64}Ni is required for target preparation. Several methods are reported for

electroplating nickel or zinc for the production of ^{64}Cu, depending on the energy and the beam used (Matarrese et al., 2010; Kim, Park, & Chun, 2001; Manrique-Arias & Avila-Rodriguez, 2014). Electroplating of enriched ^{64}Ni on a gold foil was reported by McCarthy et al. (1997). Nickel oxide was first dissolved in 6 M nitric acid and evaporated to dryness prior to the addition of concentrated sulphuric acid, dilution with water and further evaporation to dryness. The residue was diluted with water, adjusted to pH 9 with ammonium hydroxide and then used for electroplating of the Ni onto a gold foil using a graphite or platinum electrode.

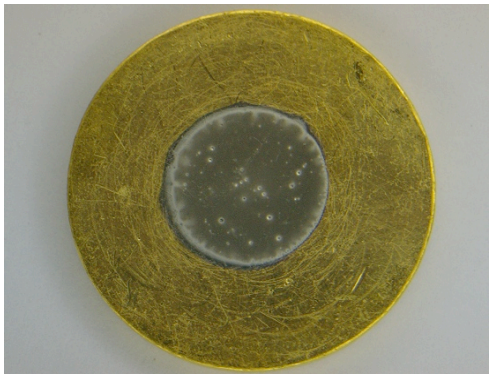

Figure 1.18 One-cm diameter layer of ^{64}Ni plated onto gold foil.

1.5.5 Current Methods for Radiochemical Separation of ^{64}Cu

Several methods such as ion exchange chromatography, solvent extraction, electroplating and precipitation have been described for the separation of ^{64}Cu from ^{64}Ni and other isotopic impurities (i.e. ^{61}Co, ^{55}Co, ^{57}Co, ^{60}Cu and ^{61}Cu) produced during irradiation of the target (Hou et al., 2002). Ion exchange chromatography is considered to be the best method used for no-carrier-added ^{64}Cu (Manrique-Arias & Avila-Rodriguez, 2014; McCarthy et al., 1997. Briefly, the irradiated enriched ^{64}Ni target is dissolved in concentrated hydrochloric acid. The solution is evaporated to dryness, redissolved in concentrated hydrochloric acid and transferred to an anion exchange column (AG1-X8). The ^{64}Ni target material and Co isotopes are eluted with 6 M HCl while most of the ^{64}Cu

remains on the column. The desired ^{64}Cu is then eluted from the ion exchange column with 0.1-0.5 M HCl with efficiencies ranging 90-95% depending on the volumes used (Avila-Rodriguez et al., 2007; McCarthy et al., 1997). Hou et al., 2002, reported ^{64}Cu separation by ion exchange chromatography using low (0.3 M) concentration of HCl in ethanol solution (72%) to separate Ni and Co from Cu ion. In the last step, the Cu is finally eluted with water (Figure 1.19). Watanabe et al. (2009) developed a new method of ^{64}Cu separation using a chelating resin bearing iminodiacetic acid groups. Briefly, Ni and Co ion were eluted off the column with 0.1 M HCl and ^{64}Cu was eluted with 2 M HCl with radiochemical purity over 99%.

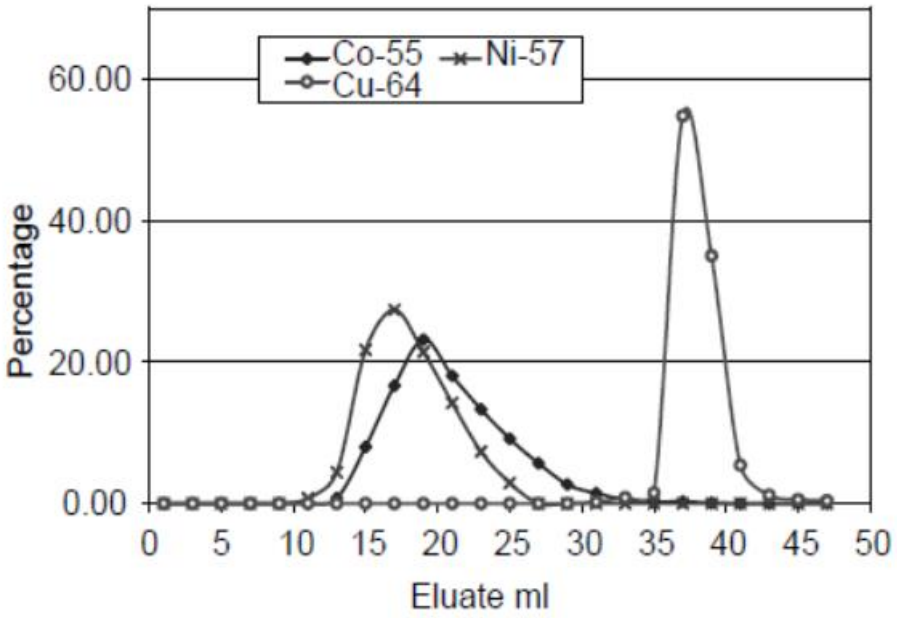

Figure 1.19 Separation of Cu, Co and Ni by ion exchange column (1.0 cm × 12 cm), elution of Ni and Co with 28 mL of 0.3 M HCl in ethanol solution (72%), followed by elution of Cu with 18 mL of water (adapted from Hou et al., 2002).

1.5.6 Specific Activity of Final Product

The concentration of a radioactive isotope in a sample in comparison with the total 'cold' mass of element to which that isotope belongs is described by the "specific activity" and is expressed as radioactivity per total elemental mass (e.g.

Bq/mol, GBq/μmol). The specific activity of (say) ^{64}Cu in a solution can be determined experimentally. For example, measurement of the ^{64}Cu radioactivity compared with the total Cu content can be performed by titration with a chelator (i.e. TETA) as described by McCarthy et al. (1997), this yields the *effective* specific activity. ICP-MS is a more direct way to measure the specific activity precisely by determining the Cu ion concentration in the final ^{64}Cu solution (Jeffery et al., 2012; Mastren et al., 2014). If the radioisotope of atomic number Z is separated and purified from a bombarded target containing no isotopes with the same Z (as for the ^{64}Ni(p,n)^{64}Cu reaction) this determination is known as the *no-carrier-added* specific activity.

1.6 Bifunctional Chelators for Cu Isotopes

Bifunctional chelators (BFCs) that form kinetically stable radiometal complexes are required for bioconjugation of the radiometal to targeting molecules (i.e. peptide, protein or nanoparticles) used in PET and targeted radiotherapy (De Silva et al., 2012; Cooper et al., 2012). Many types of chelators have been used for complexing Cu, as illustrated in Figure 1.20.

Acyclic chelating agents such as ethylenediamine tetraacetic acid (EDTA) and diethylenetriamine pentaacetic acid (DTPA) were initially used as chelators for Cu^{2+} complexes. However, though possessing high thermodynamic stability, their low kinetic stability prevented them from being used *in vivo* (Moi, Keares, McCall, Cole & De Nardo, 1985). Due to the acyclic nature of these chelators, their complexes are kinetically labile and suffer transchelation in the presence of competing species in solution. A series of BFCs that are derivatives of the macrocyclics 1,4,7,10-tetra-azacylcododecane-N,N′,N″,N‴-tetraacetic acid (DOTA) and 1,4,8,11-tetraazacyclotetra decane-N,N′,N″,N‴-tetraacetic acid (TETA) have been developed for the complexation of Cu isotopes. These macrocyclic chelating agents form complexes with Cu^{2+} that are kinetically more inert compared to Cu^{2+}- EDTA and Cu^{2+}- DTPA. However, they still have

limitations with regards to *in vivo* stability and slow formation rates of their complexes (Boswell et al., 2004), which can result in high uptake of activity by non-target organs such as the liver (Rogers et al., 2003; Rogers, Della Manna, & Safavy, 2004). Previous studies have demonstrated the high stability of the 1,4,7-triazacyclononane-1,4,7-triacetic acid (NOTA) Cu^{2+} complex and described NOTA as a BFC of choice for labelling ^{64}Cu (Craft et al., 2012 ; Dearling et al., 2011). Other types of chelators include hexa-aza cages such as 3,6,10,13,16,19-hexaazabicyclo[6.6.6]eicosane-1,8-diamine pentahydrate (diamsar, (e)) and 1-*N*-(4-aminobenzyl)-3,6,10,13,16,19-hexaazabicyclo[6.6.6]eicosane-1,8-diamine (SarAr-NH_2, (f)), which form Cu^{2+} complexes that are both kinetically and thermodynamically stable. They can complex Cu isotopes rapidly, at room temperature, over pH ranges 4 to 9 and at low concentrations (μM) (Smith, 2004).

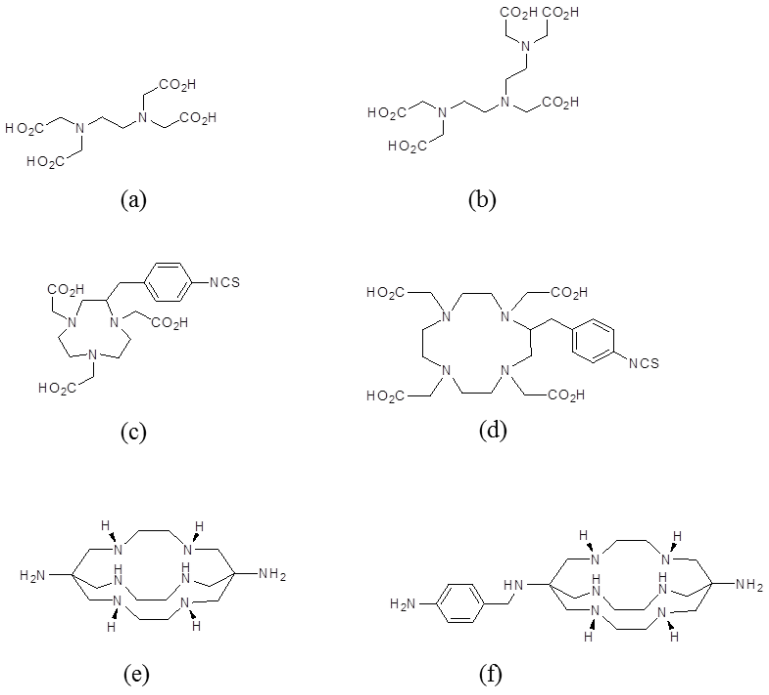

Figure 1.20 Structures of some chelators used for complexing Cu^{2+}. (a) EDTA, (b) DTPA, (c) NOTA-NCS, (d) DOTA-NCS, (e) diamsar and (f) SarAr-NH_2.

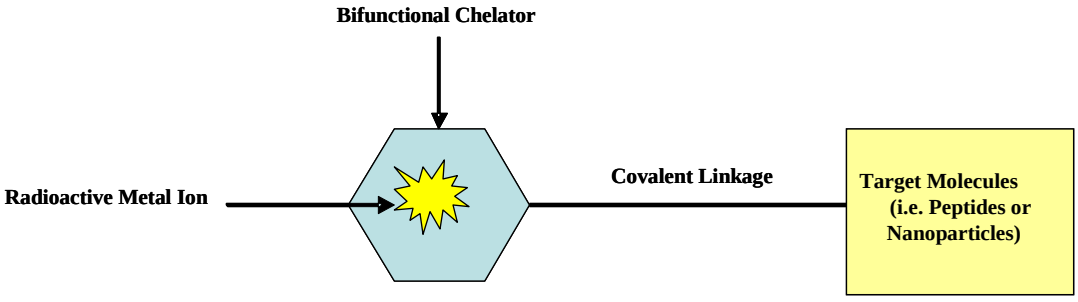

Figure 1.21 Schematic diagram of the role of bifunctional chelators (BFCs), which bind the radiometal at one terminus and contain a functional group at the second terminus for the covalent linkage to a target. The choice of BFC is determined by the donor groups present, the metal preferred coordination geometry and the metal's oxidation state.

1.7 Overview of Nanoparticles in Medicine

Cancer is a leading cause of death around the world. The World Health Organisation estimated that 84 million people died of cancer between 2005 and 2015. For effective cancer therapy, it is necessary for researchers to improve their knowledge of cancer physiopathology, discover new anti-cancer drugs and develop novel biomedical technologies. Currently, cancer therapy and diagnosis has become a multidisciplinary challenge requiring close collaboration among clinicians, biological and materials scientists, and biomedical engineers. Nanomedicine (using targeted functional nanoparticles) is a promising avenue for cancer diagnosis and therapy. There is a wide variety of nanoparticles (NPs) with diameters ranging between 1-1000 nm. Drugs may be encapsulated, adsorbed or dispersed in these NPs. NPs can vary in size, shape and chemical structure (liposomes, polymeric NPs, micellar NPs, albumin-based particles, inorganic or other solid particles (gold, iron oxide, quantum dots and carbon nanotubes). They have been extensively studied as carriers for molecules (targeting tracers or drugs) aimed at diagnosis and targeted therapy of cancers (Xiao et al., 2011; Miteva et al., 2015; Eloya et al., 2014; Rao, Gruenberga, &

Gecklera, 2015; Hanafi-Bojd et al., 2015; Krishnaraj, Muthukumaran, Ramachandran, Balakumaran, & Kalaichelvan, 2014).

In this section, a brief overview of the different types of NPs used in medicine is given. The key characteristics of NPs (size, charge, and coating) will then be discussed. Finally, the EPR effect will be introduced and the principles of passive and active targeting will be discussed.

1.7.1 Overview of the Different Types of Nanoparticles

Several nanomaterials have already been identified and have made strong contributions in biomedicine for preclinical and clinical use. Some examples are shown schematically in Figure 1.22. The work described later in this thesis will focus exclusively on inorganic silica nanospheres (Si NS) and polystyrene nanospheres (PS NS).

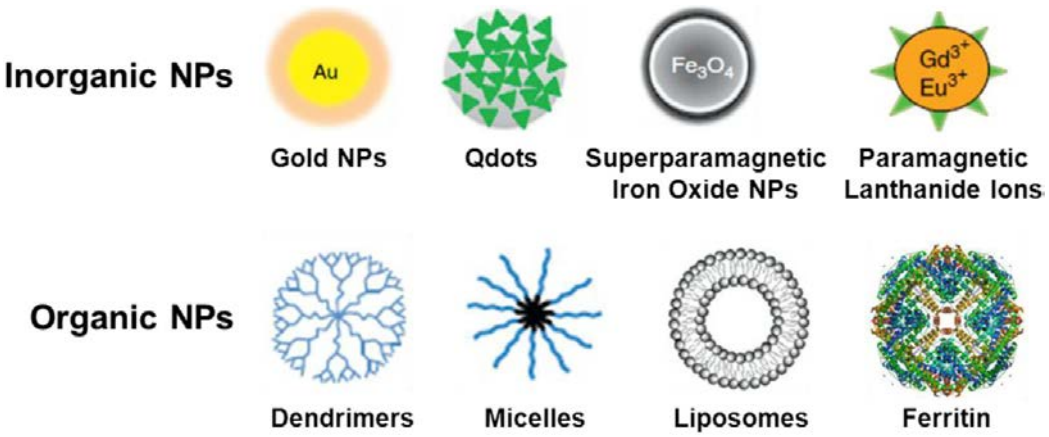

Figure 1.22 schematic representations of inorganic and organic types of nanoparticles for the construction of radiolabelling materials (Xing, Zhao, Conti, & Chen, 2014).

1.7.1.1 Polymeric Nanoparticles

The polymeric nanoparticles (10-1000 nm) are prepared from biocompatible and biodegradable polymers where the drug is dissolved, entrapped, encapsulated or attached to a nanoparticle matrix. Depending on the process used for their preparation, two different types of nanoparticles can be obtained: nanospheres and nanocapsules. Nanospheres have a matrix-type structure in which a drug is dispersed, whereas nanocapsules exhibit a membrane-wall structure with a core containing the drug (Kumari, Yadav, & Yadav, 2010; Soppimath, Aminabhavi, Kulkarni, & Rudzunski, 2001; Mohanraj & Chen, 2006). Because these systems have very high surface areas, drugs may also be adsorbed on their surfaces. Polymeric nanoparticles (P NPs) are widely used in areas such as environmental technology, sensors, conducting materials and medicine (Brahim, Narinesingh, & Elie, 2001; Zhang & Chuang, 2001). For example, polystyrene nanoparticles (PS NPs) are used as hydrophobic encapsulation materials in biomedical applications (Singer, 1987). These inexpensive, hydrophobic polymers allow physical adsorption of antibodies or proteins. These types of nanoparticles can also be functionalised on their surface with carboxylic groups that enable covalent binding of antibodies or proteins.

Polymers and biopolymers are favoured to increase the biocompatibility of a nanomaterial as well as to increase their lifetime in blood. In that respect, coating with polyethylene glycol (PEG) is the principal strategy to obviate or at least delay the action of the body's natural defenders. This is because macrophages and complement proteins need more time to detect the neutral polymer.

1.7.1.2 Inorganic Nanoparticles

Many types of inorganic NPs have been developed as nanoprobes for imaging and therapy applications (e.g. semiconductor, metal, metal-oxide and lanthanide-doped NPs). This section briefly describes silica nanoparticles (Si NPs), which were studied in this work.

1.7.1.2.1 Silica Nanoparticles

Silica nanoparticles (Si NPs) have received much attention because of their practical importance in a variety of plastic, construction composite, drug delivery, and theranostic applications (Santra, Zhang, Wang, Tapec, & Tan, 2001; Jain, Roy, De, & Maitra, 1998; Tolnai et al., 2001; Shibata, Tanighuchi, Yano, & Yamane, 1997, Van Helden, Jansen, & Vrji, 1980; Butterwort, Illum, & Davis, 2001; Liu & Chen, 1999; Chen, 1998). Si NPs are produced by the sol-gel process (Stöber method) (Stöber, Fink, & Bohn, 1968; Patra et al., 1999; Achatz, Heiligtag, Li, Link, & Wolfbeis, 2010) or by reverse microemulsion (water-in-oil, W/O) (Wang et al., 2009; Ke, Yang, Xia, Xu, & Li, 2010; Ye, Tan, Wang, & Yuan, 2005). A sol-gel process requires precursors in solution that react with water and yield an oxide network through inorganic polymerisation (Figure 1.23). Typical precursors are metallo-organic compounds such as metallic alkoxides M(OR)n, where M is a metal or metalloid (titanium, zirconium, aluminium, silicon, etc.) and R is an alkyl group (methyl CH_3, ethyl C_2H_5, etc.). Silica is one of the most studied metals of the sol-gel process, because of the lower costs of its precursors and the greater flexibility of silica chemistry. Tetramethoxysilane (TMOS) $Si–(OCH_3)_4$ and tetraethoxysilane (TEOS) $Si–(OC_2H_5)_4$ are the most common silicon precursors (Schubert, Husing, & Lorenz, 1995). Figure 1.23 shows the synthesis silica nanoparticles by sol-gel process.

In the reverse microemulsion method, monodispersed core/shell silica nanoparticles (C/S-Si NPs) can be easily constructed with a controllable size. Tang, Li, & Chen (2012) investigated how the amount of ammonium hydroxide, surfactant, tetraethyl orthosilicate (TEOS), H_2O and reaction time affects the size of Si NPs. They found that the size of the dye-doped Si NPs was reverse-proportional to the concentration of ammonium hydroxide and water to surfactant molar ratio, but directly-proportional to the amount of TEOS and reaction time. Zhao, Trewyn, Slowing, & Lin (2009) found that they could affect the surface area occupied by surfactant molecules by varying the organic solvents, while the diameter of the water droplet could be increased with the

length of the organic molecule (Bagwe, Yang, Hilliard, & Tan, 2004; Jin et al., 2008). Silica nanoparticles are being considered for several biomedical applications due to their biocompatibility, low toxicity, and scalable synthetic availability (Liberman, Mendez, Trogler, & Kumme, 2014). In recent years, Si NPs have been used for *in vitro* and *in vivo* diagnosis, analysis, and measurements inside intact biological systems (e.g. tissues, blood, and single cells). Along with the use of nanoparticle devices, they have attracted considerable attention (Jain et al., 1998; Tolnai et al., 1998; Butterworth et al., 2001; Gruttner & Teller, 1999).

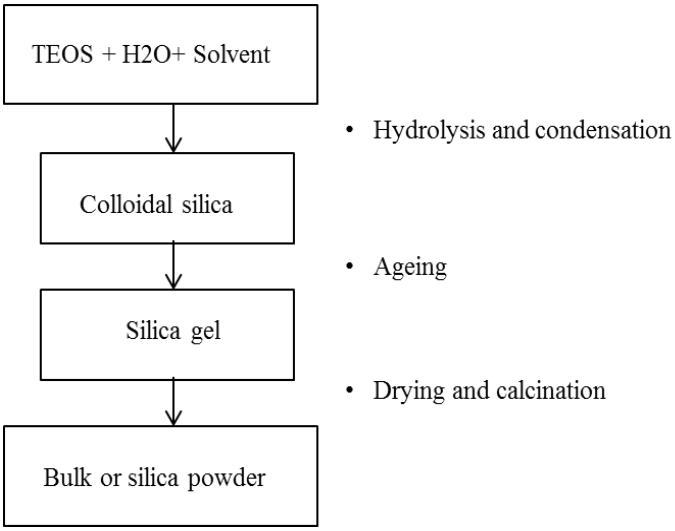

Figure 1.23 Flow chart of a typical sol-gel process (adapted from Rahman & Padavettan, 2012).

1.7.2 Key Characteristics of Nanoparticles

1.7.2.1 Particle Size

The size of the particles is an important factor in determining the performance of nanoparticles systems *in vitro* as well as *in vivo*. It has an advantage for delivering NPs drugs, allowing direct injection into the systemic circulation without the risk of blocking blood vessels (Letchford & Burt, 2007; Gref et al.,

1995; Douglas, Davis, & Illum, 1987). The circulation time of NPs can be increased by the inclusion of surface bound hydrophilic molecules such as polyethylene glycol (PEG) (Gref et al., 1994; Klibanov, Maruyama, Torchilin, & Huang, 1990). These NPs can cross tumour mass barriers and become preferentially retained within target cells via the enhanced permeability and retention (EPR) effect (Maeda, 2012; Maeda, Bharate, & Daruwalla, 2009; Torchilin, 2004; Ernsting, Murakami, Roy, & Li, 2013). The conditions used for the preparation of the particles highly affect their size (Lu, Wu, Hung, & Mou, 2009; Pan et al., 2012; Rossi, Shi, Quina, & Rosenzweig, 2005). NPs size may affect the active or passive uptake efficiency, kinetics and subcellular distribution. A size-dependent uptake in different cell lines has been observed for gold NPs (Wang, Lee, Chiou, Wei, 2010), mesoporous Si NPs (Lin & Haynes, 2010), and PS NPs (Varela, Bexiga, Åberg, Simpson, & Dawson, 2012) with maximum cellular uptake for core sizes in the range of 30-50 nm. For active uptake, Rejman, Oberle, Zuhorn, & Hoekstrta (2004) used a range of latex beads sizes (50-1000 nm) to investigate the size effects on the entry pathway in non-phagocytic B16 cells. They found beads with diameters less than 200 nm were optimum for targeting this pathway. Mironava, Hadjiargyrou, Simon, Jurukovski, & Rafalovich (2010) reported that 45 nm gold NPs penetrated cells via clathrin-mediated endocytosis, while the smaller 13 nm NPs entered mostly via phagocytosis.

In addition to active transport, NPs may also enter cells by passive penetration of the cell membrane. In fact, for cells lacking the endocytosis machinery such as red blood cells (RBCs), passive transport is the only option (Shang, Nienhaus, & Nienhaus, 2014). Geiser et al. (2005) analysed the uptake of PS NPs by red blood cells (RBCs) and found that particles less than 200 nm entered the RBC most effectively. Table 1.5 lists particle sizes, their interactions with biological systems, and some examples of applications.

Table 1.5 Impact of particle size on interaction with biological systems (adapted from Bae & Park, 2011)

Particle size	Biological Impact
4.5 nm	Abundant small pores present in normal tissue endothelium
25 nm	Relatively few large pores present in normal tissue endothelium
20-50 nm	Average size of polymeric micelles without loaded drugs
100 nm	Frequently tested size of drug-loaded polymer micelles
150 nm	Proposed cut-off size for particle extravasation in liver. Liver has blood vessels with fenestrations of 100-175 nm
200 nm	Nanoparticles less than 200 nm have significantly longer circulation time due to low uptake by the reticuloendothelial system (RES)
380 nm	A tumour-dependent functional pore cut off size ranges from 200 nm to 1.2 μm, but the pore cut off size of porous blood vessels in the majority tumours is known to be 380-780 nm. Therefore, the range for using the EPR effect should be similar.
400 nm	Sterically stabilized liposomes of 400 nm in diameter were able to penetrate into tumour interstitium. Accumulation of hyaluronic acid-coated nanoparticles (400 nm) in tumour tissue
500 nm	The maximum size of nanoparticles allowing penetration through cell membranes is known to be 500 nm
1 μm	Particles below 1 μm were taken up by Peyer's patches and then migrated to mesenteric lymph nodes
5 μm	The upper limit for rigid particles circulating within the smallest capillaries
40 μm	Particles larger than 40 μm haven been used for embolization therapy

1.7.2.2 Surface Charge

The surface of NPs can be net negatively, positively or neutrally charged with or without further modification, depending on the type of NPs. It has been reported that surface charge is a very important factor for determining the efficiency and mechanism of cellular uptake, and the *in vivo* fate of NPs (Osaka, Nakanishi, Shanmugam, Takahama, & Zhang, 2009; Juliano & Stamp, 1975; He, Hu, Yin,

Tang, & Yin 2010; Chung et al., 2007). For example, Si based NS are usually negatively charged because of the presence of the hydroxyl group after hydrolysis of TEOS. It is possible to modify the charge of these particles by functionalising them with amine, carboxyl or PEG by hydrolysis of the corresponding silanes (Wu, Wu, & Zhao, 2014). When nanoparticles with hydrophobic surfaces are administered they are recognised easily by lymphatic cells in the body as foreign substances. To circumvent this problem, the surface of the nanoparticles is often modified with a hydrophilic polymer, which acts as a shield between NPs and lymphatic cells (Nishioka & Yoshino, 2001). Surface properties of NPs can be measured by various methods (e.g. zeta potential, x-ray photoelectron spectroscopy and column chromatography). These methods are used to estimate the surface charge, density or surface hydrophilicity of the functional groups. For example, the zeta potential provides information regarding the ionic nature of carrier particles: a zeta potential of -30 mV indicates a strongly anionic nature. Zeta potentials between +10 and -10 mV indicate neutral behaviour, and zeta potentials over 30 mV indicate a cationic nature (Clogston & Patri, 2011). To avoid the aggregation of the particles, those with a zeta potential in the range ± 30 mV have been shown to be more stable in suspension (Selvaraj, Karthikeyan, & Saravanakumar, 2012).

1.8 Polyethylene glycol (PEG)

Polyethylene glycol (PEG)-coated nanoparticles have attracted interest since they have shown increased circulation time and reduced reticuloendothelial system uptake compared to non-PEGylated nanoparticles after intravenous administration (Gref et al., 1994; Bazile et al., 1995; Gref, Couvreur, Barratt, & Mysiakine, 2003; Moghimi & Szebeni, 2003; Vonarbourg, Passirani, Saulnier, & Benoit, 2006). Nanoparticles modified with PEG possess favourable intrinsic physicochemical properties (e.g. high flexibility, hydrophilicity, low toxicity and immunogenicity), and have been found to reduce nanoparticle accumulation in organs such as liver and spleen (Knop, Hoogenboom, Fischer, & Schubert,

2010). The shape, density and length of PEG chains attached to nanoparticles have an effect on surface hydrophilicity and phagocytosis (Gref et al., 2000). For example, long PEG chains increase the size of nanoparticles and would create more effective blocking than small PEG chains (Vonarbourg et al., 2006). PEG surface coating can counteract the hydrophobic and electrostatic interactions between NPs and plasma proteins or macrophages, resulting in a reduction in reticuloendothelial system (RES) uptake and prolonged blood circulation time (Zahr, Davis, & Pishko, 2006).

1.9 EPR Effect and Principle of Passive and Active Targeting

1.9.1 Enhanced Permeability and Retention (EPR) Effect

The main tumour-targeting principle of many drug delivery systems is based on the EPR effect of NPs first proposed by Maeda, Ueda, Morinaga, & Matsumoto (1985) and Matsumura & Maeda, (1986) who observed that macromolecules such as polymers and proteins with molecular weight larger than 40-50 kDa showed selective accumulation in tumour tissues (far more than that observed in normal tissues) and that they were retained in tumour tissues for long periods, i.e. > 24 h. This was attributed to the Enhance Permeability and Retention (EPR) effect. EPR effect is a phenomenon resulting from the unique anatomical and pathophysiological characteristics of solid tumours. Most solid tumours show a higher vascular density (hypervascularity) compared to normal tissues and organs.

Irregular or inconsistent blood flow is also commonly observed in tumours, and most solid tumours have blood vessels with defective architecture, such as large gaps between endothelial cells (e.g. ~ 1 μm) plus a lack of smooth muscle layers. As a result, macromolecules will have the opportunity to escape from tumour blood vessels and accumulate selectively in tumour tissues, in a manner which would otherwise not be possible in normal blood vessels. Although the main

factor influencing the EPR effect is the particle size (> 40 kDa), biocompatibility and surface charge are also key factors in the EPR effect (Maeda, Nakamura, & Fang, 2013). Ideally, the chosen nanomedicinal or macromolecular drug should present no interaction with blood components or blood vessels, no antigenicity, no RES clearance and no cell lysis. Positively charged polymeric drugs will tend to bind non-specifically to the luminal surface of the vascular walls, which are negatively charged, and then are rapidly cleared from the blood circulation. Negatively charged particles, however, will result in blood coagulation. Weakly negative to near neutral particles are ideal for the use of the EPR effect in nanomedicine

Table 1.6 Ideal Characteristics of the EPR effect of nanomedicines and macromolecular drugs (adapted from Maeda et al., 2013).

Drug Characteristic	Ideal Properties
Biocompatibility	No interaction with blood components or blood vessels, no antigenicity, no clearance by the reticuloendothelial system, no cell lysis.
Molecular size	Larger than 40 kDa (larger than the renal clearance threshold)
Surface charge	Weakly negative to near neutral
Time required to achieve	Longer than several hours in systemic circulation in mice, with distinct accumulation seen at 30 min
Drug retention time	Usually days to weeks, in great contrast to passive targeting, in which low-molecular-weight molecules are rapidly cleared and enter the systemic circulation in a few minutes (compare with low-molecular-weight contrast agents).

1.9.2 Passive Targeting of Tumours

The most common type of *passive* tumour targeting is targeting by the EPR effect. It can be observed in almost all human cancers with the exception of hypovascular tumours such as prostate cancer or pancreatic cancer (Maeda et al., 2009), and is applicable in almost all rapidly growing solid tumours (Dobrovolskaia & McNeil, 2007). The desired particle size of NPs is designed to be around 10-100 nm to allow NPs to extravasate from defects in tumour vasculature (Phillips, Gran, & Peppas, 2010). The nanocarrier's size should be more than 10 nm to avoid glomerular filtration by the kidneys, and less than 100 nm to avoid specific capture by the liver and RES clearance (Xing et al., 2014). Generally, when NPs are administered intravascularly, most are removed by the cells of the RES while only a small fraction of NPs will reach the tumour (Maeda, Sawa, & Komo, 2001). This is why, for optimal EPR effect, NPs should be less than 100 nm, and their surfaces should be biocompatible (i.e. hydrophilic and almost neutral in electric charge) to minimise RES clearance.

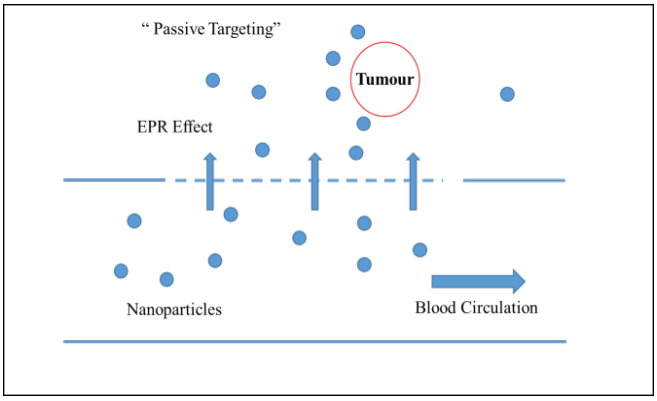

Figure 1.24 Passive targeting by EPR effect: NPs can be passively extravasated through leaky vascularisation, leading to their accumulation at the tumour region.

1.9.3 Active Targeting of Tumours

Active targeting consists of coupling a ligand to the surface of NPs that can interact with its specific receptor at the target cell site (Danhier et al., 2009), which occurs only after blood circulation and extravasation. The ligand is chosen to bind to a receptor overexpressed by tumour cells or tumour vasculature and not to various receptors expressed by normal cells. Representative ligands include antibodies, proteins, peptides, nucleic acids, sugars, and small molecules such as vitamins (Saha et al., 2010). The interaction of the ligand-functionalised NP systems with its target is enhanced by the multivalent nature of the NP's architecture. Multiple copies of the ligand on the NP surface will increase the avidity of the NP for its target (Wang et al., 2010). When evaluating the efficiency of an active-targeting system, there are two important factors to consider; the *targeting specificity* and the *delivery capacity*. The targeting specificity is determined by the biodistribution of the ligand-functionalised NPs and by how the conjugated ligand and the NPs system interact with off-target molecules and cells. It is defined by both the ligand and the NP's properties. The delivery capacity is related to the NP's material and structure (Kamaly, Xiao, Valencia, Radovic-Moreno, & Farokhzad, 2012).

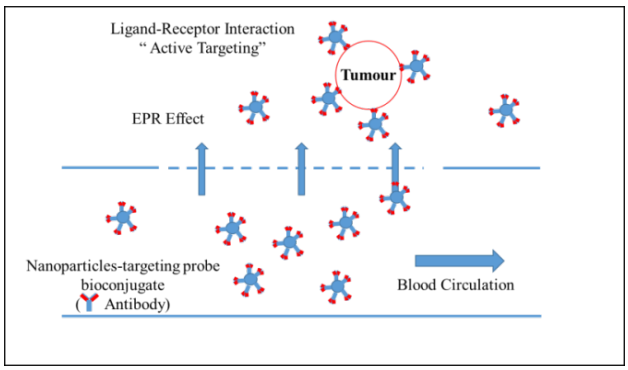

Figure 1.25 The delivery of NPs to the tumour. Some of the NPs circulating in blood accumulate at the tumour region through the EPR effect. If for example, the NPs possess a chelator to a specific marker on tumour cells, specific chelator–receptor interactions can occur.

1.10 Aims

The aims of this thesis, as linked to successive chapters are:

Chapter 2

- To measure precisely the primary proton beam energy of an isochronous auto-extraction cyclotron to ensure optimum production of radioisotopes using solid targetry. This section was focused on the development of a simple and practical method for cyclotron beam energy measurement, avoiding the use of complex analytical methods or an array of energy-specific degraders. This method was also used subsequently to evaluate a custom degrader constructed to reduce the 18 MeV proton beam to the optimal energy for the thin-target production of the desired isotopes.

Chapter 3

- To determine the excitation functions of the accessible ^{nat}Zn (p,x) reactions using a high purity natural-zinc target and proton energies up to 17.6 MeV, delivered by an IBA 18/18 MeV cyclotron with an in-house designed solid targetry system.

Chapter 4

- To evaluate methods for the separation and purification of ^{61}Cu produced from enriched ^{64}Zn target or ^{nat}Zn target. To develop a chemically novel and cost effective separation process that may be applied in routine production, which yields the highest purity final product. This also involved the assessment of three different chelators NOTA-NCS, DOTA-NCS and the macrobicyclic sarcophagine diamsar for determining the effective specific activities of replicated ^{61}Cu productions, and the

comparison of these values with the NCA specific activities obtained from ICP-MS analysis.

Chapter 5

- To radiolabel functionalised polystyrene and silica nanospheres with ^{64}Cu, ^{57}Co or ^{61}Cu and determine the most effective bifunctional chelator from the group SarAr-NH_2, NOTA-NCS, DOTA-NCS and MeSar-Ph-NCS for this purpose. MeSar-Ph-NCS is a novel macrobicyclic sarcophagine developed recently by collaborators of our laboratory.

Chapter 6

- To evaluate the stabilities and some physical properties of ^{61}Cu labelled silica nanosphere complexes, where radiolabelling is achieved using three separate bifunctional chelators; NOTA-NCS, DOTA-NCS and MeSar-Ph-NCS. The *in vivo* biodistributions of these complexes would then be studied comparatively at two time-points in an immunodeficient mouse model using μPET/CT and post-imaging dissection plus γ-counting.

CHAPTER TWO

PRECISE MEASUREMENT OF CYCLOTRON BEAM ENERGY

A version of this chapter was published in:

Asad, A.H., Chan, S., Cryer, D., Burrage, J.W., Siddiqui, S.A. & Price R.I. (2015). A New, Simple & Precise Method for Measuring Cyclotron Proton Beam Energies Using the Activity vs. Depth Profile of Zinc-65 in a Thick Target of Stacked Copper Foils. *Applied Radiation and Isotopes, 105*, 20-25.

2.1 Introduction

It is periodically important to precisely measure the primary beam energy of a cyclotron; for example, following alterations to components controlling the beam, for research applications including measurement of reaction cross sections, or to optimise the yield of a particular isotope while suppressing the production of co-produced 'contaminating' radionuclides (Gagnon et al., 2011; Asad et al., 2014; Kim, Park, Kim, Lee, & Chun, 2006).

This is particularly relevant when producing the radiometal ^{64}Cu from the ^{64}Ni(p,n)^{64}Cu reaction, as a proton beam energy of 11.5-12 MeV is specifically and precisely selected to avoid the production of ^{61}Co, because at this energy, the yield of the side-reaction ^{64}Ni(p,α)^{61}Co is significantly reduced (Avil-Rodriguez et al., 2007). To accurately degrade the proton energy to the desired value, a good knowledge of the primary beam energy is required in order to calculate the appropriate thickness of material (e.g. copper, graphite, or aluminium) used to degrade the beam. These stopping power calculations are conducted using industry software such as Stopping and Range of Ions in Matter (SRIM) software (Ziegler, Ziegler, & Biersack, 2011).

In the current work an IBA isochronous 18/9 cyclotron is used. The IBA isochronous 18/9 (or 18/18 in its proton-only beam mode) cyclotron (Ion Beam Applications, Belgium) accelerates negative hydrogen ions (H^-) extracted from its ion source up to a nominal energy of 18 MeV, with a maximum extracted current of 150 μA. The circulating beam experiences a magnetic field that varies harmonically with orbit azimuth, resulting in a non-circular beam path, unlike in an idealised classical cyclotron (Strijckmans, 1994). Consequently, it is difficult to calculate the beam energy of an isochronous cyclotron from knowledge of the magnetic field strength and nominal beam orbit diameter alone (more details are given in Section 1.3 in the previous chapter).

Conventional cyclotrons used for medical PET radionuclide productions usually do not include apparatus for direct beam energy measurements, such as those based on time-of-flight principles or by use of magnetic energy analysers (Kormány, 1994; Chêne, Garnir, Marchal, Mathis, & Stivay, 2008). Therefore, several indirect methods have been devised to sample the energy of the beam following its extraction from the cyclotron, using one or two nuclear reactions in a target containing high-purity metal foils of precise thicknesses. The cross sections of these 'monitor' reactions, which are usually chosen from the group $^{nat}Cu(p,x)^{62,63,65}Zn$ to cover useful proton irradiation energies up to 19 MeV, are well documented and intended for comparison purposes (IAEA, 2009). One of these methods requires measurement of the ratio of activities of ^{62}Zn to ^{65}Zn co-produced in the same monitor foil. This ratio is then used to determine the ratio of the respective cross sections of these isotopes at the sampled energy in the foil. In turn, this calculation is compared with the ratio of cross sections as a function of energy from published data, and therefore the beam energy can be determined provided that it falls within the monotonic section of this calibration curve. Though the method requires a gamma energy detector calibrated with standard sources (since it requires the measurement of the activities of two isotopes) it does not need a direct measurement of beam current on the target (Kopecky, 1985).

Another method uses activity measurements from only one monitor reaction and requires neither calibrated gamma-spectroscopy nor knowledge of beam current. In this process, two monitor foils are bracketed by aluminium energy-degraders of precise thickness; one specific degrader for each contiguous energy segment comprising the measureable energy range. The activity of ^{63}Zn from the ^{nat}Cu(p,x)^{63}Zn reaction is measured in each foil and its ratio between the foils (reflecting different mean beam energies in the foils) is used to calculate the equivalent ratio of cross sections (Gagnon et al., 2011).

This study reports an extension of the method of Burrage et al. (2009) which utilises the ^{65}Cu(p,n)^{65}Zn monitor reaction to measure energies below and beyond the nominal energy of the proton beam of the cyclotron. The technique requires neither a direct beam-current measurement nor gamma-spectroscopy efficiency calibration with standard sources; though a characteristic reaction photopeak must be identified. Briefly, the method employs the well-known stacked foil technique (Qaim, 1982) in a 'thick target' configuration, to sample an interval of the well-characterised monitor reaction excitation function. This is combined with an iterative method (using 'incident beam energy' as the regression variable) for achieving congruence of the experimental and calculated ^{65}Zn activity vs. depth profiles in the target stack. The technique exploits the uniqueness of the shape of the activity profile vs. depth of the monitored isotope in the target stack for specified incident energy. It represents the uniqueness of the sampled section of the reaction cross-section, but does not require the entire cross section to be sampled.

In summary, the proposed method is based on a comparison of the normalised profile of activities measured in the monitor-foil stack with the calculated normalised profile derived using the published monitor-reaction excitation function. Since the latter profile depends on the assumed starting energy of the beam, that energy is adjusted iteratively until the experimental and theoretical values agree.

In this work the method was used to measure the primary beam energy before and after a scheduled cyclotron upgrade. This upgrade comprised a change of configuration (from18/9 proton/deuteron to 18/18 proton/proton configuration) as well as upgrades to beam generation and (nonmagnetic) control components of the IBA cyclotron at the Department of Medical Technology and Physics, Sir Charles Gairdner Hospital (Perth, Australia). The same method was also used to validate a custom-designed water-cooled graphite degrader to reduce the primary beam energy to 11.6 MeV at the target face, which was required for routine production of both ^{89}Zr and ^{64}Cu using an in-house designed solid-targetry system.

2.2 Materials and Methods

2.2.1 Targetry and Irradiation

Natural-Cu foils (^{nat}Cu; 99.99% chemical purity; 69.15% ^{63}Cu, 30.85% ^{65}Cu) of diameter 25 mm and nominal thicknesses 25, 50, 75 and 100 μm were used as the target materials (Goodfellow, Huntington, UK). The mean thickness of each foil was calculated from its density prior to irradiation by measuring its diameter and weight, and it was this measurement that was used for thickness calculations rather than the nominal value. For each independent experiment (indexed by foil thickness) a stack of total thickness of approximately 700 μm was constructed to stop the beam according to simulations in SRIM software (Ziegler et al., 2011). Each stack was placed in an in-house constructed solid-target holder and bombarded by a proton beam of approximately 9 mm in diameter following passage through a water-cooled graphite collimator and a 'vacuum window' of 50 μm thick Havar® foil (Goodfellow), but without a beam degrader. The target was cooled on its front face by a flow of helium gas (between the Havar® and the leading target foil) and from behind by a chilled water jet (further details are given in Section 1.3.1 in the previous chapter). Nominal target currents were measured with a Fluke 289 multimeter using Fluke View software (Ver. 3,

Fluke, Everett, Washington, USA), though these measurements were not used in the beam energy determination. Irradiation was for 60 s (measured precisely) at approximately 10 μA.

Target stacks of 50 μm-thick Cu foils were used to re-measure the cyclotron energy following a cyclotron beam system upgrade. This intervention had altered the beam configuration from 18/9 MeV (proton/deuteron) to 18/18 MeV (proton/proton) and raised the primary beam current (as measured on a beam-stop at one of the cyclotron's eight exit ports) from 100 μA to 150 μA. All experiments were performed in triplicate.

2.2.2 Measurement of Activity Profile of Foil Target Stack

Irradiation of a stack of ^{nat}Cu foils by protons at the nominal energy of the cyclotron is known to produce three Zn isotopes (^{62,63,65}Zn) by the (p,x) reactions shown in Figure 2.1 (IAEA, 2009). After an irradiation, the activity of ^{65}Zn ($T_{1/2}$ = 243.66 d) was measured by gamma spectrometry, by integration of the 1115 keV signature photopeak several days following end of bombardment (EOB) in each of the foils. A HPGe γ-spectrograph (Canberra Industries, Meriden, USA) was used, incorporating a S5000 multi-channel analyser (MCA), and a cryogenically-cooled GC1018 high-purity germanium (HPGe) detector. Though the γ-spectrograph was calibrated for sensitivity and photopeak energies, a sensitivity calibration was not an essential requirement since only the relative activities of the foils were required. For comparison, the activities of ^{62}Zn ($T_{1/2}$ = 9.186 h) and ^{63}Zn ($T_{1/2}$ = 38.47 min) were also measured at 2 h following EOB by integration of the 596 and 669 keV signature photopeaks, respectively. Each foil was placed 25 cm from the detector end cap and dead times were less than 5%. The net counts (N_c, in units of Bq.s^{-1}) in a photopeak were calculated by subtracting continuum counts in the spectrum from total photopeak counts, performed automatically by the CAM tools program of the Genie 2000 (Gamma Acquisition & Analysis) software (Canberra). Activities forming each profile were corrected to EOB, A_{EOB}, using the relation:

$$A_{EOB} = \frac{\lambda N_c T_c}{\varepsilon \eta (1 - e^{-\lambda T_c}) e^{-\lambda T_e}} \quad (1)$$

where

λ (=ln [2]/$T_{1/2}$) is the decay constant for the produced isotope,

$T_{1/2}$ is the half-life of the isotope,

N_c is the net peak area,

T_c is the counting time for the photopeak,

ε is the detection efficiency of the γ-spectrograph at the photopeak energy,

η is the branching fraction for the decay mode leading to the photopeak, and

T_e is the elapsed time between EOB and the start of counting.

Since the measured activity profile in a stack was normalized (i.e. foil activity/maximum activity seen across all foils), ε and η may be set to unity, obviating the need for sensitivity calibration of the spectrograph. However, its detection efficiency at the chosen photopeak energy must be stable over time and the relevant characteristic photopeak must be able to be identified.

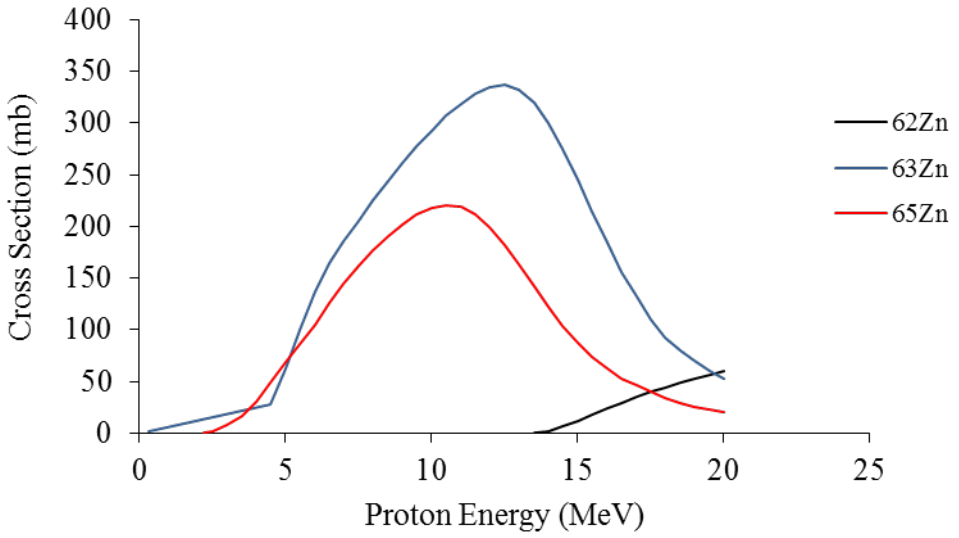

Figure 2.1 Cross sections of the $^{nat}Cu(p,x)^{62,63,65}Zn$ reactions as a function of proton energy from IAEA recommended cross section data (adapted from IAEA, 2009).

2.2.3 Calculation of Expected Activities of Foils

Incident proton energy was described briefly in the following steps. (i) The stopping power for a proton in solid ^{nat}Cu was expressed as a continuous function of proton energy (from 1×10^{-3} to > 20 MeV) using data from The National Institute of Standards & Technology (Berger, Coursey, Zucker, & Chang, 2005) and curve-fitting equations from CurveExpert 1.4 (copyright 2013, Daniel Hyams). (ii) Similarly, a combination of fitted curves were used together with published cross section data to represent the excitation function for the $^{65}Cu(p,n)^{65}Zn$ monitor reaction as a continuous function of proton energy (IAEA, 2009). (iii) The target stack was modelled as being divided into 0.001 mm penetration increments, (indexed as $i = 1,\ldots,n$) along the beam path. A plausible starting estimate of the primary beam energy, E_0, was assumed. The proton energy at the entrance and exit of each penetration increment 'i' was then calculated using the fitted stopping power curve. The exit energy from one increment was used as the entrance energy for the next. The beam energy, E_i, assigned to the penetration increment 'i' was the mean of these entrance and exit

energies. (iv) If beam straggling of the penetrating beam is ignored (Section 2.2.5), then E_i uniquely represents the beam energy in the very thin penetration increment '*i*' and $\sigma(E_i)$ is its unique representative monitor-reaction cross section. The activity, $A_i(E_i)$ (in Bq) of ^{65}Zn arising from proton transport through penetration increment '*i*' at EOB is then given by the simple equation:

$$A_i(E_i) = \frac{6.24*10^{21} N_A(1-\exp^{-\lambda T})\rho FxI\sigma(E_i)}{M} \qquad (2)$$

where A_i is expressed in Bq, N_A is Avogadro's number; T is the bombardment time (s); ρ is the target material density (kg m^{-3}); F is the atom fraction of the ^{65}Cu isotope in ^{nat}Cu; x is the thickness of a penetration increment '*i*' (in this calculation, $x = 1 \times 10^{-6}$ m; total target stack thickness = nx); I is the incident proton beam current and assumed constant (A); $\sigma(E_i)$ is the reaction microscopic cross section at energy E_i (m^2) and M is the molar mass of ^{nat}Cu (g.mol^{-1}).

The constant arises from the choice of units for the variables on the RHS of the equation. By computing the activity of ^{65}Zn produced in each penetration increment '*i*' and then summing these activities over the increments comprising the complete irradiated foil, the expected total activity of ^{65}Zn in that foil was calculated.

The process was repeated for each irradiated foil in the stack, so that the calculated expected activity profile along the axis of the stack of foils was determined for the specified trial incident energy E_0. In this computation the beam current (strictly, the total received proton charge on target) need not to be known and was set at an arbitrarily value. The expected activity profile was subsequently normalized to unity at peak activity for comparison with the normalized experimentally determined profile described in the previous section.

2.2.4 Iterative Calculation of Primary Beam Energy

For each foil in an irradiated stack the measured and expected normalized ^{65}Zn activities were compared and the residual calculated. Residuals were then squared, summed and used in an iterative least-squares minimisation technique to adjust the trial incident beam energy E_0 for the re-calculation of the expected activity for each foil using equation (2), until the residual sum of squares was minimised. Figure 2.2 shows the analysis of a single experiment where the target stack consisted of fourteen 50 μm-thick foils (foil '1' at the front face). The normalised measured ^{65}Zn activities are shown as solid circles. The optimal (best fit) profile resulting from minimisation of the sum of squared residuals is shown as solid triangles, yielding a beam energy of 18.15 MeV (solid connecting lines to aid visualisation; profile B). Sample 'outlier' profiles under-estimating (A) and over-estimating (C) energy by 0.5 MeV are also shown for comparison. Convergence of the regression as a function of trial beam energy, to reflect 'best-fit' profile B, is shown in the insert.

Though their data were not required obligatorily for determining the beam energy, the profiles of the monitor isotopes ^{62}Zn and ^{63}Zn were also measured and compared with calculations in order to predict beam energy using the same methods, and consequently to determine if the technique was adaptable to these isotopes. (Inclusion of ^{62}Zn and ^{63}Zn was only possible because the γ-spectrograph used in this study was calibrated with standard sources whose combined energy range covered the characteristic photopeaks). Though it was believed that 50 μm-thick foils were appropriate for building a target stack (being thin but robust) other foil thicknesses (i.e. 25, 75 and 100 μm) were also measured to determine if foil thickness influenced results.

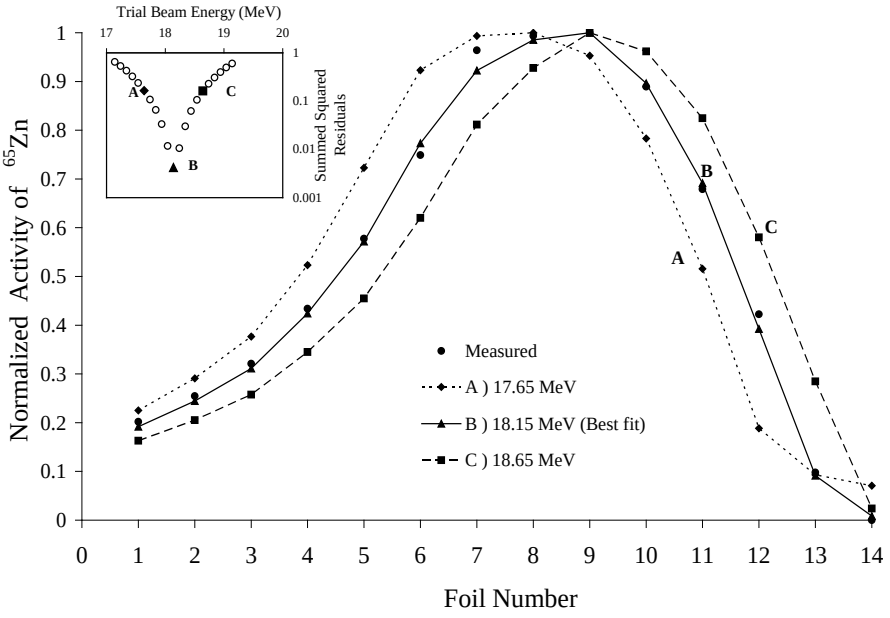

Figure 2.2 Example of a beam energy determination. Normalised measured ^{65}Zn activities of 50 µm-thick ^{nat}Cu foils of a target stack (solid circles). Equivalent best-fit regression calculation of normalised activities, yielding a beam energy of 18.15 MeV (Profile B), compared with sample profiles underestimating (A) and overestimating (C) energy by 0.5 MeV. Insert: convergence of the regression to B. Foil '1' is the target front face.

2.2.5 Effect of Energy Straggling

It can be shown for a monoenergetic proton beam of energy < 100 MeV penetrating a 'thick' target that its energy at any depth is not a unique value but assumes an approximately Gaussian distribution (Noshad & Bahador, 2012), which can be computed using the SRIM Monte Carlo code (Ziegler et al., 2011) This study used the method of Burrage et al. (2009) to assess the effect of beam straggling on computed beam energy. Briefly, the propagation of the energy-straggling effect through the target, in depth-increments of 0.05 mm was considered. Starting with a monoenergetic beam, the distribution of beam energies at depth *z* was derived from a SRIM-based simulation of the energy spread. These data were then described by a fitted curve of the form:

$$y(E,z) = a\exp\left(-\frac{[E-\bar{E}_z]^2}{[2s^2]}\right) \quad (3)$$

where E is the proton energy, $\overline{E}z$ is the mean energy of protons at penetration depth z, and where a and s are fitting parameters with s^2 being an estimate of the variance of the (assumed Gaussian) energy distribution. Those parameters (a, $\overline{E}z$, s) describing the evolution of the shape of the energy straggling distribution vary smoothly with z, allowing continuous functions to be fitted that describe the variation of these parameters with penetration depth, particularly for the discreet values $z = ix$ (i=1,…,n). Each $y(E,ix)$ was then approximated by a normalized histogram with $p(i)$ elements, $H(i,j)$ (j=1,…, $p[i]$), with energy increments ΔE = 0.01 MeV. The element $H(i,j)$ represents the fraction of protons with energies between $E(i,j)$ and $E(i,j+1)$, where $E(i,j+1) - E(i,j) = \Delta E$, and where $E(i,j)$ is the energy of the jth histogram element at penetration depth $z = ix$. Then, to account for energy straggling, $\sigma(E_i)$ in equation (2) was replaced by the summation over (j=1,…,$p[i]$) of $\Sigma H(i,j)\ \Sigma\ (E[i,j])$ for the iterative calculation of beam energy. Since the effect of beam straggling on the best-fit derived beam energy was found to be < 0.1% (as was also found by Burrage et al., 2009) it was therefore ignored.

2.2.6 Choice and Measurement of Beam Degrader

In cyclotrons, without a tuneable beam energy, the primary beam energy can be degraded using materials placed in the beam path (Anferov, 2003). Candidate materials include copper, graphite and aluminium. In this study the degrader may be positioned 48.5 mm up-beam from the solid target.

Beam angular divergence occurs within the degrader because of scattering; however, divergence can be minimised by the choice of degrader material. This is illustrated in Figure 2.3 which shows the results of SRIM scattering calculations that assume a thin collimated proton beam encountering a degrader at normal incidence (Ziegler et al., 2011). Beam scattering is expressed as

normalized counts/unit solid angle, as a function of the scattering angle. The computational thickness of each degrader material was set so that the on-target beam energy was 11.6 MeV, following correction for prior transport through the 50 µm-thick Havar® foil immediately anterior to the target. It is seen that the angular spread of the beam at the point of exiting from the degrader is minimised if the choice is graphite. Havar® would not normally be used to significantly degrade the beam because of its poor thermal conductivity, but it is included as a comparison.

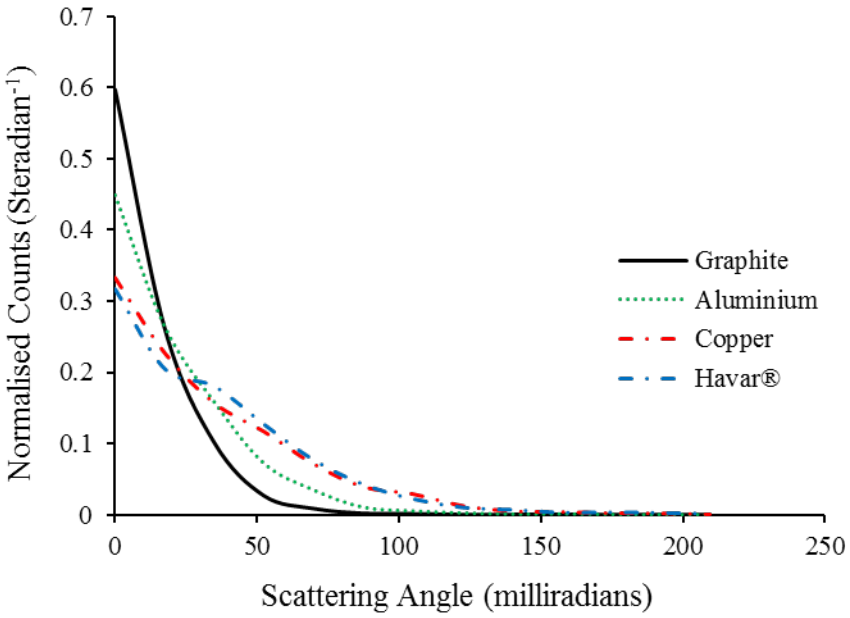

Figure 2.3 Calculated scattering profiles, per unit solid angle, for a thin collimated proton beam emerging from various degrader materials. Each degrader is designed to reduce beam energy from 18.1 MeV to an on-target value of 11.6 MeV, after accounting for a 50 µm-thick Havar® vacuum window immediately anterior to the target. Area under each scattering profile is normalised to unity.

Following the measurement of primary beam energy without a degrader, separate replicate measurements of the energy loss in the degrader were also made, during routine production of the PET radionuclides ^{89}Zr, ^{64}Cu and ^{61}Cu. The degrader consisted of a machined graphite disc (ρ = 1.85g/cm^3) with thickness 1020 µm,

inserted in the custom-constructed water-cooled graphite collimator which lies up-beam of the Havar® vacuum window. According to a SRIM calculation, this degrader converted a primary beam energy of 18.1 MeV (see Results & Discussion) to 11.6 MeV at the target after accounting for energy loss in the vacuum window, immediately up-beam of the target.

Using 50 µm-thick copper foils, the $^{65}Cu(p,n)^{65}Zn$ monitor reaction and the above methods, the degraded proton beam energy was measured as 11.65 ± 0.06 (SD) MeV (CV=0.5%; N=3; 95% CI=11.50-11.80) at the target. The difference between the measured and the calculated values was not significant. Thus the method proved valid for accurately assessing the decrease in beam energy arising from this degrader insert, when compared with the theoretical estimate.

2.2.7 Measurement of Beam Cross Sectional Intensity Profile

The transverse proton-beam intensity profile at the target face was checked before and following insertion of the degrader described above, as shown in Figure 2.4. Gafchromic films EBT and EBT2 (International Specialty Products, Wayne, USA) were used as reported by Avila-Rodriguez, Wilson, & McQuarrie (2009). This identified the beam shape as well as any intensity 'hot spots' (see Figure 2.5). This technique also proved useful when checking off-axis or asymmetric behaviour of the beam following cyclotron maintenance and installation of new stripper foils.

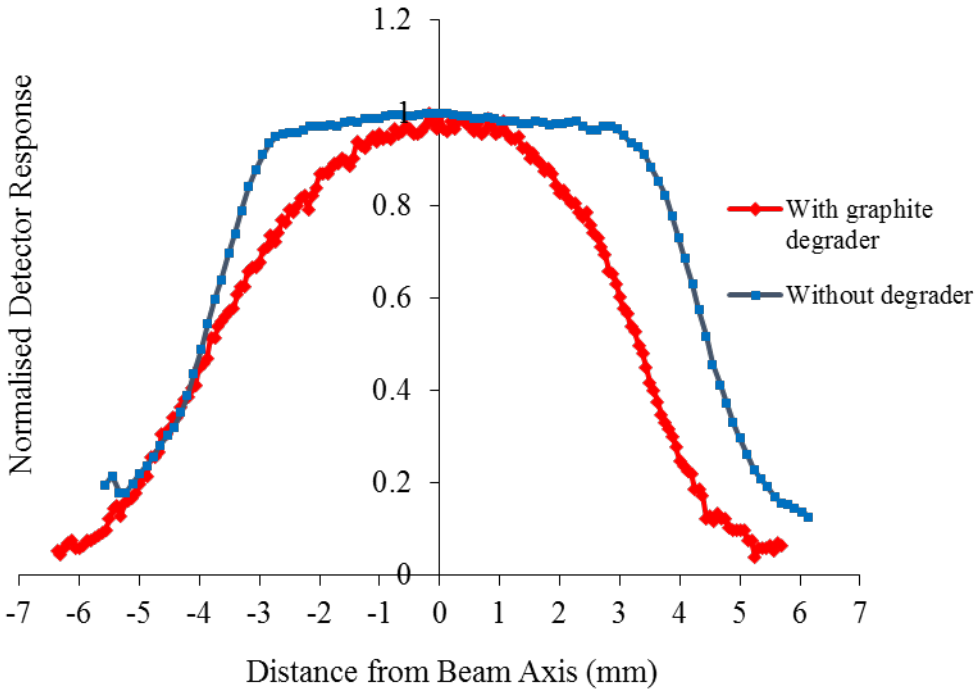

Figure 2.4 Normalised transaxial intensity profile of the proton beam at the target position, measured from exposed Gafchromic film.

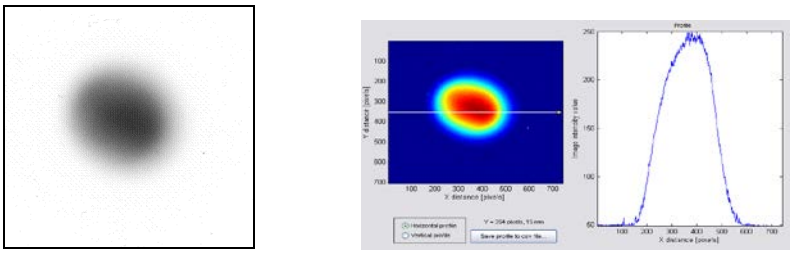

(a) (b)

Figure 2.5 The autoradiographic image on Radiochromic EBT film without degrader analysed with DoseLab (DoseLab software, 2009) shows (a) a beam “hot spot”, just off-centre. (b) This has implications for heat dissipation in the target material, in order to avoid burning or melting of target at high or sustained beam currents.

2.3 Results and Discussion

This study describes a simple, indirect method for determining the primary proton beam energy using the stacked-foils technique and the monitor reaction $^{65}Cu(p,n)^{65}Zn$, without a direct measurement of beam current. It relies on the uniqueness of the shape of the activity profile of the monitor isotope in a foil stack, at a specified energy. Calibration of the sensitivity of the γ-spectrograph was not required, though the measurement system needed to be able to recognise a characteristic photopeak. Measurement in the foils of the relative activities of only one monitor isotope is required. The monitor isotope, ^{65}Zn is recommended because of its long half-life, which allows measurements of activity to be made conveniently several days following irradiation. Fifty micron thick ^{nat}Cu foils were considered the most appropriate for the monitor foil, because they were sufficiently mechanically robust. Concurrent measurements were also made of ^{62}Zn and ^{63}Zn activities in the same foils. In additional foils of 25, 75 and 100 μm nominal thicknesses were also assessed in an effort to assess the sensitivity of analysis methods to foils' thickness.

The Table 2.1 and Figure 2.6 show the primary beam energy (corrected for energy loss in the obligatory Havar® foil vacuum window) derived from the activity profiles of all three monitor isotopes in the stacks of ^{nat}Cu foils of different thicknesses. The ^{65}Zn measured in 50 μm foils was considered to be the 'index' result. Measurements were performed before and after an upgrade of the non-magnetic components of the cyclotron beam control. Estimates of primary beam energy were similar for all three monitor isotopes, with a mean value over all isotopes and foil thicknesses of 18.06 ± 0.12(SD) MeV (CV = 0.7%; N = 36; 95%CI =18.02-18.10), and 18.05 ± 0.05(SD) for ^{65}Zn alone (CV = 0.3%; N = 12; 95%CI = 18.02-18.08; NS). The value for ^{65}Zn in 50 μm foils alone was 18.03 ± 0.02 MeV (CV = 0.1%; N = 3; 95%CI = 17.98-18.08; NS).

The upgrade of the cyclotron included replacement of ion sources and targetry, enhancement of RF power, revision of the station supporting the beam strippers and the addition of magnetic compensator coils for dual-beam operations. However, the basic magnetic field configuration was not changed during the upgrade, which suggests that the beam energy at exit should not change significantly. Indeed, measurement following the upgrade with ^{65}Zn using 50 µm foils revealed an energy of 18.11 ± 0.05 MeV (CV = 0.3%; N = 3; 95%CI = 18.00-18.23; NS compared with 'before') which was in close agreement with the other monitor isotopes (^{62}Zn and ^{63}Zn) and their combination. The two sets of measurements were separated and bracketed a significant (18 month) period. The data clearly demonstrate that alterations to beam management software and hardware (including to the beam-stripping apparatus) did not alter the energy of the extracted beam.

The monitor isotope ^{62}Zn is not useful if the beam energy is less than about 15 MeV since the reaction ^{63}Cu(p,2n)^{62}Zn has a threshold energy of 13.5 MeV. However, the concordance of ^{62}Zn data with other isotopes in the table show that the iterative method is sufficiently sensitive to the shape of the ^{62}Zn excitation curve that comparison with only a segment of its lower tail (approximately 14-18 MeV of the full range 14 to ~36 MeV) is required to produce an accurate estimate of the energy (IAEA, 2009). Examination of the ^{62}Zn curve over its full energy range suggests that the iterative method applied to the ^{62}Zn monitor reaction alone would be suitable for assessing proton beam energies over the continuous range 18 to ~33 MeV. This exceeds the ranges accessible to those methods reliant on ratios of cross sections. The ratio for ^{63}Zn at different energies addresses the range 11-18 MeV (using a suite of customised beam degraders) while the ratio of ^{62}Zn to ^{65}Zn at the same energy spans about 14-24 MeV (Gagnon et al., 2011; Kopecky, 1985). In the broader context beyond smaller cyclotrons, application of the iterative method of this study to the monitor reactions ^{nat}Ti(p,x)^{48}V (relevant for ~10-30 MeV) and ^{27}Al(p,x)^{22,24}Na (> 30 MeV) also seems feasible (IAEA, 2009).

This indirect method indicates excellent *precision* (CV = 0.1-0.5%) as shown in the table. Therefore, it is expected to be highly sensitive to *changes* in beam energy (e.g. insertion of a degrader). However, *accuracy* of the method is likely to be poorer because of inherent uncertainties (systematic or otherwise) in contributing variables. A predominant contribution to the inherent uncertainties are counting statistics (2%), foils thickness (1%), energy straggling (2.7%, based on SRIM calculations of average energy spread with target depth, Section 2.2.5), stopping power (6%) and published monitor-reaction cross section data (5%). Collectively these errors result in an overall uncertainty of approximately 8.6% in the absolute value of the beam energy. This level of uncertainty is not inconsistent with other indirect methods.

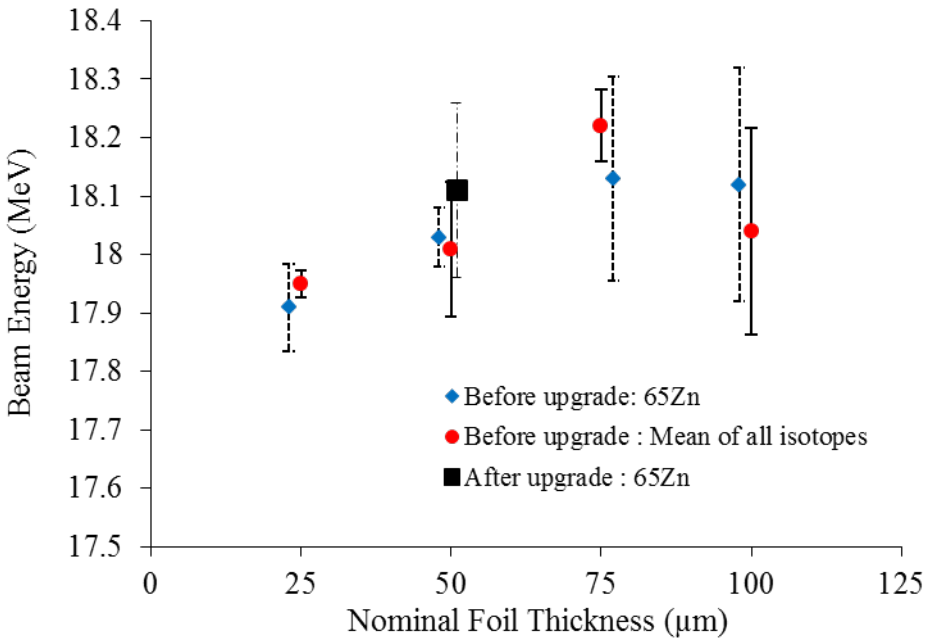

Figure 2.6 Measured proton primary beam energy vs. copper foils thickness, for monitor isotope ^{65}Zn alone (diamonds) and for combined monitor isotopes (circles). Copper foils of 50 µm thickness were used for the measurements following the cyclotron upgrade (square). Some data are slightly displaced along abscissa axis for clarity. Uncertainties are ± 95% CI.

Table 2.1 Primary beam energy determined from each of three Zn monitor isotopic activities in stacks of ^{nat}Cu foils of different nominal thicknesses. Measurement using the isotope ^{65}Zn and 50 µm foils (bold) is considered the most convenient. Comparisons between isotopes or between foil thicknesses are not significant.

Foil Thickness (µm)	^{62}Zn	^{63}Zn	^{65}Zn	All
Before Upgrade	MeV	MeV	MeV	MeV
100	17.77 ± 0.10	18.22 ± 0.09	18.12 ± 0.08	18.04 ± 0.23
75	18.28 ± 0.15	18.24 ± 0.07	18.13 ± 0.07	18.22 ± 0.08
50	17.86 ± 0.21	18.15 ± 0.05	**18.03 ± 0.02**	18.01 ± 0.15
25	17.96 ± 0.03	17.97 ± 0.10	17.91 ± 0.02	17.95 ± 0.03
*Mean	17.97 ±0.12	18.15 ± 0.08	18.05 ± 0.05	18.06 ± 0.12
After Upgrade				
50	18.12 ± 0.12	18.18 ± 0.11	18.11 ± 0.05	18.14 ± 0.09

*(Mean ± SD MeV, N = 3)

2.4 Conclusions

A novel method that exploits the energy-dependent uniqueness of the shape of a monitoring isotope cross section was developed for determination of the energy of a degraded beam. The primary beam energy of a nominally 18 MeV isochronous proton cyclotron was measured indirectly though precisely, using this method, which is a variation of the stacked foils technique. This method exploits the energy-dependent uniqueness of the shape of the profile of ^{65}Zn activity in the stack of natural copper foils comprising the irradiated 'thick' target. The monitor reaction ^{65}Cu(p,n)^{65}Zn was used. This method does not require a direct measurement of beam current or extensive calibration of the gamma spectrograph. The recommended technique uses activated 50 µm-thick copper foils to monitor ^{65}Zn. In this study, the co-produced ^{62,63}Zn was also

monitored and the effect of different thicknesses of copper foil was investigated. The data showed excellent internal agreement between the three monitor isotopes as well as a range of copper foils (25 to100 μm-thick)

This method has some advantages over other published methods (Kopecky et al., 1985; Gagnon et al., 2011) that utilise ratios of reaction cross sections. In particular, the new method has the capacity to measure energies across virtually the entire range of a chosen monitor reaction. It also lacks the need for customized degraders, without sacrificing the measurement precision attributable to these methods. The method may be applicable to proton energies above 18 MeV and indeed 30 MeV, using IAEA-recommended (p,x) monitor reactions with titanium or aluminum targets.

CHAPTER THREE

EXCITATION FUNCTIONS OF ^{NAT}ZN(P,X) NUCLEAR REACTIONS

A version of this chapter was published in:

Asad, A.H., Chan,S., Morandeau, L., Cryer, D., Smith, S.V. & Price, R.I. (2014). Excitation functions of ^{nat}Zn(p,x) nuclear reactions with proton beam energy below 18 MeV. *Applied Radiation and Isotopes, 94*, 67-71.

3.1 Introduction

The relatively short half-life of ^{61}Cu (3.33 h) makes it suitable for the radiolabelling of small molecules such as ATSM and PTSM, for hypoxia and blood flow measurements, respectively (Jalilian, Shanesazzadah, Rowshanfarzad, Bolourinovin, & Majdabadi, 2008; Jalilian et al., 2009). ^{61}Cu can be produced by cyclotron proton bombardment of natural zinc (^{nat}Zn) and enriched zinc (^{64}Zn) targets. Understanding variation in the cross sections and theoretical yields of the desired isotopes and of co-isotopes is essential for optimising the energy and current to produce the highest quality (specific activity and radionuclide purity) ^{61}Cu for pre-clinical and clinical use. It is also important for determining the most reliable, rapid and cost effective method for the production of ^{61}Cu.

There are a number of isotopes that are co-produced when bombarding ^{nat}Zn with protons. They include ^{66}Ga, ^{67}Ga, ^{68}Ga and ^{65}Zn. The nuclear and decay properties of these isotopes and potential nuclear reactions are given in Table 3.1.

There have been several reports of proton induced (up to 100 MeV) excitation functions for reactions on ^{nat}Zn target (Barrandon et al., 1975; Little & Lagunas-Solar, 1983; Nortier, Mills, & Steyn, 1991; Kopecky, 1990; Hermanne, 1997; Szelecsényi et al., 2005B; Al Saleh, Mungren, & Azzam, 2007; Uddin et al., 2007). Al Saleh et al. (2007) reported cross section data for all the Ga and Zn isotopes (e.g. ^{66}Ga, ^{67}Ga, ^{68}Ga, ^{62}Zn and ^{65}Zn) up to 27.5 MeV. Uddin et al. (2007) all reported data (at 40 MeV) for the same isotopes including ^{61}Cu. Less recently, Szelecsényi et al. (2005B) published the excitation functions of ^{61}Cu from ^{nat}Zn, ^{66}Zn, ^{68}Zn at energies up to 100 MeV. On the whole, there are not many ^{61}Cu data available to compare in the reported literature to date. Therefore, this chapter aims to determine the excitation function in the region relevant to the energy range of the IBA Cyclone at Sir Charles Gairdner Hospital (Perth, Australia) and to determine which set of reported data is more reliable.

In this study we measured ^{nat}Zn(p,x) excitation functions of ^{61}Cu, ^{66}Ga, ^{67}Ga and ^{65}Zn for energies ranging from the effective threshold of the particular reaction up to 17.6 MeV, using the stacked-foils activation technique. Three independent experiments were conducted and the data averaged.

Table 3.1 Nuclear and decay properties of isotopes produced from ^{nat}Zn (p,x) reactions below 17.6 MeV.

Radionuclide	Half-life[a]	*Decay mode[a]	*E_γ (keV)[a]	*I_γ (%)[a]	Reactions[b]	E_{th} (MeV)[b]
^{61}Cu	3.33 h	EC (38.5%); β+ (61.5%)	282.956 656.008	12.20 10.77	^{64}Zn(p,α)	6
^{64}Cu[c]	12.70 h	EC (43.1%); β+ (17.4%)	1345.77	0.776	^{68}Zn(p,αn) ^{67}Zn(p,α)	8.5 9.5
^{67}Cu[c]	61.83 h	β- (99.0%)	91.26 93.31 184.57	7.0 16.1 48.7	^{70}Zn(p,2p)	7.7
^{65}Zn	244.26 d	EC (98.6%); β+ (1.4%)	1115.5	50.60	^{66}Zn(p,d) ^{66}Zn(p,n+p) ^{67}Zn(p,t)	8.9 11.2 9.7
^{66}Ga	9.49 h	EC (45.3%); β+ (56%)	833.537 1039.231	5.88 36.90	^{66}Zn(p,n) ^{67}Zn(p,2n)	6 13.6
^{67}Ga	3.26 d	EC (99.8%)	184.6 300.2	21.2 16.8	^{67}Zn(p,n) ^{68}Zn(p,2n)	1.8 10.3
^{68}Ga[c]	67.63 min	EC (38%); β+ (62%)	1077	3	^{68}Zn(p,n)	3.75

Eγ energies of γ- ray emissions.; **Iγ**, probability of γ-ray emission per nuclear disintegration; **E_{th}**, threshold energy of reaction ; **a**, data from Table of Nuclides; http://atom.kaeri.re.kr/ (Table of Nuclides); **b**, data from Experimental Nuclear Reaction Database (EXFOR).

3.2 Experimental Methods

Excitation functions for the $^{nat}Zn(p,x)$ reactions were measured by the stacked-foils activation technique (Qaim, Stocklin, & Weinreich, 1997). High-purity natural zinc foils (99.99+% elemental purity), of natural composition (see Table 3.2) with thickness of 0.025 ± 0.004 (SD) mm were purchased from Goodfellow Metals Ltd, UK. Copper monitor foils of 15 mm diameter were employed to measure beam flux and energy in the stack using the characteristics of the well-documented $^{63}Cu(p,n)^{63}Zn$ and $^{65}Cu(p,n)^{65}Zn$ reactions (IAEA, 2009). These foils had a thickness of 0.025 ± 0.004 (SD) mm (99.99+% elemental purity; Goodfellow Metals Ltd, UK).

Table 3.2 Isotopic composition of natural zinc

Isotope	^{64}Zn	^{66}Zn	^{67}Zn	^{68}Zn	^{70}Zn
Present Abundance	48.6%	27.9%	4.1%	18.8%	0.6%

The foil stacks consisted of appropriate combinations of the Cu and Zn foils, with one monitor Cu foil at the target front face, plus single Cu foils interleaved with the Zn foils. The energy degradation within each foil including the Havar® foil was calculated by SRIM 2011 software (Ziegler et al., 2011).

A typical stack consisted of four units of four Zn foils sandwiched between single Cu monitor foils (Cu-4×Zn-Cu), with the last (fifth) stack consisting of (Cu-8×Zn-Cu) so that the exit energy of the beam from the final stack was well below the threshold energy of the studied reaction. For each experiment, a stack was inserted into an external solid targetry beam line, where the target was cooled in front by helium gas flow and from behind by a cooled water jet (described previously in Section 1.3.1 of Chapter 1). A schematic of the solid

targety setup is given in Figure 3.1. The proton source employed was an IBA 18/18 MeV isochronous cyclotron (IBA, Louvain le Neuve, Belgium).

Foil stacks were irradiated with a primary beam of energy 17.6 MeV, accounting for beam degradation by an obligatory 0.025 ± 0.0005 (SD) mm-thick Havar® foil vacuum window. Irradiation was for 3 min using a target beam current of 5 µA.

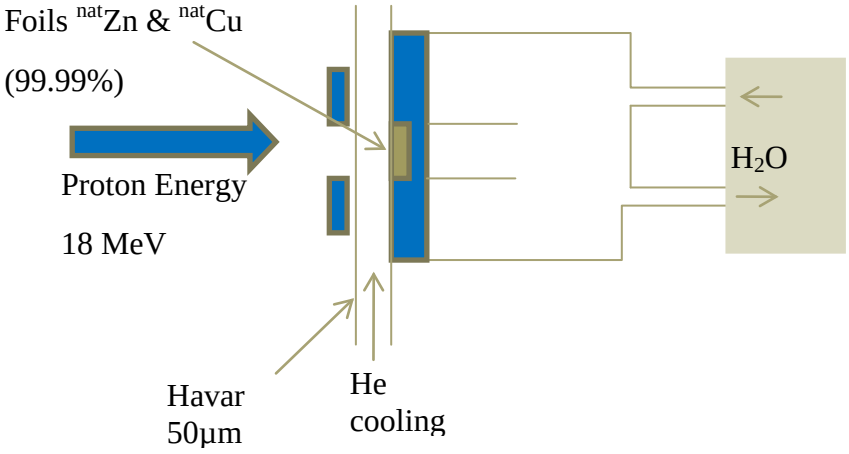

Figure 3.1 Scheme of solid targetry apparatus.

Activities of the irradiated foils were measured at 3 h post end of bombardment (EOB) by cryo HPGe gamma spectroscopy (Canberra, Meriden, USA; S5000 MCA & GC1018 Ge detector). The distance between the specimen and the end cup of the HPGe detector was set at 50 cm, in order to reduce the dead time of each measurement to less than 5%.

The gamma spectrometer was independently calibrated with certified standard sources of ^{60}Co, ^{57}Co, ^{137}Cs, ^{65}Zn, ^{109}Cd and ^{133}Ba (Canberra Industries, Oak Ridge, TN, USA), with an uncertainty in the intrinsic efficiency curve of 5%.

Beam flux for each measurement, was determined using the Cu foils (i.e. ^{63}Cu(p,n)^{63}Zn and ^{65}Cu(p,n)^{65}Zn reactions) as described in Chapter 2. The

experimental cross sections of ^{61}Cu, ^{66}Ga, ^{67}Ga and ^{65}Zn were calculated using the equation:

$$\sigma = \frac{[A_{EOB}]}{\eta\phi(1-e^{-\lambda t})} \qquad (1)$$

where: [A_{EOB}] = activity of the respective radionuclide at EOB [Bq]

η = number of target nuclei per cm

σ = cross section in cm^2

Φ = incident proton flux (particles $s^{-1}.cm^{-2}$)

λ = decay constant for the nuclide ($s^{-1)}$

t = bombardment time (s)

The uncertainty in the derived reaction cross section data is a function of the independent uncertainties encountered in the act of the measurement. This includes beam current (10-12%), detector efficiency (5%), counting statistics (4-8%), foil thickness (4-7%) and time of irradiation (1-2%). Thus, the total uncertainty in these experimental data ranged from 13 to 16%. The uncertainty in the proton energy in each Cu foil was derived from analysis of the ^{63}Zn and ^{65}Zn present. Three independent experiments were performed and the uncertainty in the final energy for each cross section was determined from the spread in the calculated energy values.

3.3 Results and Discussion

The cross section of each radionuclide produced from the ^{nat}Zn(p,x) reactions as a function of proton energy was calculated from equation (1) and are given in Table 3.3. Comparisons between the results of this study and the published literature are presented in Figures 3.2 to 3.5.

Table 3.3 Measured reaction cross sections for the production of ^{61}Cu, ^{66}Ga, ^{67}Ga and ^{65}Zn radionuclides from ^{nat}Zn target.

	Reaction Cross Section (mb)			
Proton Energy (MeV)	^{nat}Zn(p,α)^{61}Cu	^{nat}Zn(p,x)^{66}Ga	^{nat}Zn(p,x)^{67}Ga	^{nat}Zn(p,x)^{65}Zn
17.45 ± 0.25	21.80 ± 3.03	61.84 ± 8.59	101.82 ± 14.14	118.17 ± 12.85
17.1 ± 0.25	23.36 ± 3.35	67.99 ± 10.86	94.49 ± 15.12	113.26 ± 12.83
16.75 ± 0.25	26.67 ± 3.73	72.22 ± 11.09	95.42 ± 15.27	102.55 ± 10.71
16.4 ± 0.25	27.20 ± 3.75	80.06 ± 11.62	90.91 ± 11.82	99.24 ± 10.69
15.63 ± 0.25	30.64 ± 4.66	98.06 ± 14.10	83.31 ± 12.68	69.58 ± 7.62
15.26 ± 0.25	29.43 ± 3.96	106.46 ± 14.33	72.46 ± 11.41	55.87 ± 5.69
14.89 ± 0.25	30.77 ± 4.14	114.12 ± 15.37	75.53 ± 9.82	42.42 ± 4.32
14.52 ± 0.30	31.47 ± 4.35	123.80±17.60	62.89 ± 8.81	32.47 ± 3.36
13.68 ± 0.30	31.23 ± 4.31	142.11 ± 20.07	41.34 ± 5.79	11.04 ± 1.17
13.28 ± 0.30	32.47 ± 4.88	146.75 ± 21.30	33.19 ± 5.38	
12.87 ± 0.35	33.80 ± 4.62	148.61 ± 22.85	25.58 ± 3.50	
11.94 ± 0.35	32.69 ± 4.62	149.88 ± 21.19	20.66 ± 2.69	
11.48 ± 0.35	30.18 ± 3.91	145.64 ± 20.25	19.16 ± 2.99	
11.01± 0.35	28.03 ± 3.91	142.60 ± 19.88	19.51 ± 2.54	
10.53 ± 0.35	24.69 ± 3.65	136.18 ± 20.15	20.37 ± 2.77	
9.18 ± 0.40	22.54 ± 3.07	132.28 ± 18.01	22.22 ± 3.11	
8.36 ± 0.45	18.54 ± 2.52	113.97 ± 15.47	18.44 ± 2.58	
7.77 ± 0.50	14.25 ± 2.16	99.99 ± 15.15	19.13 ± 2.87	
7.13 ± 0.50	10.67 ± 1.43	86.86 ± 11.64	16.29 ± 2.12	
6.46 ± 0.55	6.66 ± 0.89	64.77 ± 8.69	15.46 ± 2.07	
5.73 ± 0.60	3.61 ± 0.50	36.30 ± 5.05	12.87 ± 2.06	
4.92 ± 0.70		9.43 ± 1.37	10.66 ± 1.49	
4.00 ± 0.75		0.85 ± 0.12	7.51 ± 1.14	
3.21 ± 0.85			2.81 ± 1.52	

Uncertainties are ± 2SD. Each data point is derived from the mean of three experiments.

3.3.1 $^{nat}Zn(p,\alpha)^{61}Cu$ Reaction

The excitation function of ^{61}Cu produced from the $^{64}Zn(p,\alpha)^{61}Cu$ reaction was measured in the proton energy range from 17.45 ± 0.25 MeV down to 5.73 ± 0.60 MeV. The results were compared with previously published data (Barrandon et al., 1975; Szelecsényi et al., 2005; Uddin et al., 2007) and are plotted in Figure 3.2. The cross section values determined for energy range 14-14.5 MeV (peak maximum) in the current study are slightly lower than those of Uddin et al. (2007) (39 ± 5.0 MeV) and Szelecsényi et al. (2005) (42.15 ± 4.65 MeV). The data reported by Barrandon et al. (1975) are significantly different from the present study as well as those of Uddin et al. (2007) and Szelecsényi et al. (2005). The data obtained in the present study are more likely to be accurate, and with more data points than those presented in the other literature.

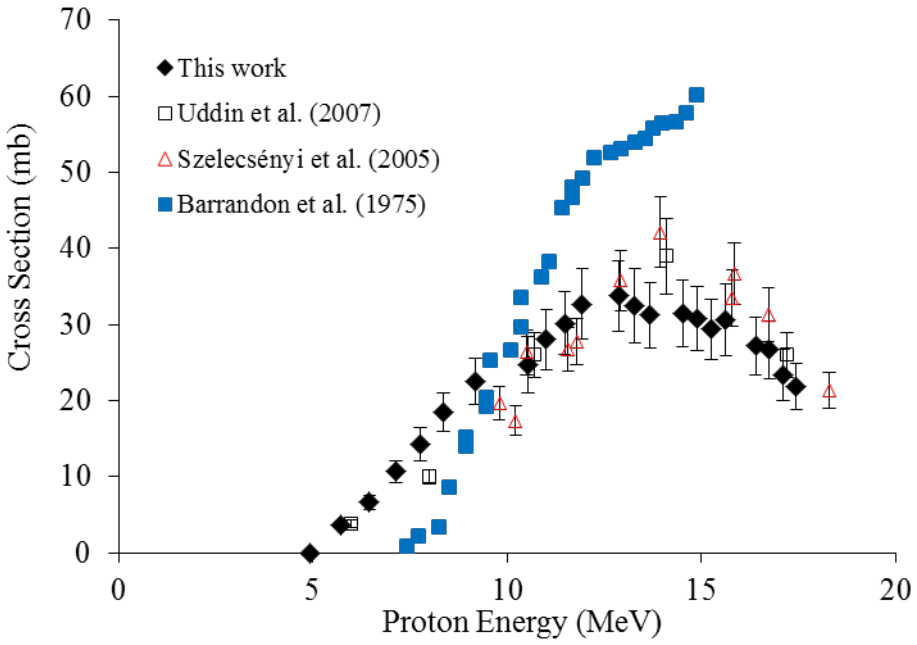

Figure 3.2 Measured excitation function of the $^{nat}Zn(p,\alpha)^{61}Cu$ reaction, in comparison with published data. Uncertainties are ± 2SD.

3.3.2 $^{nat}Zn(p,x)^{66}Ga$ Reactions

The cross section data for the production of ^{66}Ga acquired in this study are shown in Figure 3.3, together with the other published data. The data in this study are in general agreement with data from Hermanne (1997), Al Saleh et al. (2007), Uddin et al. (2007) and Szelecsényi et al. (2005B) for energies greater than 12 MeV. For energies less than 9 MeV the data are in good agreement with Szelecsényi et al. (2005B). However, for all other reported literature the data in this present study are consistently higher.

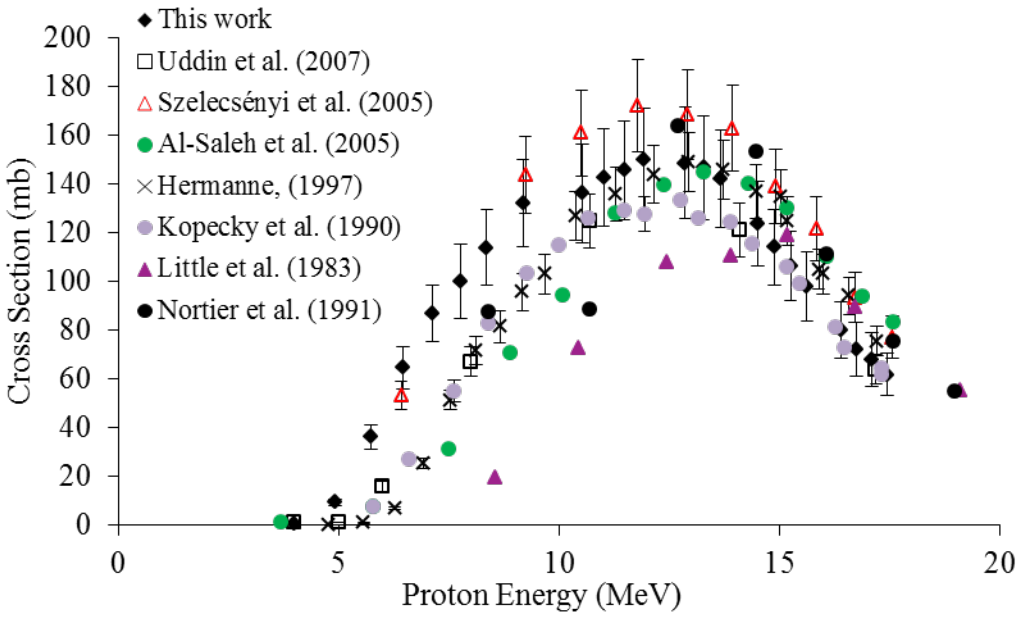

Figure 3.3 Measured summed excitation functions of the $^{nat}Zn(p,x)^{66}Ga$ reactions, in comparison with published data.

3.3.3 $^{nat}Zn(p,x)^{67}Ga$ Reactions

Gallium-67 is produced from ^{nat}Zn target below 18 MeV via two separate reactions: $^{67}Zn(p,n)$ and $^{68}Zn(p,2n)$ (Table 3.1). Figure 3.4 shows the data from the current study are in generally good agreement between the summed excitation functions for these two reactions as presented in this work as well as previous studies (Kopecky, 1990; Hermanne, 1997; Al Saleh et al., 2007; Uddin et al., 2007). The exceptions are Szelecsényi et al. (2005B) (at higher energies), Little and Lagunas-Solar (1983) and Barrandon et al. (1975).

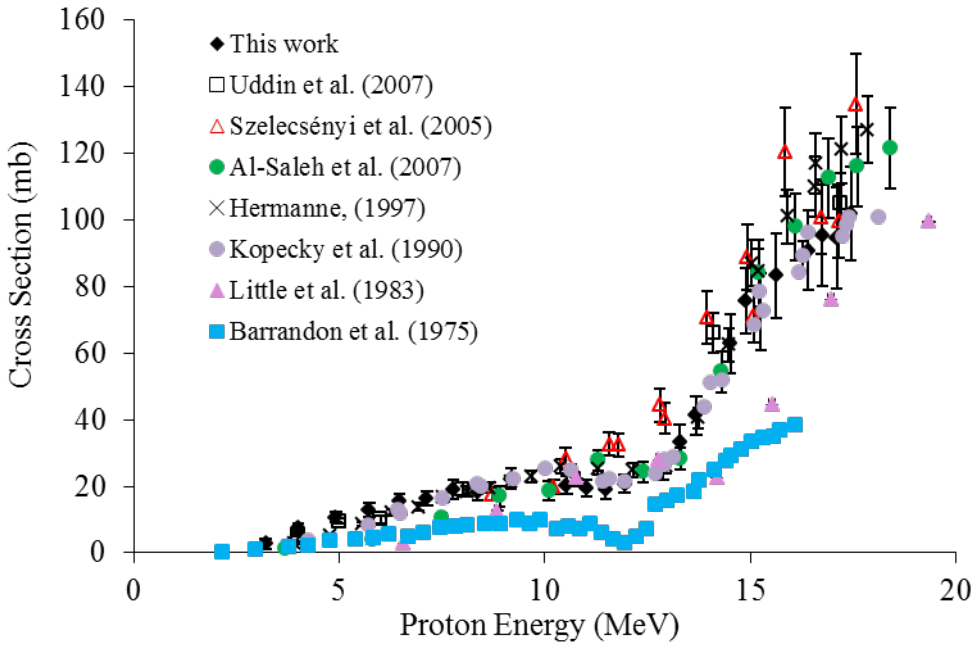

Figure 3.4 Measured summed excitation functions of the $^{nat}Zn(p,x)^{67}Ga$ reactions, in comparison with published data.

3.3.4 $^{nat}Zn(p,x)^{65}Zn$ Reactions

The isotope ^{65}Zn is one of the monitoring isotopes used to determine beam flux or beam energy using the stacked-foils method. The ^{65}Zn nuclide ($t_{1/2}$ = 244.26 d; $\beta^{+,}$ 1.4%; EC, 98.6%) can be produced from three different nuclear reactions when using a ^{nat}Zn target, as shown in Table 3.1. ^{65}Zn can be used as a standard source for calibration of gamma-spectroscopy. It is also suitable for thin layer activation (TLA) studies (Uddin et al., 2007).

Accumulated cross section data for the production of ^{65}Zn is given in Figure 3.5. Included in the same figure are data from Al Saleh et al., 2007 and Uddin et al., 2007. The current data are in good agreement with the literature data. However, the energy threshold determined in the present study was significantly higher (i.e. 13.7 MeV) as compared to the reported thresholds 11.3 MeV (Al Saleh et al., 2007) and 10.7 MeV (Uddin et al., 2007). This variation may be explained by the higher current used in this work.

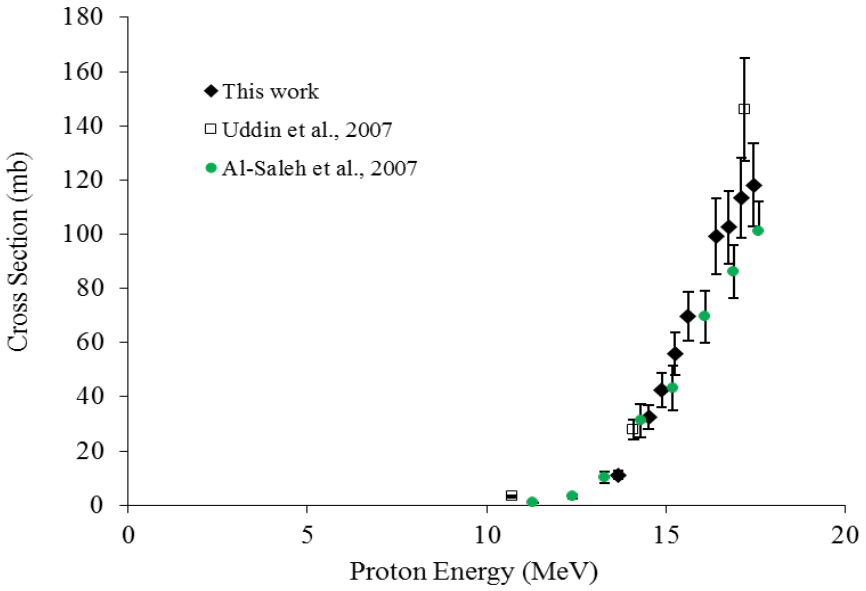

Figure 3.5 Measured summed excitation functions of the $^{nat}Zn(p,x)^{65}Zn$ reactions, in comparison with published data.

3.3.5 Other Reactions

Copper-64 can be produced from ^{68}Zn (18.8% natural abundance) via the ^{68}Zn(p,αn)^{64}Cu (Hilgers et al., 2003; Levkovskij, 1991) reaction. The cross sections reported in the literature are quite low: the reported maxima are 12 mb at 17.6 MeV (Hilgers et al., 2003) and 19 mb at 17.5 MeV (Levkovskij, 1991), respectively. Therefore, a thick target using 5 μA for 3 min produces only 1.2 kBq, which is too low for analysis in the current study, consequently this nuclide was not expected to be observed. Despite an extensive search of the published literature, there are no published data for ^{64}Cu production via this reaction in the relevant energy range.

Copper-67 is produced from ^{70}Zn (0.6% in natural Zn) via the ^{70}Zn(p,α)^{67}Cu reaction (Kastleiner, Coenen, & Qaim, 1999). The theoretical thick-target activity calculated from data of that study, assuming a beam current of 5 μA and 3 min irradiation, was only approximately 4.6 kBq. Thus, investigation of the reaction ^{70}Zn(p,α)^{67}Cu is restricted in the current study due to poor counting statistics. This conclusion is also supported by the previous data (Levkovskij, 1991).

Gallium-68 can be produced from ^{68}Zn (18.8% in natural Zn) via the ^{68}Zn(p,n)^{68}Ga reaction using a ^{nat}Zn target (Nortier et al., 1991; Al Saleh et al., 2007) and by other groups using an enriched target (Szelecsényi, Boothe, Tarács, Tárkányi, & Tavano, 1998; Tárkányi, Szelecsènyi, Kovàcs, & Sudar, 1990). Indeed, this reaction with an enriched target has been recommended as the chosen path for ^{68}Ga production when employing a biomedical cyclotron (Sadeghi, Aboudzadeh, Zali, & Zeinali, 2009; Asad et al., 2012). The cross section, when corrected for the natural abundance of ^{68}Zn, has a maximum of 160 mb at 12 MeV. The low current, timing of gamma analysis measurements and the relatively short half-life of ^{68}Ga precluded its quantitative assessment in this study.

3.3.6 Integral Thick-Target Yield

Cross sections were used to determine integral yields for each of the isotopes produced in this study. The activities per μA per hour as a function of beam energy were calculated by integrating the cross section over the energy range of the present data using equation (2).

$$A = Nv.I.(1 - e^{-\lambda t}).\int_{Eth}^{Ep} \sigma(E).[\frac{dE}{dX}.(E)]^{-1}.dE \qquad (2)$$

In equation (2) N_v is the number of target nuclei for the desired reaction per unit area (related to target thickness), I is the incident particle flux (related to beam intensity), λ is the radioactive constant of the produced isotope, t is the duration of the irradiation, E_p is the beam energy, E_{th} is the reaction threshold energy, $\sigma(E)$ is the excitation function and dE/dX is the stopping power of the target material.

The integral thick-target yields for the production of ^{61}Cu, ^{66}Ga, ^{67}Ga and ^{65}Zn produced from a ^{nat}Zn target with primary beam energy 17.6 MeV as a function of proton energy were calculated using the excitation functions measured. Results are given in Figure 3.6. The results (up to 17.6 MeV) were in good agreement with Uddin et al. (2007) but were in less agreement with Szelecsényi et al. (2005B), as shown in Figure 3.7.

The results demonstrate that if the ^{nat}Zn target were replaced by a highly enriched ^{64}Zn target, then the yield of ^{61}Cu produced could be doubled. For example, a simple calculation shows that an enriched ^{64}Zn target of thickness 100 mm can be used to produce 0.85 GBq of ^{61}Cu at EOB with a 40 μA beam at normal incidence and 1 h irradiation using17.6 MeV protons. Furthermore, the production of ^{66}Ga, ^{67}Ga, ^{68}Ga and ^{65}Zn contaminants would be significantly lower at EOB.

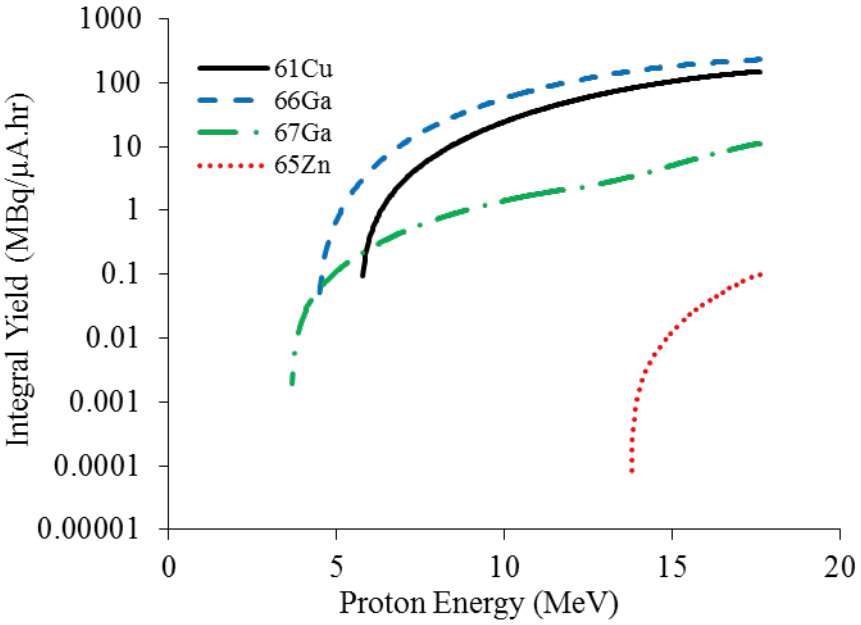

Figure 3.6 Calculated thick-target integral yields per μA beam current per hour irradiation, as a function of beam energy, for the isotopes produced in a natural Zn target from the measured excitation functions determined in the current study.

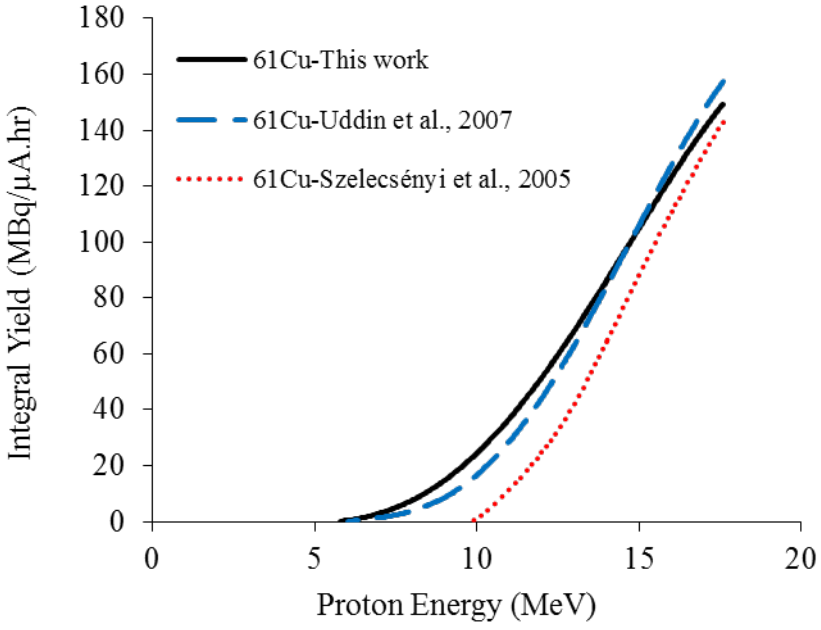

Figure 3.7 Calculated thick-target integral yield for ^{61}Cu in a natural Zn target per μA beam current per hour irradiation, as a function of beam energy, from this study and in comparison with published data.

3.4 Conclusions

Cross section data for ^{nat}Zn(p,x) reactions yielding ^{61}Cu, ^{66}Ga, ^{67}Ga and ^{65}Zn isotopes have been measured using proton irradiation of a high-purity natural zinc target, employing the stacked-foils activation technique, at proton energies up to 17.6 MeV produced by a conventional isochronous PET production cyclotron. The results are generally in good agreement with recent published data, except for ^{66}Ga. The results of this study for ^{66}Ga are in agreement with one published data set, but are higher than other publications for energies below 10 MeV. This suggests that further investigation of the cross section for the ^{nat}Zn(p,x) production of ^{66}Ga may be necessary, particularly for lower energies. All of the produced isotopes could potentially be used in clinical or preclinical studies, following chemical separations of the zinc, gallium and copper elements (Asad et al., 2012). In the case of ^{61}Cu, higher activities for clinical applications could be achieved (and co-produced radionuclidic impurities minimised) by using an isotopically enriched ^{64}Zn target.

CHAPTER 4

PRODUCTION AND SEPARATION OF ^{61}CU PRODUCED FROM ^{NAT}ZN AND ENRICHED ^{64}ZN TARGETS – SPECIFIC ACTIVITY DETERMINATION

A version of this chapter was published in:

Asad, A.H., Smith, S.V., Morandeau, L.M., Chan, S., Jeffery, C.M. & Price, R.I. (2015). Production of ^{61}Cu by the ^{nat}Zn(p,α) Reaction: Improved Separation and Specific Activity Determination by Titration with Three Chelators. *Journal of Radioanalytic and Nuclear Chemistry, 307,* 899-906.

4.1 Introduction

Copper has four widely used radioisotopes for positron emission tomography (PET) imaging, ^{60}Cu ($t_{1/2}$ = 20.7 min), ^{61}Cu ($t_{1/2}$ = 3.33 h), ^{62}Cu ($t_{1/2}$ = 9.8 min) and ^{64}Cu ($t_{1/2}$ = 12.7 h) (Smith, 2004). ^{64}Cu also has a therapeutic β^- emission that can be used for radiotherapy. Diacetyl-bis(N^4-methylthiosemicarbazone) (ATSM) and pyruvaldehyde-bis (N^4-methylthiosemicarbazone) (PTSM) have been radiolabelled with each of these radionuclides for imaging hypoxia (Laforest, Dehdashti, Lewis & Schwarz, 2005) and blood perfusion (Wong et al., 2008) respectively. While the majority of published works have used the long-lived ^{64}Cu; the shorter half-life of ^{61}Cu, with its high abundant positron emission (β^+ = 1.22 MeV, 61.5%; EC = 38.5%) and the absence of β^- emission make it a potentially more attractive option for imaging hypoxia (Thieme et al., 2013).

Several methods have been reported for the cyclotron production of ^{61}Cu using Ni and Zn targets (McCarthy et al., 1999; Szelecsényi et al., 1993; Piel et al., 1992; Tanaka et al., 1972; Szelecsényi et al., 2005; Asad et al., 2014; Al Saleh et al., 2007; Uddin et al., 2007; Cohen et al., 1954). Both ^{61}Ni and ^{62}Ni targets can

be used to produce ^{61}Cu via the (p,n) and (p,2n) nuclear reactions respectively (McCarthy et al., 1999; Szelecsényi et al., 1993; Piel et al., 1992; Tanaka et al., 1972). The production of ^{61}Cu via these routes is very high yielding (σ > 300 mb) and the optimum proton energies for these nuclear reactions [10.3 MeV for ^{61}Ni (Szelecsényi et al., 1993) and 14 MeV for ^{62}Ni (Piel et al., 1992)] are ideal for commercially available low energy cyclotrons. However, the high cost of the ^{61}Ni ($37 per mg) and ^{62}Ni ($14.70 per mg) can be prohibitive when one considers the total inventory required (which includes chemical loss on recycling and recovery) to maintain routine production of ^{61}Cu.

Proton reactions on zinc targets have been studied as an alternative approach to Ni targets for the production of ^{61}Cu (Szelecsényi et al., 2005; Asad et al., 2014; Al Saleh et al., 2007; Uddin et al., 2007; Cohen et al., 1954) via the (p,α) reaction. For example, natural Zn (^{nat}Zn, with ^{64}Zn natural abundance 48.6%) and enriched ^{64}Zn (99%) using the ^{64}Zn(p,α)^{61}Cu reaction have reasonable cross sections (39 and 79 mb at 15 MeV, respectively) (Cohen et al. 1954; Rowshafarzad et al., 2006). The Zn target materials are considerably cheaper (e.g. ^{64}Zn $5 per mg) than the Ni targets. Enriched ^{64}Zn targets also present the added advantage of being available commercially as foils. Use of the latter avoids the need to establish an in-house electroplating and recycle process as well as requalifying procedures for human use, as the ^{64}Zn target is considered a consumable.

However, the proton bombardment of the natural zinc target presents some challenges, such as the co-production of Ga radionuclides [^{66}Ga ($t_{1/2}$ = 9.49 h), ^{67}Ga ($t_{1/2}$ = 3.26 d) and ^{68}Ga ($t_{1/2}$ = 68 min)] and of the longer-lived ^{65}Zn nuclide ($t_{1/2}$ = 244 d) (Asad et al., 2014; Al Saleh et al., 2007; Uddin et al., 2007). Figure 4.1 illustrates the cross sections of ^{nat}Zn(p,x) reactions for incident proton energies < 18 MeV, showing that the production of ^{61}Cu can be optimised to avoid collateral ^{65}Zn contamination by using proton energies < 13.7 MeV.

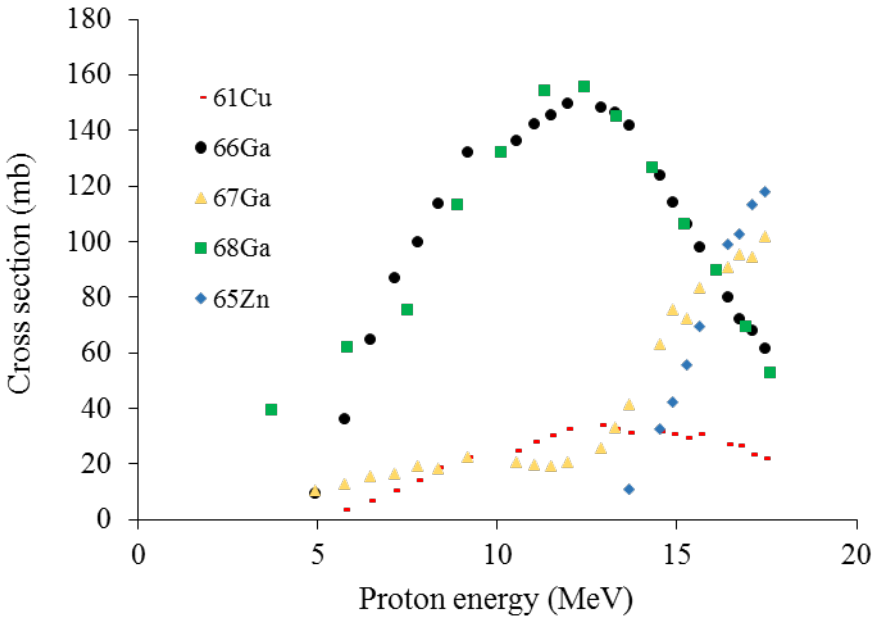

Figure 4.1 Excitation functions of ^{nat}Zn(p,α) reactions up to 18 MeV for the production of ^{61}Cu, ^{66}Ga, ^{67}Ga, ^{65}Zn (adapted from Asad et al., 2014) and ^{68}Ga (adapted from Al-Saleh el al., 2007).

Several separation methods have been reported in the literature for isolating Cu and Ga from the Zn target materials by cation and anion exchange chromatography (Rowshafarzad et al., 2006; Dasqupta et al., 1991; Schwarzbach et al., 1995). For example, Rowshanfarzad et al. (2006) irradiated a ^{nat}Zn target using 22 MeV proton beam energy at 180 µA.h. They isolated the ^{61}Cu with a combination of cation and anion exchange columns, using large volumes of concentrated HCl to separate the Cu from the Ga and Zn by-products. Unfortunately, the specific activity of the isolated products was not reported.

Determination of the effective specific activity (ESA) of radiometals is important as metallic contaminants can have an impact on the radiolabelling efficiency. ICP-MS is one of several methods for determining the specific activity for the quality control of radiometals production. However, cyclotron facilities cannot always afford its regular use. The other common method to determine effective specific activity of Cu isotopes is the titration method using chelators such as 1,4,8,11-tetraazaclotetradecane-1,4,8,11-tetraacetic acid (TETA). This method

consists in incubating the isolated radiocopper isotope in buffered solution in the presence of increasing known concentrations of the chelator. After a suitable time, the solutions are analysed by Instant Thin Layer Chromatography (ITLC) allowing the separation of free Cu from bound Cu; the percentage of [Cu-TETA]$^{2-}$ bound is calculated (McCarthy et al., 1997; Matarrese et al., 2010; Avila-Rodriguez et al., 2007). The estimated concentration of TETA at 50% labelling is multiplied by 2 to give the TETA concentration required for 100% complexation of Cu and thus the corresponding Cu concentration. The specific activity is then calculated in GBq/µL or GBq/µg of Cu after correcting the total activity and molecular weight of TETA.

Thieme et al. (2012) also reported the use of TETA for determining the ESA of ^{64}Cu and compared the results with the non-carrier-added specific activity (NCA-SA) determined from ICP-MS data. They found that for ^{64}Cu, the ESA values increased by 30% when incubating the mixtures at 80 °C vs. room temperature. In all cases, the ESA values were 1-5 fold lower compared to NCA-SA determined from ICP-MS, and were dependant on the metallic backing materials used for targetry. For ^{61}Cu, the same authors also reported similar ratios between the titration method using TETA and ICP-MS when comparing ESA and NCA-SA, respectively (Thieme et al., 2013). Recently, Mastren et al. (2014) compared the use of ICP-MS and ion chromatography HPLC analysis for determining the specific activity of ^{64}Cu, with the titration method using TETA at 80 °C. The ESA values obtained with the titration method were 1.5-5.0 fold lower than the ones obtained with ICP-MS.

The proposed reason for these consistently lower specific activities obtained by the titration method vs the ICP-MS is due to lower selectivity of the titration method. ICP-MS is by its nature a highly selective method, where other metal ions give distinctly different MS responses to Cu ions. However, while the polyazacarboxylate chelators show good complexation with Cu, they are not necessarily selective for Cu and will form complexes with other alkali, alkaline earth and transition-metal contaminating ions present in solution. For this reason,

these chelators would complex other metal ions present in solution, contributing to an artificially high percentage activity of $[Cu\text{-}TETA]^{2-}$, thereby giving lower resultant specific activities than the ICP-MS method. More recently, a wide range of commercially available polyaza, polycarboxylate and hexa-aza cages have been reported to preferentially form complexes with Cu^{2+} (Smith, 2004, Jarrett, Gustafsoon, Kukis, & Louie, 2008; Craft et al., 2012; Jeffery et al., 2012). It is of interest to assess some of these chelators for determining the specific activity of no-carrier-added (NCA) ^{61}Cu by the titration method.

In this chapter, investigation of the production of ^{61}Cu from ^{nat}Zn and ^{64}Zn target is described. The development of a novel separation method for ^{61}Cu produced from both ^{nat}Zn and ^{64}Zn targets is then given. Ideally, the separation of ^{61}Cu should be faster, more cost-effective and less cumbersome compared to known methods. Finally, the NCA specific activity of the resultant ^{61}Cu as determined by ICP-MS will be compared to the ESA obtained as determined by the titration method using the following three chelators; DOTA-NCS, NOTA-NCS and diamsar. These were chosen for their known greater selectivity for Cu compared to TETA (Smith, 2004). Their chemical structures are shown in Figure 4.2.

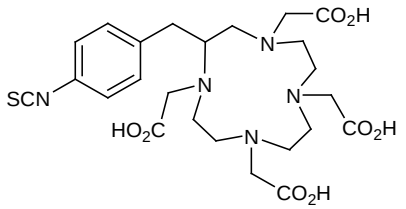

DOTA-NCS

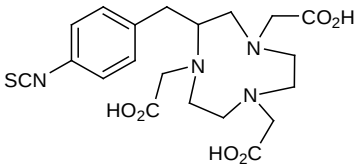

NOTA-NCS

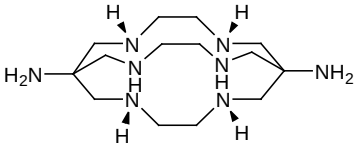

Diamsar

Figure 4.2 Chemical structures of the chelators; DOTA-NCS, NOTA-NCS and diamsar used to determine ESA.

4.2 Experimental

4.2.1 Materials

Enriched ^{64}Zn metal foils (^{64}Zn 99.30%, ^{66}Zn 0.45%, ^{67}Zn 0.06%, ^{68}Zn 0.17% and ^{70}Zn 0.02%) (0.05 mm thick) were purchased from Trace Sciences International Corp. (TX, USA). High-purity (99.99%) ^{nat}Zn foils (0.05 mm thick) with composition (^{64}Zn 48.6%, ^{66}Zn 27.7%, ^{67}Zn 4.1%, ^{68}Zn 18.8% and ^{70}Zn 0.6%) were purchased from Goodfellow Metals Ltd. (Cambridge, UK). Hydrochloric acid, sodium acetate and TraceSELECT water were purchased from Sigma Aldrich (NSW, Australia). Anion exchange resin AG1-X8 (200-400 mesh) and cation exchange resin AG50 W-X8 (200-400 mesh) were supplied by BioRad (NSW, Australia). Cu-Resin (100-150 mm) was purchased from Eichrom Technologies (IL, USA). Instant thin-layer chromatography (ITLC-SA) paper (Pacific Laboratory Products; VIC, Australia) was used to separate free $^{61}Cu^{2+}$ from complexed $^{61}Cu^{2+}$. S-2-(4-isothiocyanatobenzyl)-1,4,7-triazacyclononane-1,4, 7-triacetic acid (NOTA-NCS; >94%) and 2-(4-isothiocyanatobenzyl)- 1,4,7,10-tetraazacyclododecane-1,4,7,10- tetraacetic acid (DOTA-NCS; >94%) were purchased from Macrocyclics, (TX, USA). The third chelator, 3,6,10,13,16,19-hexaazabicyclo[6.6.6]eicosane-1,8-diamine pentahydrate (diamsar; >87%) was purchased from Clarity Pharmaceuticals (NSW, Australia) (Figure 2).

4.2.2 Instrumentation

The radionuclidic purity of the final product was determined by γ-spectroscopy using a high-purity germanium detector (HPGe; Canberra model GC2018) coupled to a calibrated Canberra Inspector 2000 multichannel analyser (Canberra Industries; TN, USA) and the data were processed using Genie-2000 software (Canberra). The Automatic Wizard 2 Gamma Counter (Perkin Elmer; MA, USA) was used for counting TLC strips cut into several pieces to determine the % of complexed ^{61}Cu.

4.2.3 Production of ^{61}Cu from ^{nat}Zn and Enriched ^{64}Zn Targets

4.2.3.1 Irradiation of Zinc Foils

To minimise unwanted co-products from the zinc targets, as well as investigate the differences between ^{nat}Zn and ^{64}Zn targets, a series of eight irradiations were performed. Four targets each of ^{nat}Zn and enriched ^{64}Zn foils were irradiated at 20-40 µA for 30 min. The foils were positioned in a removable custom-made aluminium disc holder with a lid (25 mm diameter and thickness 0.50 mm) (Figure 4.3). The front and back of the target holder were cooled with He gas and chilled water, respectively (Asad et al., 2014). A graphite degrader (1020 µm thick) was used to reduce the proton energy from 17.6 to 11.70 MeV (Asad et al., 2014). All irradiations were performed using an IBA 18/18 MeV cyclotron (IBA, Louvain la Neuve, Belgium). The production activity and impurities were measured by γ-spectroscopy. The final activity of ^{61}Cu was calculated as a weighted average of its two gamma-lines at 282 keV (12.20% abundance) and 656 keV (10.77%). The irradiation yield of ^{61}Cu was calculated as the mean of four irradiations.

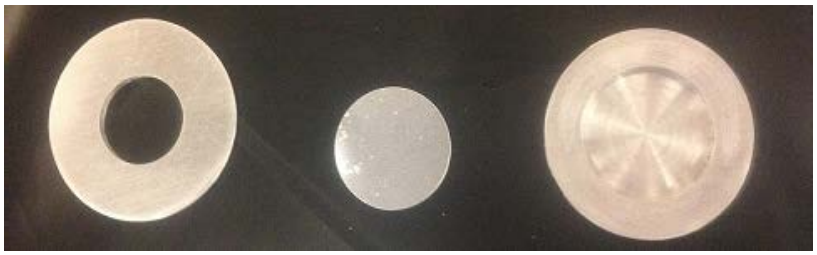

Figure 4.3 Zinc foil target that is contained between an aluminium target annulus (left) and an aluminium cradle (right).

4.2.3.2 Target Dissolution

At end of bombardment (EOB) the target remained in the solid targetry apparatus for 1-3 h to allow for some decay of the short-lived ^{68}Ga activity ($t_{1/2}$ = 68 min). The chemical separation was performed in a shielded fume hood. The irradiated ^{nat}Zn or ^{64}Zn foil was first dissolved in 1 mL of 8 M HCl at 150 °C, then the solution was evaporated to dryness. High purity TraceSELECT water (1 mL) was added to the residue and evaporated to dryness; this step was repeated once. Finally, the residue was dissolved in 2 mL of 0.01 M HCl and an aliquot (1 µL) was taken for analysis by gamma spectroscopy.

4.2.4 Separation and Purification of ^{61}Cu

4.2.4.1 From ^{nat}Zn Target

A combination of three columns connected in series was used (Figure 4.4a):

Column 1: Separation of Cu^{2+} from Zn^{2+} and Ga^{3+} on Cu-resin

0.5 mg of Cu-resin was pre-conditioned with 20 mL of 0.01 M HCl solution and placed in a small plastic column. The target was dissolved in 2 mL of 0.01 M HCl solution and loaded onto the column. The column was then washed with 25 mL of 0.01 M HCl to remove the Zn target material as well as the ^{66,67,68}Ga radionuclides impurities. ^{61}Cu was then eluted off the column with 1.5-2.0 mL of 8 M HCl, which was directed to the cation exchange column (column 2) connected in series with the anion exchange column (column 3) in order to remove both residual Zn^{2+} and Ga^{3+} impurities.

Column 2: Separation of Cu^{2+} and residual Zn^{2+} from residual Ga^{3+} on a cation exchange column.

The cation exchange resin (AG5 W-X8) (1.0 g) was pre-conditioned with 20 mL of TraceSELECT water followed by 8 M HCl (5 mL) and was placed in a small plastic column. The residual Ga impurities were retained on the cation exchange column while the ^{61}Cu and residual Zn impurities were flushed onto the anion exchange column 3.

Column 3: Separation of Cu^{2+} from residual Zn^{2+} on an anion exchange column.

The final step of the separation process was to elute the $^{61}CuCl_2$ from the anion exchange column (AG1-X8 resin (1.0 g) pre-conditioned with 5 mL of 8 M HCl) with 3.0 mL of 2 M HCl. The solution was evaporated to dryness. The residue was dissolved in 1 mL of TraceSELECT water and evaporated to dryness; this step was repeated three times. The final product was then dissolved in 400-800 µL of 0.01 M HCl and sampled for analysis by γ-spectroscopy. Comparison of γ-spectroscopic analysis of radionuclidic composition before and following separation is shown in Table 4.1.

4.2.4.2 From Enriched ^{64}Zn Target

Single Cu-resin column

The separation and purification of ^{61}Cu from the irradiated enriched ^{64}Zn target material is shown schematically in Figure 4.4b. The solution was loaded onto a Cu-resin column, pre-conditioned with 20 mL of 0.01 M HCl. The Zn and Ga impurities were eluted with 25 mL of 0.01 M HCl and kept for recovery of ^{64}Zn if required. The ^{61}Cu trapped on the Cu-resin column was then eluted off with 1.5-2.0 mL of 8 M HCl, followed by drying steps as described in the previous section. The final product was then dissolved in 400-800 µL of 0.01 M HCl and sampled for analysis by γ-spectroscopy.

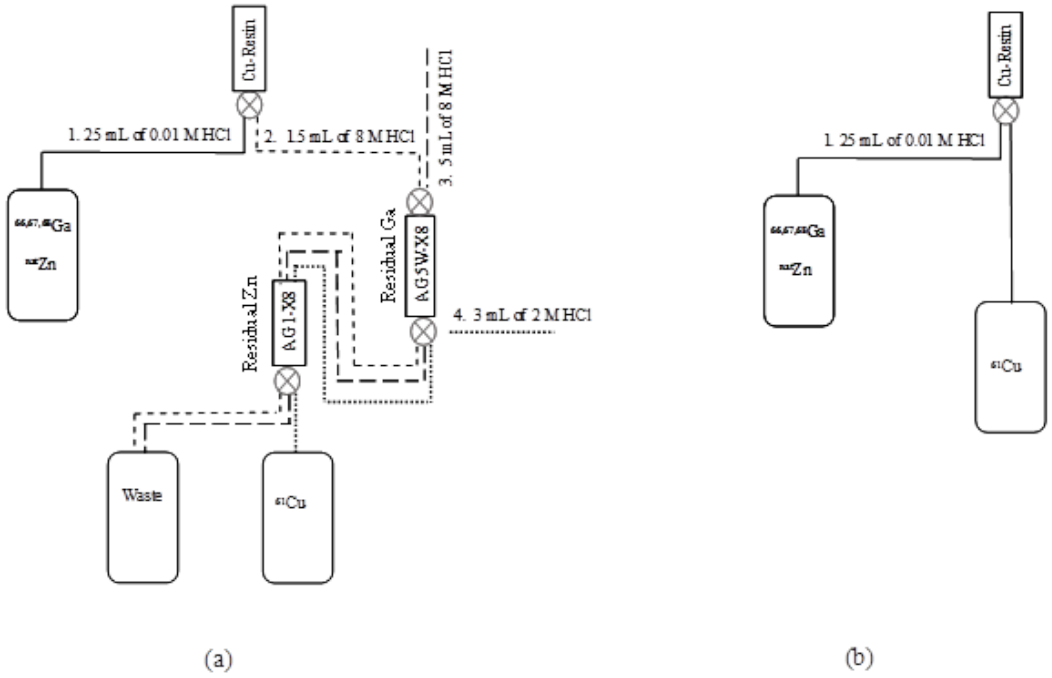

Figure 4.4 Schematic representations of the column chromatography purification of ^{61}Cu from (a) irradiated ^{nat}Zn foil target and; (b) irradiated ^{64}Zn foil target.

^{64}Zn Target Recovery

In order to test the feasibility of recovery of the enriched ^{64}Zn target material, following decay of the Ga radionuclides, the 25 mL of Zn and Ga in HCl solution were evaporated to dryness. Then, the residue was redissolved in 5 mL of 8 M HCl and transferred to a cation exchange column (pre-conditioned with 20 mL of Trace-SELECT water), followed by 10 mL of 8 M HCl. The solution was evaporated to dryness. The recovery of ^{64}Zn for potential electroplating was 94 ± 5%.

4.2.5 Specific Activity

The specific activity of ^{61}Cu (in GBq/µmol) was determined by the titration method, using purified ^{61}Cu in 0.01 M HCl and the chelating agents NOTA-NCS, DOTA-NCS and diamsar (Figure 4.2). The specific activity was converted to GBq/µg, as described in the Results section.

Complexation of the ^{61}Cu was achieved in a similar manner to that described by McCarthy et al. (1997). Briefly, increasing concentrations (1×10^{-9} to 1×10^{-2} M) of each chelator solution were prepared in 0.1 M sodium acetate buffer (pH 6.5). Twenty microlitre of each chelator solution was added to 10 µL of the ^{61}Cu solution which had previously been adjusted to pH 6.5 with 0.1 M sodium acetate buffer. The mixture was then incubated at room temperature for 30 min. After incubation, aliquots of 2 µL were withdrawn from each reaction mixture and spotted directly onto 10 cm ITLC–SA strips. Different mobile phases were used to separate free Cu^{2+} from complexed Cu^{2+}:

(i) for diamsar the mobile phase was 0.1 M NaCl : 0.1 M EDTA (9:1). The retardation factor (R_f) was < 0.2 for Cu-diamsar while free Cu^{2+} migrated to $R_f > 0.8$.

(ii) DOTA and NOTA Cu^{2+} complexes were separated using 0.1 M sodium acetate (pH 4.5) : H_2O : MeOH : ammonium hydroxide (20:18:2:1 v/v) mobile phase. Cu-DOTA and Cu-NOTA complexes migrated at $R_f > 0.8$ while free Cu^{2+} had a $R_f < 0.2$.

The ITLC strips were cut into 2-cm pieces and counted on the calibrated γ-counter using a dynamic energy window of 282 keV. The minimum chelator concentration for which 100% labelling occurred was estimated by doubling the measured value at 50% complexation. The specific activity of ^{61}Cu, in GBq/µmol of Cu^{2+}, was then calculated by correcting for the total activity and molecular weight of the chelator and ^{61}Cu.

After complete decay of the ^{61}Cu samples, aliquots (10-20 µL) from each production run were diluted with 1% of HNO_3, adjusted to a final volume of 10mL and sent for inductively coupled plasma mass spectrometry (ICP-MS) analysis (Curtin University, WA, Australia).

4.3 Results and Discussion

4.3.1 Production of ^{61}Cu

Production of ^{61}Cu using the ^{nat,64}Zn(p,α)^{61}Cu nuclear reaction was performed under irradiation at 11.7 MeV with 20-40 µA. Two separate target materials were used, ^{nat}Zn and enriched ^{64}Zn. The yield (corrected to EOB) of purified ^{61}Cu after irradiation of ^{nat}Zn foil target was approximately 9.7-19.7 MBq/µA.h which was about 20% of the activity produced from an enriched ^{64}Zn target of the same thickness, for the same µA.h irradiation. If considering the natural abundance of ^{64}Zn in ^{nat}Zn (48.6%), the activity of ^{61}Cu produced from a high-purity ^{nat}Zn foil target (99.99%, 0.05 mm thick) was lower than expected compared to that of the enriched ^{64}Zn target (99.3%, 0.05 mm thick). Rowshanfarzad et al. (2006) reported that the production yield of electroplated ^{nat}Zn with an 80µm thickness was 445 MBq/µA.h at a proton beam energy of 22-12 MeV. The results in the present study were much lower than this result, most likely due to the energy, incident angle of the proton beam and the target size before and after the separation.

The activity of ^{61}Cu produced from a highly enriched ^{64}Zn foil target (corrected to EOB) was within the range 517-723 MBq, for an irradiation of approximately 20 µA.h. This represented a yield of 29-36 MBq/µA.h. Thieme et al. (2013) reported that the yield from electroplated ^{64}Zn with a thickness ranging between 244-597 µm was 20.7-48.3 MBq/µA.h with a primary proton energy of 16 MeV. The comparatively higher yields obtained for the present study are most likely a consequence of the higher purity (and possibly density) of the enriched ^{64}Zn foils

that were used, compared to electroplated ^{64}Zn layers prepared as targets reported in Thieme et al. (2013).

To ensure that no contaminating ^{65}Zn was produced, the incident proton energy was reduced to 11.7 MeV (Asad et al., 2012). After EOB, γ-spectroscopy of the digested foil prior to separation showed no evidence of ^{65}Zn. At EOB, the co-produced activities of ^{66}Ga and ^{68}Ga were significantly higher than that of ^{61}Cu, but ^{67}Ga activity was negligible (Table 4.1).

4.3.2 Separation and Purification of ^{61}Cu from ^{nat}Zn and Enriched ^{64}Zn Targets

The desired ^{61}Cu product was separated from the irradiated ^{nat}Zn target using a three-step purification process, as illustrated in Figure 4.4(a). The first step involved loading the dissolved target onto a Cu-resin column to separate out the Zn and ^{66,67,68}Ga impurities. A cation-exchange column was used to separate (by retention) any remaining traces of Ga ions from the eluted ^{61}Cu. The final step involved an anion exchange column to retain any remaining Zn ions from the eluted ^{61}Cu solution, which was collected as $^{61}CuCl_2$ with a radionuclidic purity > 99%. The final product was also analysed by ICP-MS for trace metal contaminants. The results of this analysis are shown in Figure 4.5.

For the separation and purification of ^{61}Cu from irradiation of an enriched ^{64}Zn target, only a single Cu-resin column (Figure 4.4 (b)) was necessary since the Ga radionuclide contamination was low. Table 4.1 shows the γ-spectroscopy analysis of the radionuclidic composition before and following separation: no radionuclidic impurity was detected in the ^{61}Cu product obtained from both purifications. Figure 4.6 presents the ICP-MS analyses of trace metal contaminants for each ^{61}Cu separation.

Table 4.1 Typical radionuclidic compositions of digested foils prior to column chromatography separation, and purified ^{61}Cu product following separation. Results for both target materials are corrected to EOB and expressed as percentage of total counts attributed to the characteristic photopeak of the radionuclide, corrected for the branching fraction of the decay mode.

Target Material	Radionuclide	Prior to Separation (%)	Purified Product (%)
*^{nat}Zn	^{61}Cu	7.3	100
	^{66}Ga	12.2	Not detected
	^{67}Ga	0.2	Not detected
	^{68}Ga	80.3	Not detected
†Enriched ^{64}Zn	^{61}Cu	90.06	100
	^{66}Ga	1.67	Not detected
	^{67}Ga	Not detected	Not detected
	^{68}Ga	8.27	Not detected

*Target bombarded at 20 µA for 30 min

†Target bombarded at 40 µA for 30 min

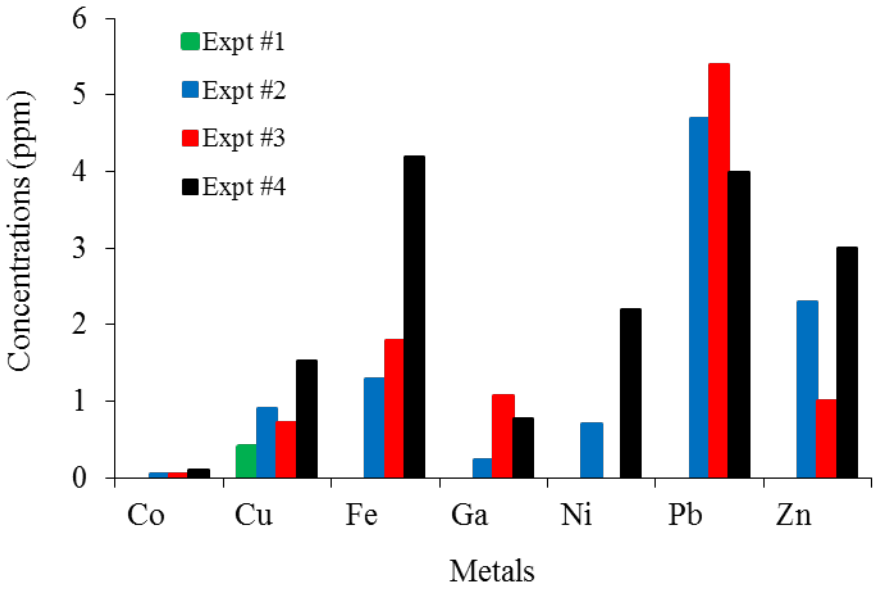

Figure 4.5 ICP-MS results from irradiated natural Zn. Relative amount (ppm) of Cobalt, Copper, Iron, Gallium, Nickel, Lead and Zinc ions present in 47-85 MBq of produced ^{61}Cu.

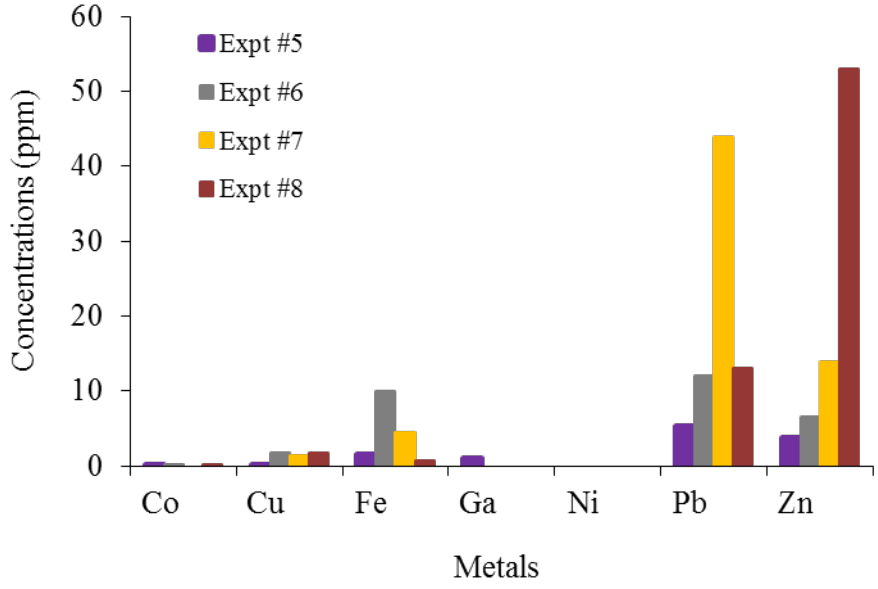

Figure 4.6 ICP-MS results from irradiated enriched ^{64}Zn. Relative amount (ppm) of Cobalt, Copper, Iron, Gallium, Nickel, Lead and Zinc present in 105-571 MBq of produced ^{61}Cu.

Several general separation methods have been reported in the literature for isolating Cu isotopes and Ga isotopes from the Zn target materials by cation and anion exchange chromatography (Rowshafarzad et al., 2006; Dasqupta et al., 1991; Schwarzbach et al., 1995). In the case of ^{61}Cu, Rowshanfarzad et al. (2006) irradiated a ^{nat}Zn target using 22 MeV proton beam energy at 180 µA.h. They isolated the ^{61}Cu with a combination of cation and anion exchange columns, using large volumes of concentrated HCl to separate the Cu from the Ga and Zn by-products. Unfortunately, the specific activity of the isolated products was not reported.

As part of this work, the cation/anion exchange chromatography method as described by Rowshanfarzad et al. (2006) was reproduced for the purification of product obtained from ^{nat}Zn and ^{64}Zn targets (for results see Asad et al., 2012; and Appendix A "purification methods"). This led to the development of an improved method outlined in this chapter. This improved method presents the following advantages:

i) Decreased separation time by a factor 4 (from 120 min to 30 min).
ii) Smaller volumes of acid used for the purification.
iii) Decreased radiation exposure by 20%.
iv) Reduced metal contamination and therefore increased specific activity of the final product.
v) Improved radionuclidic purity (from > 95% to > 99%).

4.3.3 Specific Activity of ^{61}Cu

ICP-MS was used to assess both the total non-radioactive Cu content and the presence of the contaminating metal ions Co, Fe, Ni, Pb, Ga and Zn in 'cold' samples of the purified solutions containing ^{61}Cu. Figures 4.5 and 4.6 summarise the trace metal content in each target experiment derived from both types of target. The ICP-MS values for Cu were used to determine the no-carrier-added specific activity (NCA-SA) of the ^{61}Cu at EOB, and these data are compared with the effective specific activities (ESA) obtained by titration with chelators.

The ESA values for the ^{61}Cu were determined using three chelators, DOTA-NCS, NOTA-NCS and diamsar. Typical titration curves for each of the three chelators are shown in Figure 4.7. A comparison of ESA and NCA-SA values are presented in Table 4.2.

Table 4.2 Comparison between no-carrier-added specific activities (NCA-SA) of purified ^{61}Cu determined from ICP-MS and effective specific activities (ESA) determined by titration with each of three Cu^{2+} chelators: diamsar, NOTA-NCS and DOTA-NCS. Uncertainties are ± SD, with 4 experiments for each target material. Experiment numbers equate to those shown in Figures 4.5 and 4.6.

Target Material	ESA by titration with chelator (MBq/µg)			NCA-SA by ICP-MS (MBq/µg)
	diamsar	NOTA	DOTA	
^{nat}Zn				
Expt #1	185.9 ± 6.5	74.06 ± 2.7	18.6 ± 0.6	233.3 ± 23.3
Expt #2	92.2 ± 5.1	23.4 ± 1.4	5.9 ± 0.3	191.9 ± 19.2
Expt #3	84.7 ± 4.7	26.6 ± 1.7	4.7 ± 0.2	143.3 ± 14.3
Expt #4	137.5 ± 2.8	70.3 ± 4.1	35.9 ± 0.6	169.4 ± 16.9
Enriched ^{64}Zn				
Expt #5	379.7 ± 9.5	31.7 ± 1.1	19.0 ± 1.1	434.4 ± 43.4
Expt #6	326.5 ± 10.1	63.3 ± 3.7	30.3 ± 1.8	482.1 ± 48.2
Expt #7	412.5 ± 15.3	82.7 ± 5.4	8.3 ± 0.4	506.2 ± 50.6
Expt #8	368.9 ± 11.8	19.7 ± 1.1	16.9 ± 0.2	496.4 ± 49.6

For ^{61}Cu derived from the ^{nat}Zn target irradiation, the NCA-SA values were in reasonable agreement with the calculated ESA values using the diamsar chelator (approximately 1.2-2.1 higher). For the ^{64}Zn target they were 1.1-1.5 higher. Thus the specific activities determined using titration with diamsar are considered to be in good agreement with specific activities calculated from ICP-MS, particularly as they were achieved in the presence of relatively high concentrations of Zn^{2+} and Pb^{2+} (Figures 4.5 and 4.6). The metal impurities may have arisen from air contamination, since the separation experiments were not performed in a certified clean room environment.Titration with the two other

chelators NOTA-NCS and DOTA-NCS produced ESA values that were significantly lower than the ICP-MS derived values (Table 4.2).
Thieme et al. (2013) found that the ESA values for ^{61}Cu using the TETA chelator were 3-fold less than the ICP-MS values. In this study, we found that diamsar was the best chelator to use in determining the ESA with the titration method, if the ICP-MS derived NCA-SA is considered as the more reliable 'gold standard'. This is because it has a higher selectivity for the Cu^{2+} ions over other metal-ion contaminants present in the radioactive solutions. In the case of NOTA-NCS and DOTA-NCS, Fe $^{2+/3+}$ and Zn^{2+} ions were likely the main competitors of Cu^{2+} ions. The relatively high concentration of Zn^{2+} derives from residual zinc target material (Zn > 50 ppm) (Chakravarty, Chakraborty, Dash, & Pillia, 2013).

The complexation of ^{61}Cu with the different chelators was analysed after incubation at room temperature for 30 min as shown in Figure 4.7. The data indicate that the complexation yield of diamsar could be achieved with μmolar concentrations of chelator, which was better than NOTA-NCS or DOTA-NCS under the same conditions. NOTA-NCS achieved 100% complexation at lower concentrations than DOTA-NCS. Heating would likely improve the labelling efficiency with DOTA-NCS but also facilitate complexation of other metal ions more avidly. These results suggest that the use of diamsar as titration chelator to calculate the specific activity is more accurate than the use of DOTA-NCS or NOTA-NCS, because of the high selectivity of diamsar towards the Cu^{2+} ion. Furthermore, Smith (2004) reported that > 99.9% complexation of ^{64}Cu could be obtained in 2 min with SarAr (functionalised diamsar) at very low concentrations (1 μmolar), at room temperature using a 1:1 molar ratio ligand:metal and a pH range of 4-9. These findings and the results obtained in the present study support the case for further development of the hexa-aza bicyclic cages for clinical and pre-clinical studies (Paterson et al., 2014; Wei et al., 2009; Liu, Li, & Conti, 2014)

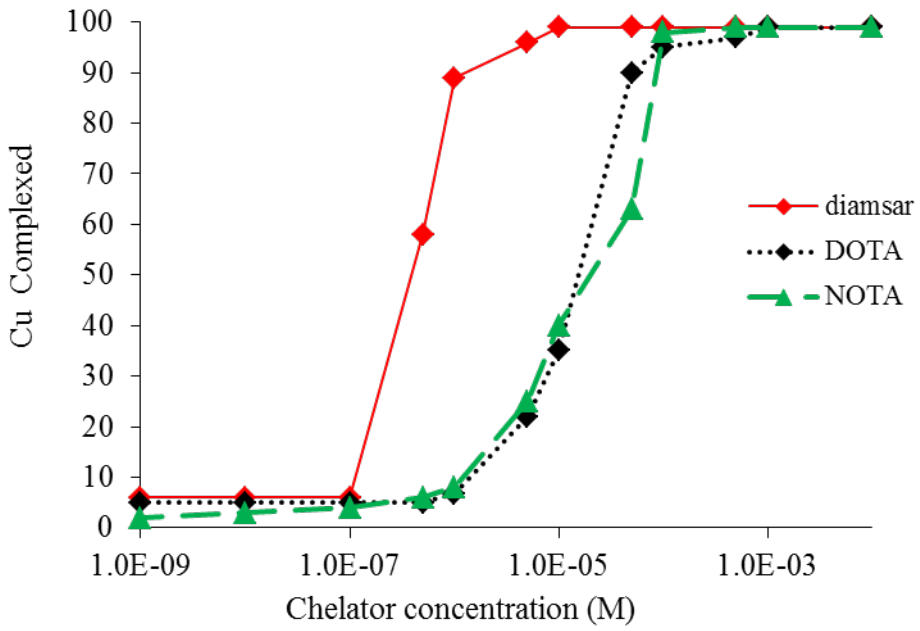

Figure 4.7 Complexation of ^{61}Cu with increasing concentrations of the Cu^{2+} chelators diamsar, NOTA-NCS and DOTA-NCS (room temperature, 30 min reaction).

4.4 Conclusions

The desired ^{61}Cu nuclide was produced from the $^{64,nat}Zn(p,\alpha)^{61}Cu$ reaction using a 11.7 MeV proton beam energy to irradiate ^{nat}Zn and ^{64}Zn disc targets. This was followed by column chromatography separation and purification (three columns for ^{nat}Zn, one for ^{64}Zn), yielding ^{61}Cu as $^{61}CuCl_2$ with high radionuclidic purity (> 95%) from each target. Separation and purification from the ^{nat}Zn target using a combination of three columns was fast (< 30 min), efficient and straightforward.

The overall cost to produce the ^{61}Cu was considerably cheaper using ^{nat}Zn or ^{64}Zn target, when compared to the cost of using an electroplated ^{61}Ni target; the ^{nat}Zn target being the most cost-effective. Effective specific activities of the purified ^{61}Cu were measured by the titration method using the three chelators diamsar, NOTA-NCS and DOTA-NCS. These results were compared with no-

carrier-added specific activities obtained by ICP-MS. While low agreement was found for NOTA-NCS and DOTA-NCS, relatively good agreement was found with diamsar. This was due to the superior selectivity of diamsar for Cu ion.

CHAPTER FIVE
CONJUGATION AND ^{64}CU-RADIOLABELLING OF POLYSTYRENE AND SILICA NANOSPHERES

5.1 Introduction

The application of nano- and micro-materials in the diagnosis and therapy of disease has evolved significantly in the last few years. Both organic and inorganic materials have been chemically modified to incorporate targeting agents and drugs for the treatment of specific diseases (Thorek, Elias, & Tsourkas, 2009). These modifications are designed to increase specificity and uptake of the desired drug at the site of interest, therefore increasing effectiveness of treatments. By varying the charge, size and surface properties of the particle, the uptake of drugs to non-specific organs has also been significantly reduced (Liu & Welch, 2012). Smaller nanoparticles (100 nm in diameter) are comparable in size to antibodies and DNA, and are permeable to tumour vasculatures (Gunasekera, Pankhurst, & Douek, 2009). Moderate size nanoparticles (< 500 nm in diameter) are used for intravascular targeting; for example, they can cross the microfold cells in the Payer's patch and the mesentery on the surface of the gastrointestinal mucosa. Larger particles, between 1 and 125 μm, are more suitable for use in the oral delivery of drugs (Jain, 2000). For smaller carrier molecules and/or target molecules (such as peptides that clear rapidly from biological systems) nanoparticles have been used as carriers to lengthen their biological half-life, and so reduce the need for frequent administration (Bodmeier & McGinity, 1988). Encapsulation of the peptide in a particle has resulted in improvements in their transportation across biological barriers, by increasing diffusivity and lowering partition coefficients; resulting in significant increased uptake at the target sites (Couverur & Puiseux, 1993).

This chapter explores the radiolabelling of two types of nanomaterials. The first type is polystyrene nanospheres, which are non-biodegradable organic particles. They are widely used as model and reference particles to study the interactions between the particles and cells (Varela et al., 2012). They are non-immunogenic and have been shown to have low cytotoxicity *in vitro* (Papageorgiou et al., 2007) and *in vivo* (Yacobi et al., 2008). Polystyrene is easily chemically modified, and so one can change the physical properties of the particle (i.e. size, surface overall charge, shape and chemical composition) to tailor its interaction with cells and blood (Silva, 2007; Yoo, Doshi, & Mitragotri, 2010; Decuzzi et al., 2010; Makino et al., 2003; Foged, Brodin, Frojaer, & Sundblad, 2005). Because of their hydrophobic nature (Heslinga, Mastria, & Eniola-Adefeso, 2009) polystyrene particles often localise in lysosomes within the cell (Lorenz et al., 2010; Xiao et al., 2010).

The other types of nanomaterials that have been investigated widely are silica-based particles. These are classified as inorganic materials, with hydrophilic surfaces that make them particularly attractive for *in vivo* applications (Tang & Cheng, 2013; Slowing, Vivero-Escoto, Wu, & Lin, 2008; Barbe et al., 2004). Silica particles are under development in a number of biomedical imaging, assaying, therapeutic delivery and monitoring applications (Liberman et al., 2014; Desai et al. 2004). In contrast to polystyrene particles, they are biodegradable and also have low cytotoxicity *in vivo*. Their synthesis is readily scalable and the particle surfaces are easily modified to increase drug loading, blood circulation and site specific targeting (Liberman et al., 2014).

As discussed in Chapter 1, polyazacarboxylate chelators such as DOTA, TETA and NOTA have been widely used for radiolabelling particles (Chapter 1; Section 1.6). There are two significant problems with the use of DOTA or TETA chelators; the requirement of heat for radiolabelling (above room temperature) and the kinetic lability of the resultant Cu^{2+} complex *in vivo* (Bass, Wang, Wlech, & Anderson, 2000; Boswell et al., 2004; Rogers et al., 2003,

2004). NOTA chelator has been shown to possess better Cu^{2+} complexation under mild conditions (Chapter 1; Section 1.6).

The charge of the final Cu^{2+} bifunctional chelator (BFC) complex can influence the biodistribution of radioactivity *in vivo* (Cooper et al., 2012; Lewis et al., 2001; Dearling et al., 2011). The sarcophagine macrocycles, for example SarAr-NH_2 and MeSar-Ph-NCS, are particularly attractive for use in radiolabelling of functionalised particles. The sarcophagine chelators are known to form ^{64}Cu:BFC 1:1 complexes comparably faster at room temperature at pH 5-9 and at µmolar concentration. Both are reported to be effective in radiolabelling a range of bioactive target agents (Clift et al., 2008; Di Bartolo, Sargeson, & Smith, 2006; Kong, Mume, Triani, & Smith, 2013; Mume et al., 2013; Smith, 2004), (Chapter 1; Section 1.6) and show high *in vivo* stability (Paterson et al., 2014). Indeed, *in vitro* and *in vivo* stability of the resultant Cu^{2+} SarAr bioconjugates have been shown to be at least as stable as the analogous Cu^{2+} DOTA, TETA and NOTA bioconjugates (Liu, 2008; Di Bartolo et al., 2006). Because SarAr forms metal:chelator complexes of 1:1 over a wide range of pH, it is particularly useful in quantifying functional groups on the particle surface (Hung, Joso, Fuchs, Barner, & Smith, 2008).

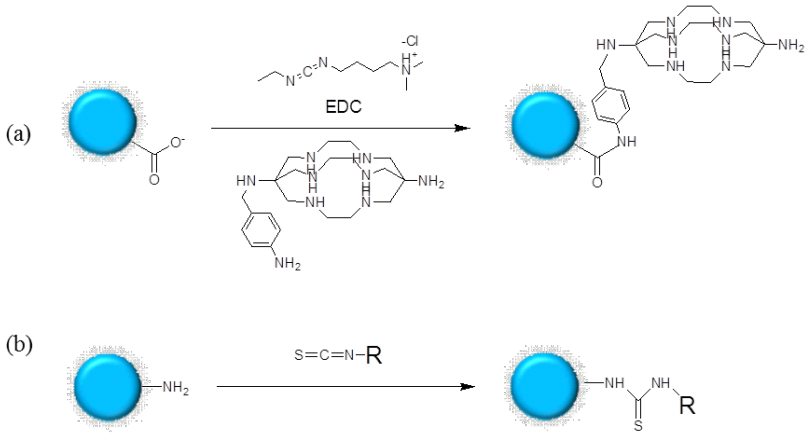

Figure 5.1 Schematics of (a) the SarAr-NH_2/EDC conjugation reaction with polystyrene nanospheres (PS NS), (b) Conjugation of a BFC (R = DOTA-NCS, NOTA-NCS or MeSar-Ph-NCS) onto the surface of silica nanospheres (Si NS).

The overall efficiency of the conjugation of BFCs to the NS can be determined using a number of routes. For example, by radiolabelling of SarAr chelator conjugated to NS with a radionuclide such as ^{57}Co ($t_{1/2}$ = 271.8) days (Kong et al, 2013) the efficiency can be inferred from a measurement of the final radioactivity. As both metals Co^{2+} and Cu^{2+} form complexes of similar geometry with all the complexing BFCs under investigation, ^{57}Co was used as a surrogate for assessing the stability of the functionalised NS for long range *in vitro* studies

In this study the polystyrene nanospheres (PS NS) were activated with carboxylate groups on their surface while the silica nanospheres (Si NS) were activated with amino groups. The PS NS were conjugated with the SarAr-NH_2 chelator using the classical EDC method (see Figure 5.1 a). The Si NS were conjugated with three BFCs, DOTA-NCS, NOTA-NCS and the new MeSar-Ph-NCS chelator, to form an isothiourea bond with the isothiocyanate groups (see Figure 5.1 b) (McDevitt et al., 2007; Lang, Ma, Kiesewetter, & Chen, 2014).

The aim of this chapter is to assess the effectiveness of radiolabelling with a range of BFCs (DOTA-NCS, NOTA-NCS, and MeSar-Ph-NCS) on two types of functionalised NS. More specifically;

a) To radiolabel a series of PS NS of different sizes (i.e. 365, 680 and 840 nm diameter) functionalised with carboxylate groups with $^{57/nat}Co^{2+}$ or $^{64/nat}Cu^{2+}$.

b) To radiolabel amino functionalised Si NS with MeSar-Ph-NCS, NOTA-NCS and DOTA-NCS.

c) To compare the number of each chelator conjugated on the surface of the NS.

5.2 Experimental

All reagents and solvents used were of analytical grade and were obtained from commercial sources unless otherwise stated. All chemicals used in these studies were greater than 99% pure unless otherwise stated. TraceSELECT high purity water; anhydrous sodium acetate anhydrous; MES [2-(N-morpholino)-ethanesulfonic acid], EDC [*N*-(3-Dimethylaminopropyl)-*N*′-ethylcarbodiimide hydrochloride], styrene [$C_5H_6CH=CH_2$], inhibitor remover [4,4′-Azobis (4-cyanovaleric acid)] ($\geq$ 98%), analytical standard solutions of $CoCl_2$ and $CuCl_2$ (0.01M) and eppendorf tubes (1.5 mL) were purchased from Sigma-Aldrich (Australia). The SarAr-NH_2 chelator N1, N8-bis [(4-aminophenyl) methyl]-3,6,10,13,16,19 hexaazabicyclo [6.6.6]eicosane-1,8-diamine] was purchased from Clarity Pharmaceuticals (Australia), in powder form (19.9% chemically pure with carrier salt for storage stability). Isothiocyanate derivatives of [Mg(CH_3)(*p*-NCS-Ph)sar](CF3SO_3)$_2$ (MeSar-Ph-NCS) were kindly provided by Dr Paul Donnelly (Melbourne University, Australia). The *p*-isothiocyanato benzyl derivatives of BFCs such as 1,4,7,10 tetraazacyclododecane1,4,7,10-tetraacetic acid (DOTA-NCS), 1,4,7-triazacyclononane-1,4,7-triacetic acid (NOTA-NCS) were purchased from Macrocyclics (USA). Si NS were supplied by Corpuscular (NY, USA). Trace SELECT water was used in the preparation of buffers and cold solutions of Co^{2+} and Cu^{2+}. High specific activity (SA) radioisotopes, ^{64}Cu ($t_{1/2}$ = 12.7 h; SA = 6.34 x 10^6 GBq g^{-1}) and ^{61}Cu ($t_{1/2}$ = 3.3 h; SA = 1.2 x 10^6 GBq g^{-1}) were obtained from RAPID Labs, (SCGH, Perth,

Australia). ^{57}Co ($t_{1/2}$ = 271.8 days; SA = 3.12 x 10^5 GBq g^{-1}) was obtained from PerkinElmer (IL, USA). Equipment used for this study included a Gamma counter Wizard model 2470 (PerkinElmer) and a Multi mixer (TRO-1300) from Chromalytic Technology.

5.2.1 Preparation of Polystyrene Nanospheres

PS NS of 365, 680 and 840 nm diameter were a gift from senior research chemist Linggen Kong at ANSTO [Australian Nuclear Science and Technology Organisation]. Table 5.1 gives the components used to generate each particle size. A typical synthesis involved mixing styrene and NaOH in a 250 mL round bottom flask. The styrene was added through a syringe filled with inhibitor. Then, water was added until the desired total mass was reached. The flask was capped and deoxygenated with nitrogen gas for 15 min, then immersed in a 37 °C oil bath with constant stirring for at least 20 h. After cooling to room temperature, the mixture was centrifuged at 6000 rpm. The polymer particles were washed twice with water to remove free monomers, and then resuspended in water. A small amount (in triplicate) of the particle suspension was freeze-dried to determine the solid content of the slurry. The size and morphology of the PS NS were analysed using transmission electron microscopy [TEM: JEOL 2000 FXII] and the diameters of individual particles were confirmed (see Figure 5.2).

Table 5.1 Chemical components used to synthesize the polystyrene polymer particles and their resultant physical properties.

Styrene (mmol)	38	76	76
Inhibitor (mmol)	0.384	0.768	0.384
Estimated -COOH group added (mol %)	2	2	1
Total mass produced (g)	140	40	40
Mass of solid particles (g)	3.266	7.028	6.57
Average nanosphere size (nm) (as determined by TEM)	365	680	840

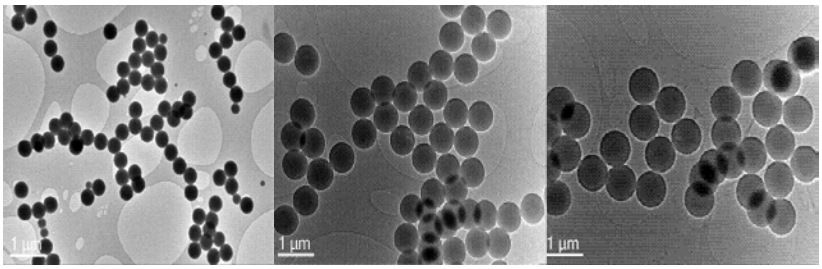

(a) (b) (c)

Figure 5.2 TEM images of PS NS (a) 365 nm (b) 680 nm (c) 840 nm.

5.2.2 Optimisation of the Conjugation of SarAr-NH_2 to Polystyrene Nanospheres

To seven vials (2.0 mg in 100 µL) of 680 nm diameter PS NS in 1.5 mL eppendorf tubes were added varying amounts (1, 50, 100, 250, 350, 500, and 750 nmol) of a freshly prepared solution of SarAr-NH_2 in 0.1 M MES buffer (pH 5) in presense of an excess of EDC (10:1 EDC/SarAr-NH_2 molar ratio). The final volume of the reaction mixture was adjusted to 0.9 mL with 0.1 M MES buffer (pH 5). The mixture was vortexed then rotated by a MultiMix (360 °C continuous rotation) for 2 h at room temperature (23 °C). The

suspension was then centrifuged for 10 min at 5000 rpm before the supernatant was removed. Conjugated nanospheres (SarAr-NH_2-PS NS) were washed a further two times with 0.1 M MES buffer (pH 5) in a similar manner to that described above to remove unreacted SarAr-NH_2. The supernatant was discarded each time. The resultant seven batches of conjugated nanospheres were then suspended in 100 µL of 0.1 M sodium acetate buffer (pH 6.5) for radiolabelling.

5.2.3 Optimisation of the Conjugation of NOTA-NCS and DOTA-NCS to Silica Nanospheres

To six vials (2.5 mg in 100 µL) of 200 nm diameter Si NS in 1.5 mL eppendorf tubes were added varying amounts of (1, 50, 100, 250, 350, 500, and 750 nmol) of a freshly prepared solution of BFC (NOTA-NCS or DOTA-NCS) in 0.1 M PBS buffer (pH 8). The buffer pH value was selected from the optimised pH range of 8-9 (Figure 5.3). The final volume of the reaction mixture was adjusted to 0.9 mL with 0.1 M PBS buffer (pH 8). The mixture was vortexed, then rotated using a MultiMix (360 °C continuous rotation) overnight at room temperature (23 °C). The suspension was then centrifuged for 10 min at 5000 rpm before the supernatant was removed. Each conjugated batch of nanospheres (BFC-Si NS) was washed a further two times with 0.1 M PBS buffer (pH 8) in a similar manner to that described above, to remove unreacted chelator. The supernatant was discarded each time. The resultant six batches of conjugated nanospheres were then suspended in 100 µL of 0.1 M sodium acetate buffer (pH 6.5) for radiolabelling.

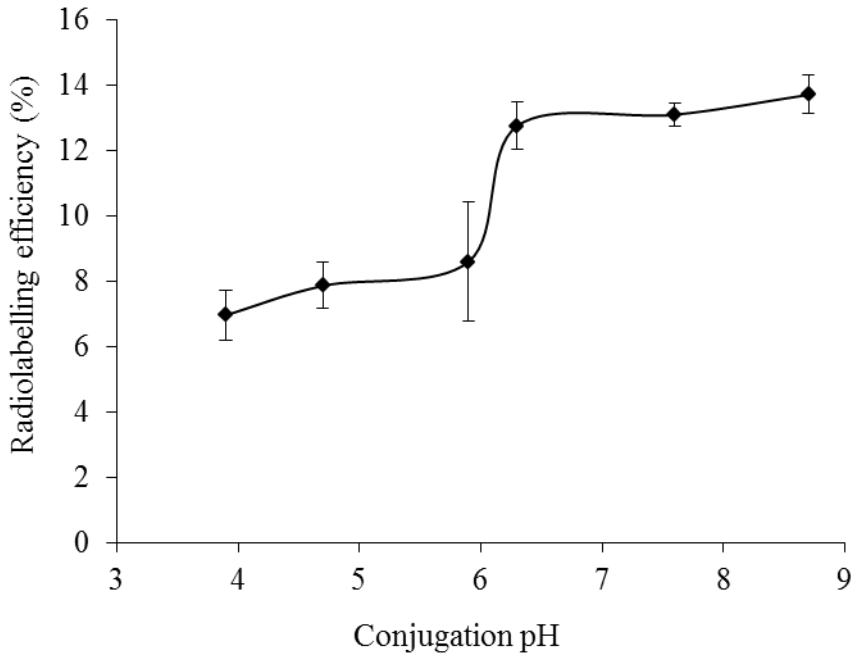

Figure 5.3 Effect of pH on radiolabelling efficiency of Si NPs using DOTA-NCS. Experimental conditions: Si NS = 2.5 mg, DOTA-NCS = 500 nmol, radiolabelling at pH 7 at room temperature (23 °C). (Mean±SD, N = 3)

5.2.4 Optimisation of the Conjugation of MeSar-Ph-NCS to Silica Nanospheres

To six vials (2.5 mg in 100 µL) of 200 nm diameter Si NS in 1.5 mL eppendorf tubes were added varying amounts (10, 25, 50, 100, 150 and 200 nmol) of a freshly prepared solution of MeSar-Ph-NCS in 0.1 M PBS buffer (pH 8). The final volume of the reaction mixture was adjusted to 0.9 mL with 0.1 M PBS buffer (pH 8). The mixture was vortexed then rotated by a MultiMix (360 °C continuous rotation) for 2 h at room temperature (23 °C), as described previously by Paterson et al. (2014). The suspension was then centrifuged for 10 min at 5000 rpm before the supernatant was removed. Then, 0.1 M sodium acetate buffer (pH 6) was added to the conjugated NS (BFC-Si NS) for up to 2 h for further mixing to remove the Mg^{2+} from the chelator. The suspension was then centrifuged for 10 min at 5000 rpm, the supernatant removed and the slurry taken in 0.1 M PBS buffer (pH 7). The process was repeated twice to remove unreacted chelator. After the last wash, the resultant 6 batches of conjugated

particles were then suspended in 100 µL of 0.1 M sodium acetate buffer (pH 6.5) for radiolabelling.

5.2.5 Radiolabelling of SarAr-NH_2 – Polystyrene Nanospheres Conjugation

The SarAr-NH_2 conjugated PS NS (suspended in 100 µL of 0.1 M sodium acetate buffer pH 6.5) were exposed to a known amount (1 nmol, 10 µL) of $^{57/nat}Co^{2+}$ or $^{64/nat}Cu^{2+}$ in the same buffer. The total volume of the mixture was adjusted with acetate buffer (pH 6.5) to 0.9 mL, vortexed and subsequently rotated on a MultiMix (360 °C continuous rotation) for 1.25 h to 24 h at room temperature (23 °C). The mixtures were then centrifuged for 10 min at 10000 rpm and washed with acetate buffer (pH 6.5). After each wash, the supernatant was collected and transferred to a test tube for counting on the gamma counter. The washing step was repeated until no further release of radioactivity could be detected (up to 4 times). All reactions were conducted in triplicate and results are reported as an average of the triplicates. The percentages of radiolabelling efficiency and metal ions associated with the particle were calculated from the equations (1 & 2) respectively:

$$Radiolabelling\ efficiency = \frac{Activity_{pellets}}{Activity_{pellets} + Sum\ of\ Activity_{supernantant}} X\ 100\% \quad (1)$$

$$Moles\ of\ Cu^{2+}_{associated} = Cu^{2+}_{initial}\ X\ radiolabelling\ efficiency \quad (2)$$

where $Activity_{pellets}$ is the total activity of the pellets after the last wash; $Activity_{supernatant}$ is the summed activity of the total washes; $Cu^{2+}{}_{associated}$ is the total number of moles of Cu ions attached to particles and $Cu^{2+}{}_{initial}$ is the initial number of moles of Cu ions added to the particles.

5.2.6 Radiolabelling of Bifunctional Chelators - Silica Nanospheres Conjugation

The conjugated Si NS (NOTA-Si NS, DOTA-Si NS or MeSar-Ph-Si NS) suspended in 100 µL of 0.1 M sodium acetate buffer (pH 6.5) were exposed to a known amount (1 nmol, 10 µL) of $^{64/nat}Cu^{2+}$ in the same buffer. The total volume of the mixture was adjusted with acetate buffer (pH 6.5) to 0.9 mL, vortexed and subsequently rotated on a MultiMix (360 °C continuous rotation) for 2 h at room temperature (23 °C). The mixtures were then centrifuged for 10 min at 10000 rpm and washed with acetate buffer (pH 6.5). After each wash, the supernatant was collected and transferred to a test tube for counting on the gamma counter. The washing step was repeated until no further release of radioactivity could be detected (up to 4 times). All reactions were conducted in triplicate and results are reported as an average of the triplicates. The percentage of radiolabelling efficiency and metal ions associated with the particle was calculated from the equations 1 & 2 in Section 5.2.5.

5.3 Results and Discussion

5.3.1 Optimisation of the Conjugation of SarAr-NH_2 to Carboxylate Functionalised Polystyrene Nanospheres

SarAr-NH_2 was conjugated to three different sizes of PS NS. The conjugationswere performed under mild conditions using EDC activating agent. The EDC activates the carboxylate group on the surface of the PS NS allowing the rapid formation of an amide bond with the aromatic amine of the SarAr-NH_2 chelator. The conjugation via this amine has been confirmed in the literature (Naoki Nakajima & Ikada, 1995; Vashist, 2012). Optimisation of the conjugation reaction was conducted by varying the concentration of the SarAr-NH_2 chelator exposed to a fixed amount of PS NS. In each case the resultant SarAr-conjugated NS were washed and resuspended in acetate buffer (pH 6.5) for radiolabelling

with $^{57/nat}Co^{2+}$ or $^{64/nat}Cu^{2+}$. The radiolabelling solutions contained known concentrations of the cold metal ions $^{nat}Co^{2+}$ or $^{nat}Cu^{2+}$, spiked with traces amounts of ^{57}Co and ^{64}Cu respectively. The gamma emission of the radioisotope present was used to determine the amount of isotope complexed and therefore the concentration of metal ions complexed to the SarAr-NH_2 conjugated particles. Uncomplexed metal ions were removed by washing and centrifugation. Each wash was checked using the γ-counter and when radioactivity was no longer detected in the wash, the final product activity was assessed. Each batch of conjugated NS were radiolabelled with both $^{57/nat}Co^{2+}$ and $^{64/nat}Cu^{2+}$ solutions. Figure 5.4 illustrates typical radiolabelling efficiency curves of a SarAr-NH_2 conjugated nanospheres of 680 nm diameter with both for $^{57/nat}Co^{2+}$ and $^{64/nat}Cu^{2+}$. The shapes of the curves are similar and demonstrate that the sites on the SarAr-NH_2 conjugated NS are saturated when exposed to ≥ 100 nmol of SarAr-NH_2. A plot of the number of moles of $^{57/nat}Co^{2+}$ and $^{64/nat}Cu^{2+}$ added vs the number of moles of SarAr-NH_2 conjugated to the NS is given in Figures 5.5 a & b. For the 365 nm and 840 nm diameter PS, the amount of moles of SarAr-NH_2 used for each conjugation was set at an excess of 250 nmoles to ensure saturation of all available carboxylate sites based on the Figure 5.4 for 680 nm size.

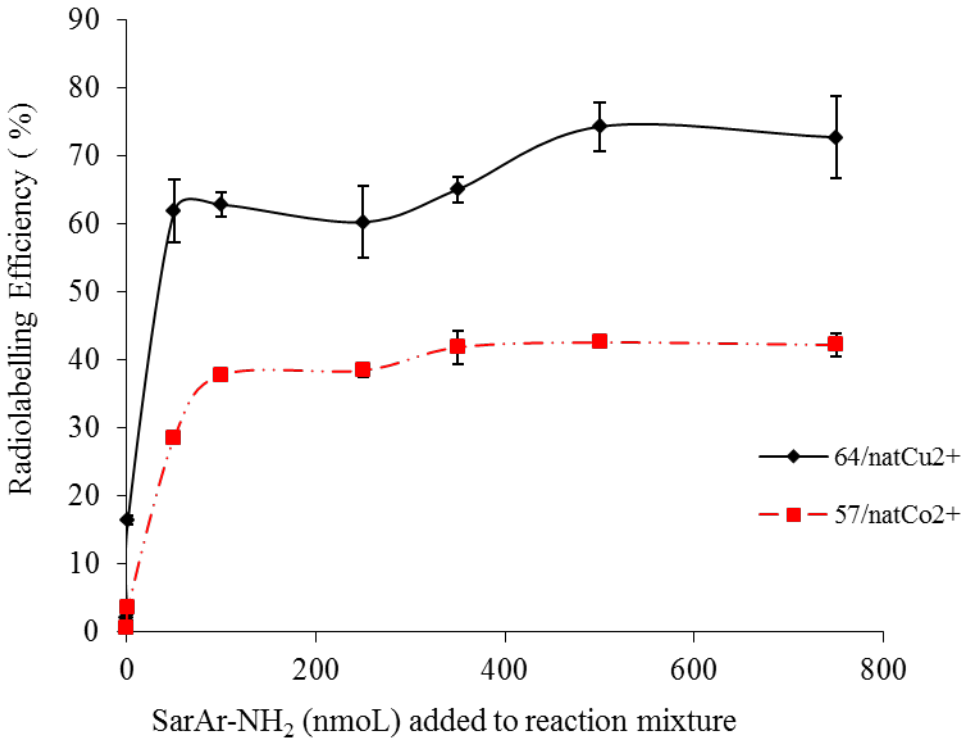

Figure 5.4 Effect of concentration of SarAr-NH_2 on radiolabelling efficiency of PS NS. Experimental conditions: PS NS size = 680 nm, $^{57/nat}Co^{2+}$ or $^{64/nat}Cu^{2+}$ = 1 nmol; radiolabelling pH 7 at room temperature (23 °C). (Mean ± SD, N = 3)

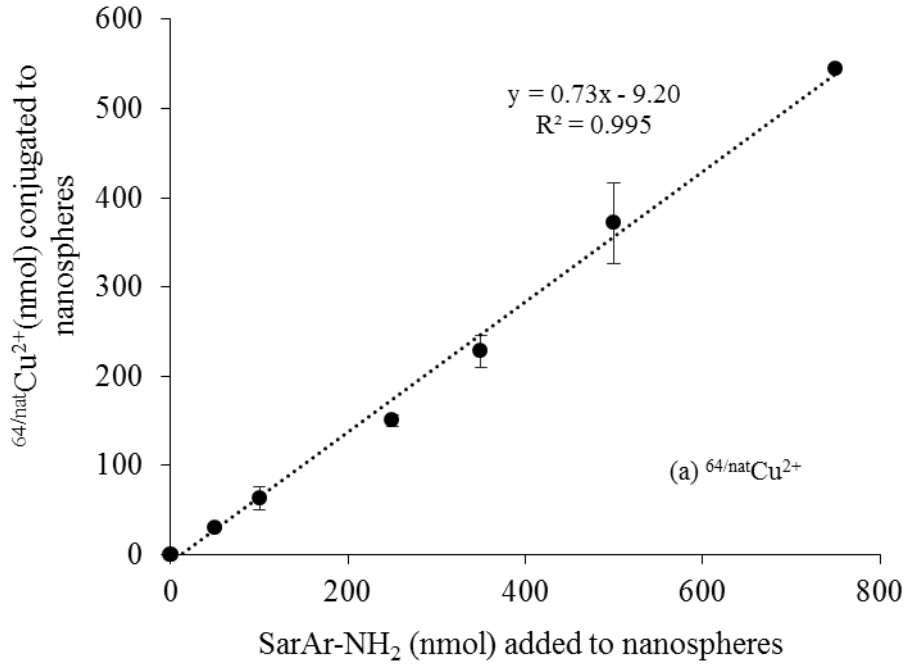

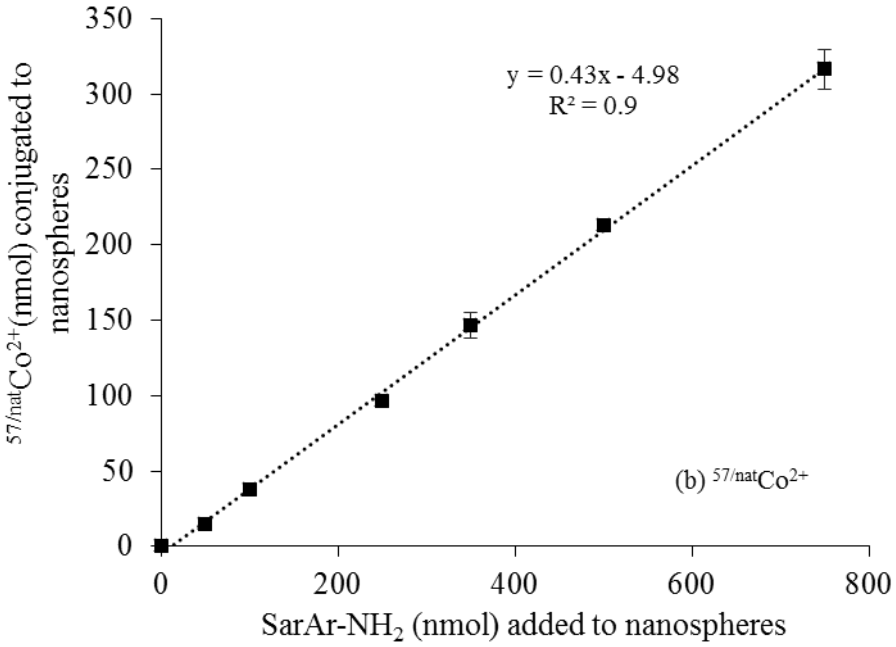

Figure 5.5 Comparison of radiolabelling efficiency of $^{64/nat}Cu^{2+}$ and $^{57/nat}Co^{2+}$ at 1 h and 2 h respectively with 2.0 mg of PS NS size = 680nm (a) The number of moles of $^{64/nat}Cu^{2+}$ conjugated to PS NS vs. the number of moles of SarAr-NH_2 used in the conjugation reaction with the NS. (b) The number of moles of $^{57/nat}Co^{2+}$ conjugated to PS NS vs. the number of moles of SarAr-NH_2 used in the conjugation reaction with the NS.

The radiolabelling conditions of the conjugated SarAr-PS NS with metal ions were optimised for reaction time, temperature and amounts of SarAr-NH_2. Figure 5.6 illustrates the effect of reaction time (up to 24 h) on radiolabelling $^{57/nat}Co^{2+}$ with SarAr-PS NS (680 nm size). In this study, the reaction time of 24 h was used for all three NS sizes because of the expected slower complexation kinetics of Co^{2+} with SarAr-NH_2 compared with Cu^{2+}. The reaction temperature of the radiolabelling was monitored at 23 °C. In general, it was found that the radiolabelling efficiency of $^{57/nat}Co^{2+}$ at 37 °C was 34 ± 9% SD (n=3; $p > 0.01$; NS) higher than that achieved at 23 °C (using a 1.25 h reaction time) for the full range of added $^{57/nat}Co^{2+}$ nmole amounts.

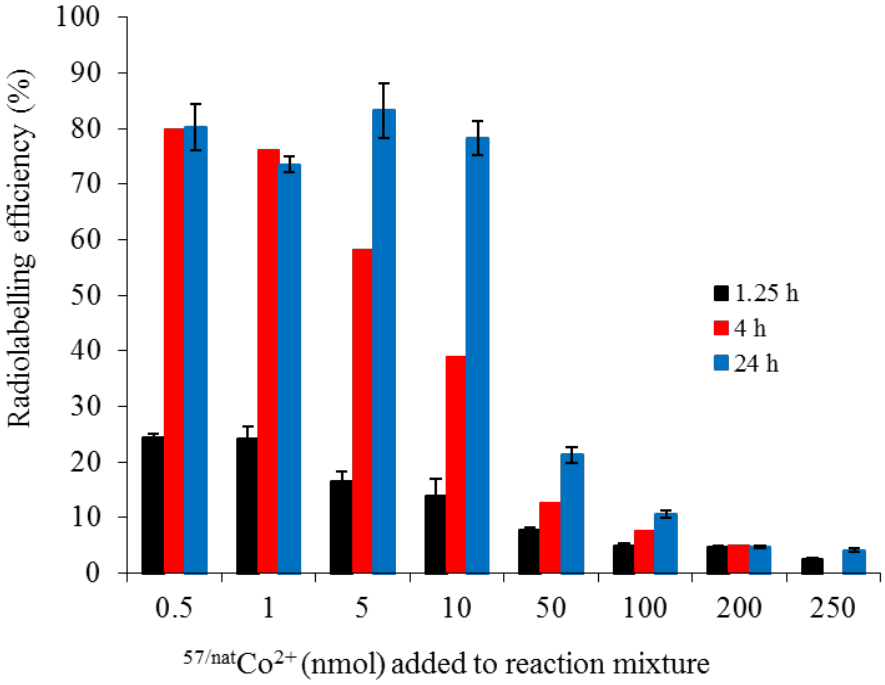

Figure 5.6 Effect of time on the radiolabelling efficiency of $^{57/nat}Co^{2+}$ with BFC-PS NS. Experimental conditions: SarAr-NH_2 = 250 nmol, PNS = 680 nm, size = 2mg radiolabelling pH 7 at room temperature (23 °C). (Mean ± SD, N = 3).

5.3.2 Determination of the Number of Active Sites per Nanosphere

Using the optimised conditions, the conjugation each nanosphere (i.e. 365 nm, 680 nm and 840 nm diameter) was achieved. The NSs were treated with an excess of SarAr-NH_2 (250 nmol per 2 mg) and an excess of EDC (2.5 mmol per 2 mg). The reactions were conducted in MES buffer (pH 5). The final product was then exposed to varying known concentrations of $^{57/nat}Co^{2+}$ in acetate buffer (pH 6.5) and incubated at 23 °C for 24 h. Figures 5.7 a, b & c compare the radiolabelling efficiency for each NS diameter, as well as the equivalent number of moles of Co^{2+} bound to the particles. The data clearly show that the amount of $^{57/nat}Co^{2+}$ ion required to saturate all available SarAr-NH_2 sites varied for each NS size. For example, for 365 nm, 680 nm and 840 nm sizes NS, all reach saturation at approximately 50 nmol of SarAr-NH_2. However, the total number

of Co^{2+} ions attached per NS was greater for NS of 680 nm diameter compared to NS of 840 nm diameter. This indicates that for 2.0 mg of 680 nm diameter NS, the number of available carboxylate sites present for conjugation of the SarAr-NH_2 was higher than the number of sites present on the 840 nm NS; this would normally indicate that the surface area of these NS is higher. Surprisingly the radiolabelling efficiency for 365 nm is similar to 840 nm size, at 0.1 nmol of Co^{2+}. Figure 5.8 illustrates the Co^{2+} associated per NS (nmol) with the amount of Co^{2+} added in each particle size. These data suggest that the activated surface area (i.e. the number of *available* carboxylate groups or conjugated chelators) did not increase as the particle size decreased, as was expected. These results may be due to subtle inconsistencies in the reaction conditions for the preparation of the three sizes of activated NS. Alternatively, the degree of carboxylate activation of NS may be directly dependent on NS size, though if so this relationship remains to be elucidated.

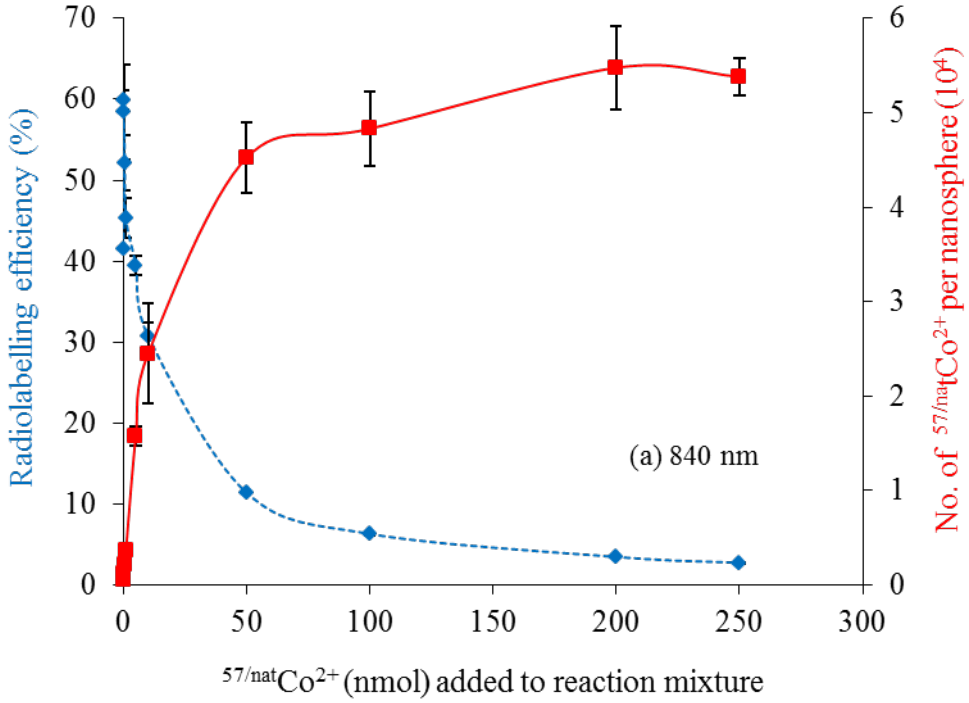

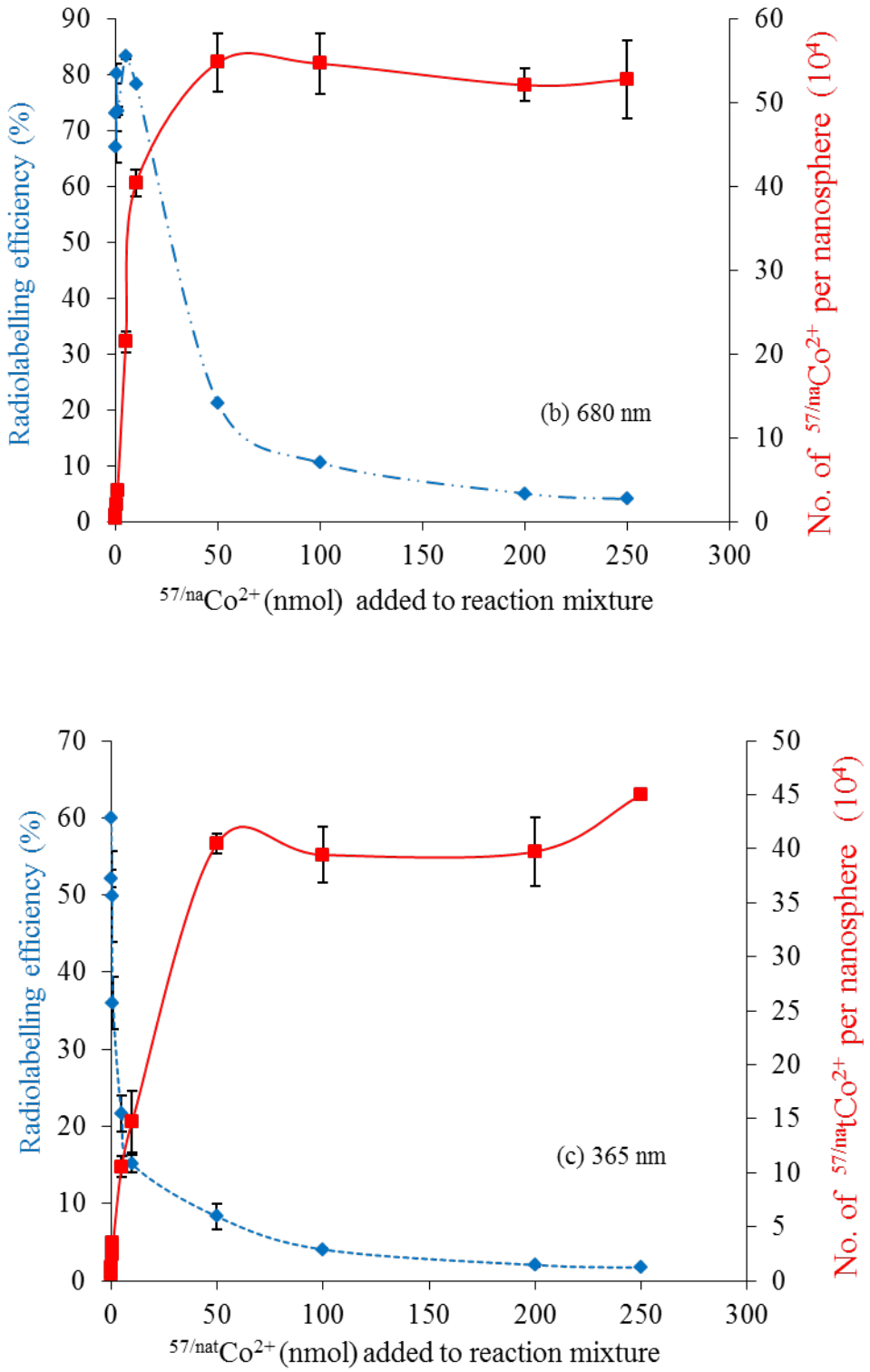

Figure 5.7 Radiolabelling efficiency and the number of $^{57/nat}Co^{2+}$ per NS for different amounts of $^{57/nat}Co^{2+}$ added to reaction mixture. Experimental conditions: Amount SarAr-NH_2 = 250 nmol, PS NS size (a) 365 nm (b) 680 nm (c) 840 nm, radiolabelling pH 7 at room temperature (23 °C). (Mean ± SD, N = 3).

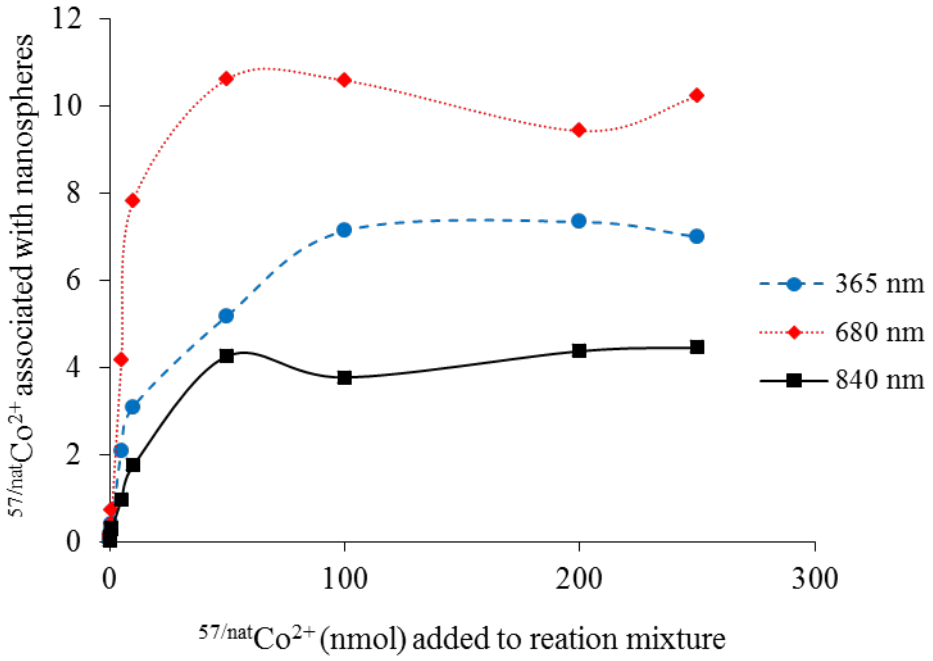

Figure 5.8 The amount (nmol) of $^{57/nat}Co^{2}$ exposed to SarAr-NH_2-NS. NS vs. actual number of nmoles of Co^{2+} specifically bound to each NS. Experimental conditions: Amount SarAr-NH_2 = 250 nmol, radiolabelling pH 7 at room temperature (23 °C). (Mean ± SD, N = 3).

5.3.3 ^{64}Cu-Radiolabelling of SarAr-NH_2 - Polystyrene Nanospheres Conjugation: Effect of Reaction Temperature

The 680 nm size SarAr-NH_2-PS NS were radiolabelled with ^{64}Cu, using the same radiolabelling procedure as used with $^{57/nat}Co^{2+}$. Two experiments were run in parallel at different reaction temperatures, with 250 nmol of SarAr-NH_2 conjugated to the surface of carboxylate-activated PS NS by EDC chemistry at pH 5 for 2 h at 23 °C. Several washes were applied to remove unreacted SarAr-NH_2 from the NS. The mixture was radiolabelled by treatment with a solution of Cu^{2+} doped with ^{64}Cu for 75 min at 23 °C and 37 °C. As the results demonstrate (Figure 5.9), no significant temperature-related differences in the $^{64/nat}Cu^{2+}$ radiolabelling efficiency could be detected. This confirms the relatively fast complexation of $^{64/nat}Cu^{2+}$ by SarAr-NH_2-PS NS at room temperature, proceeding to completion in the first few minutes of reaction.

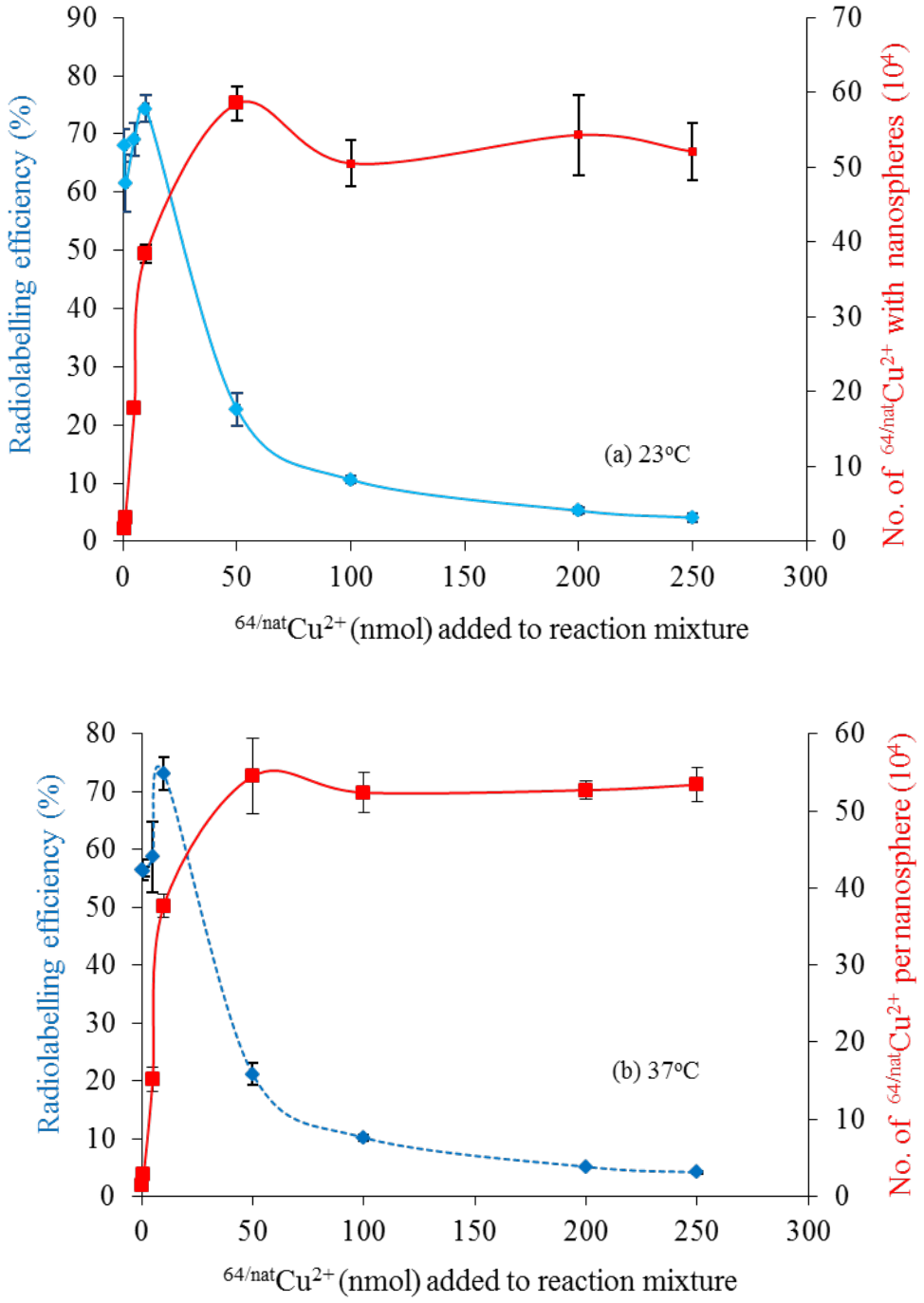

Figure 5.9 Effect of temperature on radiolabelling efficiency of Cu^{2+}. Experimental conditions: Amount SarAr-NH_2 = 250 nmol, PS NS size = 680 nm, radiolabelling pH 7 at (a) room temperature (23 °C) and (b) 37 °C. (Mean ± SD, N = 3).

The physical characteristics of the SarAr-NH_2 conjugated PS NS are summarised in Table 5.2. The average areas occupied by a SarAr-NH_2 molecule on the surfaces of 365 nm, 680 nm and 840 nm PS were 8.28, 2.61 and 5.56 nm^2, respectively. The highest number of conjugated SarAr-NH_2 was observed using the 680 nm diameter NS, which also demonstrated the highest radiolabelling efficiency. The number of SarAr-NH_2 groups attached to a typical 840 nm NS was considerably less than expected. This is most likely due to the different number of available binding sites and the different chemical components used to produce the particles.

Table 5.2 Physical Characteristics of SarAr-NH_2 conjugated PS NS.

TEM-measured diameter (nm) of NS		365	680	840
Theoretical	Number of NS in 2 mg of solution (10^{10})[a]	7.48	1.16	0.61
	Surface area per NS (nm^2) (10^5)	4.19	14.5	22.2
Experimental[b]	Co^{2+} (nmol) saturated	6.28	10.68	4.06
Calculated	SarAr-NH_2 attached to NS at saturation (10^{15})	3.78	6.43	2.44
	SarAr-NH_2 attached per NS (10^5)	0.50	5.56	3.98
	Area occupied by one SarAr-NH_2 (nm^2) on surface of NS	8.28	2.61	5.56

[a]Density of these particles is assumed to be ~1.05 g/cm^3. [b] Data taken from Figure 5.8.

5.3.4 Optimisation of the Conjugation of Different Bifunctional Chelators to Silica Nanospheres

The conjugation of BFC-NCS with Si NS (200 nm) were optimised using the two chelators MeSar-Ph-NCS and NOTA-NCS. The *p*-isothiocyanato benzyl derivative of each chelator was reacted with the amine group on the surface of the Si NS to form an isothiourea bond (see Figure 5.1 b). The conjugation via this amine group has been described in the literature (Kong et al., 2013). Optimisation of these conjugation reactions was conducted by varying the concentration of the chelator exposed to a fixed amount of Si NS. In each case the resultant chelator-conjugated nanosphere was washed and resuspended in 0.1 M acetate buffer (pH 6.5) for radiolabelling with $^{64/nat}Cu^{2+}$. The radiolabelling solutions contained known concentrations of cold Cu^{2+} ion spiked with ^{64}Cu. The gamma emission for the radioisotope present was used to determine the amount of isotope complexed and therefore the concentration of metal ions complexed to the chelator conjugated NS. Each wash was checked for radioactivity until no activity was present in the supernatant. Each batch of conjugated NS was radiolabelled with $^{64/nat}Cu^{2+}$ solution. Figure 5.10 illustrates typical radiolabelling efficiency curves for $^{64/nat}Cu^{2+}$ of the NOTA-NCS and MeSar-Ph-NCS conjugated to 200 nm diameter Si NS. Figure 5.10 (a) shows that the sites on the MeSar-Ph-NCS-conjugated Si NS are saturated when ≥ 125 nmol of MeSar-Ph-NCS reactant was added. In the case of NOTA-NCS, Figure 5.10 (b) shows the NOTA-conjugated NS were saturated when the amount of BFC reacted exceeded 500 nmol. Similar results were found with DOTA-NCS (not shown). Therefore, the conjugation reaction of 100 nm diameter Si NS with MeSar-Ph-NCS, NOTA-NCS and DOTA-NCS were set at an excess of 125, 500 and 500 of BFC, respectively, to ensure all available amine sites were reacted.

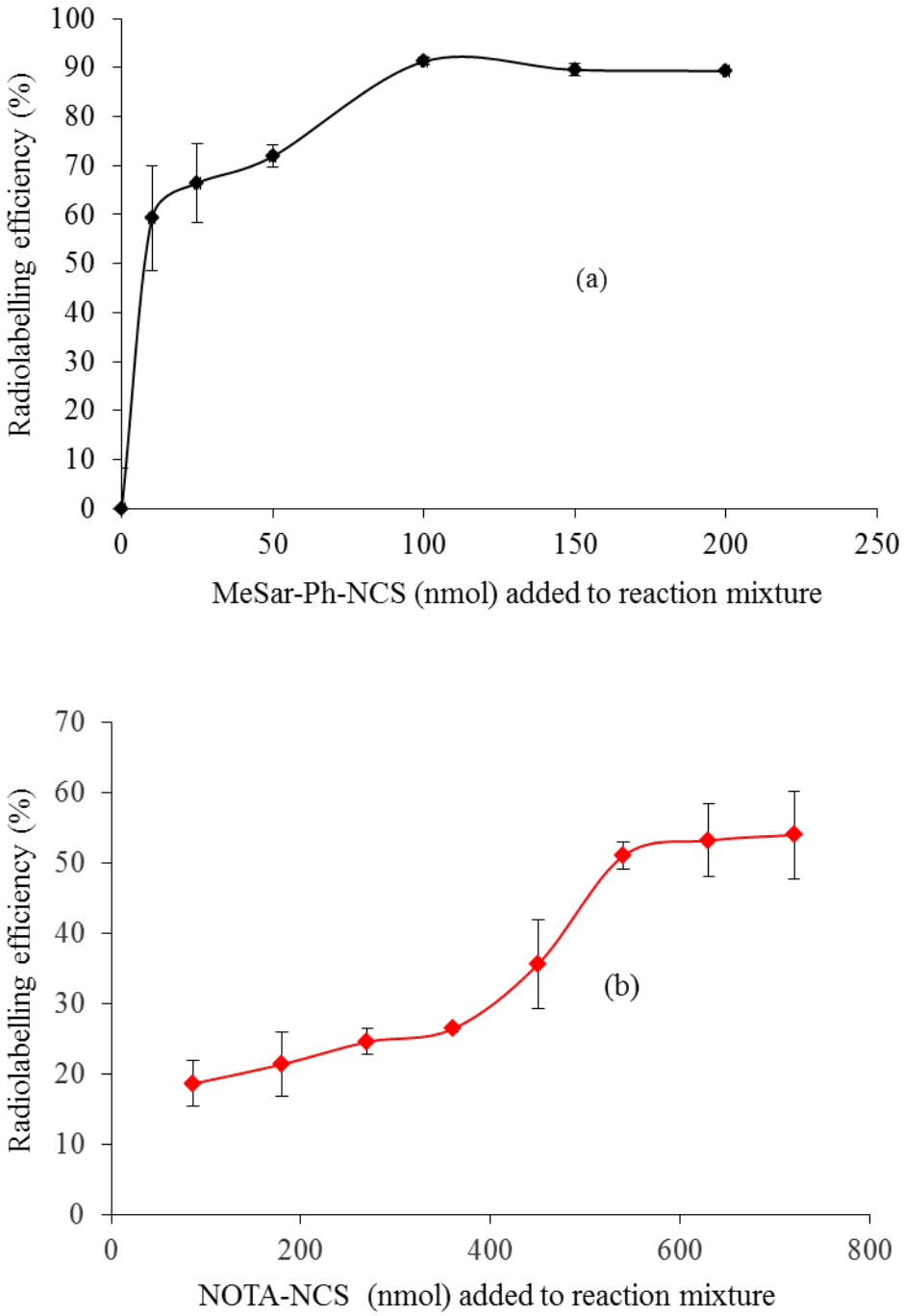

Figure 5.10 Radiolabelling efficiency vs. varying concentrations of (a) MeSar-Ph-NCS and (b) NOTA-NCS added to the reaction mixture. Experimental conditions: silica nanospheres size = 200 nm, Amount $^{64/nat}Cu^{2+}$ = 1 nmol, radiolabelling pH 7 at room temperature (23 °C).

5.3.5 ^{64}Cu-Radiolabelling of DOTA-NCS-, NOTA-NCS- and MeSar-Ph-NCS-Conjugated Silica Nanospheres

5.3.5.1 ^{64}Cu-DOTA-NCS-Silica Nanospheres

The conjugation of DOTA-NCS to amino-functionalised Si NS was performed by adding 500 nmol of DOTA-NCS to 2.5 mg of 100 nm size Si NS. The unconjugated DOTA-NCS was removed by washing the NS 3 times with 0.1 M PBS buffer (pH 8). The isolated DOTA-NCS conjugated NS were then exposed to varying amounts of $^{64/nat}Cu^{2+}$, including high excess for up to 2 h at 23 °C. The radiolabelled NS were washed with 0.1 M sodium acetate buffer (pH 6.5) to remove non-specifically bound $^{64/nat}Cu^{2+}$. Figure 5.11 illustrates the radiolabelling efficiency of $^{64/nat}Cu^{2+}$ with DOTA-NCS-conjugated Si NS of 100 nm diameter.

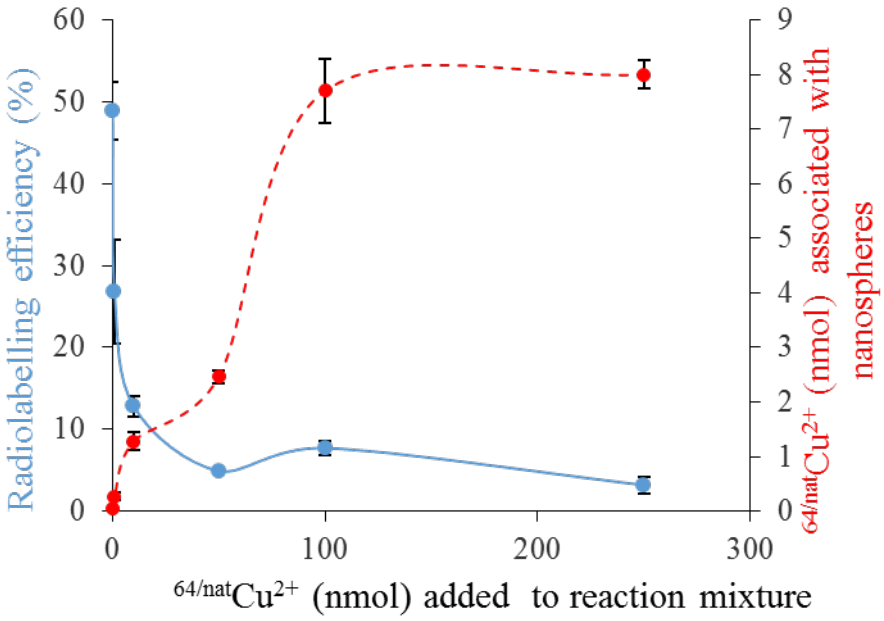

Figure 5.11 Radiolabelling efficiency of $^{64/nat}Cu^{2+}$- DOTA-NCS-Si NS and $^{64/nat}Cu^{2+}$ associated with NS (nmol). Experimental conditions; Amount DOTA-NCS = 500 nmol; Si NS size 100 nm (mean ± SD, N = 3).

5.3.5.2 ^{64}Cu-NOTA-NCS-Silica Nanospheres

The conjugation and radiolabelling of Si NS (at 23 °C) with NOTA-NCS was conducted under similar procedures as described for DOTA-NCS. The data are illustrated in Figure 5.12 and show clearly that the radiolabelling efficiency for NOTA-NCS-Si NS (80%) is significantly higher than that for DOTA-NCS-Si NS (49%) using the same conditions for conjugation and radiolabelling.

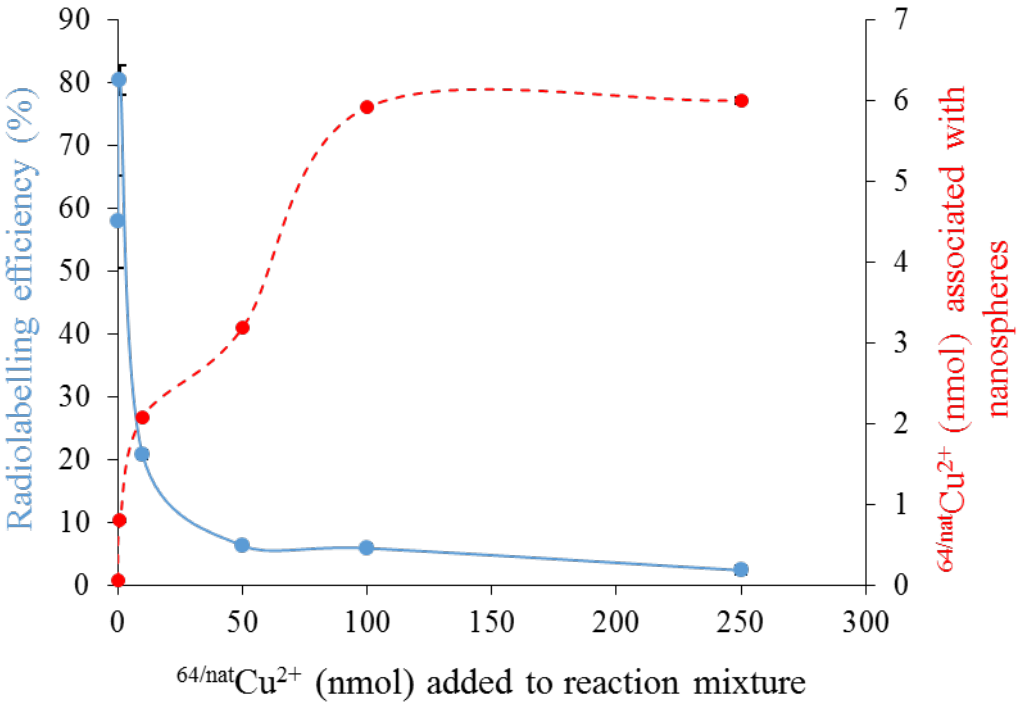

Figure 5.12 Radiolabelling efficiency of $^{64/nat}Cu^{2+}$- NOTA-NCS-Si NS and $^{64/nat}Cu^{2+}$ associated with NS (nmol). Experimental conditions; Amount NOTA-NCS = 500 nmol; Si NS size 100 nm (mean ± SD, N = 3).

5.3.5.3 ^{64}Cu-MeSar-Ph-NCS-Silica Nanospheres

Due to the limited supply of MeSar-Ph-NCS ligand, only 100 nm NS were conjugated and then radiolabelled with $^{64/nat}Cu^{2+}$. The conjugation of MeSar-Ph-NCS to Si NS follows a slightly different procedure than that described for NOTA-NCS and DOTA-NCS. An extra step was necessary for the removal of

the Mg^{2+} stabiliser from the sarcophagine, before radiolabelling with $^{64/nat}Cu^{2+}$. PBS buffer (pH 8) was used to conjugate Si NS with MeSar-Ph-NCS for 2 h at (23 °C). This was followed by a washing procedure and a centrifugation step (15 min at 5000 rpm). After the last wash, in order to extract Mg^{2+} from the chelator it was necessary to drop the pH to 6 by addition of sodium acetate buffer (pH 6). The samples were left to incubate (23 °C, 1 h) to allow time for the acetate-mediated extraction of the Mg^{2+} before a final centrifugation. The supernatant buffer (containing the extracted Mg^{2+}) was then replaced with 0.1 M sodium acetate (pH 6.5) in preparation for radiolabelling. Figure 5.13 illustrates the radiolabelling efficiency of MeSar-Ph-NCS-conjugated Si NS using the conditions 23 °C for 60 min.

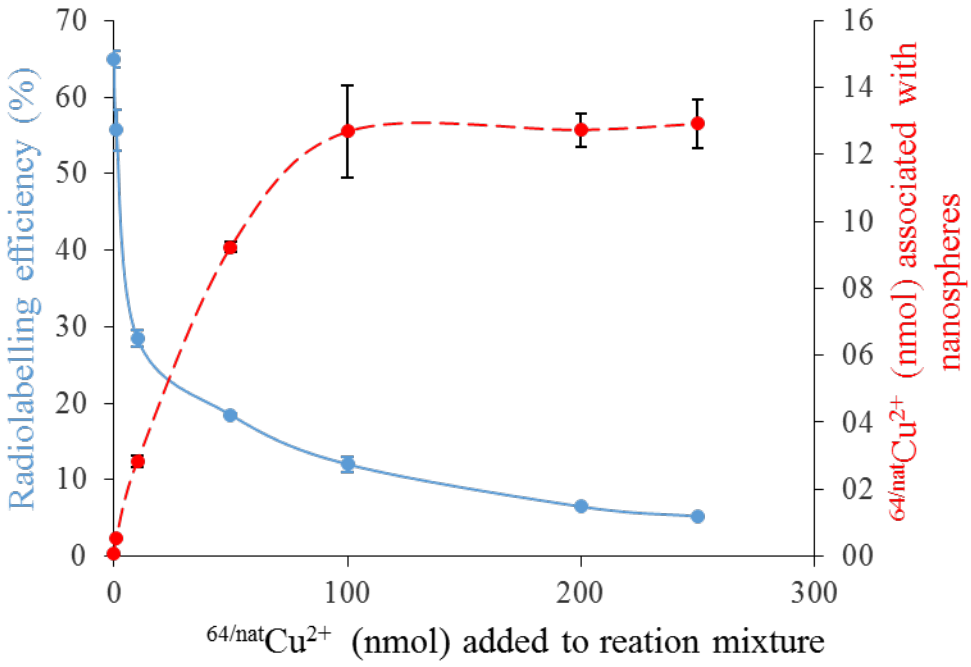

Figure 5.13 Radiolabelling efficiency of $^{64/nat}Cu^{2+}$- MeSar-Ph-NCS-Si NS and $^{64/nat}Cu^{2+}$ associated with NS (nmol). Experimental conditions: Amount MeSar-Ph-NCS = 125 nmol; Si NS size 100 nm (mean ± SD, N = 3).

Table 5.3 summarises the estimated number of each BFC on the surface of each conjugated nanosphere. The measured number of available conjugated BFCs on the Si NS were in the following order MeSar-Ph-NCS (2080) > NOTA-NCS

(1260) > DOTA-NCS (980). One Cu-MeSar-Ph-NCS complex was calculated to occupy 15.09 nm^2 on the nanosphere surface area. The estimated areas occupied for the Cu-DOTA-NCS and Cu-NOTA-NCS on the same size nanosphere were larger, at 31.93 and 24.88 nm^2, respectively.

Table 5.3 Number of available BFCs conjugated to the surface of a 100 nm diameter Si NS.

	Chelator		
	MeSar-Ph-NCS	DOTA-NCS	NOTA-NCS
Measured No. chelators attached to 2.5 mg of NS at saturation ($\times 10^{15}$)	7.65	4.64	3.61
Measured No. chelators attached per NS ($\times 10^{3}$)	2.08	0.98	1.26
Calculated area occupied by one chelator (nm^2) on the surface of NS	15.09	31.93	24.88

Density of Si NS taken as ~1.30 g/cm^3

5.4 Conclusions

Two types of functionalised NS (Si-amino and PS-carboxylate) were conjugated with selected BFCs (i.e. SarAr-NH_2, MeSar-Ph-NCS, NOTA-NCS and DOTA-NCS). A significant difference in the conjugation efficiency of the BFCs to the PS NS and the Si NS appears to be reflective of both the availability of the function groups (e.g. amino or carboxylate) present on the NS surface and the specific chelator's ability to complex the Cu^{2+} and Co^{2+} metal ions. Temperature, concentration of reactant, and incubation time each needed to be carefully controlled to optimise $^{57/nat}Co^{2+}$ labelling for all BFCs. $^{64/nat}Cu^{2+}$ radiolabelling of BFCs conjugated to the NS proved less sensitive to temperature.

The SarAr-NH_2 BFC was conjugated to a range of PS NS and the data show that NS size was not the dominant factor in labelling efficiency. The data suggest that the chemical conditions used to produce each PS NS may have varied and therefore, the available carboxylate groups (per unit area) for SarAr-NH_2 to attach was not consistent across all NS sizes.

A comparison of the efficiency of radiolabelling Si NS using MeSar-Ph-NCS, NOTA-NCS and DOTA-NCS showed that MeSar-Ph-NCS had the most radioactivity attached per NS. It was not possible to determine if the same number of BFCs (i.e. MeSar-Ph-NCS, NOTA-NCS and DOTA-NCS) were attached to each NS, or if the metal complexes formed were so highly charged that the neighbouring chelators could not accommodate further metal ions. However, the data clearly show the highest specific activity product (i.e. radiolabelled Si NS) could be achieved with the MeSar-Ph-NCS.

It is of interest to establish if the charges (due to conjugated chelators) on the final product (radiolabelled NS) affect the biodistribution of these labelled NS in

animal models. The following chapter (Chapter 6) will explore the effect of bifunctional chelators on the biodistribution of Si NS in animal models.

CHAPTER SIX

IN VIVO BIODISTRIBUTIONS OF COPPER-61 LABELLED NANOSPHERES USING DIFFERENT BIFUNCTIONAL CHELATORS

6.1 Introduction

Nanomaterials such as gold and iron oxide particles, quantum dots and carbon nanotubes have been used as carriers for the delivery of therapeutic and diagnostic agents (Pengo & Pasquato, 2015; Sundaresan et al., 2014; Liu et al., 2016; Razzazan, Atyabi, Kazemi, & Dinarvand, 2015). In recent times, a wide range of nanospheres/nanoparticles have been shown to significantly increase the residence time of their conjugated chemotherapeutic agents at target sites, while reducing the side effects of the applied chemotherapy. There are even reports of liposomes, polymer and lipid nanoparticles having the ability to overcome drug resistance (Pillai, 2014). Prolonged on-target residence time and a desired drug-release pattern have been achieved by controlling the size and architecture of nanoparticles.

Silica nanoparticles/nanospheres (Si NPs/NS) have been widely used in medical applications such as diagnostics (Arap et al., 2013; Wang, Yang, Tan, 2005) drug delivery (Slowing, Trewyn, Giri., & Lin, 2007 ; Xie et al., 2016; Lu, Liong, Zink, & Tamanoi, 2007) to control drug release (Trewyn, Giri, Slowing, & Lin, 2007; Wang et al., 2015), gene transfection (Lin, Zhao, Yan, Hu, Xu, 2015; Slowing et al., 2008) and multimodal imaging (Liberman et al., 2014). These types of particles can be synthesized using the Stöber method for the size range (50 - 1000 nm) (Stöber et al., 1968) or the micromulsion method for the particle size ≤50 nm (Osseo-Asare & Arriagada, 1990). Furthermore, Si NPs have been used in theranostics (Ryu et al., 2014) and in vitro (Tamba et al., 2015).

The size of the particles is an important factor for nanomedicine applications. The human body has several filters controlling the size of the drug delivery to the specific target. For example, small particles with size up to 5-6 nm are excreted by the kidneys (Choi et al., 2007), while the spleen filters any particles larger than 200 nm from the blood circulation (Moghimi, 1995). In addition to the size of the particles, the shape and surface are also important factors and can be controlled. For example, colloidal Si NPs have a negative charge which causes their aggregation in biological fluids (Vanblaaderen, Vangeest, & Vrij, 1992). This property is explained by the fact that the Si NPs are coated to serum proteins (opsonins) that activate the capture by the reticuloendothelial system (RES) once they are injected in the blood stream. They are then removed by circulation (Moghimi, Hunter, & Murray, 2001; Gref et al., 1995) and accumulated in the lungs and capillary vessels (Borchardt, Brandriss, Kreuter, & Margel, 1994). There are two ways to avoid the aggregation of the Si NPs and to increase their biocompatibility. The first method is to attach short functional groups to the Si surface such as free amino, carboxyl, carboxylate, thiol or phosphonate groups. This method however does not always protect against aggregation since the short functional groups are easily attached to serum proteins. In the second method, the surface of the Si NP is conjugated with large molecules (e.g. PEG) resulting in an increase in the blood circulation half-life of the particles by several orders of magnitude (Ownes & Peppas, 2006). The properties of PEG provide high stability of nanoparticles in biological fluids (Gref et al., 1994).

Various particles have been labelled with SPECT and PET radioisotopes for mapping their clearance and uptake paths, sometimes (in a 'theranostic' role) prior to the delivery of radiotherapeutic doses to kill cancer cells (Liu & Welch, 2012; Dearling et al., 2011; Rogers et al., 2004; Kong et al., 2013). Passive targeting of tumour tissues by nanoparticles loaded with therapeutic agents is a size-dependent process. It is also influenced by the pathophysiological characteristics of the tumour vessels, such as a leaky vasculature and poor lymphatic drainage. The Enhanced Permeation and Retention (EPR) effect is the

term used to describe the extravasation of nanoparticles into the tumour tissue and their retention there.

The schematic of NS functionalised with amino groups (1) is shown figure 6.1. After a bifunctional chelator (BFC) is conjugated to (1), the resultant complex (2) is added to the radiosotope for radiolabelling (3). The radiolabelled NS is ready for *in vivo* administration (4). However, once *in vivo,* the disintegration of this complex, leaving the NS separated from its isotopically-labelled BFC is possible. This depends on the stability of the BFC link to the functionalised NS (5). 'Dechelation' of the isotope from the BFC is also possible. This may conceivably happen at any time after the injection, and depends on the thermodynamic and (particularly) kinetic stabilities of the chelation mechanism.

In chapter four of this thesis we described a more efficient route for the production of ^{61}Cu from a ^{nat}Zn or an enriched ^{64}Zn target. Copper-61 has physical properties ($t_{1/2}$ = 3.33 h; β^+_{max} = 1.22 MeV; β^+ = 60%, EC = 40%) suggesting PET imaging applications where the biological mechanism under study has a characteristic lifetime of a few hours. The capacity to produce ^{61}Cu using small biomedical cyclotrons (Asad et al., 2015) at high radionuclidic purity (> 99%) makes it an attractive option for potential clinical use. Chapter five described the investigation of radiolabelling of silica nanospheres (Si NS) using three bifunctional chelators (BFC) i.e. diamsar, NOTA-NCS and DOTA-NCS. This chapter investigates aspects of the pharmacokinetics of ^{61}Cu-labelled Si NS in immunodeficient inbred mice using the tools of PET imaging and post-mortem radioactivity biodistribution analysis. Three bifunctional chelators, NOTA-NCS and DOTA-NCS and the novel sarcophagine 'MeSar-Ph-NCS' were used to radiolabel amino-functionalised Si NS (see Figure 6.2). The molecule MeSar-Ph-NCS (representing $[Mg(CH_3)(p\text{-NCS-Ph})Sar](CF_3SO_3)_2$ was developed recently by collaborators of our laboratory (Paterson et al., 2014).

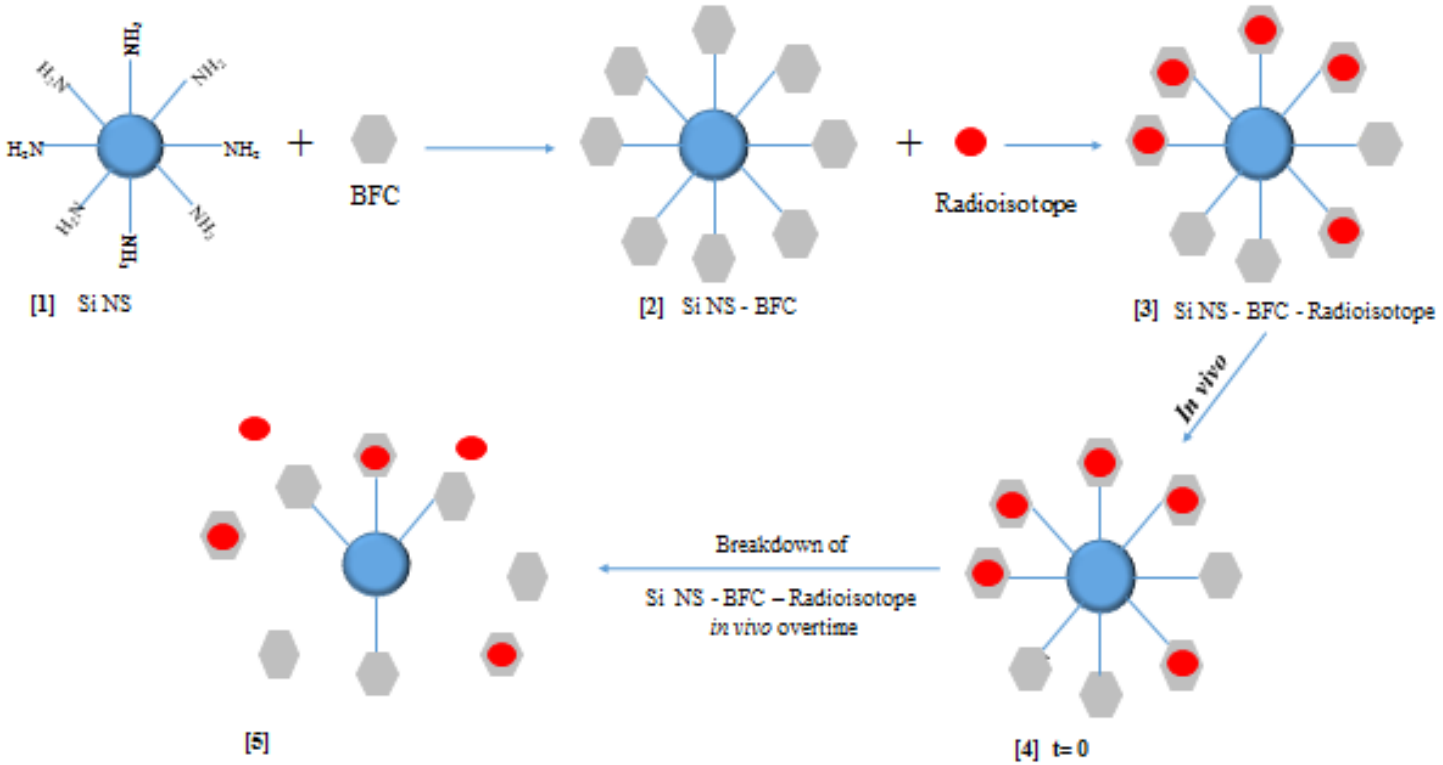

Figure 6.1 Schematic for the conjugation of BFC to NS and subsequent radiolabelling with radioisotope [1 to 3] – Breakdown *in vivo* following injection [4 to 5].

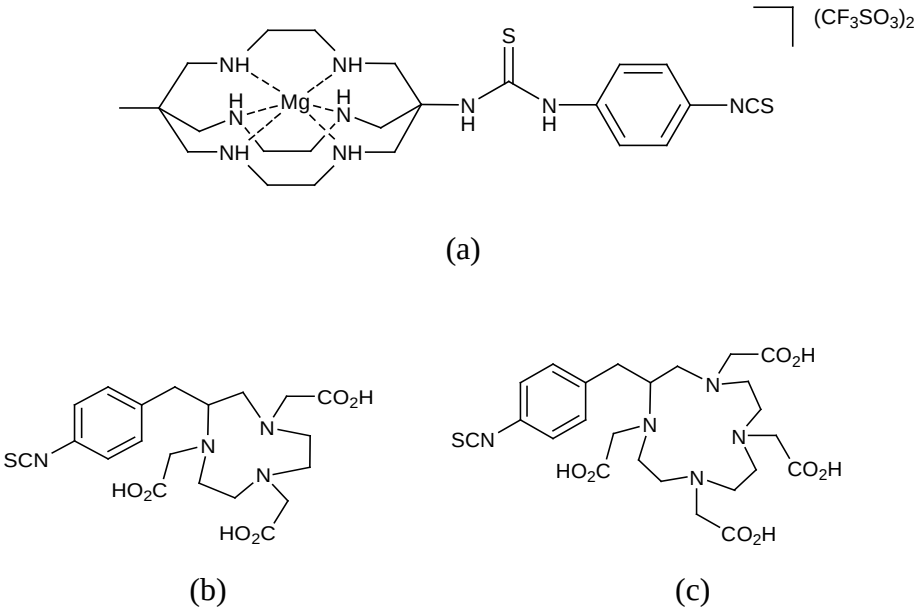

Figure 6.2 Bifunctional Cu^{2+} chelators used in this study (a) MeSar-Ph-NCS, (b) NOTA-NCS and (c) DOTA-NCS. In MeSar-Ph-NCS, the metal protector magnesium ion is extruded from the molecule following conjugation to the NS and prior to radiolabelling.

6.2 Materials and Methods

6.2.1 Production of No-Carrier-Added ^{61}Cu

Copper-61 isotope was prepared using a proton beam from an IBA 18/18 MeV cyclotron by the $^{64}Zn(p,\alpha)^{61}Cu$ nuclear reaction, using an enriched ^{64}Zn target (though a ^{nat}Zn target would have been possible). No-carrier-added (NCA) ^{61}Cu as the chloride was produced and isolated under optimised conditions by the method described previously in Chapter four (Asad et al., 2015). Briefly, the irradiated enriched ^{64}Zn target material was dissolved in 1 mL of 8 M HCl at 150^{o}C and evaporated to dryness. The residue was dissolved in high purity TraceSELECT water (1 mL), evaporated to dryness twice and dissolved in 2 mL of 0.1 M HCl. The solution was loaded onto a Cu-resin column (pre-conditioned with 20 mL of 0.01 M HCl). The Zn and Ga were eluted with 25 mL of 0.01 M

HCl (and kept for recovery of ^{64}Zn if required). The ^{61}Cu trapped on the Cu-resin column was then eluted off with 1.5 - 2 mL of 8 M HCl, followed by drying steps (addition of 1mL of TraceSELECT water and evaporation to dryness three times). The final product was then dissolved in 400-800 µL of 0.01 M HCl. The average recovery efficiency of NCA ^{61}Cu from the irradiated target was 95%. The radionuclide purity was consistently > 99%. The specific activity assessed by the titration method was approximately $1.2x10^6$ GBq/g of copper.

6.2.2 Preparation of ^{61}Cu Labelled Bifunctional Chelator-Silica Nanospheres

In separate experiments, three BFCs (MeSar-Ph-NCS, NOTA-NCS and DOTA-NCS) were used to radiolabel Si NS of nominal diameter 100 nm, as described in Chapter five, except that in this study a different Sar molecule (MeSar-Ph-NCS) was used. Briefly, 5 mM chelator solutions were prepared by dissolution in 0.1 M sodium phosphate buffer (PBS), pH 8. To 100 µL of a chelator solution, Si NS (100 µL, 2.5 mg) were added and the final volume adjusted to 900 µL with the same buffer. The conjugated Si NS were radiolabelled as described in Chapter five; ^{61}Cu-chloride (10 µL in 0.01 M HCl, 50-60 MBq) was added to each suspension of the conjugated NS and left to incubate for 2 h at 37^{o}C. Finally, the radiolabelled NS were then washed with 0.1 M sodium acetate buffer (NaOAc) pH 7 to remove any free ^{61}Cu and then resuspended in the same buffer for injection in animals.

6.2.3 Surface Charge of Silica Nanospheres

The zeta potential was determined using zetasizer version 7.11 (Malvern Instruments Ltd., U.K.). Measurements were performed at 25^{o}C and pH 7. All samples were diluted in PBS buffer and injected into the flow cell chamber.

6.2.4 *In Vitro* Stability of Radiotracers

In vitro stability of the ^{61}Cu-BFC-NCS-Si NS, for each BFC was studied in triplicate experiments (n = 3) in normal saline at room temperature and also separately in foetal bovine serum (FBS) (Sigma-Aldrich, Australia). To 500 μL of ^{61}Cu-labelled conjugated Si NS in 0.1 M sodium acetate buffer pH 7 (~3 MBq) was added 100 μL of saline or FBS. The solution was then incubated at 37 °C. At specific time intervals, the ^{61}Cu labelled conjugated BFC-NCS-Si NS were centrifuged at 5000 rpm for 5 min, the supernatant carefully removed by pipette and the pellets formed were counted on a gamma counter (600 μL for each sample). New saline or FBS was added to the pellets and they were then returned to the reaction mixture. *In vitro* results suggest good stability in saline and FBS at 1 and 4 h. However, *in vivo* stability has not been assessed.

6.2.5 Animal Groups for *In Vivo* Activity Biodistribution Study

All animal studies were performed in compliance with the requirements of the Harry Perkins Institute of Medical Research Animal Studies Committee and in accordance with the Australian Code of Pratise for the Care and Use of Animals for Scientific Purposes, 8th Edn. In this study, healthy female nude mice (Balb/c nu/nu) were used to study the biodistribution of each organ. The mice were divided into 4 groups of three animals each, as follows:

Group 1 were controls for this study, receiving ^{61}Cu as the chloride, only.
Group 2 received ^{61}Cu-MeSar-Ph-NCS-Si NS.
Group 3 received ^{61}Cu-NOTA-NCS-Si NS.
Group 4 received ^{61}Cu-DOTA-NCS-Si NS.
Figure 6.3 illustrates the injection and biodistribution sampling protocol.

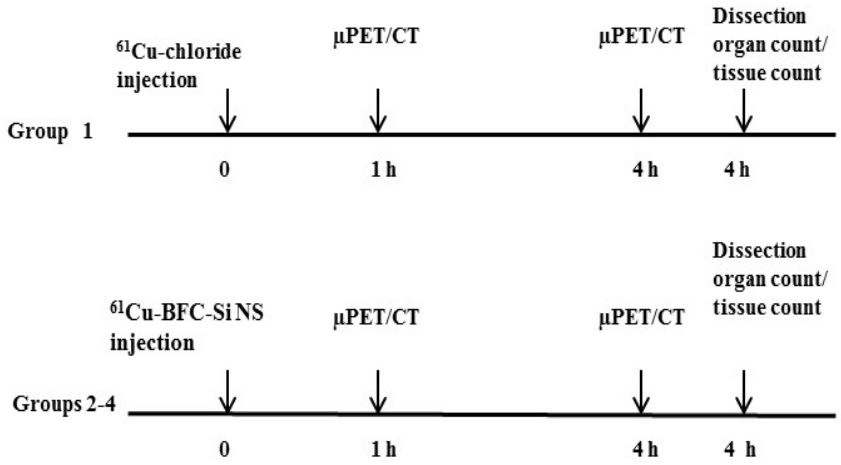

Figure 6.3 Time points for injection of Balb/c (nu/nu) mice, imaging using µPET/CT and (finally) dissection and γ-counting following sacrifice; in the control group and in groups injected with Si NS ^{61}Cu-radiolabelled using different bifunctional chelators (BFCs). Group 1 were controls injected with ^{61}Cu as the chloride. Groups 2-4 were administered with ^{61}Cu-MeSar-Ph-NCS-Si NS, ^{61}Cu-NOTA-NCS-Si NS and ^{61}Cu-DOTA-NCS-Si NS, respectively.

6.2.6 *In Vivo* Activity Biodistribution Data by µPET Imaging

In all groups, healthy mice weighing 12.5-20.4 g were anesthetized with 1-2% isoflurane and injected via the retro-orbital route with 5.4 ± 0.5 (SD) MBq of ^{61}Cu chloride or ^{61}Cu-BFC-Si NS (0.25 mg of Si NS) in 100-120 µL of a 0.1 M NaOAc (pH 6.5) solution in saline. Imaging was performed using a Super Argus µPET/CT (Sedecal, Madrid, Spain). Images were reconstructed using an ordered-subset expectation maximization (OSEM, 2D) algorithm. At 1 h and 4 h the mice were re-anesthetized and then scanned for 15 min for a PET acquisition (two bed positions) followed by 10 min to acquire a co-registered CT image. The regions of interest (ROIs) were quantified by identifying margins in three dimensions in the selected tissues and averaging the activity concentration over the summed voxels. ROI analysis was performed using Vivo Quant 2.0 software (Invicro, Boston, USA).

6.2.7 Dissection Activity Biodistribution Studies

In each group, mice were sacrificed immediately after the last μPET/CT scan (4 h time point). Blood, organs and tissues of interest were removed, weighed and their radioactivity counted in a γ-counter calibrated for photopeak energy and energy-dependent detector sensitivity (PerkinElmer, Illinois, USA). The total activities in blood, bone and muscle were calculated assuming that these tissues represented an average of 6%, 11%, 41% of the mouse weight, respectively (Sun et al., 2005). All the data were corrected for physical decay. Uptake in each tissue sample was calculated as a fraction of the injected dose. The results were expressed as a percentage of injected dose per gram of tissue (%ID/g).

6.3 Results

6.3.1 Zeta Potential

The zeta potentials of the Si NS were measured in PBS buffer at pH 7 and the results are shown below (Table 6.1). The amino functionalised nanospheres are positively charged (23.4 mV). The zeta potentials of the NS after conjugation with the BFCs were lower, ranging between 2.2-11.3 mV and increased after Cu^{2+} labelling (5.3-20.3 mV).

Table 6.1 Zeta potential of surface of Si NS in PBS solution

Nanospheres	Zeta potential in 0.1 mM PBS (mV)
Si NS	23.4
Si NS-NOTA-NCS	2.2
Si NS-DOTA-NCS	4.1
Si NS-MeSar-NCS	11.3
Si NS-NOTA-NCS- Cu^{2+}	5.3
Si NS-DOTA-NCS- Cu^{2+}	10.2
Si NS-MeSar-NCS- Cu^{2+}	20.3

6.3.2 *In Vitro* Stability of Labelled Bifunctional Chelator-Silica Nanospheres

After 1 and 4 h the ^{61}Cu-radiolabelled BFC-NCS-Si NS were all found to be stable in saline (> 93%). However, incubation of the ^{61}Cu labelled BFC-NCS-Si NS in FBS at 37 °C all showed significant increase of 'free' ^{61}Cu at 4 h (between 11% and 16%) as shown in Table 6.2.

Table 6.2 Degree of stability of constructs at two time points.

Si NS-BFC-^{61}Cu	saline			FBS	
	1 h	4 h		1 h	4 h
Si NS DOTA-NCS-^{61}Cu	98%	97%		95%	84%
Si NS-NOTA-NCS-^{61}Cu	98%	93%		94%	89%
Si NS-MeSar-Ph-NCS-^{61}Cu	97%	95%		97%	86%

6.3.3 Dissection-Derived Normalised Activity Biodistributions

***Group1*; Control mice (n = 3)**

The biodistribution of 'free' ^{61}Cu (injected as the chloride), derived by dissection and γ-counting at 4 h post-injection (see protocol in Figure 6.3) is shown in Figure 6.4. Data for selected organs is shown in Table 6.3. These represented controls for this study. Weight-normalised activities in major organs and tissues are expressed as percent of injected dose per gram of issue (%ID/g). At 4 h post-injection ^{61}Cu activity was found mainly in the liver (including gallbladder, since these were not separated at dissection) and kidneys, with levels of 26.6 ± 0.6 (SD) %ID/g and 12.3 ± 3.1%ID/g, respectively. Spleen uptake of 'free' ^{61}Cu was 5.1 ± 3.6%ID/g and bladder with 3.8 ± 2.0%ID/g.

***Groups 2-4*; ^{61}Cu-BFC-NCS-Si NS**

The biodistributions at 4 h of Groups 2-4 (n = 3, each) injected with ^{61}Cu-labelled MeSar-Ph-NCS-Si NS, ^{61}Cu-NOTA-NCS-Si NS and ^{61}Cu-DOTA-NCS-Si NS, respectively and derived by dissection are also shown in Figure 6.4. Data for selected organs is shown in Table 6.3. After 4 h, relatively low uptake was found in the blood, bone, heart, muscle and stomach. Higher activities were measured in the organs of the mononuclear phagocytic system; the liver (incorporating gall bladder) and spleen. Liver accumulated 38.5 ± 8.1, 48.1 ± 4.5 and 44.5 ± 6.0%ID/g of ^{61}Cu-MeSar-Ph-NCS-Si NS, ^{61}Cu-NOTA-NCS-Si NS and ^{61}Cu-DOTA-NCS-Si NS respectively. Spleen took up 43.3 ± 9.3, 63.6 ± 4.1 and 70.2 ± 8.8%ID/g of ^{61}Cu-labelled MeSar-Ph-NCS-Si NS, ^{61}Cu-NOTA-NCS-Si NS and ^{61}Cu-DOTA-NCS-Si NS, respectively. There was a higher level of accumulated radioactivity in lungs for the ^{61}Cu-labelled MeSar-Ph-NCS-Si NS (37.4 ± 5.7%ID/g) compared to the polyazacarboxylate conjugated Si NS (i.e. NOTA-NCS 7.4 ± 2.2 and DOTA-NCS 17.7 ± 6.1%ID/g) at 4 h. Kidneys and intestines accumulated intermediate activities (9.8 ± 2.3, 6.0 ± 1.1 and 9.4 ± 2.0 %ID/g for MeSar-Ph, NOTA-NCS and DOTA-NCS [kidneys] and 13.2 ± 2.7, 5.1 ± 1.1 and 9.3 ± 1.0%ID/g for MeSar-Ph-NCS, NOTA-NCS and DOTA-NCS [intestines]). Furthermore, at 4 h there was a high level of washed out ^{61}Cu or ^{61}Cu-BFC (breakdown, see "6" Figure 6.1) in the bladder for MeSar-Ph-NCS (14.8 ± 1.90%ID/g), compared to the free ^{61}Cu group, and the NOTA-NCS and DOTA-NCS groups (3.8 ± 2.0%ID/g, 2.4 ± 0.5%ID/g and 4.8 ± 0.8%ID/g).

An interesting observation (due to a reviewer) is that if the kidneys, liver and spleen are combined into a single 'reticuloendothelial system' and the activity of this "super-organ" is calculated, then there are no differences between any of the ^{61}Cu-BFC-NCS-Si NS, though all are different from the control group ($p < 0.01$) (last column of table 6.3). This supports the tentative conclusion that the lungs are differentially trapping extra radiotracer, in the case of ^{61}Cu-MeSar-Ph-NCS-Si NS.

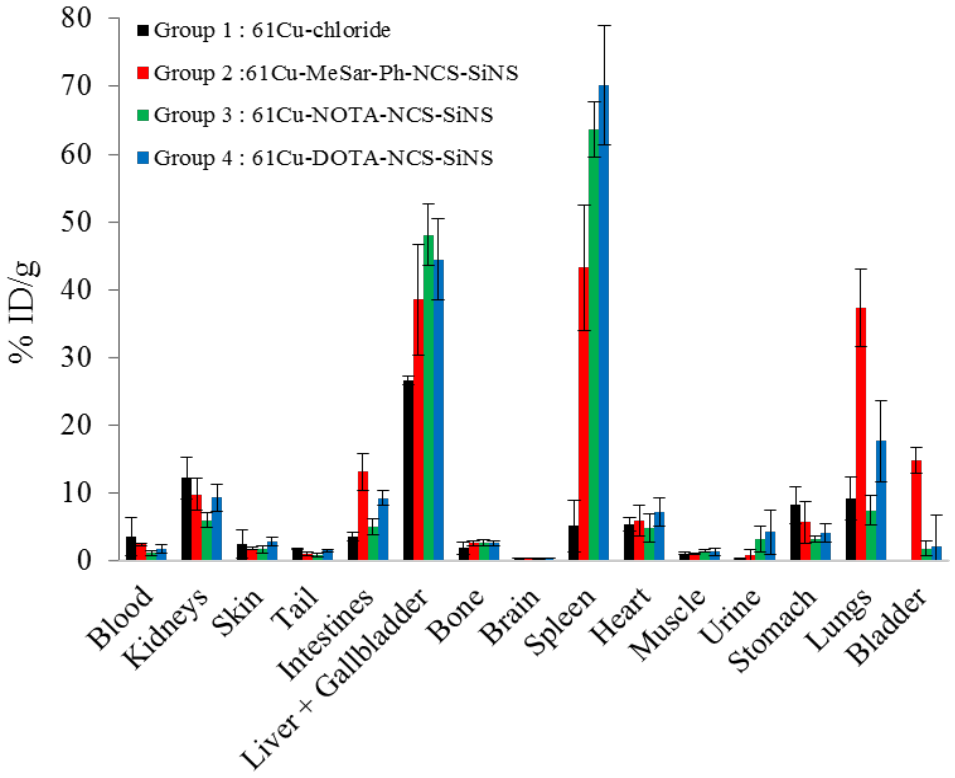

Figure 6.4 Dissection-derived biodistributions of 'free' ^{61}Cu (Group 1, controls) and ^{61}Cu-BFC-NCS-Si NS (Groups 2-4) in female Balb/c nu/nu mice (n = 3 each group) following sacrifice at 4 h. The percent injected dose per gram of tissue (%ID/g) was determined by normalising for organ weight plus radioactive decay correction. Data are represented by the mean ± SD.

6.3.4 µPET/CT Imaging and Biodistribution Studies

Representative maximum-intensity projection uptake PET images of the four groups at 1 h and 4 h post-injection are shown in Figure 6.5(a) & 6.5(b), respectively. The column marked 'Group 1' shows the distribution of activity concentration for 'free' ^{61}Cu. The columns 'Group 2', 'Group 3' and 'Group 4' represent the equivalent data for the three ^{61}Cu-BFC-NCS-Si NS tracers. For each time point the activity concentration maps for the three BFCs may be *qualitatively* visually compared, but not with the Group 1 controls map which has a different activity concentration scale for purposes of visual reproduction.

At 1 h post-injection the µPET images showed uptake of 'free' ^{61}Cu in the liver and lungs but not the spleen. For ^{61}Cu-BFC-NCS-Si NS activity was seen

primarily in the liver, spleen and lungs. Other organs such as the heart and bladder revealed significantly lower signals. In comparing different BFCs, it is seen that at 1 h the lungs of group 2 (^{61}Cu-MeSar-Ph-NCS-Si NS) (clearly located by µCT) accumulated significant activity as detected by µPET, whereas the signals in the lungs of group 3 (^{61}Cu-NOTA-NCS-Si NS) and group 4 (^{61}Cu-DOTA-NCS-Si NS) were lower. The uptake in the kidneys was probably significant at the 1-h time point but was not reported because of marked discord between the results for animals within Group 1. The activity of ^{61}Cu-DOTA-NCS was accumulated in bladder at 1 h (23 ± 0.4%ID/g) but not for other groups.

The equivalent images and derived activities for the biodistribution at 4 h are shown in Figures 6.5(b). The results are broadly similar to the 1-h time point except for the 'free' ^{61}Cu (Group 1) and ^{61}Cu-MeSar-Ph-NCS-Si NS (group 2), where the activity has been partly washed out. At 4 h the activity for ^{61}Cu-NOTA-NCS-Si NS and ^{61}Cu-DOTA-NCS-Si NS is retained in the liver, spleen, lungs, whereas the activity of free ^{61}Cu in liver and lungs (with no detectable signal in the spleen) decreases faster than physical decay would suggest.

At both time points the activity in the lungs of ^{61}Cu-MeSar-Ph-NCS-Si NS exceeds that of the other two BFCs. This is qualitatively in accord with the dissection-derived biodistribution results shown in Figure 6.4 for 4 h post-injection, and with qualitative examination of the images in Figure 6.5(a) & (b). Comparison of the normalised accumulated activities expressed as %ID/g between dissection and imaging for selected organs is shown in Table 6.3 and Table 6.4. As noted in Section 6.3.3, the equality of activity for all three chelators in the combined 'reticuloendothelial' organs (though each different from control group; see last column of table 6.3) suggests that though these organs retain the same proportion of injected activity at 4 h, the radiopharmaceutical 61Cu-MeSar-Ph-NCS-Si NS is preferential retained in the lungs.

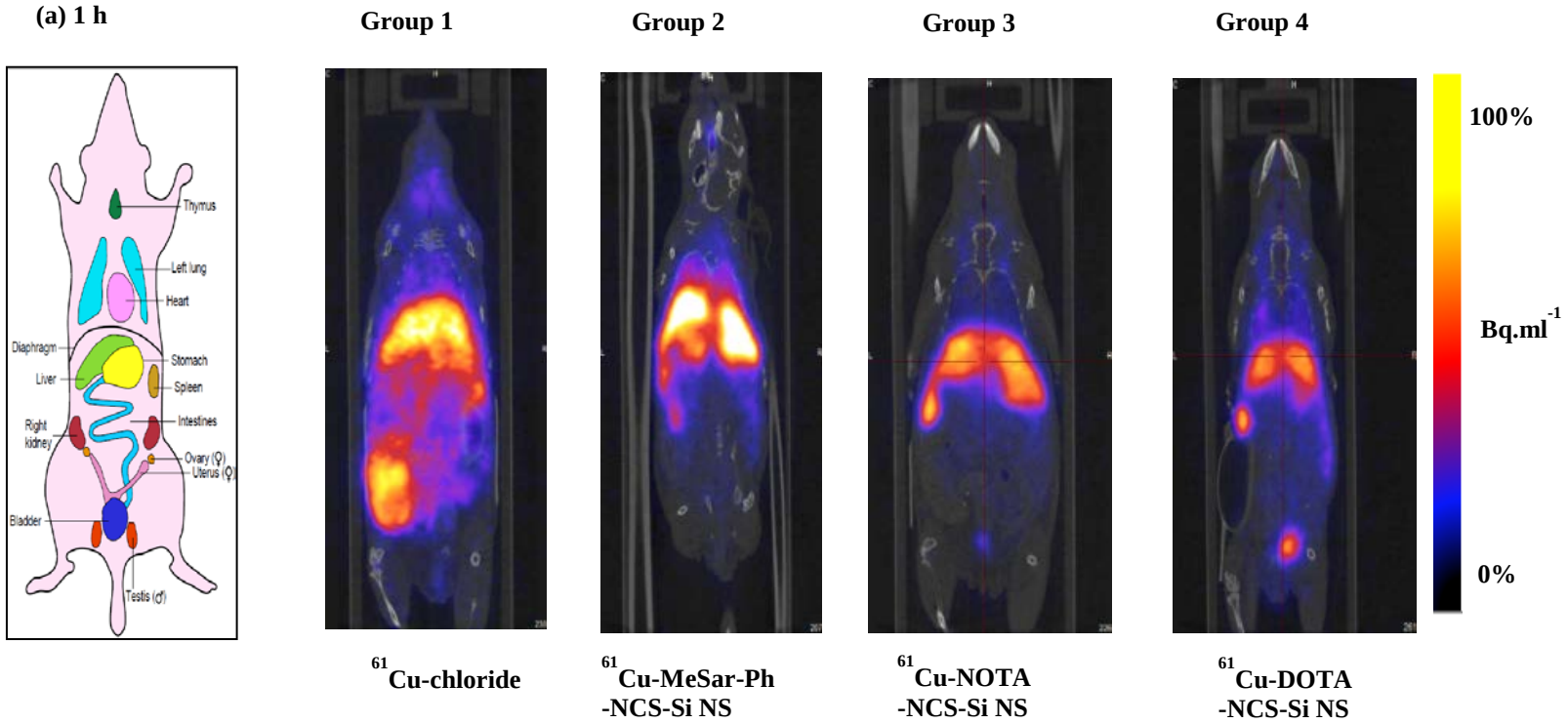
(a) 1 h
Group 1
Group 2
Group 3
Group 4
Thymus
Left lung
Heart
Diaphragm
Stomach
Liver
Spleen
Right kidney
Intestines
Ovary (♀)
Uterus (♀)
Bladder
Testis (♂)
100%
Bq.ml-1
0%
61Cu-chloride
61Cu-MeSar-Ph -NCS-Si NS
61Cu-NOTA -NCS-Si NS
61Cu-DOTA -NCS-Si NS

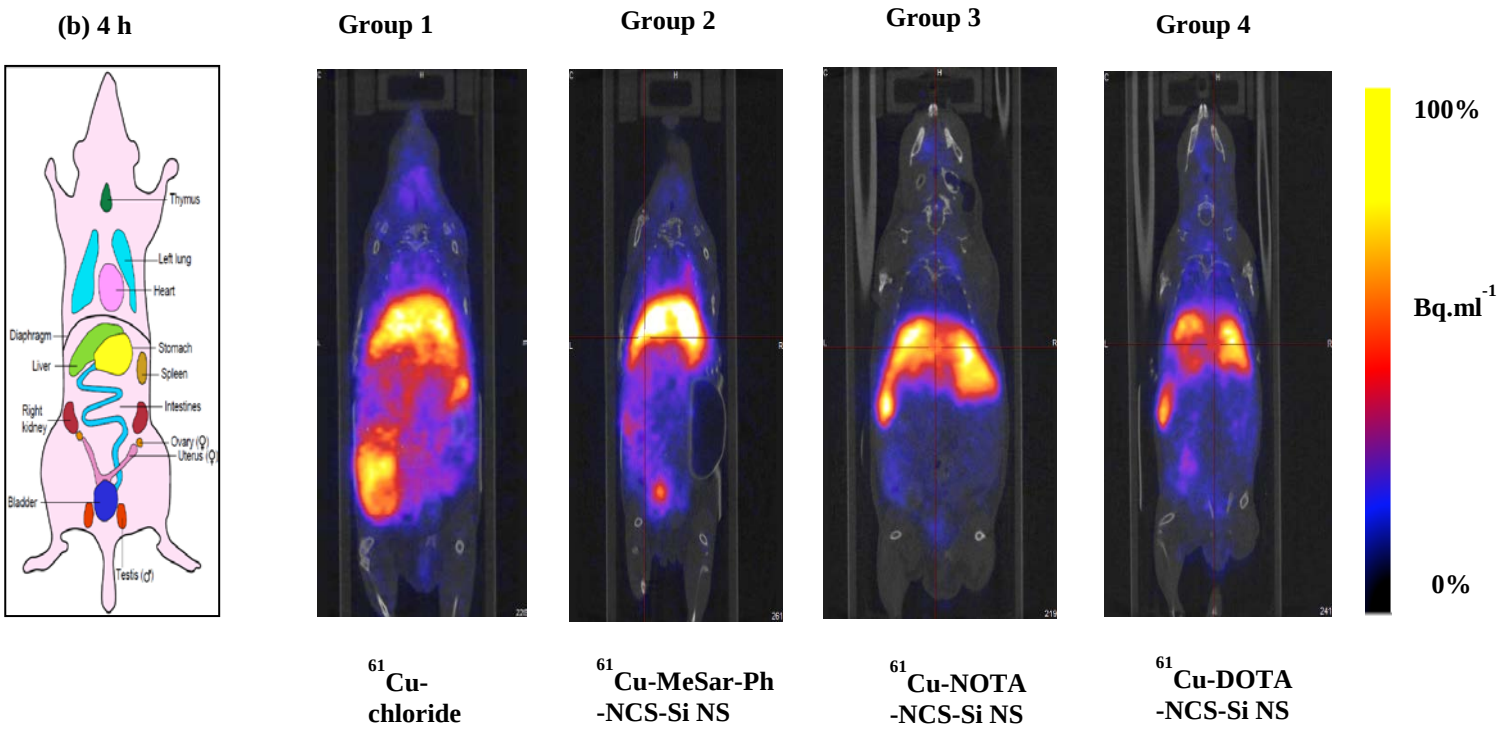

Figure 6.5 Representative microPET maximum-intensity projection images for each of the ^{61}Cu-injected groups at (a) 1 h and (b) 4 h post-injection.

Table 6.3 Biodistributions derived from the same mice by post-imaging dissection and radioactive counting (4 h) are shown for comparison. Data expressed as mean ± SD in units of % ID/g.

	Dissection-derived Biodistributions					
Organ	[a]Liver	Spleen	Lungs	Kidneys	Bladder	[f]Reticuloen-dothelial system
	4 h	4 h	4 h	4 h	4 h	4 h
Radiotracer						
'Free' ^{61}Cu[b]	26.6 ± 0.6	5.1 ± 3.6	9.2 ± 3.2**	12.3 ± 3.1	3.8 ± 2.0	19.20 ± 0.7[xx]
^{61}Cu-MeSar-Ph-NCS-Si NS[c]	38.5 ± 8.1	43.2 ± 9.3	**37.4 ± 5.7**	9.8 ± 2.3	14.9 ± 1.9	38.40 ± 6.2
^{61}Cu-NOTA-NCS-Si NS[d]	48.1 ± 4.5	63.6 ± 4.1	7.4 ± 2.2***	6.0 ± 1.1	2.4 ± 0.5	42.50 ± 3.6
^{61}Cu-DOTA-NCS-Si NS[e]	44.5 ± 6.0	70.2 ± 8.8	17.7 ± 6.1*	9.4 ± 2.0	4.8 ± 0.8	45.50 ± 5.0

a: Incorporating gall bladder. b: Injected as the chloride (Group 1). c: Group 2. d: Group 3. e: Group 4. *: $p < 0.05$ Group 4 vs Group 2. **: $p < 0.01$ Group 1 vs Group 2. ***: $p < 0.005$ Group 3 vs Group 2; [f]Reticuloendothelial system combined liver (including gallbladder), spleen and lungs. [xx]: $p < 0.01$ Group 1 compared with all other groups. For the reticuloendothelial system, Group 2, 3 & 4 were not different from each other. Two-tailed unpaired *t*-test, with Bonferroni correction.

Table 6.4 Biodistribution data for selected organs derived from quantitative analysis of microPET images of the four groups of Balb/c nu/nu mice (n = 3 animals each) injected with radiotracers. Images were collected at (a) 1 h and (b) 4 h post-injection. Data expressed as mean ± SD in units of % ID/g.

(a)

	MicroPET-derived Biodistributions				
Organ	Liver[a]	Spleen	Lungs	Kidneys	Bladder
Time point	1 h	1 h	1 h	1 h	1 h
Radiotracer					
'Free' ^{61}Cu[b]	51.3 ± 4.7	N/A	16.3 ± 4.5	#	TL
^{61}Cu-MeSar-Ph-NCS-Si NS[c]	35.0 ± 3.2	12.9 ± 2.4	11.8 ± 0.8	TL	TL
^{61}Cu-NOTA-NCS-Si NS[d]	35.6 ± 2.9	26.9 ± 8.0	6.2 ± 2.2	TL	TL
^{61}Cu-DOTA-NCS-Si NS[e]	31.9 ± 3.1	23.6 ± 9.5	8.1 ± 0.7	TL	23 ± 0.4

(b)

Modality	MicroPET-derived Biodistributions				
Organ	Liver[a]	Spleen	Lungs	Kidneys	Bladder
Time point	4 h	4 h	4 h	4 h	4 h
Radiotracer					
'Free' ^{61}Cu[b]	46.3 ± 2.2	N/A	18.1 ± 2.3	26.8 ± 10.3	TL
^{61}Cu-MeSar-Ph-NCS-Si NS[c]	30.8 ± 2.1	14.4 ± 5.7	8.5 ± 0.2	TL	12 ± 1.1
^{61}Cu-NOTA-NCS-Si NS[d]	39.2 ± 3.0	34.1 ± 2.1	4.5 ± 0.8	TL	TL
^{61}Cu-DOTA-NCS-Si NS[e]	34.5 ± 2.7	29.2 ± 5.0	6.3 ± 1.0	TL	TL

a: Incorporating gall bladder. b: Injected as the chloride (Group 1). c: Group 2. d: Group 3. e: Group 4. TL: signal too low for quantitation. #: Inconsistent results between animals within the group.

6.4 Discussion

Quantitative *in vivo* measurements of the time-dependent biodistribution of a radioactively labelled target-specific molecule or nanosphere ('delivery vehicle') are becoming increasingly important in selected areas of cancer diagnosis and molecular radiotherapy (MRT) planning, where the tools of the relatively new clinical science of 'theranostics' are applicable (Kraeber-Bodéré et al., 2015). In the (idealised) diagnostic phase of theranostics the 4-D spatial-temporal distribution of a particular cell or tissue type (for example, tumour cell or mass of pathologically formed blood capillaries) can be mapped and the proportional dose to collateral organs and tissues for preservation during subsequent MRT can be calculated ('dose-ranging'). In the (idealised) therapeutic phase the (γ or β^+ emitting) diagnostic-imaging radioisotope (PET or SPECT) is swapped for a (β^-, α or Auger-electron emitting) therapy isotope with the same Z-value. Thus, the same chemistry is used for binding to the molecular or nanosphere delivery vehicle ('companion theranostics'). The administered dose of the MRT to the target cells can then be titrated according to the calculated maximum permissible dose to the most radiosensitive normal tissues to be spared; using data derived from the diagnostic scan (Peng, Lutsenko, Sun, & Muzik, 2012). It is in the 'diagnostic' phase of investigatory theranostics that our 'proof of principle' study belongs.

6.4.1 Goals of These Studies

We evaluated the biodistribution of silica nanospheres in healthy immunodeficient mice. These potential drug delivery vehicles of nominal diameter 100 nm were conjugated to a novel bifunctional sarcophagine chelator (MeSar-Ph-NCS), radiolabelled with ^{61}Cu for μPET imaging. Two other conventional macrocyclic chelators NOTA-NCS and DOTA-NCS (Chakravarty et al., 2013; Schiller et al., 2013; Yang et al., 2011; Cooper et al., 2012) were

used in the same setting for comparison. We also investigated the biodistribution of free copper (^{61}Cu-chloride) as a control. Biodistributions were measured at 1 h and 4 h by analysis of quantitative μPET images, and at 4 h by dissection and radioactive counting following sacrifice, as shown in Figure 6.3.

Our first goal was to determine whether the novel isothiocyanate sarcophagine chelator MeSar-Ph-NCS offered advantages in respect of radiolabelling stability of the $^{61}Cu^{2+}$ radiolabelled complex when conjugated to Si NS, compared with the radiolabelled macrocyclic chelators ^{61}Cu-NOTA-NCS and ^{61}Cu-DOTA-NCS. The second goal was to determine the biodistributions of these radiotracers using both microPET imaging (1 h and 4 h) and post-sacrifice dissection and radioactive counting (4 h). Our final goal was to differentiate the uptake of the radiotracers in key organs (liver, spleen, lungs, kidneys, bladder), based on the biodistribution results. These studies were in general anticipation of future studies examining the use of radiolabelled Si NS in tumour theranostic applications (for example, harnessing the EPR effect), including the possibility of utilising the companion theranostic combination of ^{61}Cu (diagnostic mapping and organ dose-ranging) and ^{67}Cu (molecular radiotherapy).

6.4.2 Zeta Potential

In the literature, it has been reported that both the plasma protein absorbance and non-specific cellular uptake in the blood circulation decrease with the negative charge of nanoparticles (Li and Huang, 2008; Alexis, Pridgen, Molnar, & Farokhzad, 2008; Xiao et al., 2011). Nanoparticles with positive charge are known to aggregate in serum proteins (negatively charged) following administration (Li & Huang, 2008). In this study the positively-charged Si nanospheres accumulated in the liver and the lungs.

6.4.3 Bifunctional Chelators Stability Studies

The stability of macrocyclic and sarcophagine macrobicyclic bifunctional chelators of copper radioisotopes under physiological conditions is a key property in considering their clinical applications. Increasing the stability of copper complexes has been a major focus in the development of copper radiopharmaceuticals for a variety of copper-based diagnostic and therapeutic strategies (Wadas et al, 2007; Liu, 2008; Smith, 2004, 2008; Wei et al., 2009). In this study, *in vitro* stability experiments showed that ^{61}Cu-MeSar-Ph-NCS-, ^{61}Cu-NOTA-NCS- and ^{61}Cu-DOTA-NCS-Si NS were between 93% - 98% intact in NaCl 0.9% at 4 h, whereas their radiochemical stability in FBS at 4 h dropped significantly (to approximately 84%). Other investigators have reported the dechelation of copper from tetra-aza macrocyclic chelators under physiological conditions (Cutler et al., 2000; Jones-Wilson et al., 1998; Woodin et al., 2005). However, our assumption is that the instability arises mainly from the deconjugation of the ^{61}Cu-labelled BFCs from the Si NS. (Our method of repeated centrifugation and radioactive counting of the supernatant cannot uniquely confirm this; see Section (6.3.1). Clearly, this finding has implications for the interpretation of the *in vivo* images, particularly at the four-hour time point, and also for the dissection studies.

6.4.4 Dissection-Derived Biodistributions

The *ex vivo* dissection-derived biodistributions of 'free' ^{61}Cu and ^{61}Cu- BFC-NCS-Si NS in healthy Balb/c nu/nu immunodeficient mice, at 4 h post retro-orbital injection are shown in Figure 6.4. Values expressed in %ID/g are given in Table 6.3 for selected organs.

Control ^{61}Cu Tracer

The 'free' ^{61}Cu is partly accumulated in the liver, which is known to be a reservoir for many metals especially copper through binding to serum ceruloplasmin (Jalilian et al., 2009). The kidneys were the second organ showing relatively high accumulation of the ^{61}Cu-chloride at 4 h, though the radiotracer would be expected to wash out via the urinary tract due to the high water solubility of the Cu^{2+} cation (Jalilian et al., 2009). On the other hand, the uptakes of other organs were low. Peng et al. (2012) reported dynamic microPET biodistribution studies of ^{64}Cu-chloride with knock-out mice and wild type (WT) C57BL mice. Their results at 1 h for the WT mice are in qualitative agreement with our data for the liver, kidneys, lungs, heart; as regards ranking of copper-accumulating organs. However, their results are about 50% less than this study. This broad difference could be attributed to differences between the studies in regard to the method of assessing biodistributions, the time points for comparison and the type of mice.

From an examination of the uptake of 'free' ^{61}Cu in the kidneys (Group 1, Figure 6.4) and the observed deconjugation at 4 h of labelled ^{61}Cu from Si NS in the *in vitro* stability experiments conducted with foetal bovine serum (Section 6.3.1), it is possible that the kidney activity of ^{61}Cu-BFC-NCS-Si NS at 4 h mainly reflects ^{61}Cu labelled BFC or 'free' ^{61}Cu. This explanation may also apply to those organs with small uptakes such as bone and heart, where the 'free ^{61}Cu' and ^{61}Cu-BFC-NCS-Si NS uptakes are similar.

BFC ^{61}Cu Tracers; Particularly in Lungs

According to the dissection results, the three ^{61}Cu-BFC-NCS-Si NS radiotracers accumulated predominantly in the liver (including gallbladder) and spleen within four hours post-injection (see Figure 6.4). However, at this time point the lungs uptake of ^{61}Cu-MeSar-Ph-NCS-Si NS was also significant, and higher than that for NOTA-NCS and DOTA-NCS. The precise reason for the relatively enhanced

uptake of the sarcophagine-conjugated Si NS in the lungs is unknown. However, an hypothesis is that it is caused by a net positive charge of the ^{61}Cu-MeSar moiety that confers cationic properties. In support of this notion are the following observations; (i) the renal uptake of a ^{64}Cu-labelled *antibody* conjugated with a series of Sar derivatives with decreasing charge was proportional to the net positive charge of the conjugated sarcophagine, with SarAr (with the highest charge) delivering a relatively high dose to the kidney (Dearling et al., 2015). (ii) This was postulated to be a cationic effect resulting in increased binding of the labelled antibody to the negatively charged basal cells of the glomerulus. (iii) Interestingly, the interstitium of the lung also carries a net negative charge (Charan & Carvalho, 2002). The interstitium includes the alveolar epithelium, pulmonary capillary endothelium, basement membrane, perivascular and perilymphatic tissues. Thus it is possible that the same cationic effect is operating in the lung as it acquires a sarcophagine-complexed radiolabel. (iv) This preferential accumulation and retention of *nanoparticles* in the lungs is likely not due to unique properties of the Si NS. Blanco, Shen, & Ferrari (2015) note that the penetration of tissues by nanospheres depend in part on their size, shape and charge. Other factors equal, nanospheres of spherical shape and diameter ~100 nm can penetrate lung tissue, but not the kidney, which requires the size to be < 5 nm. This would explain, for example, how the lungs could accumulate a high activity of a sarcophagine-conjugated Si NS, while in the same animal the kidneys did not; even though the basal cells of the glomerulus are negatively charged (Dearling et al., 2015) (Figure 6.4 & Table 6.3). The modest (and approximately equal with 'free' ^{61}Cu) activities of ^{61}Cu-BFC-NCS-Si NS in the kidneys at four hours may mainly reflect 'free' ^{61}Cu, arising from the *in vivo* part-breakdown in stability of these complexes by that elapsed time (Section 6.4.2), as noted in the above paragraph.

This difference in lung activity between the macrobicyclic sarcophagine and poly-aza macrocyclic labels was not so markedly reflected in the data derived from imaging, at either time point. This difference between techniques is unlikely to be the result of selective contamination of the Group 2 excised lungs

by blood, since the uncertainties in the lung measurements of Groups 2-4 shown in Figure 6.4 are similar.

Comparison Between μPET-Imaging and Dissection-Based Biodistributions

There was qualitative agreement between dissection-plus-counting and imaging at 4 h for the liver (see Table 6.3 & Table 6.4). The mean liver & gall bladder activity for the three BFC-NCS-Si NS radiolabels at 4 h measured by γ- counting (43.7 ± 4.9%ID/g) was 20% higher than the equivalent activity measured by μPET quantification (Figure 6.4 & Figure 6.5), which showed an average of 34.9 ± 2.0%ID/g at 4 h. The average spleen activity revealed a larger variation between the two methods; yielding mean values of 59.0 ± 14.0%ID/g with dissection-plus-counting versus 25.9 ± 10.3%ID/g with μPET (see Table 6.3 & Table 6.4). In this study, reliable activities for the kidneys at either time point could not be obtained from the BFC-NCS-Si NS images because of problems with detecting the organ boundaries. This was also true of other organs such as the heart and muscle with low activities.

6.5 Conclusions

This study compared the *in vivo* activity biodistributions of three ^{61}Cu-labelled bifunctional chelators (BFCs) conjugated to amino-functionalised silica nanospheres in a 'normal' immunodeficient murine model using microPET imaging (1 h and 4 h post retro-orbital injection) and dissection-plus γ-counting (4 h). One of the BFCs, MeSar-Ph-NCS, was a novel sarcophagine molecule developed by a collaborating laboratory. In this study, MeSar-Ph-NCS was examined for the first time for its capacity to link a radiocopper isotope to a nanoparticle capable of carrying targeting diagnostic and therapeutic agents. Copper-61 injected as the chloride was employed as a control. The principal findings were; (i) by four hours, all three BFC-conjugated Si NS radiotracers accumulated predominantly in the liver and spleen. (ii) The radiotracer utilising

the macrobicyclic sarcophagine BFC MeSar-Ph-NCS showed elevated accumulation in the lungs at 4 h, in comparison with those tracers based on the tri- and tetra-aza macrocyclic BFCs NOTA-NCS and DOTA-NCS. This preferential uptake in the lungs warrants further study, including the possibility of it being a disadvantage of sarcophagine BFCs when conjugated to nanospheres. A possible explanation that warrants further study is that it is caused by the cationic behaviour of the ^{61}Cu-MeSar-Ph-NCS moiety when passing through lung interstitium, which is net negatively charged. (iii) The PET isotope ^{61}Cu ($t_{1/2}$ = 3.33 h) can be efficiently prepared with high radionuclidic purity and NCA specific activity in a facility with access to a standard biomedical proton-beam cyclotron and solid-targetry facilities.

I would be argued that the relatively rapid clearance of all ^{61}Cu-BFC-NCS-Si NS from the blood (Figure 6.4) would not be an adventure if the EPR effect were to be harnessed for tumour treatment. However, we found that these chelators had significant uptake in reticuloendothelial tissue. Two of these chelators (DOTA & NOTA) have been used for EPR studies in the literature (Orcutt et al., 2014; Chakravarty et al., 2015). Furthermore, nanospheres are known to accumulate in liver and spleen and clear fast from the blood if they not attached with pegylation (PEG) to give them long blood circulation time. Therefore, in the future, we will do further studies with two types of nanospheres (Si NS & PS NS) in small sizes (i.e. 50 nm) with PEG attached on the nanospheres surfaces.

Nerveless, the relatively fast clearance from blood and its uptake in reticuloendothelial tissue of the BFC-NCS-Si NS in the study is a concern when exploiting the EPR effect in tumours, especially in therapy using NS. The ideal would be a compound with a relatively long blood circulation, waiting to be passively taken up by the tumour. These a reduction in the size of NS is a first step towards a achieving this, with the current model.

The positron-emitting radiometal copper-61 is eminently suited to radiolabelling of amino-functionalised silica nanospheres using a range of complementary

bifunctional chelators. These labelled complexes are subsequently able to elicit quantitative microPET images in a murine model, at least to four hours post-injection. This work shows that the choice of BFC is an important factor, as it can have an impact on the organ-specific *in vivo* distribution of the radiolabelled Si nanospheres.

Additional comments:

The in vitro stability of the copper chelates does not infer stability in vivo and should be viewed cautiously. Furthermore, molecular transformation of each complex e.g. the breaking of the thiourea bond to give small ^{61}Cu-complexed fragments will also contribute to overall non-specific signal. Also potential trans-chelation of ^{61}Cu by endogenous peptides in vivo is possible, particularly in the liver. Since these were no studies performed to look at the tissue, plasma or urine metabolites, the types of fragments of the ^{61}Cu-chelator confirm that are still capable of chelating copper are unknown. Most radiopharmaceuticals are metabolised over time. Hence, the total readout of activity in any of the organs, particularly those involved in metabolism and clearance such as liver, kidney, spleen, and bladder (derived either from tissue biodistribution or PET imaging) is sun of the ^{61}Cu activity irrespective of the species.

CHAPTER SEVEN

DISCUSSION AND FUTURE DIRECTIONS

7.1 Discussion

Over the last three decades cyclotron-produced radioisotopes have attracted considerable interest for biomedical applications. For example, the positron emission tomography (PET) isotopes ^{18}F, ^{11}C, ^{13}N and ^{15}O have established roles in diagnosis and management of human diseases, or research into their mechanisms, particularly in oncology, cardiology and neurology. However, in recent years many advanced cyclotron sites have also added solid targetry systems to produce PET radiometals and radiohalides with half-lives ranging from several minutes (e.g. ^{60}Cu) to several days (e.g. ^{89}Zr & ^{124}I). The predominant reactions are (p,x), usually with equipment-limited primary proton energies of less than 19 MeV. These transmutations facilitate chemical extraction and purification of products with high no-carrier-added (NCA) specific activities because the product atomic number (Z) is usually different from that of the target. The relatively long physical half-lives of some of the products are in accord with the characteristic lifetimes of biodistributions of numerous therapeutic and diagnostic ('theranostic') agents that utilise monoclonal antibodies, their engineered constructs, or nanoparticles as target-seeking platforms. A typical target would be a tumour-cell surface receptor. Though the radioisotope may be chosen for its half-life and radioactive emission, its independent chemical properties may pose challenges for bonding or complexing to a targeting ligand. Copper radioisotopes are an exemplar.

Recent advances in the complexation of copper isotopes using bifunctional macrocyclic chelators such as DOTA or NOTA and sarcophagine (sar) derivatives have facilitated biomedical applications of the PET-reporter isotopes ^{61}Cu and ^{64}Cu, as well as the promising radiotherapy isotope ^{67}Cu. With its

'intermediate' physical half-life of 3.33 h and relatively high positron branching ratio (β^+ = 61.5%; EC = 38.5%), ^{61}Cu seems particularly well-positioned to; (i) map the biodistributions of engineered-antibody immunoPET constructs such as diabodies and minibodies; (ii) label nanospheres capable of delivering theranostic agents to tumours using the enhanced permeation-retention (EPR) effect and; (iii) provide a tool for constructing metal-chelator imaging compounds such as Cu-ATSM that target hypoxic tissue; for example in heart, brain and the cores of some solid tumours. However, in order to apply these tools to phase-I studies of human diseases, numerous preliminary validation studies (including dosimetry) are required to be performed on cell cultures and on animal models.

This thesis describes novel contributions to the preparation, chelator-labelling and subsequent application of ^{61}Cu as a preclinical PET imaging probe. In the *first category* of this work, we studied the cyclotron-based production and subsequent purification of ^{61}Cu. In the *second category*, we investigated the chemistry of complexation of ^{61}Cu to bifunctional macrocyclic and sarcophagine Cu^{2+}-chelators. In the *final category* of studies, we investigated the application of three ^{61}Cu-labelled bifunctional chelators to mapping the *in vivo* temporal biodistibution of functionalised silica nanospheres injected in a 'normal' immunocompromised murine model. Biodistributions were measured using micro-positron emission tomography and post-mortem dissection plus γ-counting.

7.1.1 Optimisation of Production of ^{61}Cu

The first phase of the first category of studies (***Chapter 2***) addressed the precise measurement of the primary proton beam energy of a cyclotron, facilitating optimisation of the beam energy used for the subsequent production of the radiometal. In turn, this would lead to better yields and less contamination from other radioisotopes (Asad et al., 2015). The copper stacked-foils technique using ^{nat}Cu(p,xn) monitor reactions, together with a novel iterative computational

technique, was used to measure the primary proton-beam energy. Measurements were performed before and after a major upgrade of the ion sources and non-magnetic beam controls, converting a (nominal) 18/9 MeV (proton/deuteron) configuration to 18/18 MeV (proton/proton). Measured proton beam energy was 18.03 MeV ± 0.02 (SD) and 18.11 MeV ± 0.05 (NS) before and following the upgrade, respectively. This indicated that major alterations not affecting the magnetic configuration or basic beam geometry of the cyclotron leave the primary energy unchanged. The technique was also applied to the experimental validation of a custom-built graphite beam-degrader designed for ^{61}Cu production, the thickness of which had been predicted using the method of Ziegler et al., (2011) plus the experimental primary-beam energy measurement. Agreement was within reproducibility error (0.5%). The novelty of the technique is that it has advantages over published methods that utilise ratios of reaction cross sections; namely the capacity to measure energies across virtually the entire range of a chosen monitor nuclear reaction and lack of the need for customized degraders for specific energy ranges, while maintaining high measurement precision (0.3-0.5%). The method may also be applicable to proton energies above 18 MeV and indeed 30 MeV, using IAEA-recommended (p,x) monitor reactions with titanium or aluminum as target (Asad et al., 2015).

In the second phase of the first category of this study (***Chapter 3***) we measured excitation functions of nuclear reactions directly or indirectly relevant for ^{61}Cu production. Copper-61 belongs to an interesting class of radioisotopes that can be produced by proton-induced reactions in natural zinc (^{nat}Zn), that also include ^{66}Ga, ^{67}Ga, ^{68}Ga and ^{65}Zn. These isotopes are used as reporters in PET or single-photon emission computed tomography (SPECT) diagnostic or preclinical studies, depending on their radiation characteristics. Copper-61 arises from the ^{64}Zn content in ^{nat}Zn (48.6%) via the ^{64}Zn(p,α)^{61}Cu reaction. It was useful to investigate the feasibility of its production from the cheaper ^{nat}Zn target (in comparison with an enriched ^{64}Zn target), even though the radioactive by-products co-produced in ^{nat}Zn must be separated out in the purification process. In preparation for ^{61}Cu production via the ^{nat}Zn pathway, we measured the

excitation functions of accessible ^{nat}Zn(p,x) reactions up to 17.6 MeV using the stacked-foils activation technique (Asad et al., 2014). Activated foils were measured using high-purity Ge γ-spectroscopy to quantify the radionuclides ^{61}Cu, ^{66}Ga, ^{67}Ga and ^{65}Zn produced from the reactions. Thick-target integral yields were also deduced from the measured excitation functions, which aided in the design of ^{61}Cu production runs. These results were compared with the published literature and were found to be in good agreement with the most reliable and recent reports. Thus these data can contribute to the statistical weighting of published data for assembly of the 'best' composite excitation function from published results, for most of the reactions of the ^{nat}Zn(p,x) reaction set.

7.1.2 Purification of ^{61}Cu and its Complexation by Chelators

The second category of studies, described in ***Chapter 4***, devised improved methods for the production and chemical separation of ^{61}Cu from ^{nat}Zn or enriched ^{64}Zn targets. Also, the complexation of ^{61}Cu by three different bifunctional chelators was compared, using the macrocyclics NOTA-NCS (NOTA) and DOTA-NCS (DOTA) plus the macrobicyclic sarcophagine diamsar. The significance of these investigations, including as preparation for radiolabelling of nanospheres is discussed below.

Copper-61 can be produced in high yields and with high radionuclidic purity from a highly enriched ^{64}Zn target. However, as this target material is expensive and its supply in foil form is limited, we developed an improved method for the purification of ^{61}Cu resulting from the bombardment of natural zinc material. This was achieved by using a combination of 3 columns (Cu-resin, anion and cation exchange resins) within 30 min compared with 120 min as reported for previous methods (Asad et al., 2012, 2015). This yielded ^{61}Cu as chloride, with > 99% radionuclidic purity. This method is a fast and cost-effective option for the potentially routine production of ^{61}Cu.

The purification of ^{61}Cu resulting from the bombardment of enriched ^{64}Zn target was also investigated using a Cu-resin column. In this case, a one-column purification was sufficient to separate ^{61}Cu in high radionuclidic purity (> 99%) from the co-produced gallium radionuclides and the target material (allowing recycling of the enriched target material, if relevant). Either method employing a zinc target is considerably cheaper than the method based on an electroplated ^{61}Ni target using the reaction ^{61}Ni(p,n)^{61}Cu, because of the relatively high cost of the nickel enrichment.

The effective specific activity of each of eight ^{61}Cu batches (n = 4 replicates in each) was assessed using the titration method with the bifunctional chelating agents DOTA, NOTA and diamsar. These results were compared with the corresponding NCA specific activities obtained via ICP-MS analysis. Reasonable agreement was found between the two estimates of specific activity for diamsar, for ^{61}Cu derived from either ^{nat}Zn or enriched ^{64}Zn targetry. However, for NOTA and DOTA the specific activity obtained via ICP-MS analysis was 2.4-32.5 fold higher than that determined using the titration method. Generally, NCA specific activities for ^{61}Cu derived from a ^{nat}Zn target were approximately one half of those from the enriched ^{64}Zn source. As shown in Table 4.2 of Chapter four, ^{nat}Zn results ranged from 143 to 233 MBq/μg compared with 434-506 MBq/μg for ^{64}Zn (EOB-corrected), a consequence of the approximately 50% dilution of ^{64}Zn in ^{nat}Zn. ICP-MS analysis also revealed that the concordant results for diamsar were achieved, despite relatively high background concentrations of Zn^{+2} and Pb^{2+} (Figures 4.5 & 4.6 of Chapter four). Collectively, these findings demonstrated the high specificity of the sarcophagine chelator diamsar for Cu^{2+}. Generally, zinc, lead and iron compete with Cu^{2+} for chelation. The robustness of diamsar to this effect lends credence to the use of a copper chelator based on a macrobicylic sarcophagine cage.

7.1.3 Nanospheres; ^{61}Cu-Radiolabelling and Preclinical Imaging

Fortunately, we were able to incorporate a *novel* sarcophagine-based molecule as one of the bifunctional chelators in the final stage of this project (***Chapters 5 & 6***); namely; (i) characterisation of the ^{64}Cu- and ^{61}Cu-radiolabelling of nanoparticles using different bifunctional Cu^{2+}-chelators (BFC); and, (ii) the investigation of the biodistributions of one species of radiolabelled nanospheres in a 'normal' immunocompromised murine model using micro-positron emission tomography and also post-sacrifice dissection plus γ-counting. The use of Balb/c nu/nu mice was in anticipation of extending the study to xenograft 'tumourised' mice.

In ***Chapter 5*** we investigated the conjugation and ^{64}Cu-radiolabelling of carboxylate-functionalised polystyrene nanospheres (PS NS) of three sizes (365, 680 & 840 nm). These were conjugated with the sarcophagine SarAr-NH_2 and radiolabelled with $^{57}Co^{2+}$ and $^{64}Cu^{2+}$ (the latter for 680 nm only). We found that increasing the labelling temperature (23^{o}C to 37^{o}C) and reaction time (1.25 h to 24 h) did not improve the labelling efficiency for ^{64}Cu (the radiochemical surrogate for ^{61}Cu). This study provided valuable pilot data for the subsequent ^{61}*Cu*-radiolabelling of functionalised silica nanospheres (Si NS) using a novel sarcophagine; a major objective of this work.

As discussed in ***Chapter 6***, in separate replicated experiments amino-surface-functionalised Si NS of nominal diameter 100 nm were conjugated with the bifunctional macrobicyclic sarcophagine Cu^{2+}-chelator 'MeSar-Ph-NCS', followed by ^{61}Cu-radiolabelling. This was repeated for the macrocyclics NOTA-NCS and DOTA-NCS. These constructs were compared for labelling stability plus chelator occupancy density on the nanosphere surface. 'MeSar-Ph-NCS' is the novel Cu^{2+}-chelating sarcophagine, [Mg(CH_3)(*p*-NCS-Ph)Sar](CF_3SO_3)$_2$, recently developed by collaborators of our laboratory, where the metal protector magnesium ion is extruded from the molecule following conjugation to the nanosphere and prior to radiolabelling (Paterson et al., 2014). It was found that

the *in vitro* stabilities of all ^{61}Cu-BFC-Si NS complexes were approximately equal, though dissociation under 'physiological' conditions was 11-16% at 4 h. However, the occupancy areal density of ^{61}Cu-radiolabelled MeSar-Ph-NCS molecules on the silica nanosphere surface was approximately double that of the areal densities of radiolabelled NOTA-NCS or DOTA-NCS. This suggested that MeSar-Ph-NCS linkage may be a superior mechanism for maximising the labelling activity on the Si-NS. These experiments were the first time that this novel bifunctional chelator had been used to radiolabel nanospheres.

Following validation of the radiolabelling, the tracer ^{61}Cu-chloride, plus the radiolabelled nanospheres ^{61}Cu-MeSar-Ph-NCS-Si NS (^{61}Cu-MeSar-Si NS), ^{61}Cu-NOTA-NCS-Si NS (^{61}Cu-NOTA-Si NS) and ^{61}Cu-DOTA-NCS-Si NS (^{61}Cu-NOTA-Si NS) (collectively, ^{61}Cu-BFC-Si NS) were injected into Balb/c nu/nu 'normal' immunodeficient mice. The biodistributions of these tracers were measured *in vivo* by microPET imaging at 1 and 4 h post-injection and also *ex vivo* by dissection plus γ-counting of tissue samples at 4 h. The most important findings from this study were as follows:

- The control tracer injected as ^{61}Cu-chloride (and representing 'free' ^{61}Cu in circulation) showed significant uptake in liver, kidneys and (to a lesser extent) in the lungs at both time points of imaging, as revealed by both techniques (Figures 6.4 & 6.5, Table 6.3 & Tables 6.4 & 6.5).

- ^{61}Cu-BFC-Si NS showed uptake and retention in the liver (including gallbladder), spleen and (to a lesser extent) the lungs and bladder, as shown in the quantitative μPET images at 1 and 4 h. At 4 h post-injection, these results were broadly reflected in the dissection-derived biodistribution data. These data also revealed that all three ^{61}Cu-BFC-Si NS normalised activities were broadly similar in the liver (range 39-48%) and spleen (range 43-70%; Table 6.3).

- However, the normalised activity of ^{61}Cu-MeSar-Si NS in the lungs (37.4 ± 5.7%ID/g) significantly exceeded that of ^{61}Cu-NOTA-Si NS (7.4 ± 2.2; $p < 0.005$) or ^{61}Cu-DOTA-Si NS (17.7 ± 6.1; $p < 0.05$) (Table 6.3). This result was also reflected qualitatively in the μPET image-derived data, though the difference was less marked. The precise reason for the relatively enhanced uptake of the sarcophagine-conjugated Si NS in the lungs is unknown. As postulated in Section (6.4.3) a possible explanation is a relatively high net positive charge on the ^{61}Cu-MeSar moiety (Paterson et al., 2014), leading to binding of the sarcophagine-mediated complex to the net negatively charged lung interstitial tissues. The relatively high uptake of ^{61}Cu-MeSar-Si NS was not seen in the kidneys compared with NOTA and DOTA, where net negatively charged basal cells of the glomerulus might have been expected to elicit the same qualitative effect as in the lungs (Figure 6.4). However, as noted in Section (6.4.3) the silica nanospheres' (Si NS) size of about 100 nm may preclude any of the ^{61}Cu-BFC-Si NS complexes from accumulating in the kidneys, which are refractory to NS sizes above about 5 nm (Elvin, Shen, & Ferrari, 2015). Indeed, the absence of a 'spike' in accumulation of ^{61}Cu-MeSar-Ni NS in the kidneys, relative to other BFC-tracers (since kidneys and lungs both contain tissues with net negative charges), is explained by the discriminatory effect of the size of Si NS used in this study, on the kidneys – for *all* ^{61}Cu-BFC-Ni NS complexes. As noted in Section (6.4.3) it is possible that the modest (and approximately equal with 'free' ^{61}Cu-tracer) activities of ^{61}Cu-BFC-Si NS in the kidneys at 4 h may actually reflect mainly 'free' ^{61}Cu, arising from the *in vivo* breakdown in stability of these complexes by that elapsed time.

The murine biodistribution studies had several limitations. (i) Possible breakdown *in vivo* of the ^{61}Cu-BFC-Si NS complexes and release of either ^{61}Cu-BFC or 'free' ^{61}Cu (mechanisms '5' & '6', respectively of Figure 6.1). This may have confounded the results for organs and tissues with lower uptakes for the nanospheres, particularly the kidneys and particularly at 4 h post-injection. (ii) The uneven accord between results from imaging and dissection, particularly the

inability to detect a PET image signal from the kidneys for ^{61}Cu-BFC-Si NS (Table 6.3 vs Tables 6.4 & 6.5). This suggests that different techniques should be applied to analysing these images, and that the injected doses of tracers may need to be increased. (iii) The lack of a 'tumour-based' arm to the study; for example, the inclusion of 'tumourised' animals for investigation of an EPR effect.

7.2 Summary: Outcomes of Potential Clinical Significance

This is a report on the synthesis and purification of the positron-emitting radiometal ^{61}Cu, its complexation to selected bifunctional Cu^{2+}-chelators (sar macrobicyclic and poly-aza macrocyclic), an application to radiolabelling of silica nanospheres and finally a preliminary study on the measurement of their biodistributions in a murine model, by two related techniques. The first significant outcome, broadly focussed on eventual clinical applications, is the demonstration of the feasibility of the production and purification of ^{61}Cu in a clinical-radiopharmaceutical routine laboratory setting using a 'biomedical' cyclotron with the predominant daily task of producing ^{18}F. Solid targetry systems operating at less than (say) 19 MeV on such a cyclotron do not require complex and expensive external commercial beamlines, as demonstrated by Scharli et al., (2012).

The second outcome was the finding that the sarcophagines were superior to the macrocyclics DOTA and NOTA for Cu^{2+}-labelling of silica nanospheres in three respects; (i) relatively benign chemistry is required for their chelation (using diamsar and SarAr as archetypes), (ii) higher NCA radiolabelling specific activities were achievable (diamsar), and (iii) a higher areal density of conjugated ^{61}Cu-BFC complexes was achievable on the nanosphere surface (using the novel bifunctional sarcophagine MeSar-Ph-NCS).

The final outcome of potential clinical significance was the first report of biodistribution studies in an animal model, for silica nanospheres conjugated with the novel radiolabelled bifunctional sarcophagine complex ^{61}Cu-MeSar-Ph-NCS. The 'head-to-head' comparison with the biodistributions for the poly-aza macrocyclics DOTA and NOTA revealed few differences of significance, except in the lungs. In that organ (but not in the kidneys for a plausible reason based on nanoparticle size), there was the suggestion that a net positive charge on the ^{61}Cu-sarcophagine moiety may be important for its activity accumulation and retention.

The work in this thesis has spanned applied nuclear physics; radiometals separation, purification and labelling chemistries, comparison of bifunctional chelators (BFC) for ease of synthesis, stability and areal density of surface conjugation; and finally micro-PET imaging plus dissection-based measurements of the biodistributions of ^{61}Cu-radiolabelled silica nanospheres using these BFCs in a mousemodel. There are several clear directions in which these studies can be extended.

7.3 Future Directions

The most promising aspect in this research has been the "proof of principle" application of different ^{61}Cu-labelled bifunctional chelators in determining the biodistributions of silica nanospheres in an animal model - exemplifying a potential theranostic platform for diagnostic and therapeutic agents. Some immediate extensions of this work are; (i) improving the *in vivo* stability of the ^{61}Cu-BFCs; (ii) comparison of the biodistributions ^{61}Cu-BFC-NCS labels, alone, in the mouse model, thus excluding effects of the nanospheres, and (iii) inclusion in the study of sarcophagine BFCs known to have different net positive charges – in order to examine the hypothesis for explaining the relatively high accumulation of ^{61}Cu-MeSar-Si NS (and possibly other sarcophagines) in the

lungs. Until this effect is elucidated, the use of sarcophagine-based chelators in combination with nanospheres is in doubt.

More sophisticated extensions would be directed to refining the techniques for further preclinical and ultimately clinical studies. These could include (i) determining the utility of ^{61}Cu-labelled silica nanospheres in identifying tumours that exhibit the EPR effect. Initial experiments would use a xenografted immunocompromised murine model (e.g. Balb/c or non scid), utilising both micro-PET and dissection. (ii) The PET-imaging isotope ^{64}Cu could easily replace ^{61}Cu in experiments that sought to extend measurements of the pharmacokinetics of nanosphere metabolic pathways from several hours to several days. (iii) Following biodistribution analysis and 'dose-ranging' using either ^{61}Cu or ^{64}Cu, the silica 'nanoplatform' could be 'loaded' with the therapy radioisotope ^{67}Cu (without any changes in chemistries), for investigating a 'companion theranostic' treatment model. It is possible that one application of such models would be as an adjunct to conventional external-beam radiotherapy treatments, for certain classes of tumours (Wessels et al., 2008).

References

Every reasonable effort has been made to acknowledge the owners of copyright material. I would be pleased to hear from any copyright owner who has been omitted or incorrectly acknowledged.

Abbas, K.J., Kozempel, J., Bonardi, M., Groppi, F., Alfarano, A.U., Holzwarth, U., … Gibson, N. (2006). Cyclotron production of ^{64}Cu by deuteron irradiation of ^{64}Zn. *Applied Radiation and Isotopes, 64,* 1001-1005.

Abouzied, M.M., Crawford, E.S., & Nabi, H.A. (2005). ^{18}F-FDG Imaging: Pitfalls and Artifacts. *Journal of Nuclear Medicine and Technology, 33,*145-155.

Achatz, D.E, Heiligtag, F.J., Li, X.H., Link, M., & Wolfbeis, O.S. (2010). Colloidal silica nanoparticles for use in click chemistry-based conjugations and fluorescent affinity assays. *Sensors and Actuators B, 150,* 211-219

Alexis, F., Pridgen, E., Molnar, L.K., & Farokhzad, O.C. (2008). Factors affecting the clearance and biodistribution of polymeric nanoparticles. *Molecular Pharmaceutics, 5,* 505-515.

Al Saleh, F.S., Al Mugren, K.S., & Azzam, A. (2009). Excitation functions of (p,x) reactions on natural nickel between proton energies of 2.7 and 27.5MeV. *Applied Radiation and Isotopes, 65,* 104-113.

Al Saleh, F.S., Mungren, K.S.A., & Azzam, A. (2007). Excitation function measurements and integral yields estimation for ^{nat}Zn(p,x) reactions at low energies. *Applied Radiation and Isotopes, 65,* 1101-1107.

Anferov, V. (2003). Energy degrader optimization for medical beam lines. *Nuclear Instrument and Metheds in Physical Research A, 496,* 222–227.

Antropov, A.E., Gusev, V.P., Zhuravlev, Yu.Yu. Zarubin, P.P., Kolozhvari, A.A., & Smirnov, A.V. (1992). Total cross sections of (p,n) reaction on the nuclei of isotopes nickel and zink at E(p)=5.-6. MeV. *Bulletin of the Russian Academy of Sciences: Physics, 56,* 1829-1835.

Arap, W., Pasqualini, R., Montalti, M., Petrizza, L., Prodi, L., Rampazzo, E., … Marchiò, S. (2013). Luminescent Silica Nanoparticles for cancer diagnosis. *Current Medicinal Chemistry, 20*, 2195-2211.

Asabella, A.N., Cascini, G.L., Altini, C., & Paparella, D. (2014). The Copper Radioisotopes: A Systematic Review with Special Interest to ^{64}Cu. *BioMed Research International*, 2014, 9. Retrieved from http://dx.doi.org/10.1155/2014/786463.

Asad, A.H., Chan, S., Morandeau, L., Cryer, D., Smith, S.V., & Price, R.I. (2014). Excitation functions of ^{nat}Zn(p,x) nuclear reactions with proton beam energy below18 MeV. *Applied Radiation and Isotopes*, *94,* 67-71.

Asad, A.H., Smith, S.V., Chan, S., Jeffery, C.M., Morandeau, L., & Price, R.I. (2012). Cyclotron production of ^{61}Cu using natural Zn & enriched ^{64}Zn targets. *AIP Conference Proceedings, 1509,* 91-95.

Asad, A.H., Smith, S.V., Morandeau, L.M., Chan, S., Jeffery, C.M., & Price, R.I. (2015). Production of ^{61}Cu by the ^{nat}Zn(p,a) reaction: improved separation and specific activity determination by titration with three chelators. *Journal of Radioanalytical and Nuclear Chemistry*, *307,* 899-906.

Avila-Rodriguez, M.A., Nye, J.A., & Nickles, R.J. (2007). Simultaneous production of high specific activity ^{64}Cu and ^{61}Co with 11.4MeV protons on enriched ^{64}Ni nuclei. *Applied Radiation and Isotopes, 65,* 1115-1120.

Avila-Rodriguez, M.A., Wilson, J.S., & McQuarrie, S.A. (2009). The use of radiochromic films to measure and analyse the beam profile of charged particle accelerators. *Applied Radiation and Isotopes, 67,* 2025-2028.

Bae, Y.H., & Park, K. (2011). Targeted drug delivery to tumors: Myths, reality and possibility. *Journal of Controlled Release, 153,* 198-205.

Bagwe, R.P., Yang, C., Hilliard, L.R., & Tan, W. (2004). Optimization of dye-doped silica nanoparticles prepared using a reverse microemulsion method. *Langmuir, 20,* 8336-8342.

Barbe, C., Bartlett, J., Kong, L.G., Finnie, K., Lin, H.Q., Larkin, M., … Calleja G. (2004). Silica Particles: A novel Drug-Delivery System. *Advance Material, 16,* 1959-1966.

Barrandon, J.N., Debrun, J.L., Kohn, A., & Spear, R.H. (1975). A study of the main radioisotopes obtained by irradiation of Ti, V, Cr, Fe, Ni, Cu and Zn with protons from 0 to 20 MeV. *Nuclear Instrument and Methods in Physics, 127,* 269.

Bass, L.A., Wang, M., Welch, M.J., & Anderson, C.J. (2000). In Vivo Transchelation of Copper-64 from TETA-Octreotide to Superoxide Dismutase in Rat Liver. *Bioconjugate Chemistry, 11,* 527-532.

Bazile, D., Prud'homme, C., Bassoullet, M., Marlard, M., Spenlehauer, G., & Veillard, M. (1995). Stealth Me. PEG-PLA nanoparticles avoid uptake by the mononuclear phagocyte system. *Journal Pharmaceutical Science, 84,*493-498.

Berger, M.J, Coursey, J.S., Zucker, M.A., & Chang, J. (2005). Stopping power and range tables for electrons, protons and helium ions. National Institute of Standards and Technology. Retrieved from http://physics.nist.gov/PhysRefData/Star/Text/contents.html.

Beyer, T, Townsend, D.W., Brun, T., Kinahan, P.E., Charron, M., Roddy, R., … Nutt, R. (2000). A combined PET/CT scanner for clinical oncology. *Journal of Nuclear Medicine, 41,* 1369-1379.

Blanco, E., Shen, н., & Ferrari, M. (2015). Principles of nanoparticle design for overcoming biological barriers to drug delivery. *Nature Biotechnology, 33,* 941-951.

Bodmeier, R., & McGinity, J.W. (1988). Solvent selection in the preparation of poly (DL-Lactide) microspheres prepared by the solvent evaporation method. International *Journal Pharmaceutics, 43,* 179-186.

Borchardt, G., Brandriss, S., Kreuter, J., & Margel, S. (1994). Bodv Distribution of 75Se-Radiolabeled Silica Nanbparticles Covalently Coated with w-functionalized Surfactants After Intravenous Injection in Rats. *Journal of Drug Targeting, 2,* 61-77

Boswell, C.A., Sun, X., Niu, W., Weisman, G.R., Wong, E.H., Rheingold, A.L., & Anderson, C.J. (2004). Comparative in vivo stability of copper-64-labeled cross-bridged and conventional tetraazamacrocyclic complexes. *Journal of Medicinal Chemistry, 47,* 1465-1474.

Brahim, S., Narinesingh, D., & Elie, G.A. (2001). Amperometric determination of cholesterol in serum using a biosensor of cholesterol oxidase contained within a polypyrrole hydrogel membrane. *Analytic Chimica Acta, 448,* 27-36.

Burrage, J.W., Asad, A.H., Fox, R., Price, R.I., Campbell, A.M., & Siddiqui, S.A. (2009). A simple method to measure proton beam energy in a standard medical cyclotron. *Australasian Physical and Engineering Science in Medicine, 32,* 1-6.

Butterworth, M.D., Illum, L., & Davis, S.S. (2001). Preparation of ultrafine silica-and PEG-coated magnetite particles. *Colloids Surfaces A, 179,* 93-102.

Chêne, G., Garnir, H-P, Marchal, A., Mathis, F., & Strivay, D. (2008). Improved energy resolution of a cyclotron beam for RBS measurements. *Nuclear Instruments Metheds in Physics Research B, 266,* 2110-2112.

Chakravarty, R., Chakraborty, S., Dash, A., & Pillai, M.R.A. (2013). Detailed evaluation on the effect of metal ion impurities on complexation of generator eluted ^{68}Ga with different bifunctional chelators. *Nuclear Medicine and Biology, 40,* 197-205.

Chakravarty, R., Goel, S., Hong, H., Chen, F., Valdovions, H.F., Hermandez, R., … Cai, W. (2016). Functionalized Hollow Mesoporous Silica Nanoparticles for Tumor Vasculature Targeting and PET Image-Guided Drug Delivery. Nanomedicine (Lond), 10(8), 1233-1246.

Charan, N.B., & Carvalho, P. (2002). Regulation of lung water: role of the bronchial circulation. In: *Pulmonary Biology in Health and Disease*; Bittar EE (Ed.); (Springer-Verlag, NY).

Chen, S.L. (1998). Preparation of monosize silica spheres and their crystalline stack. *Colloids Surf A, 142,* 59-63.

Cherry, S.R., & Gambhir, S.S. (2001). Use of positron emission tomography in animal research. *Institute for Laboratory Animal Resources, 42,* 219 - 232.

Cherry S.R, Sorenson, J.A., Phelps M.E. "Physics in Nuclear Medicine". 3rd ed. Elsevier Science; 2003.

Choi, H.S., Liu, W., Misra, P., Tanaka, E., Zimmer, J.P., Ipe, B.I., … Frangioni, J.V. (2007). Renal clearance of quantum dots. *Nature Biotechnology, 2007,* 1165–1170.

Chung, T.H., Wu, S.H., Yao, M., Lu, C.W., Lin, Y.S., Hung, Y., … Huang, D.M. (2007). The effect of surface charge on the uptake and biological function of mesoporous silica nanoparticles in 3T3-L1 cells and human mesenchymal stem cells.*Biomaterials, 28,* 2959-2966.

Clift, M.J.D., Rothen-Rutishauser, B., Brown, D.M., Duffin, R., Donaldson, K., Proudfoot, L., … Stone V. (2008). The impact of different nanoparticle surface chemistry and size on uptake and toxicity in a murine macrophage cell line. *Toxicology and Applied Pharmacology, 232,* 418-427.

Clogston, J. D., & Patri, A.K. (2011). Zeta potential measurement. *Methods Molecular Biology, 697,* 63-70.

Cohen, B.L., Newman, E., Charpie, R.A., & Handley T.H. (1954). (P,PN) And (P,AN) Excitation Functions. *Physics Review,* 94, 620. Data downloaded via the internet from the IAEA nuclear data section (Experimental Nuclear Reaction Data). Retrieved from http://www.nndc.bnl.gov/exfor/exfor.htm

Ĉomor, J.J., Stevanoviü, Ž., Rajþeviü, M., & Košutiü, D. (2004). Modeling of thermal properties of a TeO_2 target for radioiodine production. *Nuclear Instruments and Methods in Physics Research Section A: Accelerators, Spectrometers, Detectors and Associated Equipment, 521*, 161-170.

Cooper, M.S., Ma, M.T., Sunassee, K., Shaw, K.P., Williams, J.D., Paul, R.L., … Blower P.J. (2012). Comparison of ^{64}Cu-Complexing Bifunctional Chelators for Radioimmunoconjugation: Labeling Efficiency, Specific Activity, and in Vitro/in Vivo Stability. *Bioconjugate Chemistry*, *23*, 1029-1039.

Couverur, P., & Puiseux, F. (1993). Nano- and microparticles for the delivery of peptides and proteins. *Advanced Drug Delivery Review, 5*,141-142.

Craft, J.M., De Silva, R.A., Lears, K.A., Andrews, R., Liang, K., Achilefu, S., & Rogers, B.E. (2012). In vitro and in vivo evaluation of a ^{64}Cu-labeled NOTA-Bn-SCN-Aoc-bombesin analogue in gastrin-releasing peptide receptor expressing prostate cancer. *Nuclear Medicine and Biology*, *39*, 609-616.

Cutler, C.S, Wuest, M., Anderson, C.J., Reichert, D.E., Sun, Y., Martell, A.E., & Welch, M.J. (2000). Labeling and *in Vivo* Evaluation of Novel Copper (II) Dioxotetraazamacrocyclic Complexes. *Nuclear Medicine and Biology, 27,* 375-380.

Danhier, F., Vroman, B., Lecouturier, N., Crokart, N., Pourcelle, V., Freichels, H., … Préat, V. (2009). Targeting of tumor endothelium by RGD-grafted PLGA- nanoparticles loaded with paclitaxel. *Journal of Controlled Release, 140,* 166-173.

Daraban, L., Abbas, K., Simonelli, F., Rebeles, R.A., & Gibson, N. (2008). Experimental study of excitation functions for the deuteron induced

reactions ^{64}Zn-(d,2p)^{64}Cu and ^{64}Zn(d,αn)^{61}Cu using the stacked-foil technique. *Applied Radiation and Isotopes, 66,* 261-264.

Daraban, L., Rebeles, R.A., & Hermanne, A. (2009). Study of the excitation function for the deuteron induced reaction on ^{64}Ni(d,2n) for the production of the medical radioisotope ^{64}Cu. *Applied Radiation and Isot*opes, *67,* 506-510.

Dasgupta, A.K., Mausner, L.F., & Srivastava, S.C. (1991). A new separation procedure for Cu from proton irradiated Zn. *Applied Radiation and Isotopes, 42,* 371-376.

De Silva, R.A, Jain, S., Lears, K.A., Chong, H-S., Kang, C.S., Sun, X., … Rogers, B.E. (2012). Copper-64 radiolabeling and biological evaluation of bifunctional chelators for radiopharmaceutical development. *Nuclear Medicine and Biology, 39,* 1099-1104.

Dearling, J.L.J., Paterson, B.M., Akurathi, V., Betanzos-Lara, S., Treves, S.E., Voss, S.D., … Packard, A.B. (2015). The ionic charge of copper-64 complexes conjugated to an engineered antibody affects biodistribution. *Bioconjugate Chemistry, 26,* 707-717.

Dearling, J.L.J., Voss, S.D., Dunning, P., Snay, E., Fahey, F., Smith, S.V., … Packard A.B. (2011). Imaging cancer using PET: the effect of the bifunctional chelator on the biodistribution of a ^{64}Cu-labeled antibody. *Nuclear Medicine Biology, 38,* 29-38.

Decuzzi, P., Godin, B., Tanaka, T., Lee, S-Y, Chiappini, C., Liu, X., & Ferrari M. (2010). Size and shape effects in the biodistribution of intravascularly injected particles. *Journal of Control Release, 141,*320-327.

Deri, M.A., Zeglis, B.M., Francesconi, L.C., & Lewis, J.S. (2013). PET imaging with ^{89}Zr: From radiochemistry to the clinic. *Nuclear Medicine and Biology*, *40*, 3-14.

Desai, D., Sen Karaman, D., Prabhakar, N., Tadayon, S., Duchanoy, A., Toivola, D.M., … Rosenholm, J.M. (2004). Design considerations for mesoporous silica nanoparticulate systems in facilitating biomedical applications. *Mesoporous Biomater*, *1*, 16-43.

Di Bartolo, N., Sargeson, A.M., & Smith, S.V. (2006). New ^{64}Cu PET imaging agents for personalised medicine and drug development using the hexa-aza cage, SarAr. *Organic and Biomolecullar Chemistry*, *4*, 3350-3357.

Dobrovolskaia, M.A., & McNeil, S.E. (2007). Immunological properties of engineered nanomaterials. *Nature Nanotechnology*, 2, 469-478.

Doselab Software, (2009). Retrieved from http://www.doselab.sourceforge.net/index.html.

Douglas, S.J., Davis, S.S., & Illum, L. (1987). Nanoparticles in drug delivery. *Critical Review in Therapy Drug Carrier System*, *3*, 233-261.

Elomaa, V.V., Jurttila, J., Rajander, J., & Solin, O. (2014). Automation of ^{64}Cu production at Turku PET Centre. *Applied Radiation and Isotopes ,89,* 74-78.

Eloya, J.O., De Souzaa, M.C., Petrilli, R., Barcellos, J.P.A., Lee, R.J., & Marchettia, J.M. (2014). Liposomes as carriers of hydrophilic small molecule drugs: Strategies to enhance encapsulation and delivery. *Colloids and Surf. B: Biointerfaces*, *123*, 345-363.

Elvin, B., Shen, H., & Ferrari, M. (2015). Principles of nanoparticle design for overcoming biological barriers to drug delivery. *Nature Biotechnology*, *33*, 941-951.

Ernsting, M.J, Murakami, M., Roy, A., & Li, S. (2013). Factors controlling the pharmacokinetics, biodistribution and intratumoral penetration of nanoparticles. *Journal of Controlled Release, 172,* 782-794.

Experimental Nuclear Reaction Data (EXFOR); National Nuclear Data Centre (NNDC), Brookhaven, USA, and International Atomic Energy Agency (IAEA), Vienna. Retrieved from http://www.nndc.bnl.gov/exfor/exfor.htm

Foged, C., Brodin, B., Frokjaer, S., & Sundblad, A. (2005). Particle size and surface charge affect particle uptake by human dendritic cells in an in vitro model. *International Journal of Pharmaceutics, 298,* 315-322.

Gagnon, K., Jensen, M., Thisgaard, H., Publicover, J., Lapi, S., McQuarrie, S.A., & Ruth, T.J. (2011). A new and simple calibration-independent method for measuring the beam energy of a cyclotron. *Applied Radiation and Isotopes, 69,* 247-252.

Geiser, M., Rothen-Rutishauser, B., Kapp, N., Schurch, S., Kreyling, W., Schulz, H., … Gehr, P. (2005). Ultrafine Particles Cross Cellular Membranes by Nonphagocytic Mechanisms in Lungs and in Cultured Cells. *Environmental Health Perspectives, 113,* 1555-1560.

Gref, R., Domb, A., Quellec, P., Blunk, T., Mueller, R.H., Verbavatz, J.M., & Langer, R. (1995). The controlled intravenous delivery of drugs using PEG-coated sterically stabilized nanospheres. *Advaced Drug Delivery Reviews, 16,* 215-233.

Gref, R., Lück, M., Quellec, P., Marchand, M., Dellacherie, E., Harnisch, S., … Müller, R.H. (2000). Stealth' corona-core nanoparticles surface modified by polyethylene glycol (PEG): influences of the corona (PEG chain length and surface density) and of the core composition on phagocytic uptake and plasma protein adsorption. *Colloids Surf B Biointerfaces, 18,*301-313.

Gref, R., Minamitake, Y., Peracchia, M.T., Trubetskoy, V., Torchilin, V., & Langer, R. (1994). Biodegradable long-circulating polymer nanospheres. *Science, 263,* 1600-1603.

Gref, R., Couvreur, P., Barratt, G., & Mysiakine, E. (2003). Surface-engineered nanoparticles for multiple ligand coupling. *Biomaterials*, *24,* 4529-4537.

Gruttner, C., & Teller, J. (1999). New types of silica-fortified magnetic nanoparticles as tools for molecular biology applications. *J Magnetism and Magnetic Materials, 194,* 8-15.

Gunasekera, U.A., Pankhurst, Q.A., & Douek, M. (2009). Imaging applications of nanotechnology in cancer. *Target Oncology, 4,*169-81.

Hanafi-Bojd, M.Y., Jaafari, M.R., Ramezanian, N., Xue, M., Amin, M., Shahtahmassebi, N., & Malaekeh-Nikouei, B. (2015). Surface functionalized mesoporous silica nanoparticles as an effective carrier for epirubicin delivery to cancer cells. *European Journal Pharmaceutics and Biopharmaceutics, 89,* 248-258.

He, C., Hu, Y., Yin, L., Tang, C., & Yin, C. (2010). Effects of particle size and surface charge on cellular uptake and biodistribution of polymeric nanoparticles. *Biomaterials, 31,* 3657-3666.

Hermanne, A. (1997). Evaluated cross section and thick target yield data of Zn + p processes for practical applications. Experimental Nuclear Reaction Data. Retrieved from http://www.nndc.bnl.gov/exfor .

Hermanne, A., Tarkanyi, F., Kovalev, S.F. (2007). Activation cross sections of the ^{64}Ni (d,2n) reaction for the production of the medical radionuclide ^{64}Cu. *Nuclear Instruments and Methods in Physcis Research, Section B: Beam Interactions with Materials and Atoms, 258,* 308-312.

Heslinga, M.J., Mastria, E.M., & Eniola-Adefeso, O. (2009). Fabrication of biodegradable spheroidal microparticles for drug delivery applications. *Journal of Control Release, 138*, 235-242.

Hilgers, K., Stoll, T., Skakun, Y., Coenen, H.H. & Qaim, S.M. (2003). Cross-section measurements of the nuclear reactions ^{nat}Zn(d,x)^{64}Cu, ^{66}Zn(d,α)^{64}Cu and ^{68}Zn(p,αn)^{64}Cu for production of ^{64}Cu and technical developments for small-scale production of ^{67}Cu via the ^{70}Zn(p,α)^{67}Cu process. *Applied Radiation and Isotopes*, *59,* 343-351.

Hilgers K., Qaim S.M., & Coenen H.H. (2004). New cross section data for production of the therapeutic radionuclides ^{64}Cu, ^{140}Nd and ^{192}Ir. *Conference Proceedings on Nuclear Data for Science and Technology. 2,* 1631-1633.

Hoit, B.D. (2001). New approaches to phenotypic analysis in adult mice. *Journal of Internal Medicine, 245,* 627-635.

Holland, J.P., Sheh, Y., & Lewis, J.S. (2009). Standardized methods for the production of high specific-activity zirconium-89. *Nuclear Mecidine and Biology*, 36, 729-739.

Hong, H., Zhang, Y., Sun, J., & Cai, W. (2009). Molecular imaging and therapy of cancer with radiolabeled nanoparticles. *Nanotoday, 4*, 399-413.

Hou, X., Jacobsen, U., & Jørgenesen, J.C. (2002). Separation of no-carrier-added ^{64}Cu from a proton irradiated ^{64}Ni enriched nickel target. *Applied Radiation ans Isotopes, 57,* 773-777.

Huang, S., Joso, R., Fuchs, A., Barner, L., & Smith S.V. (2008). Probing Solid-Liquid Interfaces Using Radiotracer Technology: Characterization of Functionalized Microspheres. *Chemistry of Materials, 20,* 5375-5380.

IAEA (2009). Charged-particle cross section data base for medical radioisotope production. Monitor reactions. Retrieved from (http://www-nds.iaea.org/medical/monitor_reactions.html).

Jain, R.A. (2000). The manufacturing techniques of various drug loaded biodegradable poly (lactide-co-glycolide) (PLGA) devices. *Biomaterials, 21*, 2475-2490.

Jain, T.K., Roy, I., De, T.K., & Maitra, A. (1998). Nanometer silica particles encapsulating active compounds: A novel ceramic drug carrier. *Journal of American Chemical Society, 120*, 11092-11095.

Jalilian, A.R., Rostampour, N., Rowshanfarzad, P., Shafaii, K., Dehghan, M.K., & Akhlaghi, M. (2009). Preclinical studies of [61Cu] ATSM as a PET radiopharmaceutical for fibrosarcoma imaging. *Acta Pharmaceutic*, *59,* 45-55.

Jalilian, A.R., Shanesazzadeh, S., Rowshanfarzad, P., Bolourinovin, F., & Majdabadi, A. (2008). Biodistribution study of [61Cu] pyruvaldehyde-bis (N-4 methlthiosemicarbazone) in normal rats as a PET tracer. *Journal of Nuclear Science and Technology ,19,* 159-164.

Jarrett, B. R., Gustafsson, B., Kukis, D.L., & Louie, A.Y. (2008). Synthesis of ^{64}Cu-Labeled Magnetic Nanoparticles for Multimodal Imaging. *Bioconjugate Chemistry, 19,* 1496-1504.

Jeffery, C.M., Smith, S.V., Asad, A.H., Chan, S., & Price, R.I. (2012). Routine production of copper-64 using 11.7 MeV protons. AIP Conference Proceedings, 1509, 84-90.

Jin, Y., Lohstreter, S., Pierce, D.T., Parisien, J., Wu, M., Hall, C., & Zhao, J.X. (2008). Silica nanoparticles with continuously tunable sizes: synthesis and size effects on cellular contrast imaging. *Chemistry of Materials, 20,* 4411-4419.

Johnson, C.H., Trail, C.C., & Galonsky, A. (1964). Thresholds for (p,n) reactions on 26 intermediate-weight nuclei. *Physics Review, 136,* B179.

Jones-Wilson, T.M., Deal, K.A., Anderson, C.J., McCarthy, D.W., Kovacs, Z., Motekaitis, R.J., … Welch, M.J. (1998). The *In Vivo* Behavior of Copper-64-Labeled Azamacrocyclic Complexes. *Nuclear Medicine and Biology, 25,* 523-530.

Juliano, R.L., & Stamp, D. (1975). The effect of particle size and charge on the clearance rates of liposomes and lipsome encapsulated drugs. *Biochemical and Biophyscial Research Communications, 63,* 651-658.

Kamaly, N., Xiao, Z., Valencia, P.M., Radovic-Moreno, A.F., & Farokhzad, O.C. (2012). Targeted polymeric therapeutic nanoparticles: desgn, development and clinical translation. *Chemistry Society Review, 41,* 2971-3010.

Kapoor, V., McCook, B.M., & Torok, F.S. (2004). An Introduction to PET-CT Imaging. *RadioGraphics, 24,* 523-543.

Kastleiner, S., Coenen, H.H., & Qaim, S.M. (1999). Possibility of production of ^{67}Cu at a small-sized cyclotron via the (p,α)- reaction on enriched ^{70}Zn. Radiochimica Acta *,84,* 107-110.

Ke, R., Yang, W., Xia, X., Xu, Y., & Li, Q. (2010). Tandem conjugation of enzyme and antibody on silica nanoparticle for enzyme immunoassay. *Analytical Biochemistry, 406,* 8-13.

Kim, J.H., Park, H., & Chun, K.S. (2001). Effective Separation Method of ^{64}Cu from ^{67}Ga waste product with a solvent extraction and chromatography. *Applied Radiation and Isotopes, 68,* 1623-1626

Kim, J.H., Park, H., Kim, S., Lee, J.S., & Chun, K.S. (2006). Proton beam energy measurement with the stacked Cu foil technique for medical radioisotope production. *Journal of the Korean Physical Society, 48,* 755-758.

Klibanov, A.L., Maruyama, K., Torchilin, V.P., & Huang, L. (1990). Amphipathic polyethyleneglycols effectively prolong the circulation time of liposomes. *FEBS Research Letter, 268,* 235-237.

Knop, K., Hoogenboom, R., Fischer, D., & Schubert, U.S. (2010). Poly (ethylene glycol) in drug delivery: pros and cons as well as potential alternatives. *Angewandte Chemie International Edition, 49,* 6288-6308.

Kong, L., Mume, E., Triani, G., & Smith, S.V. (2013). Optimizing Radiolabeling Amine-Functionalized Silica Nanoparitcles Using SarAr-NCS for Applications in Imaging and Radiotherapy. *Langmuir, 29,* 5609-5616

Kopecky, P. (1985). Proton beam monitoring via the $Cu(p,x)^{58}Co$, $^{63}Cu(p,2n)^{62}Zn$ and $^{65}Cu(p,n)^{65}Zn$ reactions. *The International Journal Applied Radiation and Isotopes, 36,* 657-661.

Kopecky, P. (1990). Cross sections and production yields of ^{66}Ga and ^{67}Ga for proton reactions in natural zinc. *Applied Radiation and Isotopes, 41,* 606.

Kormány, Z. (1994). A new method and apparatus for measuring the mean energy of cyclotron beams. *Nuclear Instruments Metheds in Physics Research A, 337,* 258-264.

Kraeber-Bodéré, F., Rousseau, C., Bodet-Milin, C., Mathieu, C., Guérard, F., Frampas, E., … Barbet, J. (2015). Tumor immunotargeting using innovative radionuclides. *International Journal of Molecular Sciences,* 16, 3932-3954.

Krishnaraj, C., Muthukumaran, P., Ramachandran, R., Balakumaran, M.D., & Kalaichelvan, P.T. (2014). Acalypha indica Linn: Biogenic synthesis of silver and gold nanoparticles and their cytotoxic effects against MDA-MB-231, human breast cancer cells. *Biotechnology Reports, 4,* 42-49.

Kumari, A., Yadav, S.K., & Yadav, S.C. (2010). Biodegradable polymeric nanoparticles based drug delivery systems. *Colloids and Surfaces B: Biointerfaces, 75,* 1-18.

Laforest, R., Dehdashti, F., Lewis, J.S., & Schwarz, S.W. (2005). Dosimetry of 60/61/62/64Cu-ATS: a hypoxia imaging agent for PET. *European Journal of Nuclear Medicine and Molecular Imaging, 32,* 764-770.

Lang, L., Ma, Y., Kiesewetter, D.O., & Chen, X. (2014). Stability Analysis of Glutamic Acid Linked Peptides Coupled to NOTA through Different Chemical Linkages. *Molecular Pharmaceutics, 11,* 3867-3874.

Letchford, K., & Burt, H. (2007). A review of the formation and classification of amphiphilic block copolymer nanoparticulate structures: micelles, nanospheres, nanocapsules and polymersomes. *European Journal Pharmaceutics and Biopharmaceutics, 65,* 259-269.

Levkovskij, V.N. (1991). Activation cross section nuclides of average masses (A=40-100) by protons and alpha-particles with average energies (E=10-50 MeV). Data downloaded via the internet from the IAEA nuclear data section (Experimental Nuclear Reaction Data). Retrieved from http://www.nndc.bnl.gov/exfor/exfor.htm

Lewis, M.R., Boswell, C.A., Laforest, R., Buettner, T.L., Ye, D., Connett, J.M., & Anderson, C.J. (2001). Conjugation of monoclonal antibodies with TETA using activated esters: Biological comparison of ^{64}Cu-TETA-1A3 with ^{64}Cu-BAT-2IT-1A3. *Cancer Biotherapy Radiopharmaceuticals, 16,* 483-494.

Li, S.D., & Huang, L. (2008). Pharmacokinetics and biodistribution of nanoparticles. *Molecular Pharmaceutics,* 496-504.

Liberman, A., Mendez, N., Trogler, W.C., & Kummel, A.C. (2014). Synthesis and surface functionalization of silica nanoparticles for nanomedicine. *Surface Science Reports, 69,* 132-158.

Lin, X., Zhao, N., Yan, P., Hu, H. & Xu, F.-J. (2015). The shape and size effects of polycation functionalized silica nanoparticles on gene transfection. *Acta Biomaterialia, 11,* 381-392.

Lin, Y.-S. & Haynes, C.L. (2010). Impacts of Mesoporous Silica Nanoparticle Size, Pore ordering and Pore Integrity on Hemolytic Activity. *Journal of American Chemistry Society, 132,* 4834- 4842.

Little, F.E., & Lagunas-Solar, M.C. (1983). Cyclotron production of ^{67}Ga. Cross section and thick-target yields for the ^{67}Zn(p,n) and ^{68}Zn(p,2n) reactions. *Applied Radiation and Isotopes, 34,* 631.

Liu, D.M., & Chen, I.W. (1999). Encapsulation of protein molecules in transparent porous silica matrices via an aqueous colloidal sol-gel process. *Acta Materialia, 47,* 4535- 4544.

Liu, L., Wu, S., Jing, F., Zhou, H., Jia, C., Li, G., …Zhao, J. (2016). Bead-based microarray immunoassay for lung cancer biomarkers using quantum dots as labels. *Biosensors and Bioelectronics 80,* 300-306.

Liu, S. (2008). Bifunctional coupling agents for radiolabelling of biomolecules and target-specific delivery of metallic radionuclides. *Advance Drug Delivery Reviews, 60,* 1347-1370.

Liu, S., Li, Z., & Conti, P.S. (2014). Development of Multi-Functional Chelators Based on Sarcophagine Cages. *Molecules, 19,* 4246-4255.

Liu, Y., & Welch, M.J. (2012). Nanoparticles Labeled with Positron Emitting Nuclides: Advantages, Methods, and Applications. *Bioconjugate Chemistry, 23,* 671-682.

Livingston, J.N. (1999). Genetically engineered mice in drug development. *Journal of Internal Medicine, 245,* 627-635.

Lorenz, S., Hauser, C.P., Autenrieth, B., Weiss, C.K., Landfester, K., & Mailänder, V. (2010). The softer and more hydrophobic the better: influence of the side chain of polymethacrylate nanoparticles for cellular uptake. *Macromolecular Biosciences, 10,* 1034-1042.

Lu, F., Wu, S-H, Hung, Y. & Mou, C-Y. (2009). Size effect on cell uptake in well suspended, uniform mesoporous silica nanoparticles. *Small, 5,* 1408-1413.

Lu, J., Liong, M., Zink, J.I., & Tamanoi, F. (2007). Mesoporous Silica Nanoparticles as a Delivery System for Hydrophobic Anticancer Drugs. *Small, 3,* 1341-1346.

Maeda, H. (2012). Macromolecular therapeutics in cancer treatment: the EPR effect and beyond. *Journal of Control Release, 164,*138-144.

Maeda, H., Bharate, G.Y., & Daruwalla, J. (2009). Polymeric drugs for efficient tumor-targeted drug delivery based on EPR-effect. *European Journal of Pharmaceuticals and Biopharmaceuticals, 71,* 409-419.

Maeda, H., Nakamura, H., & Fang, J. (2013). The EPR effect for macromolecular drug delivery to solid tumors: Improvement of tumor uptake, lowering of systemic toxicity, and distinct tumor imaging in vivo. *Advance Drug Delivery Review, 65,* 71-79.

Maeda, H., Sawa, T., & Konno, T. (2001). Mechanism of tumor-targeted delivery of macromolecular drugs, including the EPR effect insolid tumor and clinical overview of the prototype polymeric drug SMANCS. *Journal of Controlled Release, 74,* 47–61.

Maeda, H., Ueda, M., Morinaga, T., & Matsumotog T. (1985). Conjugation of poly (styrene-co-maleic acid) derivatives to the antitumor protein-neocarzinostatin: pronounced improvements in pharmacological properties. *Journal of Medicinal Chemistry, 28,*455-461.

Makino, K., Yamamoto, N., Higuchi, K., Harada, N., Ohshima, H., & Terada H. (2003). Phagocytic uptake of polystyrene microspheres by alveolar

macrophages: effects of the size and surface properties of the microspheres. *Colloids and Surfaces B, 27,* 33-39.

Manrique-Arias, J.C., & Avila-Rodriguez, M.A. (2014). A simple and efficient method of nickel electrodeposition for the cyclotron production of ^{64}Cu. *Applied Radiation and Isot*opes, *89,* 37-41.

Martinez, M.J., Ziegler, S.I., & Beyer, T. (2008). PET and PET/CT: Basic Principles and Instrumentation" in PET in Oncology. Berlin, Heidelberg: Springer.

Massoud, T.K., & Gambhir, S.S. (2003). Molecular imaging in living subjects: seeing fundamental biological processes in a new light. *Genes & Development, 17,* 545-580.

Mastren, T., Guthrie, J., Eisenbeis, P., Voller, T., Mebrahtu, E., Robertson, J.D., & Lapi, S.E. (2014). Specific Activity Measurement of ^{64}Cu: A comparison of Methods. *Applied Radiation and Isotopes, 90,* 117–121

Matarrese, M., Bedeschi, P., Scardaoni, R., Sudati, F., Savi, A., Pepe, A., ... Fazio, F. (2010). Automated production of copper radioisotopes and preparation of high specific activity [(^{64})Cu]Cu-ATSM for PET studies. *Applied Radiation and Isotopes, 68,* 5-13.

Matsumura, Y., & Maeda, H. (1986). A new concept for macromolecular therapeutics in cancer chemotherapy: mechanism of tumoritropic accumulation of proteins and the antitumor agent SMANCS. *Cancer Research, 46,* 6387-6392.

McCarthy, D.W., Bass, L.A., Cutler, P.D., Shefer, R.E., Klinkowstein, R.E, Herrero, P., … Welch, M.J. (1999). High purity production and potential

applications of copper-60 and copper-61. *Nuclear Medicine and Biology, 26*, 351-358.

McCarthy, D.W., Shefer, R.E., Klinkowstein, R.E., Bass, L.A., Margeneau, W.H., Cutler, C.S., … Welch M.J. (1997). Efficient Production of High Specific Activity 64Cu Using A Biomedical Cyclotron. *Nuclear Medicine and Biology, 24*, 35-43.

McDevitt, M.R., Chattopadhyay, D., Kappel, B.J., Jaggi, J.S., Schiffman, S.R., Antczak, C.,… Scheinberg, D.A. (2007). Tumor Targeting with Antibody-Functionalized Radiolabeled Carbon Nanotubes. *The Journal of Nuclear Medicine, 48*, 1180-1189.

Mironava, T., Hadjiargyrou, M., Simon, M., Jurukovski, V., & Rafalovich, M. H. (2010). Gold nanoparticles cellular toxicity and recovery: Effect of size, concentration and exposure time. *Nanotoxicology, 4*, 120-137.

Miteva, M., Kirkbride, K.C., Kilchrist, K.V., Werfel, T.A., Li, H., Nelson, C.E., … Duvall, C.L. (2015). Tuning PEGylation of mixed micelles to overcome intracellular and systemic siRNA de &y barriers. *Biomaterials*, *38*, 97-107.

Moghimi, S.M. (1995). Mechanisms of splenic clearance of blood cells and particles: towards development of new splenotropic agents. Advanced Drug Delivery Reviews 17, 103-115.

Moghimi, S.M., Hunter, A.C., & Murray, J.C. (2001). Long-Circulating and Target-Specific Nanoparticles: Theory to Practise. *Pharmacological reviews, 53*, 283-318.

Moghimi, S.M., & Szebeni, J. (2003). Stealth liposomes and long circulating nanoparticles: critical issues in pharmacokinetics, opsonization and protein-binding properties. *Progress in Lipid Research, 42*,463-478.

Mohanraj, V.J., & Chen, Y. (2006). Nanoparticles - A Review. *Tropical Journal of Pharmaceuticals Research, 5,* 561-573.

Moi, M.K., Meares, C.F., McCall, M.J., Cole, W.C., & De Nardo, S.J. (1985). Copper chelates as probes of biological systems: stable copper complexes with a macrocyclic bifunctional chelating agent. *Analytical Biochemistry, 148,* 249-53.

Mume, E., Asad, A., Di Bartolo, N.M., Kong, L., Smith, C., Sargeson, A.M., … Smith, S.V. (2013). Synthesis of Hexa Aza Cages, SarAr-NCS and AmBaSar and a study of their metal complexation, conjugation to nanomaterials and proteins for application in radioimaging and Therapy". *Dalton Transaction, 42,* 14402-14410.

Nanni, C., Di Leo, K., Tonelli, R., Pettinato, C., Rubello, D., Spinelli, A., … Fanti, S. (2007). FDG small animal PET permits early detection of malignant cells in a xenograft murine model. *European Journal of Nuclear Medicine Molecular Imaging, 34,*755-762.

Naoki Nakajima, N., & Ikada, Y. (1995). Mechanism of Amide Formation by Carbodiimide for Bioconjugation in Aqueous Media. *Bioconjugate Chemistry, 6,* 123-130.

Nishioka, Y., & Yoshino, H. (2001). Lymphatic targeting with nanoparticulate system. *Advance Drug Delivery Reviews, 47,* 55-64.

Nortier, F.M., Mills, S.J., & Steyn, G.F. (1991). Excitation functions and yields of relevance to the production of ^{67}Ga by proton bombardment of ^{nat}Zn and ^{nat}Ge up to 100 MeV. *Applied Radiation and Isotopes, 42,* 353.

Noshad, H., & Bahador, S.S. (2012). Investigation on energy straggling of

protons via Fokker-Planck equation. *Nuclear Instrument and Metheds in Physical Research B, 288,* 89-93.

Nye, J.A., Avila-Rodriguez, M.A., & Nickles, R.J. (2007). A new binary compound for the production of ^{124}I via the ^{124}Te(p,n)^{124}I reaction. *Applied Radiation and Isotopes, 65,* 407-412.

Obata, A., Kasamatsu, S., McCarthy, D.W., Welch, M.J., Saji, H., Yonekura, Y., & Fujibayashi, Y. (2003). Production of therapeutic quantities of ^{64}Cu using a 12 MeV cyclotron. *Nuclear Medicine and Biology, 30,* 535-539.

Orcutt, K.D., Rhoden, J.J., Ruiz-Yi, Benjamin, Frangioni, J.V., & Wittrup, K.D. (2012). Effect of Small Molecule Binding Affinity on Tumor Uptake In Vivo: A Systematic Study Using a Pretargeted Bispecific Antibody. Molecular Cancer Therapeutics, 11(6), 1365-1372.

Osaka, T., Nakanishi, T., Shanmugam, S., Takahama, S., & Zhang, H. (2009). Effect of surface charge of magnetite nanoparticles on their internalization into breast cancer and umbilical vein endothelial cells. *Colloids Surf B Biointerfaces, 71,*325-330.

Osseo-Asare, K., & Arriagada, F.J. (1990). Preparation of SiO_2 Nanoparticles in a Non-Ionic Reverse Micellar System. *Colloids and Surfaces, 50,* 321-339

Ottobrini, L., Ciana, P., Biserni, A., Lucignani, G., & Maggi, A. (2006). Molecular imaging: A new way to study molecular processes in vivo. *Molecular and Cellular Endocrinology, 246,* 69-75.

Oude Munnink, T.H., Nagengast, W.B., Brouwers, A.H., Schröder, C.P.,

Hospers, G.A., Lub-de Hooge, M.N,…de Vries, E.G.E. (2009). Molecular imaging of breast cancer. *The Breast, 18,* S66–S73.

Ownes, D.E., & Peppas, N.A. (2006). Opsonization, biodistribution, and pharmacokinetics of polymeric nanoparticles. *International Journal of Pharmaceutics, 307,* 93-102.

Pan, L., He, Q., Liu, J., Chen, Y., Ma, M., Zhang, L., & Shi, J. (2012). Nuclear-targeted drug delivery of TAT peptide-conjugated monodisperse mesoporous silica nanoparticles. *Journal of American Chemistry Society*, 134, 5722-5725.

Papageorgiou, I., Brown, C., Schins, R., Singh, S, Newson, R., Davis, S., … Case, C.P. (2007). The effect of nano-and micron-sized particles of cobalt-chromium alloy on human fibroblasts in vitro. *Biomaterials, 28,* 2946-2958.

Papash, A.I., & Alenitsky, Yu.G. (2008). Commercial Cyclotrons. Part I: Commercial Cyclotrons in the Energy Range 10-30 MeV for Isotope Production. *Physics of Particles and Nuclei, 39,* 597–631.

Paterson, B., M, Buncic, G., McInnes, L.E., Roselt, P., Cullinane, C., Binns, D.S., … Donnelly, P.S. (2014). Bifunctional ^{64}Cu-labelled macrobicyclic cage amine isothiocyanates for immuno-positron emission tomography. *Dalton Transactions, 44,* 4901-4909.

Patra, A., Sominska, E., Ramesh, S., Koltypin, Y., Zhong, Z., Minti, H., & Reisfeld, R. (1999). Sonochemical Preparation and Characterization of Eu2O3 and Tb2O3 Doped in and Coated on Silica and Alumina Nanoparticles. *Journal of Physical Chemistry B, 103,* 3361-3365.

Peng, F., Lutsenko, S., Sun, X., & Muzik, O. (2012). Positron Emission Tomography of Copper Metabolism in the *Atp7b*−/− Knock-out Mouse Model of Wilson's disease. *Molecular Imaging and Biology, 14*, 70-78.

Pengo, P., & Pasquato, L. (2015). Gold nanoparticles protected by fluorinated ligands: Syntheses, properties and applications. *Journal of Fluorine Chemistry, 177*, 2-10.

Piel, H., Qaim, S.M., & Stoecklin, G. (1992). Excitation functions of (p,xn)-reactions on ^{nat}Ni and highly enriched ^{62}Ni: Possibility of production of medically important radioisotope ^{62}Cu at a small cyclotron. *Radiochimica Acta*, 57, 1-5.

Pillai, G. (2014). Nanomedicines and Those under Various Stages of Development. *SOJ Pharmacy & Pharmaceutical Sciences 1*, 13.

Pillips, M.A., Gran, M.L., Peppas, N.A. (2010). Targeted nanodelivery of drugs and diagnostics. *Nanotoday, 5,* 143-159.

Qaim, S.M. (1982). Nuclear data relevant to cyclotron produced short-lived medical isotopes. *Radiochimca Acta, 30,* 147-162.

Qaim, S.M., Stocklin, G., & Weinreich, R. (1997). Excitation functions for formation of neutron deficient isotopes of bromine and krypton via high-energy deuteron induced reactions on bromine - production of ^{77}Br, ^{76}Br and ^{79}Kr. *Applied Radiation and Isotopes, 28,* 947-953.

Rahman, I.A., & Padavettan, V. (2012). Synthesis of Silica Nanoparticles by Sol-Gel: Size-Dependent Properties, Surface Modification, and Applications in Silica-Polymer Nanocomposites-A Review. *Journal of Nanomaterials, 2012,* 1-15. Retrieved from http://www.hindawi.com/journals/jnm/2012/132424/

Rao, J.P., Gruenberga, P., & Geckelera, K.E. (2015). Magnetic zero-valent metal polymer nanoparticles: Current trends, scope, and perspectives. *Progress in Polymer Science, 40,* 138-147.

Rebeles, R.A., Winkel, P.V., Hermanne, A., & Tárkányi, F. (2009). New measurement and evaluation of the excitation function of ^{64}Ni(p,n) reaction for the production of ^{64}Cu. *Nuclear Instruments and Methods in Physics Research Section B ,267,* 457-461.

Reichert, D.E, Lewis, J.S., & Anderson, C.J. (1999). Metal complexes as diagnostic tools. *Coordination Chemistry Review, 184,* 3-66.

Rejman, J., Oberle, V., Zuhorn, I.S., & Hoekstra, D. (2004). Size-dependent internalization of particles via the pathways of clathrinand caveolae-mediated endocytosis. *Biochemistry Journal, 377,* 159-169.

Rogers, B.E., Bigott, H.M., McCarthy, D.W., Della Manna, D., Kim, J., Sharp, T.L., & Welch M.J. (2003). MicroPET imaging of a gastrin-releasing peptide receptor-positive tumor in a mouse model of human prostate cancer using a ^{64}Cu-labeled bombesin analog. *Bioconjugate Chemistry,14,*756-763.

Rogers, B.E., Della Manna, D., & Safavy, A. (2004). In vitro and in vivo evaluation of a ^{64}Cu-labeled polyethylene glycol bombesin conjugate. *Cancer Biotherapy Radiopharmaceuticals, 19,* 25–34.

Rossi, L.M., Shi, L., Quina, F.H., & Rosenzweig, Z. (2005). Stober synthesis of monodispersed luminescent silica nanoparticles for bioanalytical assays. *Langmuir, 21,* 4277-4280.

Rowshanfarzad, P., Sabet, M., Jalilian, A.R., & Kamalidehghan, M. (2006). An overview of copper radionuclides and production of 61Cu by proton

irradiation of natZn at a medical cyclotron. *Applied Radiation and Isotopes, 64,* 1563-1573

Royal Adelaide Hospital, Department of Nuclear Medicine. (2015). Positron Emission Tomography [image]. Retrieved from http://www.rah.sa.gov.au/nucmed/PET/pet_info.htm

Razzazan, A., Atyabi, F., Kazemi, B., & Dinarvand, R. (2015). In vivo drug delivery of gemcitabine with PEGylated single-walled carbon nanotubes. *Materials Science and Engineering C, 62,* 614-625.

Ryu, J.H., Lee, S., Son, S., Kim, S.H., Leary, J.F., Choi, K., & Kwon, I.C. (2014). Theranostic nanoparticles for future personalized medicine. *Journal of Controlled Release, 190,* 477-484.

Sadeghi, M., Aboudzadeh, M., Zali, A., & Zeinali, B. (2009). ^{86}Y production via ^{86}Sr(p,n) for PET imaging at a cyclotron, 2009. *Applied Radiation and Isotopes, 67,* 1392-1396.

Sadeghi, M., Enferadi, M., & Nadi, H. (2011). ^{45}Ti, a candidate for positron emission tomography: Study of the cyclotron production. *Radiochemistry, 53,*411-414.

Sadeghi, M., Kakavand, T., Mokhtari, L., & Gholamzadeh, Z. (2009B). Determination of ^{68}Ga production parameters by different reactions using ALICE and TALYS codes. *Pramana -Journal of Physics, 72,* 335-341.

Saha, R.N., Vasanthakumar, S., Bende, G., & Snehalatha, M. (2010). Nanoparticulate drug delivery systems for cancer chemotherapy. *Molecular Membrane Biology, 27,* 215-231.

Saji, H. (2004). Development of radiopharmaceuticals for molecular imaging. *International Congress Series, 1264,* 139-147.

Santra, S., Zhang, P., Wang, K., Tapec, R., & Tan, W. (2001). Conjugation of biomolecules with luminophore-doped silica nanoparticles for photostable biomarkers. *Analytical Chemistry, 73,* 4988-4993.

Scharli, R.K., Price, R.I., Chan, S., Cryer, D., Jeffery, C.M., Asad, A.H., … Katsifis, A., 2012. Establishing reliable production of the PET isotope ^{89}Zr for research use: from target fabrication to preclinical imaging. *AIP Conference Proceedings, 1509,* 101-107. Retrieved from http://dx.doi.org/10.1063/1.4773949

Schiller, E., Bergmann, R., Wunderlich, G., Andreeff, M., Jacob, A. & Pietzsch, H-J. (2013). Ga-68- and Cu-64-Labeled NOTA-Albumin Conjugates forPET Sentinel Lymph Node Imaging. *ISRN Molecular Imaging, Article ID 386976, 8 pages*.

Schubert, U., Husing, N., & Lorenz, A. (1995). Hybrid inorganic-organic materials by sol gel processing of organofunctional metal alkoxides. *Chemistry of Materials, 7,* 2010- 2027.

Schwarzbach, R., Zimmermann, K., Blaeuenstein, P., Smith, A., & Schubiger, P.A. (1995). Development of a simple and selective separation of 67-Cu from irradiated zinc for use in antibody labelling (A comparison of methods). *Applied Radiation and Isotopes, 46,*329-336.

Selvaraj, S., Karthikeyan, J., & Saravanakumar, N. (2012). Chitosan loaded microspheres as an ocular delivery system for acyclovir. *International Journal of Pharmacy and Pharmaceutical Sciences, 4,* 125-132.

Shang L., Nienhaus K., & Nienhaus, G.U. (2014). Engineered nanoparticles interacting with cells: size matters. *Journal of Nanobiotechnology, 12,* 1-5. Retrieved from http://www.jnanobiotechnology.com/content/12/1/5

Shibata, S., Taniguchi, T., Yano, T., & Yamane, M. (1997). Formation of water soluble dye-doped silica particles. *Journal of Sol-Gel Science and Technology*, *10*, 263-268.

Silva, G.A. (2007). Nanotechnology approaches for drug and small molecule delivery across the blood brain barrier. *Surgical Neurology, 67,* 113-116.

Singer, J.H. (1987). The Use of Polystyrene Latexes in Medicine. In El-Aasser, M.S., Fitch, R.M. (Eds), *Future Directions in Polymer Colloids* (pp 371-394). NATO ASI series, Racin, Wisconsin; Martinus Nijhoff.

Singh, B.P., Sharma, M.K., Mustafa, M.M., Bhardwaj, H.D., & Prasad, R. (2006). A study of pre-equilibrium emission in some proton- and alpha-induced reactions. *Nuclear Instrument and Methods in Physics Research Section A, 562*, 717-720.

Slowing, I.I., Trewyn, B.G., Giri, S., Lin, V.S.-Y. (2007). Mesoporous Silica Nanoparticles for Drug Delivery and Biosensing Applications *Advance Functional Materials, 17*, 1225–1236

Slowing, I.I., Vivero-Escoto, J.L., Wu, C.W., & Lin, V.S.Y. (2008). Mesoporous silica nanoparticles as controlled release drug delivery and gene transfection carriers. *Advanced Drug Delivery Review 60,* 1278-1288.

Smith, S.V. (2004). Molecular imaging with copper-64. *Journal of Inorganic Biochemistry*, *98,* 1874-1901.

Smith, S.V. (2008). SarAr technology for the application of copper-64 in biology and materials science. The *Quarterly Journal of Nuclear Medicine and Molecular Imaging, 52*, 193-202.

Soppimath, K.S., Aminabhavi, T.M., Kulkarni, A.R., & Rudzinski, W.E. (2001). Biodegradable polymeric nanoparticles as drug delivery devices. *Journal of Controlled Release, 70,* 1-20.

Stöber, W., Fink, A. & Bohn, E. (1968). Controlled growth of monodisperse silica spheres in the micron size range. *Journal of Colloid Interface Science, 26,* 62-69.

Strijckmans, K. (1994). Charged particle accelerators. In: Chemical Analysis by Nuclear Methods (Alfassi Z.B., [Ed.], Chichester, UK, Wiley) pp 64-74.

Strijckmans, K. (2001) .The isochronous cyclotron: principles and recent developments. *Computerized Medical Imaging and Graphics, 25*, 69-78.

Sun, X., Rossin, R., Turner, J.L., Becker, M.L., Joralemon, M.J., Welch, M.J. & Wooley, K.L. (2005). An Assessment of the Effects of Shell Crosslinked Nanoparticle Size, Core Composition, and Surface PEGylation on In Vivo Biodistribution. *Biomacromolecules, 6,* 2541-2554.

Sundaresan, V., Menon, V.U., Rahimi, M., Nguyen, K.T., Aniket S., & Wadajkar, A.S. (2014). Dual-responsive polymer-coated iron oxide nanoparticles for drug delivery and imaging applications. *International Journal of Pharmaceutics, 466*, 1-7.

Suzuki, K., Satake, M., Suwada, J., Oshikiri, S., Ashino, H., Dozono, H., … Minamizawa, T. (2011). Synthesis and evaluation of a novel ^{68}Ga-chelate-conjugatedbisphosphonate as a bone-seeking agent for PET imaging. *Nuclear Medicine and Biology, 38,* 1011-1018.

Szelecsényi, F., Blessing, G., & Qaim, S.M. (1993). Excitation function of proton induced nuclear reactions on enriched ^{61}Ni and ^{64}Ni: possibility of

production of no-carrier-added ^{61}Cu and ^{64}Cu at a small cyclotron. *Applied Radiation and Isotopes, 44*, 575-580.

Szelecsényi, F., Boothe, T.E., Takács, S., Tárkányi, F., & Tavano, E. (1998). Evaluated cross section and thick target yield data bases of Zn+p processes for practical applications. *Applied Radiation and Isotopes, 49,* 1005.

Szelecsényi, F., Kovács, Z., Suzuki, K., Okada, K., van der Walt, T.N., Steyn, G. F., & Mukherjee, S. (2005). Production possibility of ^{61}Cu using proton induced nuclear reactions on zinc for PET studies. *Journal of Radioanayltical and Nuclear Chemistry, 263,* 539-546.

Szelecsényi, F., Steyn, G.F., Kovács, Z., Vermeulen, C., van der Meulen, N.P., Dolley, S.G., … Mukai, K. (2005B). Investigation of the ^{66}Zn(p,2pn)^{64}Cu and ^{68}Zn(p,x)^{64}Cu nuclear processes up to 100 MeV: Production of ^{64}Cu. *Nuclear Instruments and Methods in Physics Research Section B ,240,* 625-637.

Table of Nuclides. Retrieved from http://atom.kaeri.re.kr/.

Tai, Y-C, Ruangma, A., Rowland, D., Siegel, S., Newport, D.F., Chow, P.L. & Laforest, R. (2005). Performance Evaluation of the microPET Focus: A Third-Generation microPET Scanner Dedicated to Animal Imaging. *Journal of Nuclear Medicine, 46,* 455-463.

Tamba, B.I., Dondas, A., Leon, M., Neagu, A.N., Dodi, G., Stefanescu, C., & Tijani, A. (2015). Silica nanoparticles: Preparation, characterization and in vitro/in vivo biodistribution studies. *European Journal of Pharmaceutical Sciences, 71*, 46-55

Tanaka, S., Furukawa, M. (1959). Excitation Functions for (p,n) Reactions with Titanium, Vanadium, Chromium, Iron and Nickel up to 14 MeV. *Journal of the Physcial Society of Japan, 14*,1269.

Tanaka, S., Furukawa, M., & Chiba, M. (1972). Nuclear reactions of nickel with protons up to 56 MEV. *Journal of Inorganic and Nuclear Chemistry,* 34, 2419-2426.

Tang, F., Li, L., & Chen, D. (2012). Mesoporous silica nanoparticles: synthesis, biocompatibility and drug delivery. *Advanced Materials, 24,* 1504-1534.

Tang, L., & Cheng, J. (2013). Nonporous silica nanoparticles for nanomedicine application. *Nano Today, 8,* 290-312.

Tàrkànyi, F., Ditrói, F., Csikai, J., Takàcs, S., Uddin, M.S., Hagiwara, M., … Dityuk, A.I. (2005). Activation cross-sections of long-lived products of proton-induced nuclear reactions on zinc. *Applied Radiation and Isotopes, 62,* 73-81.

Tárkányi, F., Szelecsényi, F., Kovács, Z., & Sudar, S. (1990). Excitation functions of proton induced nuclear reactions on enriched ^{66}Zn, ^{67}Zn and ^{68}Zn-production of ^{67}Ga and ^{66}Ga. *Radiochimica Acta, 50,* 19.

Thieme, S., Walther, M., Pietzsch, H-J., Henniger, J., Preusche, S., Mäding, P., & Steinbach, J. (2012). Module-assisted preparation of ^{64}Cu with high specific activity. *Applied Radiation and Isotopes, 70,* 602-608.

Thieme, S., Walther, M., Preusche, S., Rajander, J., Pietzsch, H., Lill, J., ... Steinbach, J. (2013). High specitic activity ^{61}Cu via ^{64}Zn(p,α) ^{61}Cu reaction at low proton energies. *Applied Radiation and Isotopes, 72,* 169-176.

Thorek, D.L.J., Elias, D.R., & Tsourkas, A. (2009). Comparative Analysis of Nanoparticle-Antibody Conjugations: Carbodiimide versus Click Chemistry. *Molecular Imaging, 8,* 221-229.

Tingwell, C.I.W., Hansper, V.Y., Tims, S.G., Scott, A.F., & Sargood, D.G. (1988). Cross sections of proton induced reactions on ^{61}Ni.*Nuclear Physics A, 480,*162-174.

Tolnai, G., Csempesz, F., Kabai-Faix, M., Kalman, E., Keresztes, Z., Kovacs, A.L..., Horvolgyi, Z.S. (2001). Preparation and characterization of surface-modified silica-nanoparticles. *Langmuir, 17,* 2683-2687.

Torchilin, V.P. (2004). Targeted polymeric micelles for delivery of poorly soluble drugs. *Cellular and Molecular Life Science, 61,* 2549-2559.

Trewyn, B.G., Giri, S., Slowing, I.I., & Lin, V.S.-Y. (2007). Mesoporous silica nanoparticle based controlled release, drug delivery, and biosensor systems. *Chemistry Communications, 2007,* 3236–3245

Uddin, M.S., Khandaker, M.U., Kim, K.S., Lee, Y.S., & Kim, G.N. (2007). Excitation functions of the proton induced nuclear reactions on ^{nat}Zn up to 40 MeV. *Nuclear Instruments and Methods in Physics Research Section B, 258,* 313-320.

University of Michigan Medical School, Cyclotron and Radiochemistry. (2015). Facility Positron Emission Tomography [image]. Retrieved from http://sitemaker.umich.edu/pet.chemistry/positron_emission_tomography

Van Helden, A.K., Jansen, J.W., & Vrij, A. (1980). Preparation and characterization of sperical monodisperse silica dispersions in nonaqueous solvents. *Journal of Colloid and Interface Science, 81,*355-368.

Vanblaaderen, A., Vangeest, J., Vrij, A. (1992). Monodisperse Colloidal Silica Spheres from Tetraalkoxysilanes: Particle Formation and Growth Mechanism. *Journal of Colloid and Interface Science, 154*, 481–501.

Varela, J.A., Bexiga, M.G., Åberg, C., Simpson, J.C., & Dawson, K.A. (2012). Quantifying size-dependent interactions between fluorescently labeled polystyrene nanoparticles and mammalian cells. *Journal of Nanobiotechnology, 10*, 39. . Retrieved from http://www.jnanobiotechnology.com/content/10/1/39

Vashist, S.K. (2012). Comparison of 1-Ethyl-3-(3-Dimethylaminopropyl) Carbodiimide Based Strategies to Crosslink Antibodies on Amine-Functionalized Platforms for Immunodiagnostic Applications. *Diagnostics, 2*, 23-33.

Vonarbourg, A., Passirani, C., Saulnier, P., & Benoit J-P (2006). Parameters influencing the stealthiness of colloidal drug delivery systems. *Biomaterials, 27*, 4356-4373.

Wadas, T.J., Wong, E.H., Weisman, G.R., & Anderson, C.J. (2007). Copper chelation chemistry and its role in copper radiopharmaceuticals. *Current Pharmaceutical Design, 13*, 3-16.

Wang, G., Wang, C., Dou, W., Ma, Q., Yuan, P., & Su, X. (2009). The Synthesis of Magnetic and Fluorescent Bi-functional Silica Composite Nanoparticles via Reverse Microemulsion Method. *Journal of Fluorescence, 19, 939-946.*

Wang, L., Yang, C., & Tan, W. (2005). Dual-Luminophore-Doped Silica Nanoparticles for Multiplexed Signaling. *Nano Letters, 5*, 37-43.

Wang, J., Tian, S., Petros, R.A., Napier, M.E. & De Simone, J. (2010). The complex role of multivalency in nanoparticles targeting the transferrin receptor for cancer therapies. *Journal of American Chemistry Society, 132,* 11306-11313.

Wang, S-H., Lee, C-W, Chiou, A., & Wei, P-K. (2010). Size-dependent endocytosis of gold nanoparticles studied by three-dimensional mapping of plasmonic scattering images. *Journal of Nanobiotechnology, 8,* 1-13. Retrieved from http://www.jnanobiotechnology.com/content/8/1/33

Wang, Y., Zhao, Q., Han, N., Bai, L., Li, J., Liu, J., … Wang, S. (2015). Mesoporous silica nanoparticles in drug delivery and biomedical applications. *Nanomedicine, 11,* 313-327.

Watanabe, S., Watanabe, S., Liang, J., Hanaoka, H., Endo, K., & Ishioka, N.S. (2009). Chelating ion-exchange methods for the preparation of no-carrier-added ^{64}Cu. *Nuclear Medicine and Biology, 36,* 587-590.

Wessels, B.W., Konijnenberg, M.W., Dale, R.G., Breitz, H.B., Cremonesi, M., Meredith, R.F., … Thomas, S.R. (2008). MIRD Pamphlet No. 20: The effect of model assumptions on kidney dosimetry and response - implications for radionuclide therapy. *Journal of Nuclear Medicine 49*: 1884-1899.

Wei, L., Yea, Y., Wadas, T.J., Lewis, J.S., Welch, M.J., Achilefu, S., & Anderson, C.J. (2009). ^{64}Cu-Labeled CB-TE2A and diamsar-conjugated RGD peptide analogs for targeting angiogenesis: comparison of their biological activity. *Nuclear Medicine and Biology,36,* 277-285.

Welch, M.J., & Redvanly, C.S. (2005). Handbook of radiopharmaceuticals: Radiochemistry and applications. New York: John Wiley & Sons, Inc.

Williams, D.C., & Irvine, J.W. (1963). Nuclear excitation functions and thick-target yields: Zn+d and ^{40}Ar(d,α) . *Physics Review, 130,* 265-271.

Wong, T.Z., Lacy, J.L., Petry, N.A., Hawk, T.C., Sporn, T.A., Dewhirst, M.W., & Vlahovic, G. (2008). PET of Hypoxia and Perfusion with ^{62}Cu-ATSM and ^{62}Cu-PTSM Using a ^{62}Zn/^{62}Cu Generator. *American Journal of Roentgenology, 190,* 427-432.

Woodin, K.S., Heroux, K.J., Boswell, C.A., Wong, E.H., Weisman, G.R., Niu, W.,… Rheingold, A.L. (2005). Kinetic inertness and electrochemical behavior of copper (II) tetraazamacrocyclic complexes: possible implications for in vivo stability. *European Journal of Inorganic Chemistry*, 2005, 4829-4833.

Wu, X., Wu, M., & Zhao, J.X. (2014). Recent development of silica nanoparticles as delivery vectors for cancer imaging and therapy. *Nanomedicine, 10,* 297-312.

Xie, X., Li, F., Zhang, H., Lu, Y., Lian, S., Lin, H.,… Jia, L. (2016). EpCAM aptamer-functionalized mesoporous silica nanoparticles for efficient colon cancer cell-targeted drug delivery. *European Journal of Pharmaceutical Sciences, 83*, 28-35.

Xiao, K., Li, Y., Luo, J., Lee, J.S., Xiao, W., Gonik, A.M.,… Lam, K.S. (2011). The effect of surface charge on in vivo biodistribution of PEG-oligocholic acid based micellar nanoparticles. *Biomaterials, 32,* 3435-3446.

Xiao, Y., Forry, S.P., Gao, X., Holbrook, R.D., Telford, W.G., & Tona A. (2010). Dynamics and mechanisms of quantum dot nanoparticle cellular uptake. *Journal of Nanobiotechnology, 8,* 13.

Xing, Y., Zhao, J., Conti, P.S., & Chen K. (2014). Radiolabeled Nanoparticles for Multimodality Tumor Imaging. *Theranostics, 4,* 290-306.

Yacobi, N.R., Demaio, L., Xie, J., Hamm-Alvarez, S.F., Borok, Z., Kim, K.J., & Crandall, E.D. (2008). Polystyrene nanoparticle trafficking across alveolar epithelium. *Nanomedicine, 4,* 139-145.

Yang, X, Hong, H., Grailer, J.J., Rowland, I.J., Javadi, A., Hurley, S.A.,… Gong S. (2011). cRGD-functionalized, DOX-conjugated, and ^{64}Cu-labeled superparamagnetic iron oxide nanoparticles for targeted anticancer drug delivery and PET/MR imaging. *Biomaterials, 32,* 4151-4160.

Ye, Z., Tan, M., Wang, G. & Yuan, J. (2005). Development of functionalized terbium fluorescent nanoparticles for antibody labeling and time-resolved fluoroimmunoassay application. *Talanta, 65,* 206-210.

Yoo, J-W, Doshi, N., & Mitragotri, S. (2010). Endocytosis and intracellular distribution of PLGA particles in endothelial cells: effect of particle geometry. *Macromolecular Rapid Communications, 31,*142-148.

Zahr, A.S., Davis, C.A., & Pishko, M.V. (2006). Macrophage uptake of core-shell nanoparticles surface modified with poly (ethylene glycol). *Langmuir, 22,* 8178-8185.

Zhang, Q., & Chuang, K.T. (2001). Adsorption of organic pollutants from effluents of a kraft pulp mill on activated. *Advances in Environmental Research, 5,* 251-258.

Zhao, Y., Trewyn, B.G., Slowing, I.I., & Lin, V.S.Y. (2009). Mesoporous silica nanoparticle-based double drug delivery system for glucose-responsive controlled release of insulin and cyclic AMP. *Journal of American Chemistry Society, 131,* 8398-8400.

Ziegler, J.F., Ziegler, M.D., & Biersack J.P. (2011). The stopping and range of ions in matter. Retrieved from http://www.srim.org/SRIM/SRIM2011.htm .

Ziegler, S.I. (2005). Positron Emission Tomography: Principles, Technology, and Recent Developments .*Nuclear Physics A, 752,* 679c-687c.

Zweit, J., Smith, A.M., Downey, S., & Sharma, H.L. (1991). Excitation Functions for Deuteron Induced Reactions in Natural Nickel: Production of No-carrier-added ^{64}Cu from Enriched ^{64}Ni Targets for Positron Tomography Emission. *Applied Radiation and Isotopes, 42*, 193-197

APPENDIX A: PUBLISHED PAPERS